Aix*Marseille université
Socialement engagée

NNT : 2023AIXM0001

# THÈSE DE DOCTORAT

Soutenue à Aix-Marseille Université
le 5 Décembre 2024 par

**Antoine SCHNEEBERGER**

# Composition of the primordial matter in protoplanetary environments : Implication for the origins of the Galilean Moons and Giant Planets.

**Discipline**
Physique et Sciences de la Matière

**Spécialité**
Astrophysique et Cosmologie

**École doctorale**
ED 352

**Laboratoire/Partenaires de recherche**
Laboratoire d'Astrophysique de Marseille

**Composition du jury**

| | |
|---|---|
| Yasuhito SEKINE<br>Institute of Science Tokyo | Rapporteur |
| Nicolas ANDRE<br>Institut de Recherche en Astrophysique et Planétologie de Toulouse | Rapporteur |
| Ravit HELLED<br>Laboratoire d'Astrophysique de Marseille | Examinatrice |
| Magali DELEUIL<br>Laboratoire d'Astrophysique de Marseille | Examinatrice |
| Pierre VERNAZZA<br>Laboratoire d'Astrophysique de Marseille | Examinateur |
| Jonathan LUNINE<br>Jet Propulsion Laboratory, California Institute of Technology | Examinateur |
| Frederic MOYNIER<br>Institut de Physique du Globe de Paris | Président du jury |
| Olivier Mousis<br>Laboratoire d'Astrophysique de Marseille | Directeur de thèse |

LAM
LABORATOIRE D'ASTROPHYSIQUE DE MARSEILLE

Institut Origines, des planètes à la vie
Aix*Marseille Université

# Affidavit

Je soussigné, Antoine Schneeberger, déclare par la présente que le travail présenté dans ce manuscrit est mon propre travail, réalisé sous la direction scientifique de Olivier Mousis, dans le respect des principes d'honnêteté, d'intégrité et de responsabilité inhérents à la mission de recherche. Les travaux de recherche et la rédaction de ce manuscrit ont été réalisés dans le respect à la fois de la charte nationale de déontologie des métiers de la recherche et de la charte d'Aix-Marseille Université relative à la lutte contre le plagiat.

Ce travail n'a pas été précédemment soumis en France ou à l'étranger dans une version identique ou similaire à un organisme examinateur.

Fait à Marseille le 18/09/2024



Cette œuvre est mise à disposition selon les termes de la Licence Creative Commons Attribution - Pas d'Utilisation Commerciale - Pas de Modification 4.0 International.

# List of publications and participation in conferences

## List of publications and/or patents produced as part of the thesis project:

1. **A. Schneeberger** and O. Mousis, "Impact of jupiter's heating and self-shadowing on the jovian circumplanetary disk structure," *Planetary Science Journal*, Submitted.

2. T. Benest-Couzinou, O. Mousis, G. Danger, **A. Schneeberger**, A. Aguichine, and A. Bouquet, "Formation and transport of complex organic molecules in protoplanetary disks," *Astronomy & Astrophysics*, Submitted.

3. O. Mousis, **A. Schneeberger**, T. Cavalié, K. E. Mandt, A. Aguichine, J. I. Lunine, T. Benest Couzinou, V. Hue, and R. Moreno, "Insights on the Formation Conditions of Uranus and Neptune from Their Deep Elemental Compositions," *The Planetary Science Journal*, vol. 5, p. 173, Aug. 1, 2024, issn: 2632-3338. doi: 10.3847/PSJ/ad58d8.

4. O. Mousis, T. Cavalié, J. I. Lunine, K. E. Mandt, R. Hueso, A. Aguichine, **A. Schneeberger**, T. Benest Couzinou, D. H. Atkinson, V. Hue, M. Hofstadter, and U. Srisuchinwong, "Recipes for Forming a Carbon-Rich Giant Planet," *Space Science Reviews*, vol. 220, p. 44, Jun. 1, 2024, issn: 0038-6308. doi: 10.1007/s11214-024-01071-4.

5. J. C. Costes, J. W. Xuan, A. Vigan, J. Wang, V. D'Orazi, P. Mollière, A. Baker, R. Bartos, G. A. Blake, B. Calvin, S. Cetre, J. Delorme, G. Doppmann, D. Echeveri, L. Finnerty, M. P. Fitzgerald, C. Hsu, N. Jovanovic, R. Lopez, D. Mawet, E. Morris, J. Pezzato, C. L. Phillips, J. Ruffio, B. Sappey, **A. Schneeberger**, T. Schofield, A. J. Skemer, J. K. Wallace, and J. Wang, "Fresh view of the hot brown dwarf HD 984 B through high-resolution spectroscopy," *Astronomy & Astrophysics*, vol. 686, A294, Jun. 1, 2024, issn: 0004-6361. doi: 10.1051/0004-6361/202348370.

6. **A. Schneeberger**, O. Mousis, M. Deleuil, and J. I. Lunine, "Formation of the Trappist-1 system in a dry protoplanetary disk," *Astronomy & Astrophysics*, vol. 682, p. L10, Feb. 1, 2024, issn: 0004-6361, 1432-0746. doi: 10.1051/0004-6361/202348309.

7. O. Mousis, **A. Schneeberger**, J. I. Lunine, C. R. Glein, A. Bouquet, and S. D. Vance, "Early stages of galilean moon formation in a water-depleted environment," *The Astrophysical Journal Letters*, vol. 944, no. 2, p. L37, Feb. 1, 2023, issn: 2041-8205, 2041-8213. doi: 10.3847/2041-8213/acb5a4.

8. **A. Schneeberger**, O. Mousis, A. Aguichine, and J. I. Lunine, "Evolution of the reservoirs of volatiles in the protosolar nebula," *Astronomy & Astrophysics*, Jan. 5, 2023, issn: 0004-6361, 1432-0746. doi: 10.1051/0004-6361/202244670. arXiv: 2301.02482[astro-ph]

# Participation in conferences and summer schools during the thesis period:

1. O. Mousis, **A. Schneeberger**, T. Cavalié, K. Mandt, A. Aguichine, J. Lunine, T. Benest Couzinou, V. Hue, and R. Moreno, "Elemental Composition of Uranus and Neptune: Insights from Building Blocks," presented at the Europlanet Science Congress, Jul. 3, 2024. doi: 10.5194/epsc2024-319.

2. A. Schneeberger and O. Mousis, "Impact of jupiter's heating and self-shadowing on its Circumplanetary disk structure," presented at the Europlanet Science Congress, Jul. 3, 2024. doi: 10.5194/epsc2024-203.

3. O. Mousis, **A. Schneeberger**, K. Mandt, A. aguichine, J. Lunine, T. benest, V. Hue, and T. Cavalié, "Prediction for the deep compositions of Uranus and Neptune," presented at the AAS/Division for Planetary Sciences Meeting Abstracts, vol. 55, Oct. 1, 2023, p. 409.01. url: https://ui.adsabs.harvard.edu/abs/2023DPS....5540901M

4. O. Mousis, **A. Schneeberger**, K. E. Mandt, J. I. Lunine, V. Hue, and T. Cavalié, "Predictions for the Deep Compositions of Uranus and Neptune," presented at the LPI Contributions, vol. 2808, Jul. 1, 2023, p. 8100, isbn: 0161-5297. url: https://ui.adsabs.harvard.edu/abs/2023LPICo2808.8100M

5. **A. Schneeberger** and O. Mousis, "The fate of volatiles within Jupiter's Circumplanetary Disk," presented at the AAS/Division for Planetary Sciences Meeting Abstracts, vol. 55, Oct. 1, 2023, p. 509.02.
url: https://ui.adsabs.harvard.edu/abs/2023DPS....5550902S.

6. **A. Schneeberger**, O. Mousis, V. Hue, and T. Cavalié', "Gas-Phase Chemistry of the Jovian Circumplanetary Disk," in Interplanetary Probe Workshop, Sep. 2023.

7. **A. Schneeberger**, O. Mousis, and T. Cavalié', "Gas-Phase Chemistry of the Jovian Circumplanetary Disk," in PLanet – ESLAB, Mar. 2023.

8. **A. Schneeberger**, O. Mousis, T. Cavalié, and J. Lunine, "A 2-dimensional model of the Jovian circumplanetary disk," in European Planetary Science Congress, Sep. 2022, EPSC2022-905, EPSC2022–905. doi: 10.5194/epsc2022-905.

9. **A. Schneeberger**, O. Mousis, A. Aguichine, and J. Lunine, "Evolution of the reservoir of volatiles in the protosolar nebula," in European Planetary Science Congress, Sep. 2022, EPSC2022-881, EPSC2022–881. doi: 10.5194/epsc2022-881.

10. O. Mousis, **A. Schneeberger**, J. Lunine, C. Glein, A. Bouquet, S. Vance, and V. Vinogradoff, "The role of phyllosilicates in shaping the Galilean moons' density gradient," in European Planetary Science Congress, Sep. 2022, EPSC2022-855, EPSC2022–855. doi: 10.5194/epsc2022-855

11. **A. Schneeberger** and O. Mousis, "Phyllosilicates as a source of water in the Trappist-1 protoplanetary disk," in European Planetary Science Congress, Sep. 2022, EPSC2022-421, EPSC2022–421. doi: 10.5194/epsc2022-421.

12. O. Mousis, A. Aguichine, **A. Schneeberger**, T. Cavalié, J. I. Lunine, K. E. Mandt, and U. Srisuchinwong, "Jupiter's Possible Low Water Abundance as a Testimonial of Peculiar Formation Conditions," in LPI Contributions, ser. LPI Contributions, vol. 2686, Jul. 2022, 4037, p. 4037.

13. **A. Schneeberger**, O. Mousis, A. Aguichine, and J. Lunine, "Evolution of the reservoir of volatiles in the protosolar nebula," in EGU General Assembly Conference Abstracts, ser. EGU General Assembly Conference Abstracts, May 2022, EGU22-5270, EGU22–5270. doi: 10.5194/egusphere-egu22-5270.

14. O. Mousis, E. Marcq, A. Aguichine, F. Leblanc, K. Mandt, **A. Schneeberger**, and M. Turbet, "Io's dry body shaped by atmospheric instability," in European Planetary Science Congress, Sep. 2021, EPSC2021-187, EPSC2021–187. doi: 10.5194/epsc2021-187.

# Résumé et mots clés

Cette étude porte sur la formation des planètes géantes, sur l'évolution du système jovien, et fournit contraintes pour les prochaines missions ESA/JUICE, NASA/Europa-Clipper et NASA/Uranus Orbiter and Probe. Ce travail est divisé en deux parties. Premièrement, il examine l'imapact des espèces volatiles, considérant les condensats purs, les clathrates hydrates et la glace d'eau amorphe, dans la formation de Jupiter, Saturne, Uranus et Neptune au sein du disque protoplanétaire (PPD). L'étude montre que les clathrates rapprochent les éléments volatils du Soleil par rapport aux condensats purs, ce qui entraîne des pics d'enrichissement significatifs, tandis que la glace d'eau amorphe crée des zones d'enrichissement distinctes. La comparaison de la composition du PPD modélisée avec les atmosphères des planètes géantes observées révèle les periodes et les régions de formation des planètes. Cependant, nous ne confirmons ni n'excluons la présence de clathrates ou de glace d'eau amorphe dans la PPD, soulignant ainsi l'importance de mesures supplémentaires des compositions atmosphériques des planètes géantes pour affiner ces modèles.

La deuxième partie du travail se concentre sur le disque circumplanétaire (CPD) de Jupiter, en particulier sa structure thermique et le rôle du chauffage la chaude Jupiter et des effets d'ombre dans la formation du disque. Elle montre que les régions ombragées forment des *cold traps*, ou pièges froids, pour les espèces volatiles dans les régions chaudes du disque cirumplanétaire. En outre, nous montrons que si le disque cirumplanétaire est chaud, il devient pauvre en volatils, alors que s'il est froid, il reste riche en volatils. Nous étudions également la possibilité d'un disque "sec", où l'eau est fournie principalement par des minéraux hydratés, et nous appliquons ce concept au système exoplanétaire TRAPPIST-1, suggérant des parallèles entre la distribution de l'eau dans les planètes TRAPPIST-1 et les lunes galiléennes.

Enfin, le développement d'un modèle chimique auto-cohérent pour le CPD est présenté, en se concentrant sur la composition chimique en phase gazeuse à l'équilibre thermochimique. Les premiers résultats indiquent une stratification verticale de la composition dans le disque, bien que les processus de non-équilibre dominent probablement dans les régions plus froides. Dans l'ensemble, ce travail jette les bases pour la construction de l'histoire de la formation de Jupiter et de ses lunes, en soulignant la nécessité de disposer de données d'observation supplémentaires et d'affiner les modèles afin de découvrir les origines du système jovien.

Mots clés: Système solaire, Formation planétaire, Astrochimie, Disque protoplanétaire, Disque circumplanétaire, Lunes galiléennes

# Abstract and keywords

This study investigates the formation of giant planets and the evolution of the Jovian system, providing insights to support upcoming space missions such as ESA's JUICE, NASA's Europa Clipper and NASA's Uranus Orbiter and Probe. This work is divided into two parts. First, it examines the role of volatile species pure condensates, clathrate hydrates and amorphous water ice, in the formation of Jupiter, Saturn, Uranus, and Neptune within the sun's protoplanetary disk (PPD). The study shows that clathrates bring volatile elements closer to the Sun than pure condensates, resulting in significant enrichment peaks, while amorphous water ice creates distinct enrichment zones. Comparing the modeled PPD composition with observed giant planet atmospheres reveals timescales and regions of planet formation, however we do not confirm, nor rule out the presence of clathrates hydrates or amorphous ice in the PPD, therefore highlighting the importance of further atmospheric measurements to refine these models.

The second part of the work focuses on the circumplanetary disk (CPD) of Jupiter, particularly its thermal structure and the role of heating and shadowing effects in shaping the disk. It shows that the shadowed regions form cold traps for volatile species within hot regions of the cirumplanetary disk. Furthermore, we show that if the CPD is hot it becomes volatile poor, while if it is cold it stays volatile rich. We also investigate the possibility of a "dry" CPD, where water is delivered primarily by hydrated minerals, and applies this concept to the exoplanetary system TRAPPIST-1, suggesting parallels between the water distribution in the TRAPPIST-1 planets and the Galilean moons.

Finally, the development of a self-consistent chemical model for the CPD is presented, focusing on gas-phase chemical composition under thermochemical equilibrium. Initial results indicate vertical compositional layering in the disk, though non-equilibrium processes likely dominate in colder regions. Overall, this research lays the groundwork for understanding the formation of Jupiter and its moons, emphasizing the need for further observational data and model refinement to fully unravel the Jovian system's origins.

Keywords: Solar system, Planetary formation, Astrochemistry, Protoplanetary disks, Circumplanetary disks, Galilean moons

# Résumé en français

## 0.1. Chapitre 1 : Introduction

La formation des planètes a lieu dans un disque protoplanétaire (PPD) constitué de gaz et de poussières qui entourent le proto-Soleil pendant les premiers millions d'années de son existence. Cependant, le chemin évolutif précis qui mène du disque protoplanétaire au système planétaire actuel reste largement inconnu. Pour comprendre la formation des planètes et des lunes du système solaire, il est essentiel d'étudier la structure, la composition et l'évolution du PPD.

La matière constituant le soleil et le PPD proviennent tous deux d'un nuage moléculaire froid qui s'est effondré sur lui-même, formant un amas d'étoile ouvert contenant le soleil. La composition élémentaire originale du soleil, et donc du PPD, peut être déduite de la composition de la photosphère du Soleil (Lodders 2003, 2019, 2021). Bien que la photosphère solaire actuelle ne reflète pas exactement la composition protosolaire du Soleil, les modèles d'évolution stellaire permettent de reconstruire sa composition globale originale (Lodders 2021).

Cependant, bien que nous connaissions la composition atomique originale du PPD, nous ne connaissons pas sa composition moléculaire, et celle de la matière provenant du nuage moléculaire. Nous supposons que la composition du PPD a laissé des traces dans les compositions des planètes géantes.

En effet, nous constatons que la composition atomique de l'atmosphère de Jupiter, mesurées par les sondes NASA/Galileo et NASA/JUNO présentent des enrichissements entre 1.6 et 6.1 fois les valeurs solaires (Mahaffy et al. 2000 ; Wong et al. 2004 ; Fletcher et al. 2009). Bien que ces mesures d'abondances soient moins complètes que dans les cas de Saturne, Uranus et Neptune, elles présentent aussi des enrichissements atomiques. Ceux-ci peuvent atteindre jusqu'à 11 fois la valeur solaire dans le cas de Saturne, et jusqu'à 100 fois l'abondance solaire pour le carbone dans le cas d'Uranus et Neptune.

Nous souhaitons donc nous appuyer sur les travaux de Aguichine et al. (2022), en améliorant son modèle pour explorer la distribution des volatils au sein du PPD et tester la présence de phases d'espèces volatiles autres que les condensats purs et la vapeur. Cela permettra de mieux contraindre les processus de formation des planètes géantes et de préparer le retour scientifique de *Uranus Orbiteur and Probe* (UOP) qui

vise à étudier la composition d'Uranus dans les années 2040 (Simons et al. 2021).

Une deuxième partie de ce travail se concentre sur la formation des lunes galiléennes. Il est supposé que les lunes Galiléennes se sont formées dans un disque circumplanétaire composé de gaz, de poussières et de glaces. Ce disque serait issu de la formation de Jupiter et accréterait de la matière provenant du PPD.

Le système Galiléen, du fait de sa masse de $2.07 \times 10^{-4}$ $M_J$, et de sa structure, présentant un gradient de densité avec la distance à Jupiter, reste un challenge pour les modèles de formation. Ainsi, mieux comprendre la structure et composition du CPD est nécessaire pour affiner les modèles de formations. Ainsi, nous avons pour objectif de modéliser ce disque afin d'en étudier sa structure et sa composition.

Ce manuscrit se compose ainsi, nous présentons dans le chapitre 2 les différentes phases des espèces volatiles que nous étudions, puis nous présentons dans le chapitre 3 le modèle de PPD ainsi que d'évolution des espèces volatile. Le chapitre 4 présentes les compositions du PPD obtenus grâce au modèle et ce que cela implique pour les planètes géantes. Le chapitre 5 présente le modèle de CPD 2D développé dans le cadre de ce travail. Sa structure et composition sont présentées dans le chapitre 6, suivi de l'étude de l'impact des phyllosilicates sur la distribution d'eau dans le CPD jovien ainsi que dans le PPD de Trappist-1, un système analogue au système Jovien. Enfin, le chapitre 7 présentes des résultats préliminaire d'un modèle de réseau chimique appliqué aux conditions du CPD.

## 0.2. Chapitre 2 : Sources des espèces volatiles

Dans ce chapitre, nous présentons les différentes sources des espèces volatiles dans les disques protoplanétaires et circumplanétaire. Dans ce travail, nous considérons $H_2O$, CO, $CO_2$, $CH_4$, $NH_3$, $N_2$, $PH_3$, $H_2$, qui sont les espèces volatiles, principaux vecteurs des atomes de carbone, d'oxygènes, d'azote, de phosphore et de soufre.

Dans un premier temps, nous considérons la ligne de condensation des espèces chimiques, qui a été proposé comme un mécanisme pour enrichir en volatiles le PPD (Booth et al. 2017). Dans les régions les plus reculées du PPD, la température peut descendre jusqu'à 10 K, résultant en la condensation des espèces volatiles sur des grains orbitant dans le PPD. Ces grains vont dériver vers l'intérieur du système, perdant de l'énergie par frottement avec le gaz environnent. Jusqu'au point où les grains atteignent une zone assez chaude pour provoquer la vaporisation d'un composé volatile, cette zone est la ligne de condensation. Puisqu'à l'inverse, lorsque de la vapeur, venant des régions internes du disque, traverse cette ligne, elle va condenser sur les grains. La ligne de condensation peut être le lieu d'enrichissement en volatiles de l'ordre de 2 à 20 fois l'abondance protosolaire (Aguichine et al. 2022).

En plus des condensats purs, nous considérons dans les modèles la possibilité que les molécules des espèces volatiles puissent être piégées dans des cages de molécules d'eau, appelées clathrates. Dans le PPD, il est modélisé que les clathrates se forment

à partir de l'interaction entre la glace d'eau et la phase vapeur des volatiles (Lunine et al. 1982). De manière similaire à la ligne de condensation, il existe une ligne de clathration, à laquelle la vapeur est piégé dans des clathrates. Les clathrates se formant à plus haute température que les condensats purs, la ligne de clathration se situe plus près du soleil que la ligne de condensation. Il existe une exception à cette règle, le clathrate de $CO_2$, dont le clathrate se forme à plus température que le condensat pur.

La formation des cages de clathrate implique la présence de glace d'eau sous forme cristalline, or la glace d'eau dans le milieu interstellaire est sous forme amorphe (Gibb et al. 2004). Afin que la glace d'eau transitionne d'amorphe à cristalline, elle doit être portée à une température de 135 K (Bar-Nun et al. 2007). Ainsi, si la glace d'eau accrétée par le PPD n'est pas chauffée à cette température, elle reste sous forme amorphe. La glace d'eau amorphe est très efficace pour piéger en son sein les molécules des espèces volatiles, qui ne peuvent être relâchées dans le PPD que lorsque la glace change de conformation. Dans ce type de scénario, les volatiles sont accrétés par le PPD piégés dans de la glace amorphe et relâchés dans le PPD sous forme de vapeur seulement dans la région du disque ayant une température de 135 K, appelé dans ce travail la *Amorphous–to–Crystalline Transition Zone* (ACTZ).

Enfin, l'eau peut être transportée, non pas sous forme de glace, mais sous forme de minéraux hydratés inclus dans des roches. C'est ce qui est observé dans les chondrites CI et CM qui sont principalement composées d'une matrice de phyllosilicates, un type de minéraux hydratés (Beck et al. 2010, 2014 ; Alexander 2019). Dans les phyllosilicates, l'eau peut représenter jusqu'à 13% de la masse du minéral. La température de déshydratation des phyllosilicates à très faible pression est peu connue, nous ne disposons que de mesures à des pressions représentatives de l'atmosphère martienne, de l'ordre de $10^{-3}$ bar (Lange et al. 1982 ; Cloutis et al. 2007 ; Cloutis et al. 2008 ; Liang et al. 2022). Ainsi, nous nous sommes basés sur des modèles chimiques ad-hoc qui proposent des températures de déshydratation entre 400 et 600 K (Mousis et al. 2023). Ainsi, les phyllosilicates formeraient une source de vapeur d'eau dans les régions chaude du PPD et du CPD.

## 0.3. Chapitre 3 : Le modèle de disque protoplanétaire et de transport des espèces volatiles

Dans ce chapitre, nous présentons le modèle d'évolution du disque protoplanétaire et des espèces volatiles en son sein. Le modèle de disque suit la théorie des disques $\alpha$–visqueux développé par Shakura et al. 1973. Nous décrivons succinctement le modèle de disque $\alpha$-visqueux implémenté dans le modèle numérique que nous utilisons développé par Aguichine (2022).

Ensuite, nous présentons le modèle d'évolution des espèces volatiles dans le CPD, qui suivent une équation d'advection–diffusion. La taille des galets dans le PPD sont déterminés grâce au *two-population algorithm* développé par Birnstiel et al. (2012). Algorithme qui considère que la population de grains et galets dans le PPD peut être modélisé en considèrent seulement les grains les plus petits et les galets les plus gros pour en déduire une taille moyenne.

Dans ce modèle, nous considérons quatre phases pour les espèces volatiles. D'abord, les phases vapeur et condensats pures présentes à l'origine dans le modèle de Aguichine et al. (2022). À cela, nous avons ajouté les clathrates hydrates et la glace d'eau amorphe.

## 0.4. Chapitre 4 : Application aux planètes géantes

Nous appliquons le modèle présenté dans le chapitre précédent dans deux scénarios distincts. Dans le premier, nous faisons l'hypothèse que les espèces volatiles ont été accrétées sous forme de condensats purs. Dans le deuxième, les espèces volatiles ont été accrétées piégées dans de la glace d'eau amorphe.

De ces deux scénarios, résulte des compositions du PPD radicalement différentes. Dans le premier, les lignes de clathration et de condensation sont le lieu de pics d'enrichissement en espèce volatile entre 5 et 23 fois les abondances initiales. Cela démontre que la présence de clathrate dnas le PPD à un impact sur sa composition. Ils permettent l'apport de volatiles dans les phases solides jusqu'à 2 UA plus proche du soleil que la ligne de condensation.

Dans le second scénario, le processus de clathration ne peut se produire avec de la glace d'eau amorphe, donc les clathrates ne peuvent pas se former dans ce scénario. Les volatiles sont relâchés dans le disque sous forme de vapeur à l'ACTZ, situé à 5 UA du soleil. Cela forme des pics d'enrichissement de l'ordre de 7 à 10 fois la valeur protosolaire dans une région centrée autour de 5 UA.

Par la suite, nous comparons la composition du PPD avec les compositions atmosphériques observées des planètes géantes. Dans le premier scénario, la composition atmosphérique de Jupiter correspond à la composition du PPD dans une région autour de 4 UA après 0,8 à 1 Myr d'évolution. Cependant, dans le deuxième scenario, cette période est réduite à 20 à 100 kyr dans une région entre 4 et 6 UA.

Dans le cas de Saturne, quand l'on considère le premier scenario, aucune période de correspondance n'existe dans la région entre 5 et 7 UA. En revanche, dans le deuxième scénario, une période de concordance apparaît entre 30 et 400 kyr d'évolution du PPD.

La comparaison du modèle de PPD avec les estimations de l'enrichissement en

carbone d'Uranus et de Neptune suggère que les géantes de glace pourraient s'être formées entre 7 et 9 AU sur une période de 0.5 à 1 Myr, mais seulement en l'absence de glace amorphe. Cet endroit est proche de la ligne de condensation du CO dans notre modèle. Nous avons alors étudié la possibilité de la formation des géantes glacées à la ligne de condensation de CO. Ce faisant, nous avons montré que cela résulterait en des enrichissements jusqu'à mille fois les valeurs protosolaires en gaz nobles.

## 0.5. Chapitre 5 : Le disque circumplanétaire de Jupiter

Nous présentons dans un premier temps une revue succincte des modèles de disque circumplanetaire (CPD). Il existe deux types de modèles de disque circumplanétaire. Le modèle dit de *Minimum Mass Subnebula (MMSN)* considère que l'on peut remonter à la masse originale du CPD de Jupiter à partir de la masse des lunes Galiléennes, en faisant l'hypothèse que le CPD avait une métallicité protosolaire. Il suffit de considérer que les lunes Galiléennes représente la masse totale de poussière présente dans le CPD, et d'y ajouter la masse de gaz nécessaire afin d'atteindre la métallicité protosolaire. Ce faisant, nous pouvons déduire une masse de $10^{-2}$ $M_J$pour le CPD de Jupiter (Lunine et al. 1985 ; Mosqueira et al. 2003). Une telle masse produit un CPD très chaud , dont la température peut monter jusqu'à 2000 K.

De l'autre côté du spectre, nous trouvons le modèle *Gas Starved Disk*. Celui-ci considère que le CPD était encore alimenté par le PPD (Canup et al. 2002, 2006). Ainsi, le CPD ne contient pas, de manière instantanée, toute la masse des lunes sous forme de poussières et de glaces, résultants en un CPD beaucoup moins massif que celui considéré le modèle MMSN. De ce fait, le CPD est beaucoup plus froid que la MMSN, et permet la formation de glace d'eau proche de Jupiter.

Cependant, bien ces deux modèles permettent d'étudier l'évolution des CPD sur plusieurs millions d'années, les modèles 3D hydrodynamiques permettent une étude plus précise et physiquement réaliste. Ces modèles montrent l'importance de la luminosité de Jupiter, résultant de son accrétion finale. En effet, certains modèles 3D semblent montrer que la planète peut monter à des températures supérieures à 2000 K (Szulágyi et al. 2016).

Partant de ce constat, nous avons construit un modèle de CPD 2D, qui prend en compte les effets de l'échauffement du CPD provoqué par Jupiter. À partir du modèle présenté par Makalkin et al. (1995, 2014) et Heller (2015), nous considérons une table d'opacité plus complexe et avons construit un module se transfère radiatif en considérant l'approximation d'atmosphère grise proposée par Makalkin et al. (1995). Notre modèle de CPD est séparé en deux régions distinctes, la première est optiquement épaisse et adiabatique, située proche de la planète ou le disque est le plus massif. La deuxième est optiquement fine et verticalement isotherme, éloignée de la planète, où

le disque est peu dense. À la transition entre les deux régions, la région opaque projette une ombre sur une partie de la région optiquement fine, provoquant des chutes de températures. Enfin, le modèle est dépendant du taux d'accrétion de matière sur le CPD en fonction du temps. Nous ne modélisons pas l'accrétion de matière et nous devons nous baser sur prescriptions que nous détaillerons dans le chapitre suivant.

Dans ce chapitre, nous détaillons aussi la méthode numérique employée pour résoudre le transfère radiatif. Nous avons implémenté une méthode de résolution *Jacobian-Free Newton-Krylov (JFNK)*, qui opère une descente de gradient sur les bases de la méthode de newton, sans avoir à explicitement calculer le jacobien du système (Knoll et al. 1993).

## 0.6. Chapitre 6 : Structure du disque circumplanétaire, implication sur sa composition volatile et disque protoplanétaire de Trappist-1

Dans un premier temps, nous calculons la structure du CPD en considérant le taux d'accrétion de matière sur le système Jovien, au moment de sa formation, proposé par Mordasini (2013). Ce taux d'accrétion sur le CPD prend en compte le creusement d'un d'un sillon autour de Jupiter. Le modèle de Mordasini (2013) à la particularité de montrer une chute rapide du taux d'accrétion après la formation de Jupiter. Impliquant que le CPD ne puisse exister que seulement pendant moins de 1 Myr.

Ainsi, en considérant ce taux d'accrétion diminuant rapidement, nous montrons que le CPD à une masse maximale de seulement $10^{-4}$ $M_{\rm J}$, deux ordres de grandeurs trop faibles pour contenir de manière instantanée la quantité de poussière et de glace nécessaire à la formation des lunes Galiléennes. Cependant, la masse cumulée accrétée sur une période de 400 kyr atteint $1.2 \times 10^{-2}$ $M_{\rm J}$, suffisant pour former les lunes. De plus, nous montrons que, par l'effet combiné de l'échauffement visqueux et celui dû par Jupiter, la température du CPD peut atteindre 2270 K après 30 kyr d'évolution. Cependant, la masse du CPD diminuant rapidement, la température du CPD atteint les 800 K au plus chaud après 200 kyr d'évolution.

Nous montrons aussi que l'effet des ombres devient non négligeable dans une période entre 150 et 200 kyr d'évolution. En effet, nous constatons que ces ombres provoquent des chutes de température de l'ordre de 100 K, dans les zones chaude du CPD. Nous montrons que la durée et les morphologies de ces ombres est très dépendante de la métallicité du disque. Nous avons testé des métallicités allant de 0.1 à 10 fois la valeur protosolaire. Nous montrons que le disque à une forte métallicité, plus les ombres sont étendues et durent longtemps.

Les ombres qui traversent notre modèle de disque sont propices au piégeage d'espèces volatiles dans des zones chaudes du disque. En effet, ces ombres entrainant des chutes de températures de 100 K, les glaces de $H_2O$, $NH_3$, $CO_2$ et $H_2S$ peuvent se former en leur sein.

Dans un deuxième temps, nous avons présenté des résultats préliminaires du modèle d'évolution des espèces volatiles appliqué au CPD. À cause d'instabilités numériques, nous ne pouvons montrer l'effet des *cold traps* sur la distribution des volatiles. Nous montrons deux cas extrêmes. L'un est un disque massif et chaud, dont l'évolution du taux d'accrétion est basé sur le travail de Sasaki et al. (2010). Ce disque ne se dissipe pas avant 3 Myr après la formation de Jupiter. L'autre est le modèle présenté plus haut, mais sans considérer le chauffage par Jupiter, résultant en un disque peu massif et froid.

Dans le premier cas, nous constatons que les lignes de condensation de toutes les espèces considérées sont au-delà du rayon centrifuge du CPD situé à 50 $R_J$, sauf pour $H_2O$. La conséquence directe de cette situation est l'épuisement rapide de ces espèces en moins de 10 kyr d'évolution. Après 200 kyr d'évolution, seul $H_2O$ subsiste, avec un pic d'enrichissement au niveau de sa ligne de condensation de 1,2 fois son abondance initiale. Dans le deuxième cas, les lignes de condensation des espèces sont toutes situées dans le rayon centrifuge. Cela conduit à un enrichissement des espèces volatiles entre 0,1 et 1,2 fois leur abondance initiale, en dessous de l'unité. Cela montre qu'en raison de la dynamique rapide de la CPD, dans ce modèle, un pic d'enrichissement important ne peut pas être maintenu. Le fait que les deux cas conduisent à des résultats radicalement différents motive l'étude en cours des *cold traps*, qui pourrait montrer des différences radicales par rapport aux deux cas.

Enfin, nous avons étudié l'apport de minéraux hydratés au CPD, en effet les mesures opérées par JUNO n'excluent pas la possibilité que l'abondance en oxygène est sous-solaire Li et al. (2020). Cela serait le signe que Jupiter et son CPD se sont formés à partir de matériaux chondritic, riche en phyllosilicates. Nous explorons cette hypothèse en adaptant le modèle de CPD 1D, de type *gas staved disk* developé par Anderson et al. (2021). Nous montrons que ces minéraux peuvent être une source d'eau pour le CDP, notamment grâce à leur déshydratation qui libère de la vapeur d'eau qui condense à la ligne de condensation de l'eau. Nous pouvons produire des grains très riches en eau, cohérent avec la proportion en eau des lunes.

Ce résultat nous pousse à tester ce scénario sur le système Trappist-1. Ce système est analogue au système Galiléen grâce à sa structure et la taille de son étoile, une naine rouge. De plus, le système de Trappist-1 présent le même gradient de densité que celui présent dans le système Galiléen. Enfin, nous étudions la possibilité d'un PPD pauvre en eau, car les forts vents stellaires que les naines rouges produisent lorsqu'elles se forment peuvent détruire les molécules d'eau (Shkolnik et al. 2014 ; Parke Loyd et al. 2018). Nous montrons que, si le PPD ne contenait que des minéraux hydratés, nous pouvons former des galets avec des fractions de masse d'eau compatibles avec celles

des planètes du système (Acuña et al. 2021) . Bien que le PPD de TRAPPIST-1 n'ait pas été entièrement sec, cela suggère que les minéraux hydratés aient pu jouer un rôle dans la distribution de l'eau à l'intérieur des PPD et des CPD.

## 0.7. Chapitre 7 : Application d'un modèle chimique au disque circumplanétaire Jovien

Bien que l'étude de la composition du CPD par le prisme des lignes de condensation offre une première approximation, elle ne permet pas l'étude fine de la composition du disque. En effet, cette approche ne prend pas en compte les réactions chimiques au sein du CPD qui peuvent altérer les abondances des espèces volatiles. Ainsi, cette approche ne permet pas d'étudier les régions chaudes du CPD, où le temps caractéristique de réaction est plus court que celui du CPD. De plus, cette approche ne permet pas d'étudier les effets des rayonnements UV dans les hautes couches du CPD qui induisent de la photochimie, altérant encore plus la composition du gaz et produisant une couche d'ions à la surface du disque (Oberg et al. 2022a).

Ainsi, dans ce chapitre, nous avons pour but d'adapter le modèle chimique utilisé pour caractériser l'atmosphère de Jupiter, développé par Agúndez et al. (2012), Venot et al. (2012), Venot (2012) et Cavalié et al. (2017) , à son CPD.

Dans un premier temps, nous étudions la composition chimique du CPD à l'équilibre thermochimique avec le logiciel `ACE` développé par Agúndez et al. (2012) et Al-Refaie et al. (2021, 2022). Nous montrons qu'à l'équilibre thermochimique, les molécules étudiées forment des couches verticalement, reproduisant ce qui est observé dans les modèles de PPD (Woitke et al. 2016). De plus, les ombres projetées sur le CPD ont un impact sur sa composition, les zones ombragées présentant des abondances nettement différentes, par rapport à leur environnement.

Nous utilisons les résultats à l'équilibre thermochimique comme conditions initiales pour le modèle d'évolution hors de l'équilibre chimique. En effet, lorsque que le temps caractéristique de diffusion est plus court que celui de réaction, l'équilibre ne peut jamais être atteint, notamment dans les régions froides du CPD. Ainsi, nous présentons le travail d'adaptation de ce modèle au CPD et les problèmes numériques rencontrés.

## 0.8. Conclusion

Ce travail explore les origines du système solaire, en se concentrant sur la formation des planètes géantes au sein du PPD et des lunes galiléennes au sein du disque circumplanétaire CPD de Jupiter. Il sert de base à la construction d'une histoire cohérente du système jovien, dans le but de soutenir les objectifs scientifiques des missions

ESA/JUICE et NASA/Europa Clipper.

Ce travail est séparé en deux thématiques, la première explore les marqueurs de la formation des planètes des géantes dans leurs compositions en étudiant la composition du PPD. Nous montrons que, bien que nous puissions inférer des lieux et temps de formations, nous ne pouvons pas confirmer, ni exclure, la présence de clathrates ou de glace d'eau amorphe dans le disque. Cela demanderait des mesures plus présices des compositions atmosphériques des planètes Géantes.

La deuxième thématique explore l'origine du système galiléen par l'étude de la structure et composition du CPD jovien. Nous avons développé un modèle 2D de CPD, qui démontre l'importance du chauffage de Jupiter, qui peut augmenter les températures du CPD jusqu'à 2000 K. Ce chauffage affecte notamment les régions internes de la CPD, lorsque le disque devient moins massif et plus diffus. Si la durée de vie du CPD est inférieure à 1 Myr, pendant la phase de transition d'un disque dense à un disque peu dense, des ombres sont projetées depuis les régions internes vers les périphéries du CPD. Ces ombres influencent considérablement la structure du disque, provoquant une baisse de température pouvant atteindre 100 K et une augmentation de la pression d'un facteur d'environ deux.

Nous avons montré que les *cold traps* piégent des glaces de $H_2O$, $NH_3$, $CO_2$ et $H_2S$, ayant donc un impact sur leurs distributions dans le CPD. Nous

Ce travail théorique dépend des découvertes qui seront faites par les futures missions telles qu'ESA/JUICE et NASA/Europa–Clipper, qui amélioreront notre compréhension de la structure et de la composition du système jovien. Enfin, il souligne la nécessité de sonder l'atmosphère des planètes géantes pour comprendre et démêler les hypothèses existantes sur la séquence de formation des planètes.

# Remerciements

# Contents

**Affidavit** 2

**List of publications and participation in conferences** 3

**Résumé et mots clés** 6

**Abstract and keywords** 7

**Résumé en français** 8
- 0.1. Chapitre 1 : Introduction . . . 8
- 0.2. Chapitre 2 : Sources des espèces volatiles . . . 9
- 0.3. Chapitre 3 : Le modèle de disque protoplanétaire et de transport des espèces volatiles . . . 10
- 0.4. Chapitre 4 : Application aux planètes géantes . . . 11
- 0.5. Chapitre 5 : Le disque circumplanétaire de Jupiter . . . 12
- 0.6. Chapitre 6 : Structure du disque circumplanétaire, implication sur sa composition volatile et disque protoplanétaire de Trappist-1 . . . 13
- 0.7. Chapitre 7 : Application d'un modèle chimique au disque circumplanétaire Jovien . . . 15
- 0.8. Conclusion . . . 15

**Remerciements** 17

**Contents** 18

**List of Figures** 22

**List of Tables** 25

**1. Introduction** 26
- 1.1. Protoplanetary disk initial composition . . . 26
- 1.2. Insight from the composition of the Giant planets on their formation history . . . 29
- 1.3. The origin of the Galilean Satellites . . . 34
- 1.4. Chemistry within the circumplanetary disk . . . 37
- 1.5. Outline . . . 39

**2. Volatile bearing phases** 41
- 2.1. Condensation lines . . . 41

2.2. Clathrate hydrates . . . 42
2.3. Amorphous water . . . 45
2.4. Hydrated minerals . . . 46
2.5. Equations of States . . . 49
2.5.1. Pure condensates . . . 49
2.5.2. Clathrate hydrates . . . 52

**3. Protoplanetary disk and volatile transport models 53**
3.1. The protoplanetary disk . . . 53
3.2. Evolution of volatile species in the protoplanetary disk . . . 56
3.2.1. Volatile evolution model setup . . . 56
3.2.2. Species advection-diffusion evolution equation . . . 57
3.2.3. Dust and pebbles evolution . . . 58
3.2.4. Sources and sinks of trace species . . . 60

**4. Application to Giant planets 62**
4.1. Distribution of volatile species in the protoplanetary disk . . . 62
4.1.1. Model setup . . . 62
4.1.2. Volatile species radial distribution . . . 63
4.1.3. Water evolution in the PPD . . . 64
4.1.4. Initial delivery of pure condensates . . . 65
4.1.5. Initial delivery of species trapped in amorphous water ice . . . 68
4.1.6. Variation of the model parameters . . . 70
4.2. Implications for Giant planets formation . . . 81
4.2.1. Jupiter . . . 81
4.2.2. Saturn . . . 83
4.2.3. Uranus and Neptune . . . 85

**5. The Jovian Circumplanetary disk 97**
5.1. Existing circumplanetary disk models . . . 97
5.1.1. Minimum mass circumplanetary disk model . . . 97
5.1.2. Gas starved disk model . . . 98
5.1.3. Insights from 3D hydrodynamic models . . . 98
5.2. An improved two-dimensional circumplanetary model . . . 99
5.2.1. Radial density profile . . . 100
5.2.2. Vertical structure . . . 101
5.2.3. Thermal Structure . . . 103
5.2.4. Self-shadowing . . . 105
5.2.5. Time evolution . . . 105
5.3. Numerical scheme . . . 106
5.3.1. Discretization . . . 106
5.3.2. Surface temperature Discretization . . . 109
5.3.3. Adiabatic to isothermal transition radius . . . 110
5.3.4. Jacobian Free Newton Krylov Method . . . 112

**6. Circumplanetary disk structure implication on its volatile composition and Trappist-1 protoplanetary disk** **114**
6.1. Impact of self shadowing on the Thermal structure . . . 115
6.1.1. Model Setup . . . 115
6.1.2. Depletion timescale of the disk . . . 116
6.1.3. Thermal profile . . . 117
6.1.4. Effect of Jupiter's radiative heating . . . 121
6.1.5. Effect of CPD metallicity Variations . . . 124
6.1.6. Effect of accretion timescale Variations . . . 126
6.2. Condensation lines location . . . 128
6.3. volatile species evolution . . . 131
6.4. Delivery of phyllosilicates to a one-dimensional circumplanetary disk . 135
6.4.1. Gas starved CPD model . . . 135
6.4.2. Impact of phyllosilicate grains on the water radial distribution . 138
6.4.3. Putative Galilean moons formation sequence . . . 140
6.5. Application to the Trappist-1 System . . . 141
6.5.1. Trappist-1 planets characteristics . . . 141
6.5.2. Delivery of water to the Trappist-1 PPD . . . 143
6.5.3. Variation of phyllosilicate dehydration temperature . . . 149
6.5.4. Consequence on Trappist-1 planet formation locations . . . 152

**7. Application of a chemical network to the CPD** **153**
7.1. Thermochemical equilibrium . . . 153
7.1.1. Method : ACE software . . . 154
7.1.2. Composition of the CPD at thermochemical equilibrium . . . 154
7.1.3. Limits of the approach . . . 161
7.2. Non-equilibrium chemistry . . . 162
7.2.1. Continuity equation . . . 162
7.2.2. Description of the chemical network . . . 162
7.2.3. Flux of species . . . 165
7.3. Numerical scheme . . . 166
7.3.1. Discretization . . . 166
7.3.2. Backward Differentiation Formula integration Scheme . . . 167
7.3.3. Jacobian matrix construction and inversion . . . 169
7.3.4. Boundary conditions . . . 172
7.4. Resolution instabilities . . . 173

**Conclusion** **175**

**Bibliography** **180**

**ANNEXES** **201**

**A. Volatile radial distribution in the PPD : parameter variation** **202**
A.1. PPD initial mass . . . . . 202
A.2. Alpha viscosity . . . . . 205
A.3. Initial accretion rates . . . . . 207
A.4. Pebble's density . . . . . 211

**B. List of publication** **213**
B.1. Schneeberger et al. 2023 . . . . . 213
B.2. Schneeberger et al. 2024 . . . . . 231

# List of Figures


1.1. Barnard 68 . . . . . 27
1.2. Images from the VLT/SPHERE instruments of protoplanetary disks around T-Tauris stars. The protoplanetary disks contains substructures such as rings, gaps and denser regions. Credits: ESO/H. Avenhaus et al. (2018) and Sissa et al. (2018) /DARTT-S and SHINE collaborations . . . . . 29
1.3. The planet formation process span over 15 orders of magnitude. The figure illustrate typical sizes at different stages of the planet formation process, from the micro metric dust to the gas giant. . . . . 31
1.4. Giant planets elemental enrichments . . . . . 32
1.5. Density gradient of the Galilean Moons . . . . . 35
1.6. Images of the surface of Io (top left), Europa (top right), Ganymede (bottom left) and Callisto (bottom right). Credit: NASA/JPL/DLR . . . . 36

2.1. Condensation line effect in the Protoplanetary disk . . . . . 42
2.2. Clathration line effect in the Protoplanetary disk . . . . . 43
2.3. Pure condensate and clathrate hydrate equilibrium curves . . . . . 44
2.4. Delivery of amorphous ice . . . . . 45
2.5. Bennus samples from OSIRIS-REX . . . . . 46
2.6. Supply of phyllosilicates to the PPD . . . . . 48
2.7. Phyllosilicate equilibrium curves . . . . . 49

3.1. Standard PPD midplane properties . . . . . 56

4.1. Water radial distribution . . . . . 64
4.2. Delivery of pure condensate: volatile species radial distribution . . . . 66
4.3. Delivery of amorphous ice : radial distribution of volatile species . . . . 69
4.4. PPD midplane properties variation when varying initial PPD mass . . . 71
4.5. impact of disk mass variation on the Xe volatile distribution . . . . . 72
4.6. impact of disk mass variation on the $CH_4$ volatile distribution . . . . . 73
4.7. [PPD midplane properties variation when varying $\alpha$ . . . . . 74
4.8. Impact of $\alpha$-parameter variation on the $CH_4$ distribution . . . . . 75
4.9. Impact of $\alpha$-parameter variation on the Xe distribution . . . . . 76
4.10. Impact of pebble density variation on the $CH_4$ distribution . . . . . 77
4.11. Impact of pebble density variation on the Xe distribution . . . . . 78
4.12. Impact of pebble density variation on the $CH_4$ distribution . . . . . 79
4.13. Impact of pebble density variation on the Xe distribution . . . . . 80
4.14. Elemental enrichments at Jupiter putative formation locations . . . . . 82
4.15. Elemental enrichments at Saturn putative formation locations . . . . . 84

4.16. Pebbles' C/N and C/S ratios profiles in the PPD with a delivery of pure condensates . . . 86
4.17. Pebbles' C/N and C/S ratios profiles in the PPD with a delivery amorphous ice . . . 87
4.18. Elemental ratio evolution at the CO condensation line : Pure condensate a vapor only . . . 89
4.19. Elemental ratio evolution at the CO condensation line : Pure condensates, clathrate a vapor . . . 90
4.20. Elemental enrichment with respect to protosolar abundances predicted in the envelope of Uranus and Neptune in the reference model . . . 94
4.21. Elemental enrichment with respect to protosolar abundances predicted in the envelope of Uranus and Neptune in scenario 1 . . . 95

5.1. Diagram illustrating the structure of the circumplanetary disk model . 100
5.2. computational grid of the CPD adiabatic region . . . 108

6.1. CPD mass and accretion rate . . . 116
6.2. CPD midplane profile when irradiated by Jupiter . . . 118
6.3. Two-dimensional temperature and pressure profiles . . . 120
6.4. Two-dimensional temperature and pressure profiles without Jupiter's heating . . . 122
6.5. CPD midplane profile without Jupiter's heating . . . 123
6.6. Comparison of the gas density and temperature at the photosurface level with and without Jupiter's heating. . . . 124
6.7. Evolution of CPD temperature profiles with dust enrichment . . . 125
6.8. Two-dimensional temperature and pressure profiles evolution using accretion rates from Sasaki et al. (2010) . . . 127
6.9. Condensation lines locations in the CPD . . . 130
6.10. Volatile abundance profiles : accretion rate from Sasaki et al. (2010) . . . 132
6.11. Volatile abundance profiles : accretion rate from Sasaki et al. (2010) . . . 134
6.12. Temperature, surface density and pressure profiles in the CPD using the model of Anderson et al. (2021) . . . 137
6.13. Radial profiles of the water abundances within the CPD expressed as function of the initial abundance in phyllosilicate–rich grains. . . . 139
6.14. Galilean moons density gradient . . . 142
6.15. Delivery of water by phyllosilicate-rich grains to the inner Trappist-1 PPD 143
6.16. Trappist-1 PPD midplane properties . . . 145
6.17. Trappist-1 system water distribution . . . 146
6.18. Water mass fraction of pebbles at Trappist-1 water condensation line with a phyllosilicate dehydration temperature of 500 K . . . 148
6.19. Water mass fraction of pebbles at Trappist-1 water condensation line with a phyllosilicate dehydration temperature of 400 K . . . 150
6.20. Water mass fraction of pebbles at Trappist-1 water condensation line with a phyllosilicate dehydration temperature of 600 K . . . 151

7.1. Molar fractions of the main carbon-bearing specie, at thermochemical equilibrium . . . 157
7.2. Molar fractions of the main nitrogen-bearing species, at thermochemical equilibrium . . . 159
7.3. Molar fractions of the tracer species of planet forming regions, at thermochemical equilibrium . . . 161
7.4. Sketch of the structure of the jacobian matrix of the equation . . . 170

A.1. Volatile species radial distribution in a PSN with an initial mass of $10^{-2}$ $M_\odot$ 203
A.2. Volatile species radial distribution in a PSN with an initial mass of $1.5 \times 10^{-3}$ $M_\odot$ . . . 204
A.3. Volatile species radial distribution in a PSN with an $\alpha$–parameter of $10^{-2}$ 206
A.4. Volatile species radial distribution in a PSN with an initial accretion of $10^{-6}$ $M_\odot$ $yr^{-1}$ . . . 208
A.5. Volatile species radial distribution in a PSN with an initial accretion of $10^{-8}$ $M_\odot$ $yr^{-1}$ . . . 209
A.6. Volatile species radial distribution in a PSN with a pebble density of $5 \times 10^{-1}$ . . . 211
A.7. Volatile species radial distribution in a PSN with a pebble density of $5 \times 10^{-2}$ . . . 212

# List of Tables


2.1. Polynomial factors for the vapor pressure equations of pure condensates 51
2.2. Parameters for the dissociation pressure equations of $NH_3$ monohydrate and clathrates . . . . . 52

4.1. Model parameters . . . . . 63
4.2. Initial molar abundances of the considered trace species. . . . . 63
4.3. Enrichment peak location and magnitude when delivering pure condensate . . . . . 67
4.4. Enrichment peak location and magnitude when delivering amorphous ice 70
4.5. Predicted elemental enrichment of Uranus after 500 and 1000 kyr of PPD evolution, assuming a carbon enrichment between 40 and 50 times the protosolar value. . . . . 92
4.6. Predicted elemental enrichment of Neptune after 500 and 1000 kyr of PPD evolution, assuming a carbon enrichment between 74.7 and 114.3 times the protosolar value. . . . . 93

6.1. Nominal model parameters . . . . . 115

7.1. Nominal model parameters . . . . . 155

# 1. Introduction

## Table of Contents


1.1. Protoplanetary disk initial composition . . . . . 26
1.2. Insight from the composition of the Giant planets on their formation history . . . . . 29
1.3. The origin of the Galilean Satellites . . . . . 34
1.4. Chemistry within the circumplanetary disk . . . . . 37
1.5. Outline . . . . . 39


## 1.1. Protoplanetary disk initial composition

Planet formation occurs within a protoplanetary disk (PPD) of gas and dust that surrounds the proto-Sun during the first few million years of its existence. However, the precise pathway from the PPD to the present-day planetary system remains largely unknown. To understand the formation of the solar system's planets and moons, it is crucial to investigate the structure, composition, and evolution of the PPD.

The material in the PPD originates from the same reservoir as the Sun: a cold, dark molecular cloud, whose mass can range from a few thousand to over a million solar masses. This molecular cloud is initially a cold, opaque environment with temperatures not exceeding 20 K. It is rotationally supported, meaning that the gravitational forces acting on the cloud are balanced by the centrifugal force generated by its intrinsic rotation. Eventually, an external event disturbs this equilibrium, leading to the cloud's compression. Once disturbed, the molecular cloud begins to collapse under its own gravity, as the gravitational force overtakes the centrifugal force. During this collapse, the cloud fragments into clumps of several hundred solar masses, and eventually into protostellar cores with masses of a few solar masses.

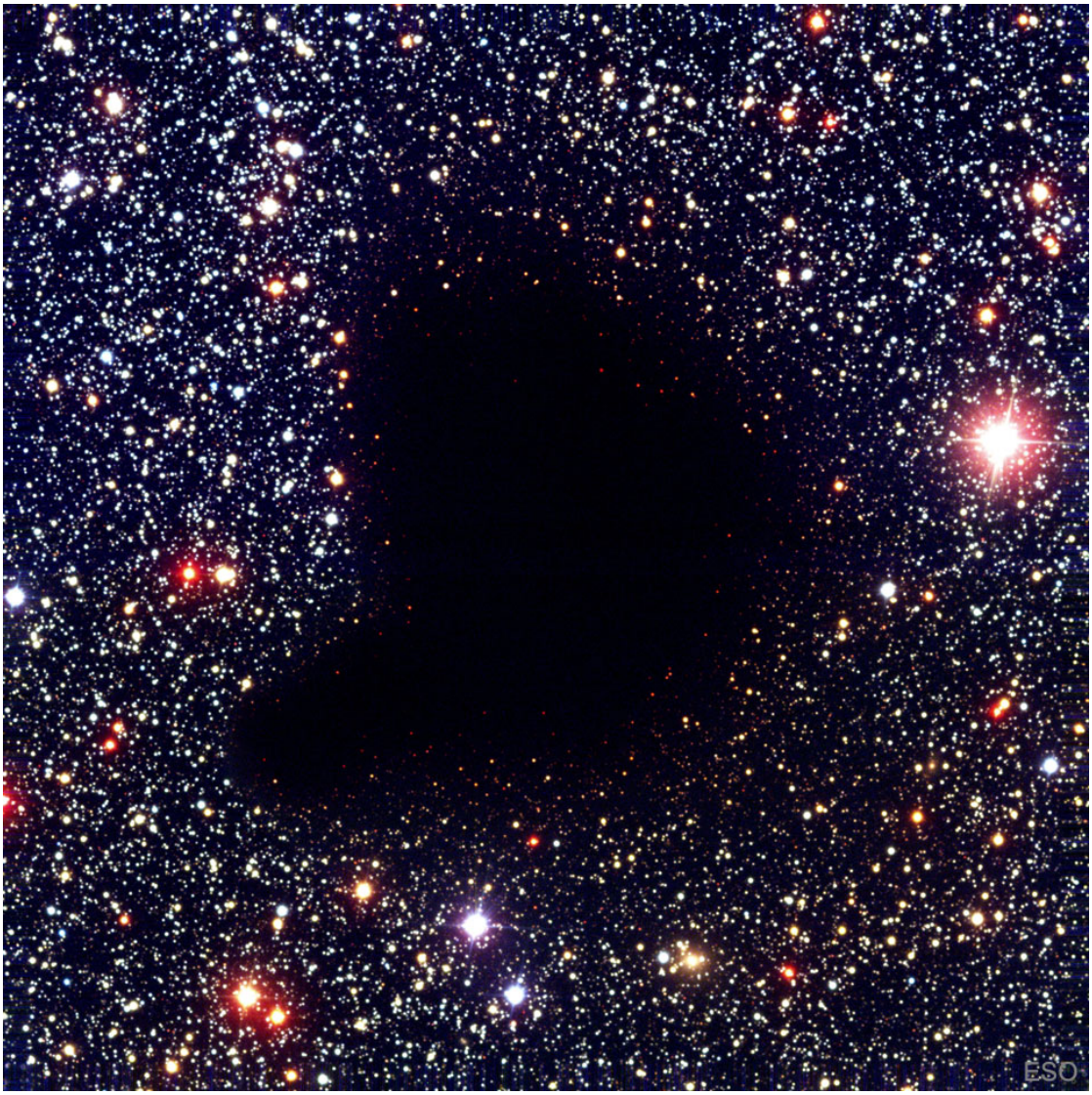


Figure 1.1.: Dark Molecular cloud Barnard 68 located in the Ophiuchus constellation. Credits: FORS Team, 8.2-meter VLT Antu, ESO

The protosolar core collapses under its own gravity, forming a star over a timescale of a few thousand years. At the center of the core, conditions of temperature and pressure become suitable for thermonuclear fusion, causing the protosun to ignite and begin shining.

As the protosun lights up, it is surrounded by a shell of gas and dust, the remnants of the protostellar core. A significant portion of this shell is blown away by the strong stellar winds generated by the young Sun, which enter its T-Tauri stage. At this stage, stellar winds are largely confined to collimated jets emanating from the poles of the star. These jets expel material into the interstellar medium, forming Herbig-Haro objects—regions of shocked gas that can extend tens of light-years in diameter, located

2–4 light-years from the star. This ejection primarily clears material from the polar regions around the Sun, while the remaining material flattens into a thin, rotating disk due to the angular momentum accumulated during the collapse of the protostellar core.

This disk is the so-called protoplanetary disk (PPD), from which all the solar system bodies, from asteroids to gas giants, eventually form. The processes at work within the solar PPD and its precise composition are still not fully understood.

The original elemental composition of the protostellar core, and thus the PPD, can be inferred from the Sun's composition (Lodders 2003, 2019, 2021). Although the current solar photosphere does not exactly reflect the Sun's protosolar composition, stellar evolution models allow for the reconstruction of its original bulk composition (Lodders 2021).

However, even with knowledge of the PPD's original elemental composition, the molecular composition and the form in which these species were delivered to the PPD remain largely unconstrained. Given that the molecular cloud is a cold environment, with temperatures as low as 10 K (Gibb et al. 2004), volatile species condense onto micrometer-sized dust grains. At such low temperatures and pressures, water condenses in an amorphous form, lacking a crystalline structure (Mayer et al. 1986; Jenniskens et al. 1995). As a result, species trapped within this amorphous matrix can only be released when the temperature rises sufficiently for the water to crystallize, around 135 K (Bar-Nun et al. 2007).

It remains uncertain whether the material accreted onto the PPD from the molecular cloud is heated enough to reach this amorphous-to-crystalline transition temperature. One hypothesis suggests that material falling from the molecular cloud onto the dense protosolar region experiences a supersonic shock at the boundary between the low-density cloud and the high-density regions of the PPD and protosolar environment (Visser et al. 2013; Miura et al. 2017; Burkhardt et al. 2019). The temperature increase produced by this accretion shock may range from 200 K (Visser et al. 2013; de la Villarmois et al. 2022) to several thousand kelvin (Vorobyov et al. 2013). In the lower temperature case, all volatile species vaporize and recondense following the shock, while at higher temperatures, non-refractory species vaporize, and molecular bonds break, forming an atomic gas. In the shock's wake, atoms recombine to form molecules, potentially different from those originally present in the molecular cloud. As such, the state and composition of the material accreted onto the PPD remains an open question.

## 1.2. Insight from the composition of the Giant planets on their formation history

The properties of the Sun's PPDs are unknown, one can only deduce them from T-Tauris stars' PPDs observations. Observations show a wide variety of PPD structures, masses, and accretion rates as illustrated by figure 1.2 which shows a sample of PPDs observed by the VLT/SPHERE instrument, and adapted from Avenhaus et al. (2018) and Sissa et al. (2018). It shows a variety of substructures such as gaps, rings and overdensities. It is supposed that those substructures are the results of planet formation processes.

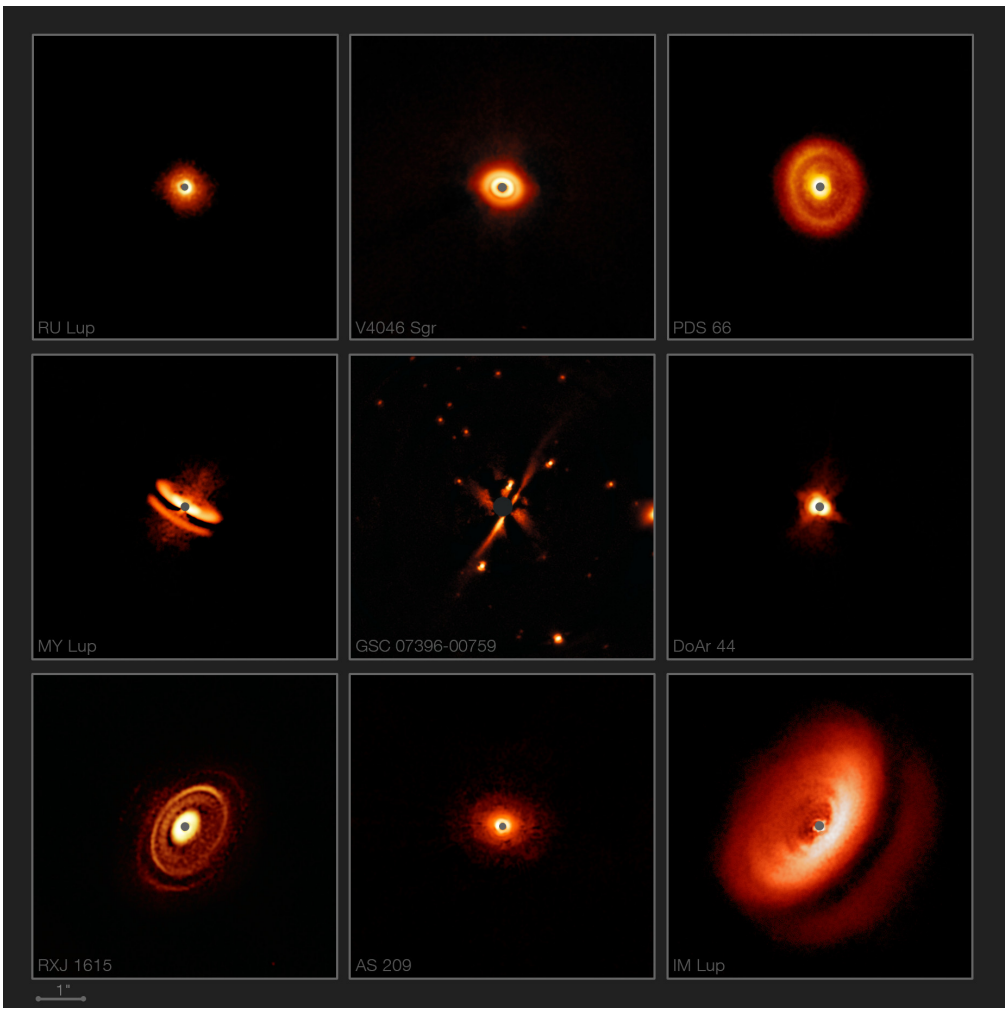


Figure 1.2.: Images from the VLT/SPHERE instruments of protoplanetary disks around T-Tauris stars. The protoplanetary disks contains substructures such as rings, gaps and denser regions. Credits: ESO/H. Avenhaus et al. (2018) and Sissa et al. (2018) /DARTT-S and SHINE collaborations

Planetesimal formation begins with the oligarchic growth of dust particles from the

micrometer to decimeter scale. In this initial stage, dust particles collide and stick together through electrostatic forces, as gravitational forces are negligible at such small scales. However, this growth halts at the pebble stage, around the decimeter scale. At this point, pebbles become both too weakly bound and too heavy, so when they collide, they either bounce off each other or fragment, abruptly stopping their growth.

To overcome this barrier, a mechanism is needed to allow pebbles to stick together and form planetesimals several kilometers in size. Several mechanisms have been proposed to bridge the gap between the decimeter and kilometer scales, many of which involve instabilities within the PPD. One possibility is that the PPD becomes locally gravitationally unstable, causing a region of the disk to collapse directly into a gas giant planet. However, this scenario requires a massive PPD and formation at tens of AU from the Sun, far from the current locations of Jupiter and Saturn.

The other class of scenarios suggests that eddies within the PPD can compact pebbles together, leading to the formation of kilometer-sized planetesimals. The subsequent growth from small planetesimals to fully formed planets remains a subject of debates, with two main theories under discussion. The first posits that planets grow by accreting other planetesimals through an oligarchic process, requiring a high number density of large planetesimals and efficient capture mechanisms. The second theory suggests that planets grow by accreting pebbles directly from the PPD, requiring a high density of pebbles and dust.

Once a protoplanet reaches a critical mass of approximately 10 $M_{\oplus}$, it undergoes runaway gas accretion, rapidly accumulating gas from the PPD over a few thousand years. This process continues until gas accretion is halted by the formation of a gap around the growing planet, eventually leading to the formation of a gas giant.

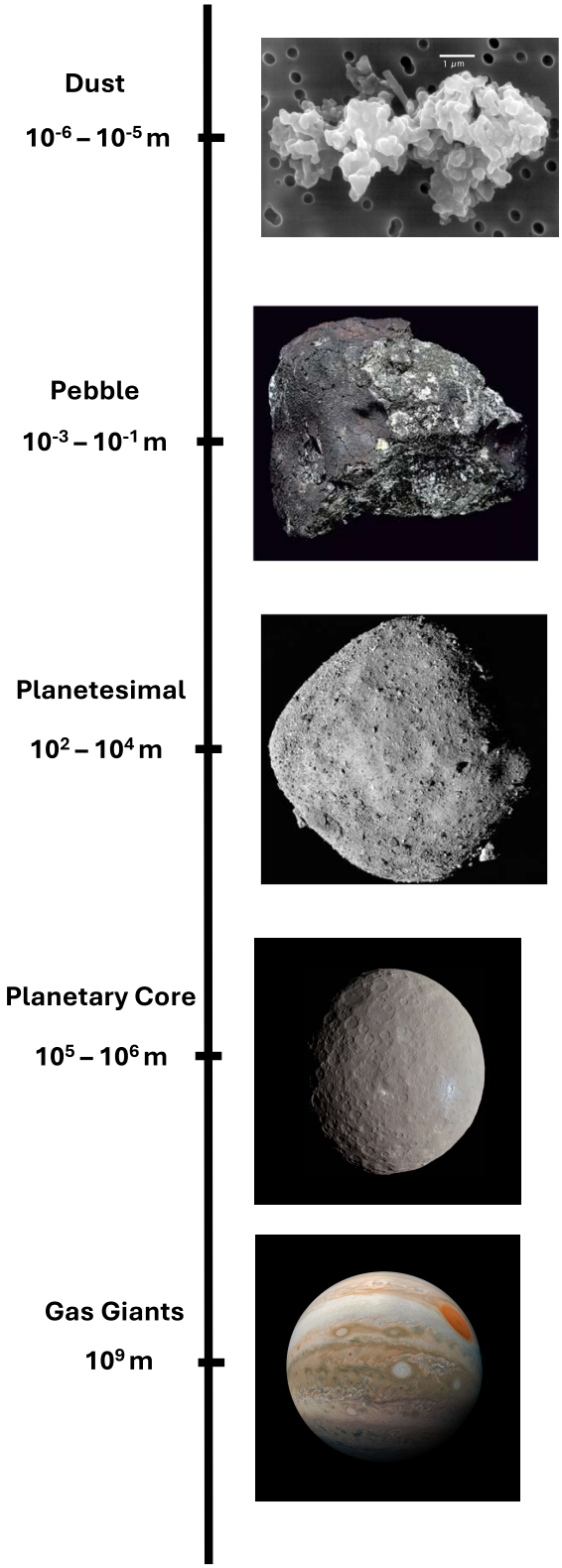


Figure 1.3.: The planet formation process span over 15 orders of magnitude. The figure illustrate typical sizes at different stages of the planet formation process, from the micro metric dust to the gas giant.

It is generally assumed that the bodies of the Solar System have bulk compositions that are representative of the material present in the PPD from which they were formed, therefore the formation processes discussed above should leave unique compositional prints into the giant planets bulk composition.

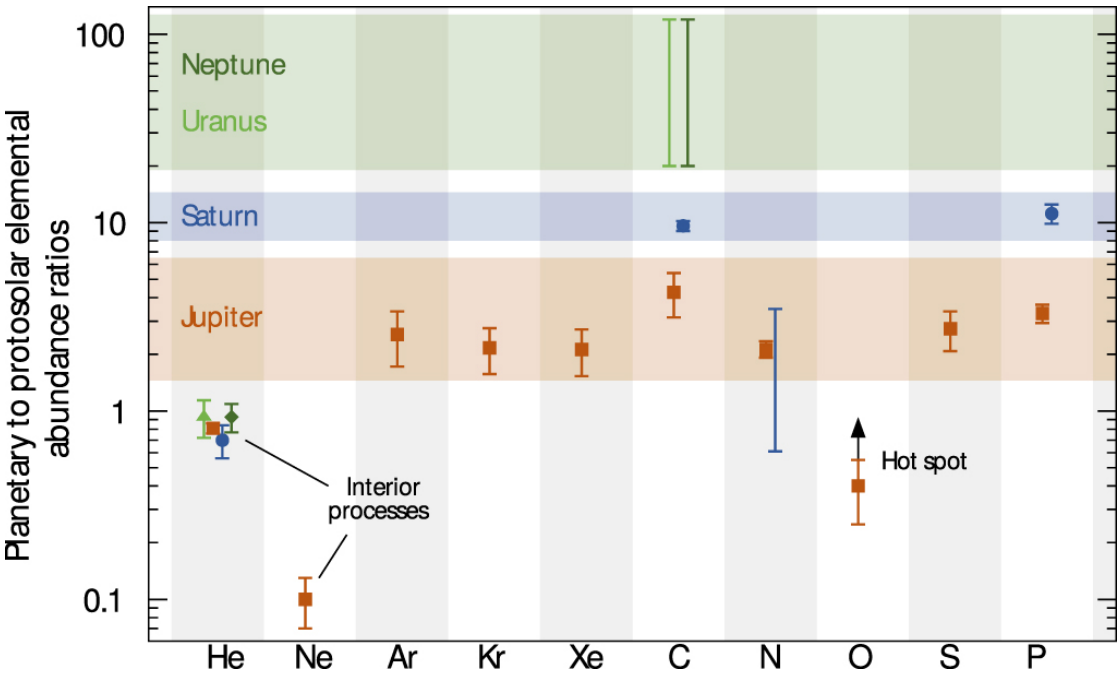


Figure 1.4.: Elemental enrichments of Hellium, Neon, Argon, Krypton, Xenon, Carbon, Nitrogen, Oxygen, Sulfure and Phosphorus in the atmosphere of Jupiter, Saturn, Uranus and Neptune, reproduced from Mousis et al. (2019).

If the PPD had a uniform composition, the gas, and ice giant planets should reflect this homogeneity.But the reality is radically different. Thanks to measurements by the Galileo and Cassini spacecraft, the composition of Jupiter's atmosphere revealed elemental abundances different from the protosolar one, with abundances 1.6-6.1 times higher than the protosolar values for argon, krypton, xenon, carbon, nitrogen, sulfur, and phosphorus (Mahaffy et al. 2000; Wong et al. 2004; Fletcher et al. 2009). The Galileo probe measured a subsolar abundance of oxygen. The leading hypothesis for this measurement is that the spacecraft probably descended into a dry region of Jupiter's upper atmosphere. The measurement of oxygen abundance was attempted again by the JUNO mission, which measured an abundance in the range of 0.1 to 5.1 times the protosolar value, with a median value of 2.2 times the protosolar value (Li et al. 2020). A recent refinement of the interpretation of the measures using a super-adiabatic atmospheric temperature profile propose an oxygen abundance between 1.5 and 8.3 times the protosolar abundance, with a median value of 4.9 times the protosolar abundance (Li et al. 2024).

Elemental abundances measurements of Saturn, Uranus, and Neptune are scarcer. Cassini measured only abundances of carbon, nitrogen, and phosphorus in Saturn troposphere, with enrichments in the range between 0.61 and 3.48 time the protosolar abundances of nitrogen, 9.6 a times protosolar abundances of carbon and 11 times the protosolar abundance of phosphorus (Fletcher et al. 2009; Fletcher et al. 2011). Finally, one only have a measurement of carbon enrichment in Uranus and Neptune troposphere in the range between 20 and 120 times the protosolar value. Enrichments were obtained from Voyager 2 radio occultation (Lindal et al. 1987, 1990; Lindal 1992). Interestingly, Hubble Space Telescope observations of Uranus revealed a complex situation, showing a large $CH_4$ abundance variation with latitude (Karkoschka et al. 2009; Sromovsky et al. 2014). Aerosol model of Sromovsky et al. (2011) fitted on those observations show the existence of a dense $CH_4$ cloud in the 1–3 bar pressure region near the equator, leading to a strong troposphere $CH_4$ depletion. Consequently, Uranus and Neptune atmosphere composition remain poorly constrained.

It is difficult to state that those measurements are representative of the bulk composition. In the case of Jupiter, it would involve that its envelope is fully convective. However, recent studies by Cavalié et al. (2023) invoke the existence of a radiative layer with reduced mixing in order to reproduce a deep supersolar $H_2O$ abundance which match the measurement of the deep oxygen abundance of 2.2 times solar by JUNO (Li et al. 2020). The existence of a radiative layer has also been invoked by Debras et al. (2019) to explain the small values of high-order gravitational moments observed by JUNO, given the measured high abundance of heavy elements. Therefore, Müller et al. (2024) proposed that this putative radiative layer is a barrier between the deep envelope and Jupiter's atmosphere. According to this interior model, the deep envelope could have a protosolar abundance of heavy element, while the atmosphere is enriched by the late accretion of small heavy-element-rich object like the comet Shoemaker-Levy 9 which impacted the planet on July 1994.

Therefore, to better constrain the origin of measured abundances and understand if they can be representative of the planet's bulk abundances, it is key to understand the distribution of volatile species in the PPD. As it has been shown that volatile species does not have a homogeneous distribution in the PPD (Aguichine 2022), assuming only two phases of volatiles : pure condensates and vapor.

We therefore aim at building upon the work of Aguichine et al. (2022), improving its model to explore the volatile distribution within the PPD to test the presence of phases of volatile species other than pure condensates and vapor. It will enable to better constrain the formation pathway of the giant planets and prepare the scientific return of the Uranus Orbiter and Probe (UOP) that aim at studying the deep composition of Uranus in the 2040's (Simons et al. 2021).

## 1.3. The origin of the Galilean Satellites

The Galilean moons formed within a circumplanetary disk (CPD) that surrounded Jupiter after its formation. While recent years have seen the first detections of CPDs around forming Jupiter-like exoplanets, such as in the PDS 70 system (Christiaens et al. 2019; Benisty et al. 2021; Blakely et al. 2024) and around GQ Lupi B* (Stolker et al. 2021), these observations reveal massive accretion disks around planets potentially still in their gas runaway accretion phases. However, the structure, composition, mass, and lifespan of such disks remain largely unconstrained. A deeper understanding of these properties is essential for explaining the characteristics of the Galilean moon system.

The Galilean satellites—Io, Europa, Ganymede, and Callisto—form the most massive satellite system in the solar system, with a combined mass of $2.07 \times 10^{-4}\ M_{\mathrm{J}}$. Modeling the formation of such massive moons, each with radii on the order of thousands of kilometers, remains challenging. Additionally, the three innermost moons Io, Europa, and Ganymede are locked in a 2:1 mean-motion resonance, which suggests a history of migration followed by resonance capture. Callisto, although outside this resonant chain, lies close to it, raising the question whether it was ejected from the resonance or never entered it.

Another notable feature of the system is the observed density gradient, shown in Figure 1.5. The Galilean moons exhibit a decrease in density with increasing distance from Jupiter, which corresponds to a rising proportion of water in their bulk compositions. Any formation and evolution models must account for this gradient in order to provide a complete explanation of the system's structure.

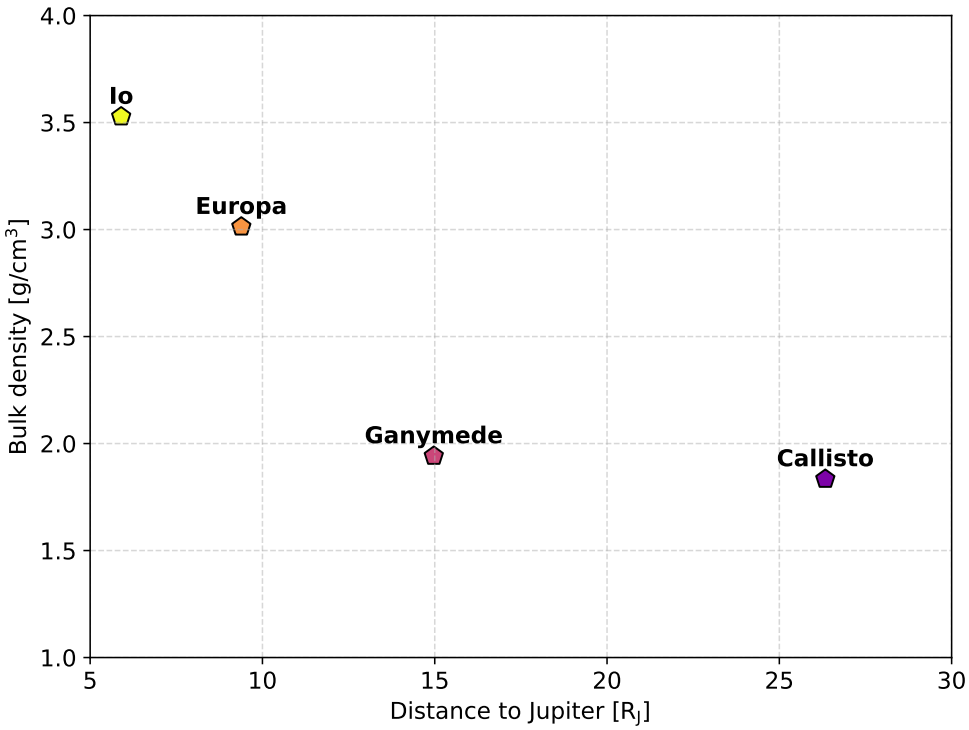


Figure 1.5.: Density of the Galilean moons as a function of their distance to Jupiter. It shows a negative density gradient which translate an increasing proportion of water in the moon's bulk composition as function of the distance.

In addition to the observed density gradient, Figure 1.6 highlights the radical differences in the surface features of the four Galilean moons, reflecting their different internal structures.

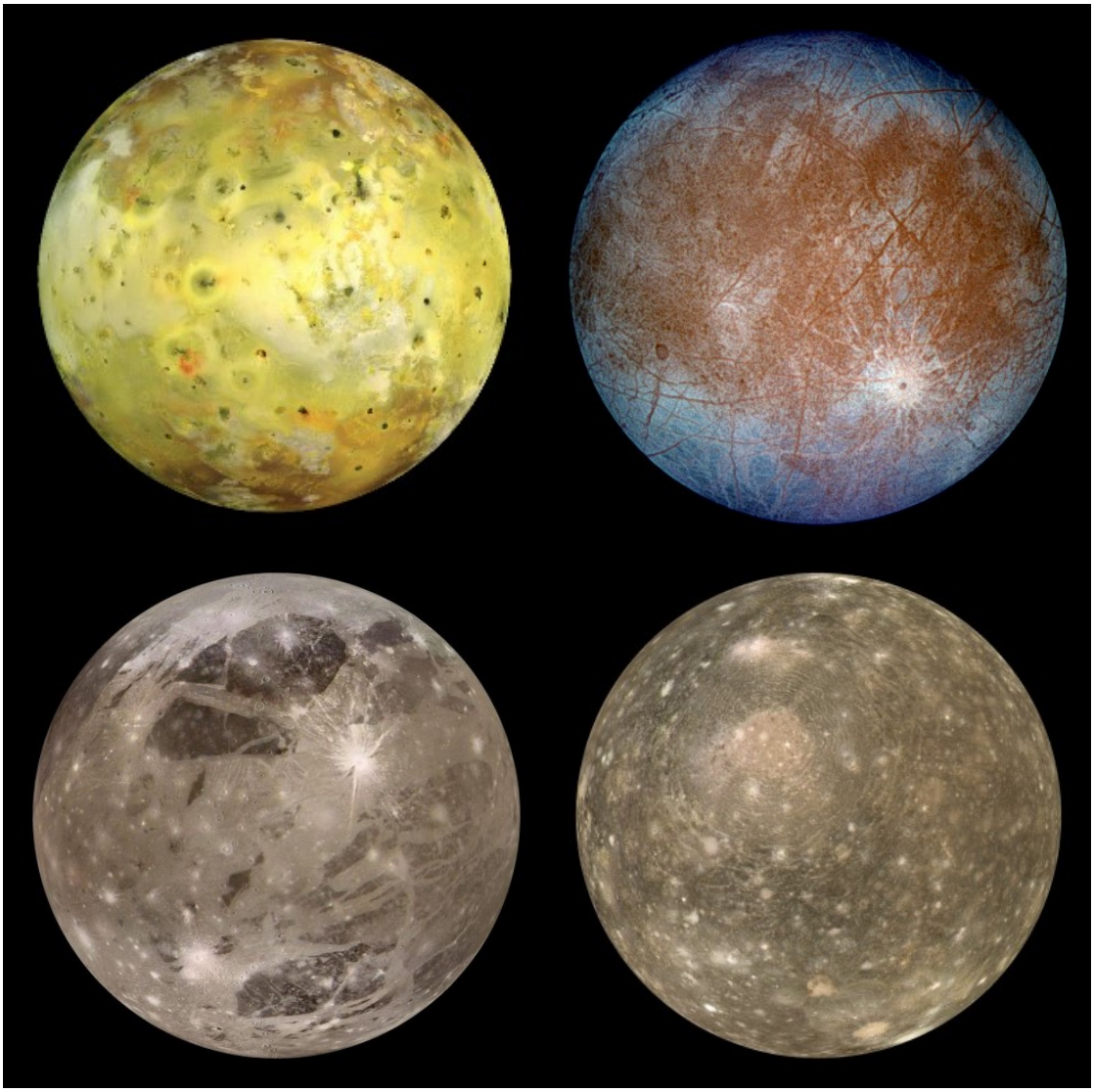

Figure 1.6.: Images of the surface of Io (top left), Europa (top right), Ganymede (bottom left) and Callisto (bottom right). Credit: NASA/JPL/DLR

Io has the highest surface density of volcanoes and calderas in the solar system and is devoid of water ice, with only $SO_2$ frost observed on its surface, originating from volcanic outgassing (Bertaux et al. 1979; Fanale et al. 1979; Nash et al. 1980; Koyama et al. 1983). Such intense volcanic activity suggests the presence of a liquid magma layer, either at shallow depths (Davies et al. 2024) or near the moon's core (Keszthelyi et al. 1997).

Europa, in contrast, displays a young, icy surface with very few impact craters, but is marked by tectonic features such as ridges (Figueredo et al. 2004; Collins et al. 2022), as well as lenticulae and chaos terrains, indicative of cryovolcanism (Lesage et al. 2021). These surface features are the signs of a subsurface ocean, located beneath an ice shell

estimated to be 10 to 30 km thick, based on gravitational and magnetic field measurements from the Galileo mission (Anderson et al. 1998; Schenk 2002; Park et al. 2015). The subsurface ocean itself is hypothesized to be around 100 km deep (Park et al. 2015).

Ganymede, like Europa, shows surface ridges and evidence of resurfacing. As the most massive moon in the solar system, even larger than Mercury, Ganymede has its own intrinsic magnetic field, discovered by the Galileo probe (Gurnett et al. 1996; Kivelson et al. 1996; Schubert et al. 1996). This magnetic field is likely generated by a molten iron core, suggesting strongly differentiated internal structure (Schubert et al. 1996). Additionally, gravity measurements from Galileo indicate the presence of a saline internal ocean, located between two layers of ice, roughly 100 km beneath the surface (Anderson et al. 1996).

Callisto's surface stands apart from the other Galilean moons, with an old, heavily cratered terrain that may be as ancient as the moon itself. The existence of a subsurface ocean on Callisto remains a topic of debate (Kuskov et al. 2005), which may be resolved by future flybys from the ESA/JUICE and NASA/Europa-Clipper missions (Van Hoolst et al. 2024). Intriguingly, despite being the second-largest moon of the Jovian system, evidence suggests that Callisto's core is probably undifferentiated, being a homogeneous mixture of water ice, silicates, and organic matter (Kuskov et al. 2005; Néri et al. 2020). This distinctive interior structure poses a challenge for theories of Galilean moon formation. It suggests that Callisto may have followed a different evolutionary path, either forming later than the other moons or possibly being a captured planetesimal that originally formed in the PPD before being captured by Jupiter (Shibaike et al. 2019). The CPD could have circularized Callisto's orbit, allowing it to grow to its present size through pebble accretion (Shibaike et al. 2019).

To better understand the formation and evolutionary pathways of the Galilean moons, this work focuses on studying the evolution and composition of the CPD. Along with examining its volatile content, we aim to explore the chemical processes occurring within its gas phase.

## 1.4. Chemistry within the circumplanetary disk

The study of the volatile species by only considering condensation and vaporization do not account for chemical reactions that alter species abundances in the PPD and CPD. This limitation hinders our ability to study the hotter regions of the disk, where the chemical timescale is short enough for in-situ formation of species. Additionally, this approach is restricted in its ability to explore the vertical distribution of species. As altitude increases, the environment becomes optically thinner, exposing vapor to high-energy radiation, especially UV radiation, which induces photochemistry and results in a layer of ions at the disk surface (Oberg et al. 2022b).

Modeling the chemical reactions occurring in the CPD, will help understand the delivery of volatile species to the CPD. Given the intense heat generated by planetary accretion, one have to consider two scenarios. In the first scenario, if the accretion shock is hot enough, it will destroy all chemical compounds in ices and vapor, leading to an influx of atomic gas into the CPD. In this case, the CPD's molecular composition would not reflect that of the PPD. In the second scenario, if the accretion shock is cold enough for molecules to be preserved in the gas phase or on icy grains, the CPD's molecular composition would be inherited from the PPD. These two scenarios lead to different outcomes. Oberg et al. (2022a) show that in a chemical reset scenario, $NH_3$ ice destroyed upon entering the CPD could not reform, as nitrogen would be trapped in $N_2$ ice or hydrates, potentially explaining the non-detection of $NH_3$ on the Galilean moons' surfaces (Oberg et al. (2022a) and references therein). Conversely, if the CPD composition is inherited from the PPD, ammonia would be the dominant nitrogen-bearing species, and $NH_3$ ice should be abundant on the moons' surfaces.

However, Néri et al. (2020) and Reynard et al. (2023) indicate that, based on moment of inertia measurements from the Galileo probe of Europa, Ganymede, and Callisto, that these moons likely contain up to 20 wt% of complex organic material in their cores, similar to that found in CI chondrites. The presence of dissolved $CO_2$ ice within Europa's subsurface ocean, hypothesized to explain the detection of $CO_2$ trapped in the ice of the Tara Regio and Powy Regio chaos terrains (Trumbo et al. 2023), could be indicative of a COM-rich cores. Soluble COMs from the core and mantle may dissolve in the subsurface ocean, forming $CO_2$ and carbonates. If these COMs originate from the PPD, it would suggest that refractory organics were not vaporized and destroyed by the accretion shock, thereby limiting the temperatures reached by the accreting material.

Studying extrasolar forming giant planets and their CPDs can provide insights into the processes that shaped the Jovian system. Recent observations of PDS 70 and TW Hya have suggested the presence of CPDs around detected forming planets. The masses of planets PDS 70 b and c are uncertain, estimated between 1 and 10 $M_J$, and both exhibit H$\alpha$ emissions indicative of active accretion onto their CPDs (Christiaens et al. 2019; Benisty et al. 2021). The tentative detection in TW Hya reveals a planet-driven outflow, traced through SO emissions, originating from a gap located 42 AU from the star (Yoshida et al. 2024). The planet responsible for this outflow has a mass of 4 $M_\oplus$ and is accreting gas at a rate between $10^{-8}$ and $10^{-6}$ $M_J$ yr$^{-1}$. As demonstrated by the TW Hya detection, chemical probes like SO are crucial for characterizing the structure and properties of extrasolar CPDs, which can, in turn, help to better constrain the architecture of the Jovian CPD.

Several species serve as chemical probes in the study of PPDs, with CO isotopologues being among the most widely used due to their high abundance, which results in strong SNRs in observations. The most commonly detected CO isotopologues are $^{12}$CO, $^{13}$CO, and $^{18}$CO (Bruderer 2013; Oberg et al. 2022b; Zhang 2024), which enable

to probe the mass distribution, temperature, and vertical structure of PPDs at different optical depth. Other abundant species and with optically thick lines such as $H_2O$, CO, HCN, $C_2H_2$ and OH serve as chemical probes, although the detection of $H_2O$ and CO vapors are challenging because their condensation lines are located within 10 AU from the stars and consequently angularly close to the star.

Therefore, a comprehensive self-consistent chemical model is needed to understand the future observation of CPDs around forming exoplanets. The interpretation of those observations will induce further understanding of the accretion processes of the giant planets and the formation of their surrounding CPDs.

## 1.5. Outline

This manuscript is divided into two main parts: the first focuses on improving a PPD model originally developed by Aguichine et al. (2022) to better constrain the origins of the giant planets. The second part explores the Jovian system and its CPD, presenting a new two-dimensional CPD model and investigating its chemical composition using a chemical network, with the aim of understanding the formation of the Galilean moons.

In Chapter 2, we discuss the sources of volatile species considered in both the PPD and CPD models. This chapter covers the roles of pure condensates, hydrates, amorphous water ice, and hydrated minerals, alongside their respective equations of state.

Chapter 3 presents the PPD model and the evolution of volatile species within it. We explain how volatile species' hydrates and amorphous water ice phases are incorporated into the existing pure condensate and vapor phases of the PPD model from Aguichine et al. (2022). The results and interpretations of the volatile species distribution are detailed in Chapter 4. First, we examine the distribution of volatile species in cases where they are delivered to the PPD as pure condensates, and then where they are trapped within amorphous water ice. Both cases are then applied to the formation of the giant planets. Finally, we investigate the formation of Uranus and Neptune at the CO condensation front, considering scenarios both with and without clathrates.

Chapter 5 reviews existing CPD models before introducing the new two-dimensional CPD model we developed. The model's structure is described in Chapter 6, beginning with the emergence of a shadow cast onto the outer regions of the CPD. We then explore the distribution of volatile species within this CPD, focusing on pure condensates and vapor. In the second part of this chapter, we investigate the possibility of a water-depleted CPD by studying the effects of phyllosilicate dehydration on water distribution. This is done using a simplified CPD model derived from the work of Anderson et al. (2021). The same approach is subsequently applied to the Trappist-1 exoplanetary system, which shares notable similarities with the Jovian system.

Finally, Chapter 7 outlines the initial development of a self-consistent chemical model aimed at studying the gaseous-phase chemical composition of the Jovian CPD. We present results from thermochemical equilibrium calculations and detail the progress made towards an out-of-equilibrium chemical model.

# 2. Volatile bearing phases

Enrichment measured in giant planet's atmospheres is a hint of the non-uniform distribution of volatile species in the PPD. There were probably enriched area in the PPD, in this section we discuss the mechanisms and source of volatile enrichment in the PPD. In this work we consider volatile species which are the main carrier of carbon, oxygen nitrogen, phosphorus and sulfur, namely $H_2O$, CO, $CO_2$, $CH_4$, $NH_3$, $N_2$, $PH_3$, $H_2$. As well as the noble gases Ar, Kr and Xe, measured in Jupiter atmosphere.

## Table of Contents


2.1. Condensation lines . . . . . 41
2.2. Clathrate hydrates . . . . . 42
2.3. Amorphous water . . . . . 45
2.4. Hydrated minerals . . . . . 46
2.5. Equations of States . . . . . 49
2.5.1. Pure condensates . . . . . 49
2.5.2. Clathrate hydrates . . . . . 52


## 2.1. Condensation lines

Numerical models show that the dynamics of the pure condensates of species and their corresponding vapors in the vicinity of their condensation lines is an efficient mechanism for enriching the composition of the PPD (Booth et al. 2017). Figure 2.1 shows the dynamics of a volatile species around its condensation line. As the pebbles drift inwards and cross the condensation line, the pure condensate of the species evaporates. The vapor then diffuses viscously both inwards and outwards. Finally, some of the vapor crosses the condensation line again and condenses on pebbles near the condensation line. As this cycle repeats, the vapor and pure condensate phases near the condensation line are enriched and an *enrichment peak* forms. Enrichment peaks can display magnitude from 2 to 20 times the initial abundances, as shown by Aguichine et al. (2022).

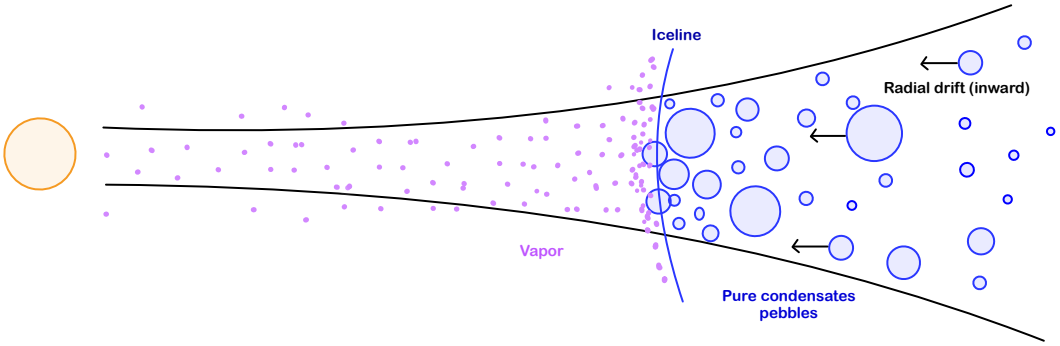


Figure 2.1.: Supply of volatile pure condensate species in the protoplanetary disk. Pure condensate grains (blue circles) drift inward, cross the condensation line and evaporate. Species vapor (purple dot) diffuses inward and outward, so some of the vapor crosses the condensation line again and condenses on pebbles. Thus, a cycle takes place, enriching the species vapor and pure condensate phases at the condensation line location.

This approach has been used to constrain the formation conditions of the gas giant (Mousis et al. 2019; Schneider et al. 2021; Aguichine et al. 2022), ice giants (Owen et al. 1999; Monga et al. 2014; Mousis et al. 2020). This approach has also been used to explain the diversity among cometary composition to determine their source and general origins of their building blocks (Mandt et al. 2020; Mousis et al. 2021a).

## 2.2. Clathrate hydrates

Clathrate hydrates are cages formed by water molecules bounded together by hydrogen bounds. Those hydrates can form two type of structure depending on the guest species trapped in the clathrate lattice (Van Der Waals 1956; Lunine et al. 1985; Holder et al. 1988). Either they form Type I structure which has a stoichiometric ratio of X-5.75$H_2O$, where X is the guest species. While Type II structure has a stoichiometric ratio of X-5.66$H_2O$. This difference in stoichiometric proportion comes from a structural difference between type I and type II clathrate hydrates. A type I clathrate hydrate unit cell consist of 48 water molecules, while a type II unit cell consist of 136 water molecules.

Study by Lunine et al. (1982), showed that clathrate hydrates cages are stable at low temperature and low pressure, comparable to the PPD thermodynamic conditions. Therefore, it is possible for species to be trapped in clathrate hydrate cages in the PPD, an hypothesis explored by Gautier et al. (2005) and Mousis et al. (2021b). One have a scenario depicted in figure 2.2. Volatile species are delivered to the PPD in a

pure condensate state. Pebbles cross the pure condensate line, causing the species to vaporize. If there is enough crystalline water, species vapor react with the crystalline water to form clathrate hydrates. It allows the species to be transported by pebbles closer to the sun than in their pure condensate state.

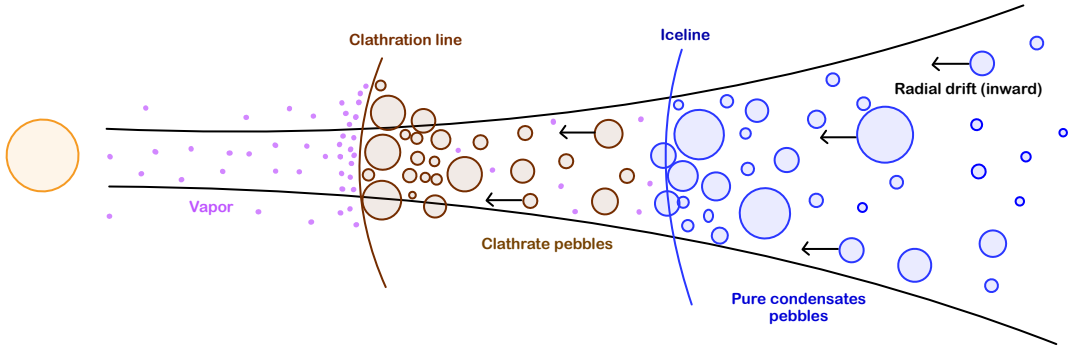


Figure 2.2.: Delivery of pure condensate and formation of clathrate hydrates in PPD. Pure condensate and clathrate hydrate pebbles are shown as blue and brown circles, respectively. In this scenario, when pure condensate vaporizes at the condensation line location, the vapor formed is trapped in clathrate hydrates if there is enough crystalline water. The clathrate hydrates then decompose at the clathration line location, releasing the volatile species in the vapor phase. As with the condensation line, the same enrichment mechanism occurs at the clathrate line position Figure adapted from Schneeberger et al. (2023)

Species can only form clathrate hydrate if the clathration line is closer to the sun than the condensation line, in other word the clathrate must be stable at a higher temperature than the specie's condensation temperature. Figure 2.3 shows the condensation and clathration temperature of eleven species considered in this work and their clathrate hydrate, except for $NH_3$ which is not enclathrated but only form a monohydrate. Equilibrium curves are computed from equations of states described in section 2.5 and the pressure–temperature of the PPD is from the model described in chapters 3 and 4 after 10 kyr of evolution. Figure 2.3 show that in the case of all the volatile species the hydrate form at higher temperature than the pure condensate except for the clathrate of $CO_2$ and $NH_3$ monohydrate in condition of the PPD disk. At higher pressures, the temperature of formation of the clathrate hydrate of CO and $NH_3$ monohydrate become higher than their condensation temperature at $1.3 \times 10^{-5}$ and $6 \times 10^{-2}$ bar, respectively.

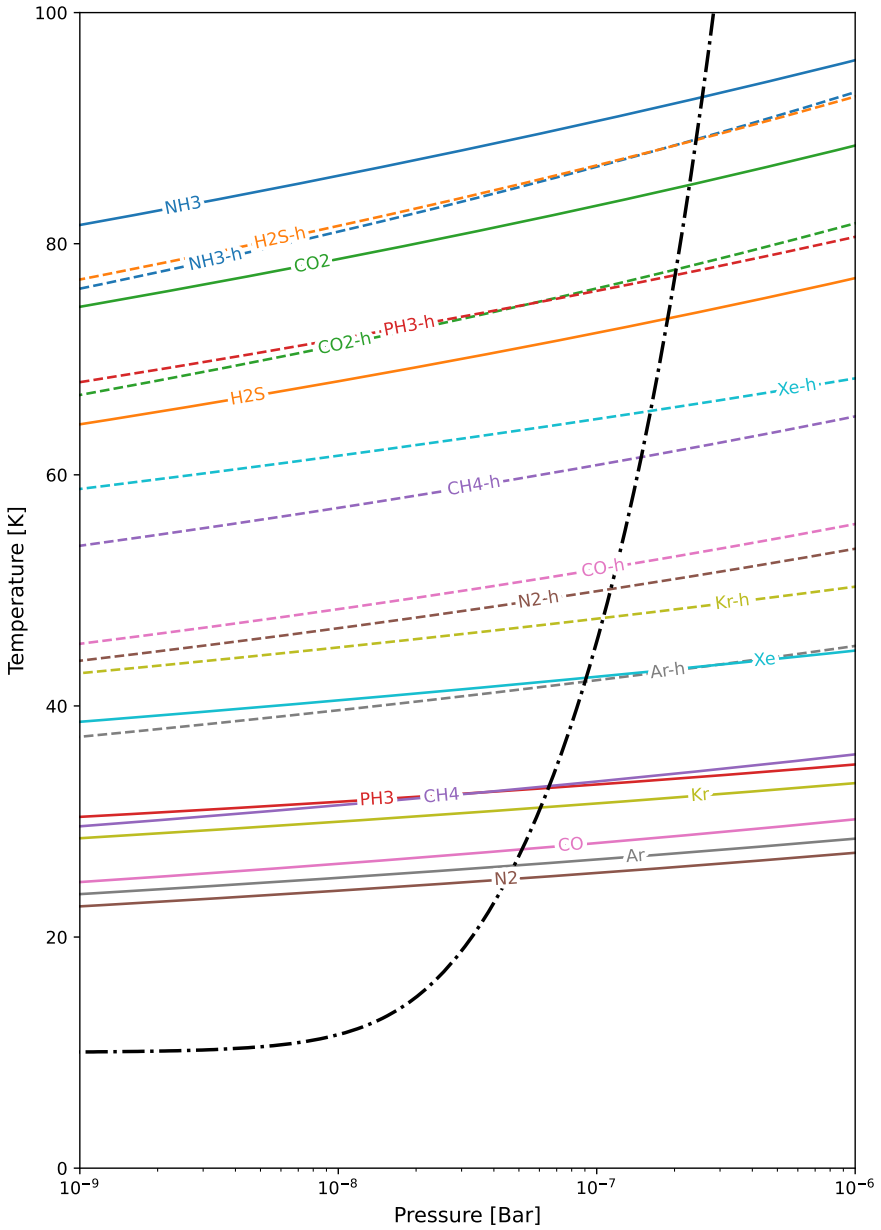


Figure 2.3.: Equilibrium curves of volatile species pure condensate (solid lines) and their corresponding clathrate hydrates, and $NH_3$ monohydrate (dashed line). The pressure-temperature profile of the PPD after 100 kyr of evolution is shown (black dashed line). It shows that under PPD conditions, $NH_3$ monohydrate and $CO_2$ clathrate hydrate form at lower temperatures than their respective pure condensates. Figure adapted from Schneeberger et al. (2023)

## 2.3. Amorphous water

The form taken by volatile that have fallen from the interstellar medium (ISM) onto the PPD is still an open question.

Icy pebbles, which are present in the PPD at its earliest stage, could have formed in the very cold environment of the ISM, at a temperature of less than 10 K (Gibb et al. 2004). At such a low temperature, water condenses in the form of amorphous ice. When amorphous water condenses in the ISM, it efficiently traps other volatile species (Mayer et al. 1986; Jenniskens et al. 1995). Water remains in its amorphous state until it is heated above its crystallization temperature of about 135 K (Bar-Nun et al. 2007). Consequently, if icy grains are not heated to this temperature as they accrete onto the PPD, volatile species trapped in amorphous water ice will be delivered to the PPD and only released when icy pebbles are close enough to the sun at the amorphous to crystalline transition zone (ACTZ). The ACTZ is located approximately at 5 AU (Mousis et al. 2019), much closer than volatile species condensation lines.

One can imagine a scenario depicted in figure 2.4 where all volatile species are delivered to the PPD trapped in amorphous water ice and only released in the vapor phase at the ACTZ location. The released vapor viscously diffuses both inward and outwards, and a small fraction of this vapor eventually cross the condensation line and condense as pure condensates onto the icy pebbles in the vicinity of the line.

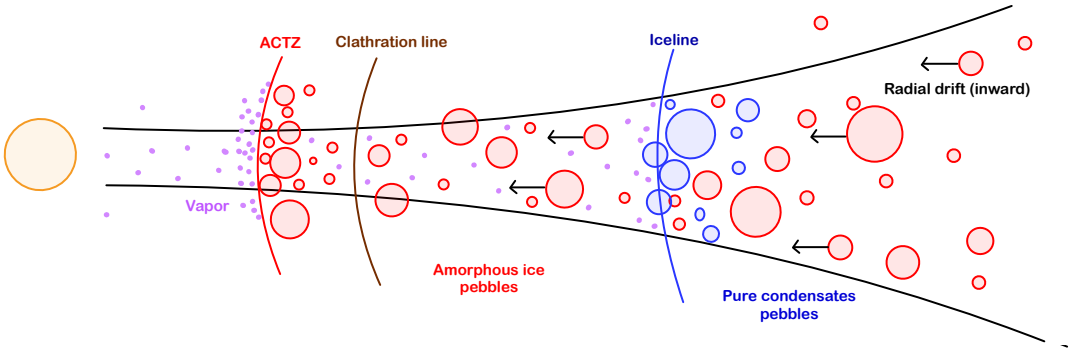


Figure 2.4.: Release of volatile species by amorphous water ice from the ISM. Amorphous water ice pebbles (red pebbles) drift from the outer edge of the PPD toward the amorphous to crystalline transition zone (ACTZ), which is located in a PPD region with a temperature higher than 135 K. As the water ice conformation changes from amorphous to crystalline, trapped volatile species are released into the vapor phase (purple dots) of the PPD. Some of the vapor diffuses outward and eventually crosses the species condensation line. The species then condenses to its pure condensate form. Figure adapted from Schneeberger et al. (2023)

However it is not clear it is not clear if the amorphous water ice survived the accretion onto the PPD. It has been proposed that accreting icy grains has been heated up to the crystallization temperature when entering the PPD by propagating shockwaves

in the accreting PPD (Visser et al. 2013; Miura et al. 2017; Burkhardt et al. 2019).

## 2.4. Hydrated minerals

CI and CM chondrites are mainly composed of a matrix of phyllosilicate minerals (Beck et al. 2010, 2014; Alexander 2019) as well as samples returned from Bennu (NASA/OSIRIS-REX) and Ruygu (JAXA/Hayabusa-2), two carbonaceous asteroids (Yokoyama et al. 2022; Lauretta et al. 2024). Phyllosilicates are a class of hydrate minerals that can contain up to 13%wt water. They are structured as sheet of silicate with water molecules bounded between each sheet. In the Solar System, phyllosilicates were formed mainly by the aqueous alteration of parent bodies which were then fragmented by collision with other bodies (Bischoff 1998; Suttle et al. 2021). This aqueous alteration occurs when a water-rich planetesimal forms outside the water condensation line. Due to the accretion energy, the interior of the planetesimal become a mixture of silicate and liquid water. The liquid water then reacts with the silicate matrix to form hydrated minerals. Alternatively, phyllosilicates may form earlier in the PPD. D'Angelo et al. (2019) and Thi et al. (2020) proposed that phyllosilicates can form on micrometer sized grains via a gas-grain reaction with warm water vapor in the inner regions of the disc. The water mass fraction of the grains could reach up to 5%wt by this process over a period of 100 kyr. The observation of a distinct D/H ratio in hydrous mineral inclusions within chondritic meteorites supports the primitive formation of hydrous minerals (Metzler et al. 1992; Ciesla et al. 2003; Piani et al. 2021). Another mechanism of primitive formation of phyllosilicate nanocrystals occurs in the wake of shock waves traversing the PPD. The travelling shock waves produce a sudden temperature rise of up to 2000 K (Ciesla et al. 2003; Burkhardt et al. 2019), which would melt silicates. The molten silicate recrystallizes and reacts with the surrounding water vapor to form phyllosilicate nanocrystals within a few days of the shock wave.

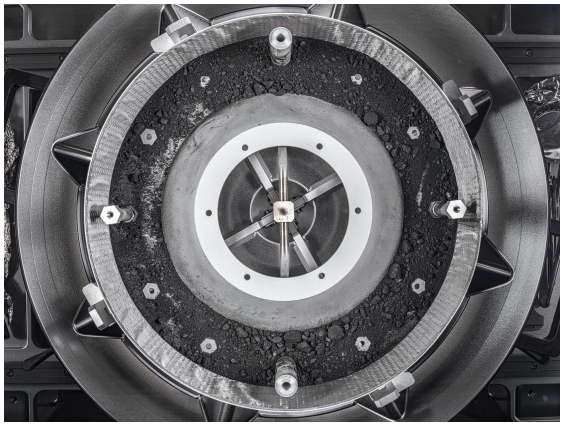

Figure 2.5.: Bennus sample returned the OSIRIS-REX mission. The black color of the sample denote the carbonaceous nature of Bennus. Credit: NASA/Erika Blumenfeld & Joseph Aebers

Dehydration of phyllosilicate at PPD pressure, of order of $10^{-5}$ bar, is poorly constrained. It only exists low pressure dehydration data at Marian pressure of order of a few millibars (Lange et al. 1982; Cloutis et al. 2007; Cloutis et al. 2008; Liang et al. 2022), consequently one need to rely on an ad-hoc chemical model which show a dehydration temperature in the range between 400 K and 600 K (Mousis et al. 2023). The study focus on the dehydration of serpentine minerals, namely antigorite, chrysotile and lizardite, because serpentine is the most abundant hydrated mineral in chondrites (Brearley 2006). The dehydration reaction of serpentine minerals at low pressure is (Fegley 2000):

$$\text{serpentine} \rightarrow \text{forstetite} + \text{enstatie} + \text{water}. \tag{2.1}$$

The dehydration temperature of serpentine is determined by determining the temperature at which the reaction is at thermodynamic equilibrium. Equilibrium constants of the dehydration reaction is calculated using the code `SUPCRTLB` (Johnson et al. 1992; Zimmer et al. 2016). Results from Mousis et al. (2023) are show in figure 2.7 , showing that lizardite and chrysotile have minimum dehydration temperature of 206 K and 215 K, respectively in the Jovian circumplanetary disk. However, those temperatures are minimum temperature, and it is unclear if the dehydration rate would be fast enough at those temperatures to release water vapor at the dehydration line (Fegley 2000). Therefore, authors choose to use higher dehydration temperatures between 400 K and 600 K.

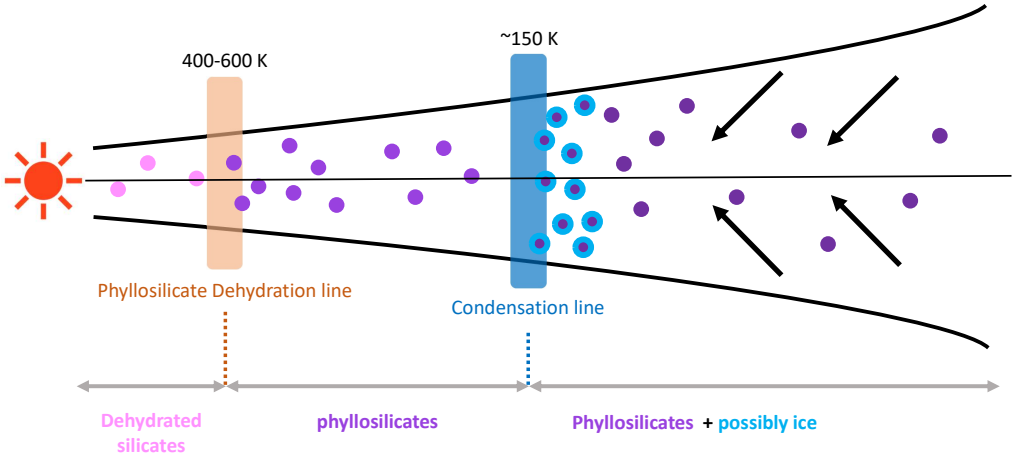


Figure 2.6.: Water supply to the inner regions of the PPD by phyllosilicates. The sketch shows a case where the PPD is initially free of water ice to illustrate the effect of phyllosilicates on the water ice budget. Phyllosilicate–rich grains (purple pebbles) drift from the outer to the inner regions of the disk, crossing the phyllosilicate dehydration line (PDL) where water vapor is released. At distances closer to the star than the PDL, only dehydrated silicate-rich grains (pink pebbles) remain. Some of the released water vapor diffuses outward and eventually crosses the water condensation line and condenses on pebbles (blue shell). Figure adapted from Schneeberger et al. (2024)

Due to the high water content of phylloscilicate minerals, they can be a source of water for the inner PPD. Figure 2.6 show the delivery of water to the inner regions of the PPD by phyllosilicates. It shows that phyllosilicates–rich grains drift from the outer disk to the inner disc, reaching hot regions of the disk. When the grains reach a temperature region between 400 K and 600 K, called the phyllosilicate dehydration line (PDL), the phyllosilicate inclusions dehydrate and release water vapor into the PPD. The water vapor diffuses both inwards and outwards and eventually crosses its condensation line to form ice on the grain surface. Therefore, phyllosilicate can be a source of water for the inner disk at temperatures lower than 400–600 K and a source of water ice enrichment at the water condensation line.

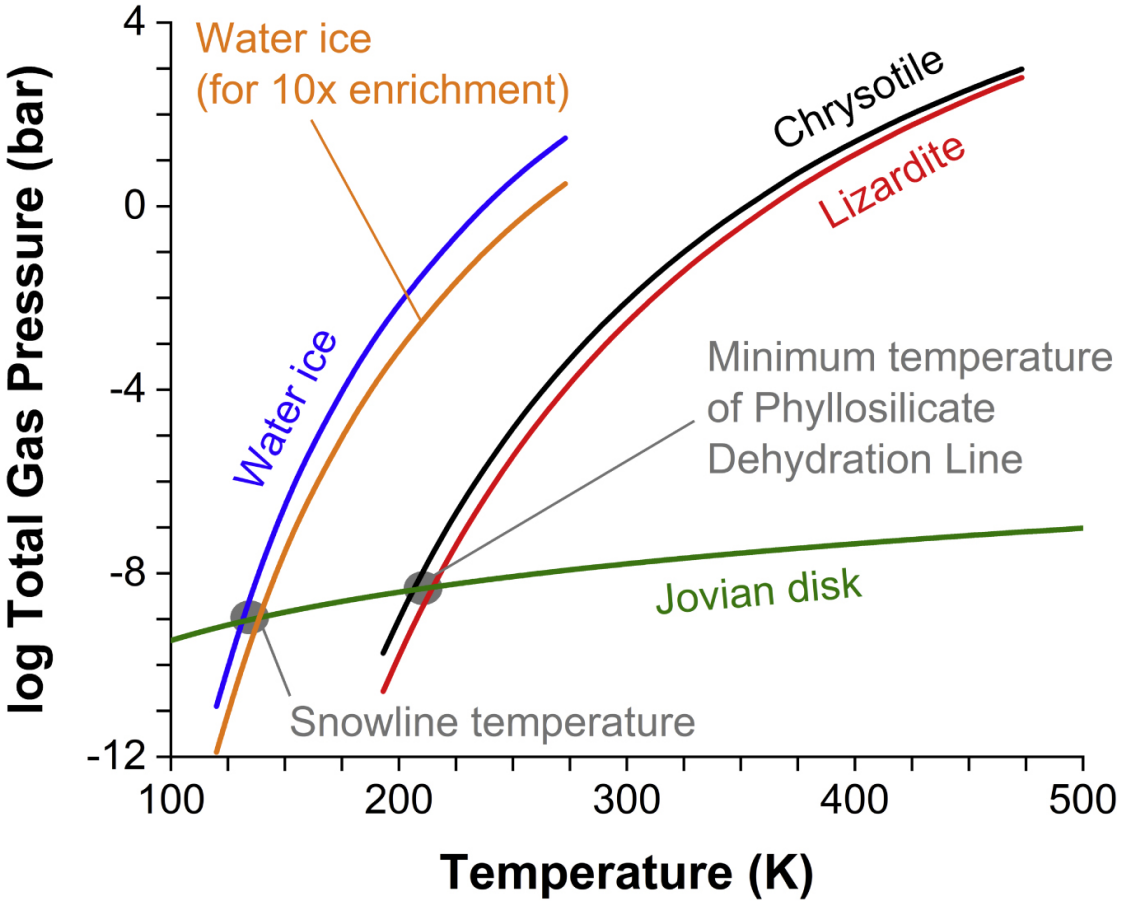


Figure 2.7.: Equilibrium dehydration curves of the serpentine polymorphs, chrysotile (black curve) and lizardite (red curve) in the presence of solar material, where the main carbon carrier is carbon monoxide. Water ice condensation curves are shown for a protosolar composition (blue curve), The PPD pressure-temperature curve after 100 kyr of evolution (green curve). Figure reproduced from Mousis et al. (2023).

## 2.5. Equations of States

This section present the equation of states (EOS) used to compute the condensation and clathration lines position in the PPD.

### 2.5.1. Pure condensates

The vapor pressures of the pure condensates considered in this work, except $H_2O$ and $NH_3$, follow the law:

$$\ln P_{\rm eq} = \sum_k a_k \left(\frac{1}{T}\right)^k, \tag{2.2}$$

where the $a_k$ factors have been determined experimentally (Fray et al. 2009) and are summarized in Table 2.1.

The vapor pressure of $H_2O$ is given by Wagner et al. (2011):

$$\begin{aligned} P_{\rm eq} = & P_{\rm tp} \exp\left\{\left(\frac{T_{\rm tp}}{T}\right)\right\}\left(-21.2144006\left(\frac{T_{\rm tp}}{T}\right)^{1/300}\right. \\ & + 27.3203819\left(\frac{T_{\rm tp}}{T}\right)^{2.10666667} \\ & \left. -6.10598130\left(\frac{T_{\rm tp}}{T}\right)^{1.70333333}\right), \end{aligned} \tag{2.3}$$

where $P_{\rm tp}$ and $T_{\rm tp}$ are the pressure and the temperature of the triple point of water, respectively.

The phosphine equilibrium pressure is given by Stull (1947):

$$\log_{10} P_{\rm eq} = 4.02591 - \frac{702.651}{T - 11.065}. \tag{2.4}$$

Table 2.1.: Polynomial factors for the vapor pressure equations of pure condensates

| Element | Temperature range (K) | $a_0$ | $a_1$ | $a_2$ | $a_3$ | $a_4$ | $a_5$ | $a_6$ |
|---|---|---|---|---|---|---|---|---|
| CO | $T \leq 61.55$ | 10.43 | -721.3 | -10740 | $2.341 \times 10^5$ | $-2.392 \times 10^6$ | $9.478 \times 10^6$ | ∅ |
| | $T > 61.55$ | 10.25 | -748.2 | -5843 | $3.939 \times 10^4$ | ∅ | ∅ | ∅ |
| $CO_2$ | $T \leq 40$ | $10^{-40}$ | ∅ | ∅ | ∅ | ∅ | ∅ | ∅ |
| | $40.0 < T \leq 194.7$ | 14.76 | -2571 | $-7.781 \times 10^4$ | $4.325 \times 10^6$ | $-1.207 \times 10^8$ | $1.350 \times 10^9$ | ∅ |
| | $T > 194.7$ | 18.61 | -4154 | $1.041 \times 10^5$ | ∅ | ∅ | ∅ | ∅ |
| $CH_4$ | all | 10.51 | -1110 | -4341 | $1.035 \times 10^5$ | $-7.910 \times 10^5$ | ∅ | ∅ |
| $H_2S$ | $T \leq 127.0$ | 12.98 | -2707 | ∅ | ∅ | ∅ | ∅ | ∅ |
| | $T > 127.0$ | 8.933 | -726.0 | $-3.504 \times 10^5$ | $2.724 \times 10^7$ | $-8.582 \times 10^8$ | ∅ | ∅ |
| $N_2$ | $T \leq 35.61$ | 12.40 | -80.74 | -3926 | $6.297 \times 10^4$ | $-4.633 \times 10^5$ | $1.325 \times 10^5$ | ∅ |
| | $T > 35.61$ | 8.514 | -456.4 | $-1.987 \times 10^4$ | $4.800 \times 10^5$ | $-4.524 \times 10^6$ | ∅ | ∅ |
| $NH_3$ | all | 15.96 | -3537 | $-3.310 \times 10^4$ | $1.742 \times 10^6$ | $-2.995 \times 10^7$ | ∅ | ∅ |
| Ar | all | 10.69 | -893.2 | -3567 | $6.574 \times 10^4$ | $-4.280 \times 10^5$ | ∅ | ∅ |
| Kr | all | 10.77 | -1223 | -8903 | $2.635 \times 10^5$ | $-4.260 \times 10^6$ | $3.575 \times 10^7$ | $-1.210 \times 10^8$ |
| Xe | all | 10.698 | -1737 | $-1.332 \times 10^4$ | $4.349 \times 10^5$ | $-7.027 \times 10^6$ | $4.447 \times 10^7$ | ∅ |

Table 2.2.: Parameters for the dissociation pressure equations of $NH_3$ monohydrate and clathrates

| Element | A | B | Reference |
|---|---|---|---|
| CO | -1685.54 | 10.9946 | Hersant et al. (2004) |
| $CO_2$ | -2544.395 | 11.411518 | Longhi (2005) |
| $CH_4$ | -2161.81 | 11.1249 | Hersant et al. (2004) |
| $H_2S$ | -3111.02 | 11.3801 | Hersant et al. (2004) |
| $N_2$ | -1677.62 | 11.1919 | Hersant et al. (2004) |
| $NH_3$ | -2878.28 | 8.00205 | Hersant et al. (2004) |
| Ar | -1481.78 | 9.95523 | Hersant et al. (2004) |
| Kr | -1987.5 | 9.99046 | Hersant et al. (2004) |
| Xe | -2899.19 | 11.0354 | Hersant et al. (2004) |
| $PH_3$ | -3011.28 | 11.95 | Lunine et al. (1985) |

### 2.5.2. Clathrate hydrates

The dissociation pressures of $NH_3$ monohydrate and clathrates follow the Antoine law:

$$\ln P_{\rm eq} = \frac{A}{T} + B, \tag{2.5}$$

with $A$ and $B$ parameters determined from experiments and summarized in Table 2.2.

# 3. Protoplanetary disk and volatile transport models

The following chapter describes the protoplanetary disk (PPD) model. The following method is adapted from Schneeberger et al. (2023) and based on the work of Aguichine et al. (2020) and Aguichine (2022).

## Table of Contents


3.1. The protoplanetary disk . . . . . 53
3.2. Evolution of volatile species in the protoplanetary disk . . . . . 56
3.2.1. Volatile evolution model setup . . . . . 56
3.2.2. Species advection-diffusion evolution equation . . . . . 57
3.2.3. Dust and pebbles evolution . . . . . 58
3.2.4. Sources and sinks of trace species . . . . . 60


## 3.1. The protoplanetary disk

The protoplanetary disk is composed of gas and dust that formed around the sun during its T-Tauri phase. We use a model presented by Shakura et al. (1973) and Lynden-Bell et al. (1974) and used in the works of Aguichine et al. (2020, 2022) . This model starts from the gas density continuity equation :

$$\frac{\partial \rho}{\partial t} + \nabla \cdot \rho \mathbf{U} \tag{3.1}$$

where $\mathbf{U}$ is the gas flow velocity and $\rho$ the gas density. Assuming that the gas in the disk is vertically at hydrostatic equilibrium, the vertical density profile is hypothesized to be Gaussian. One have :

$$\rho(r,z) = \rho_0(r) \exp\left(\frac{-z^2}{2H(r)^2}\right), \tag{3.2}$$

where $\rho(z)$ is the gas density at altitude z, and radial distance r, $\rho_0$ is the midplane gas density, and $H$ is the PPD scale height only dependent on the radial distance from the sun. By integrating the gas density over all altitude z, one have the gas surface density :

$$\Sigma(r) = \int_{-\infty}^{+\infty} \rho(r,z)dz \tag{3.3}$$

Following the procedure described by Lynden-Bell et al. (1974) and Lin et al. (1985), by assuming that the PPD is axisymmetric, one get the disk continuity equation

$$\frac{\partial \Sigma_g}{\partial t} = \frac{3}{r}\frac{\partial}{\partial r}\left[r^{1/2}\frac{\partial}{\partial r}\left(r^{1/2}\Sigma_g \nu\right)\right], \tag{3.4}$$

which describes the time evolution of a viscous accretion disk, where $\nu$ is the gas viscosity. This equation can be rewritten as a set of two first-order differential equations coupling the gas surface density, $\Sigma_g$, field and mass accretion rate, $\dot{M}$:

$$\begin{cases} \dfrac{\partial \Sigma_g}{\partial t} = \dfrac{1}{2\pi r}\dfrac{\partial \dot{M}}{\partial r} \\ \dot{M} = 3\pi\Sigma_g \nu\left(1 + 2\dfrac{\partial \ln \nu\Sigma_g}{\partial \ln r}\right) \end{cases}. \tag{3.5}$$

The first equation is a mass conservation law and the second one is a diffusion equation. The mass accretion rate is expressed as a function of the gas velocity field, $v_g$, and the radius, $r$, as $\dot{M} = -2\pi\Sigma_g v_g \mathbf{r}$.

The dynamical viscosity $\nu$ is calculated using the prescription of Shakura et al. (1973):

$$\nu = \alpha\frac{c_s^2}{\Omega_K}, \tag{3.6}$$

where $\alpha$ is the viscosity coefficient, $c_s$ is the sound speed in the PPD, and $\Omega_K$ is the Keplerian frequency; also, $\alpha$ is estimated to be in the $10^{-4}$–$10^{-2}$ range, based on models calibrated on disk observations Hartmann et al. (1998), Hersant et al. (2004), Gautier et al. (2005), Birnstiel et al. (2012), Drążkowska et al. (2017), Armitage et al. (2019), and Villenave et al. (2022). The sound speed, $c_s$, is expressed as follows:

$$c_s = \sqrt{\frac{RT}{\mu_g}}, \tag{3.7}$$

where $\mu_g$ is the mean molecular mass of the gas in the PPD, assumed here to be equal to 2.31 g.mol$^{-1}$, $T$ is the midplane temperature, and $R$ is the ideal gas constant.

Two energy sources are considered in our model, namely viscous heating, and the constant irradiation by the local environment of ambient temperature, $T_{amb}$ = 10 K. Irradiation from the young Sun is neglected because the presence of shadowing is assumed in the outer part of the disk Ohno et al. (2021). This allows the disk temperature to decrease to the condensation temperature of Ar (~20 K), allowing this species to be trapped in Jupiter's building blocks in a way consistent with the super–solar abundance observed in its envelope Mousis et al. (2009, 2012, 2021a). The temperature profile is computed by summing the energy production rates of both energy sources Hueso et al. (2005):

$$T^4 = \frac{1}{2\sigma_{SB}}\left(\frac{3}{8}\tau_R + \frac{1}{2\tau_P}\right)\Sigma_g \nu \Omega_K^2 + T_{amb}^4, \tag{3.8}$$

where $\sigma_{sb}$ is the Stefan-Boltzmann constant, while $\tau_R$ and $\tau_P$ are the Roseland and Planck optical depth, respectively. Here, we assume $\tau_P = 2.4\tau_R$, a case corresponding to the opacity generated by dust grains smaller than 10 $\mu$m Nakamoto et al. (1994); $\tau_R$ is derived from the Roseland mean opacity, $\kappa_R$, via the following expression Hueso et al. (2005):

$$\tau_R = \frac{\Sigma_g \kappa_R}{2}. \tag{3.9}$$

Here, $\kappa_R$ is computed as a sequence of power laws of the form $\kappa_R = \kappa_0 \rho^a T^b$, where $\rho$ denotes the gas density at the midplane, and $\kappa_0$, $a$, and $b$ are constants that are obtained by fits on observational data in different opacity regimes Bell et al. (1994).

The initial state of the model is computed from the self-similar solution derived by Lynden-Bell et al. (1974):

$$\Sigma_g \nu \propto \exp\left\{\left[-\left(\frac{r}{r_c}\right)^{2-p}\right]\right\}. \tag{3.10}$$

By combining Eqs. 3.10 and 3.5, and assuming $p = \frac{3}{2}$, which corresponds to the case for an early disk Lynden-Bell et al. (1974), the initial profiles of the dust surface density and mass accretion rate are given by:

$$\begin{cases} \Sigma_{g,0} = \dfrac{\dot{M}_{acc,0}}{3\pi\nu} \exp\left[-\left(\dfrac{r}{r_c}\right)^{0.5}\right] \\ \dot{M}_0 = \dot{M}_{acc,0}\left(1-\left(\dfrac{r}{r_c}\right)^{0.5}\right) \exp\left[-\left(\dfrac{r}{r_c}\right)^{0.5}\right] \end{cases}, \tag{3.11}$$

where $r_c$ is the centrifugal radius and $\dot{M}_{acc,0}$ is the initial mass accretion rate onto the central star, set to $10^{-7.6}$ $M_\odot$ yr$^{-1}$ Hartmann et al. (1998). The disk mass is related to the surface density profile via the following expression:

$$M_{disk} = 2\pi \int_{R_{min}}^{R_{max}} \Sigma r dr, \tag{3.12}$$

where $R_{min}$ and $R_{max}$ are the inner and outer bounds of our model. The total disk mass is set to $0.1 M_\odot$ and most of it (99%) is encapsulated within ~200 au. The centrifugal radius, $r_c$, is determined by solving Eqs. 3.11 with 3.12 for the chosen values of mass accretion rate and disk mass. Figure 3.1 represents the thermodynamic profiles of our PPD model assuming $\alpha = 10^{-3}$, and at $t = 10^4$, $10^5$, and $10^6$ yr of the disk evolution.

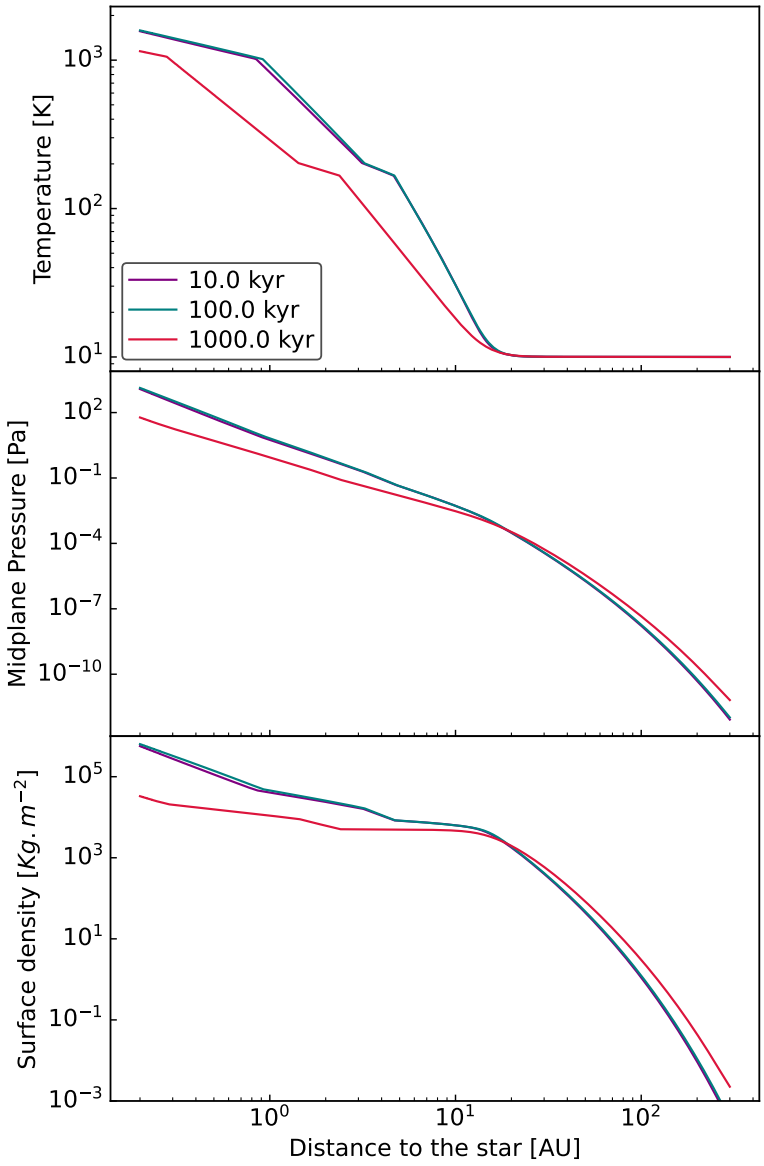


Figure 3.1.: Profiles of the disk midplane temperature, pressure and surface density calculated at $t = 10^4$, $10^5$, and $10^6$ yr as a function of heliocentric distance, assuming $\alpha = 10^{-3}$, shown from top to bottom.

## 3.2. Evolution of volatile species in the protoplanetary disk

### 3.2.1. Volatile evolution model setup

To assess the impact of the volatile species reservoir trapped either in clathrate hydrates or the amorphous water ice, use the volatile species transport model built by Aguichine (2022). This model considers the transport of volatile species in vapor and

pure condensate phases (Aguichine et al. 2020; Aguichine 2022; Aguichine et al. 2022). Therefore, to study the impact of clathrate hydrates and amorphous water ice on the volatile species distribution in the PPD, we added those two new phases to the model. Two account for the uncertainties on the survival of amorphous water ice when it is accreted by the PPD, we study two scenarios. The first scenario consider that amorphous water ice is heated up to its amorphous-to-crystalline transition temperature and released all trapped volatile species. Therefore, in scenario 1 we only consider a delivery of volatile species as pure condensates. In the second scenario, we consider that the amorphous water ice is never heated up to the amorphous-to-crystalline transition temperature and only consider a delivery of volatile species trapped in amorphous water ice (scenario 2).

### 3.2.2. Species advection-diffusion evolution equation

Trace species are considered in four distinct forms: vapors, pure condensates, entrapped in clathrates, or forming a monohydrate (case for $NH_3$ only), and adsorbed in amorphous ice. In our model, a distinct surface density is attributed to each of these forms, with $\Sigma_{\mathrm{v},i}$, $\Sigma_{\mathrm{p},i}$, $\Sigma_{\mathrm{c},i}$, and $\Sigma_{\mathrm{a},i}$ corresponding to species $i$ in vapor, pure condensate, clathrate or hydrate, or amorphous ice phases, respectively. Their time and radial evolution is governed by the advection-diffusion equation Birnstiel et al. (2012) and Desch et al. (2017):

$$\frac{\partial \Sigma_i}{\partial t} + \frac{1}{r}\frac{\partial}{\partial r}\left[r\left(\Sigma_i v_i - D_i \Sigma_\mathrm{g}\frac{\partial}{\partial r}\left(\frac{\Sigma_i}{\Sigma_\mathrm{g}}\right)\right)\right] - \dot{Q}_i = 0, \tag{3.13}$$

where $D_i$ is the diffusion coefficient and is $v_i$ is the radial speed. $\dot{Q}_i$ is a source or sink term that accounts for phase changes, counted positive/negative when some matter is created or lost.

For surface densities of vapors, we assume $D_i = D_\mathrm{g}$ and $v_i = v_\mathrm{g}$ because vapors are well coupled to the PPD gas and evolve similarly. The gas diffusivity, $D_\mathrm{g}$, is assumed to be equal to the viscosity, $\nu$, and the gas velocity is Shakura et al. (1973):

$$v_\mathrm{g} = -\frac{\dot{M}_\mathrm{acc}}{2\pi r \Sigma_\mathrm{g}}. \tag{3.14}$$

At each time and location, we assume that dust particles are formed from a mixture of all available solids. As a consequence, surface densities of solid phases, namely clathrates (and $NH_3$ monohydrate), amorphous ices, and pure condensates, are evolved with the same diffusion coefficient, $D_\mathrm{s}$, and radial velocity, $v_\mathrm{s}$. For particles of a given size, $a$, and Stokes number, St, the diffusion coefficient is given by Birnstiel et al. (2012):

$$D_\mathrm{s} = \frac{D_\mathrm{g}}{1+\mathrm{St}^2}. \tag{3.15}$$

The dust radial velocity is expressed as the sum of gas drag and drift velocities Birnstiel et al. (2012):

$$v_s = \frac{1}{1+\mathrm{St}^2} v_g + \frac{2\mathrm{St}}{1+\mathrm{St}^2} v_{\mathrm{drift}}, \tag{3.16}$$

where the drift velocity is Weidenschilling (1997):

$$v_{\mathrm{drift}} = \frac{c_s^2}{v_K} \frac{\mathrm{d}\ln P}{\mathrm{d}\ln r}. \tag{3.17}$$

The diffusion coefficient and radial velocity of solids are computed for the small and the large populations, that is, for particles of sizes $a_0$ and $a_1$. The diffusion coefficient, $D_s$, and radial velocity $v_s$ used to evolve surface densities of solids are then given by mass-averaged diffusivities and velocities of the small and large population Birnstiel et al. (2012):

$$\begin{cases} v_s = f_m v_{d,a_1} + (1-f_m) v_{d,a_0}. \\ D_s = f_m D_{d,a_1} + (1-f_m) D_{d,a_0}. \end{cases} \tag{3.18}$$

### 3.2.3. Dust and pebbles evolution

To determine the size of the dust pebbles, we rely heavily on the two-population algorithm developed by Birnstiel et al. (2012). This algorithm relies on the key idea that the dynamics of dust pebbles of many sizes can be well approximated by the dynamics of only two populations of particles, in which all particles have the same representative sizes. The first group corresponds to the small population, where grains are of constant size: $a_0 = 0.1$ $\mu$m. The second group represents a large population, where pebbles have a representative size $a_1$, which depends on the characteristics of the flow.

In the disk, pebbles grow by sticking collisions via the following law:

$$a_1(t) = a_0 \exp\left\{\left(\frac{t}{\tau_{\mathrm{growth}}}\right)\right\}, \tag{3.19}$$

where $\tau_{\mathrm{growth}}$ is the growth timescale,

$$\tau_{\mathrm{grow}} = \frac{4\Sigma_g}{\sqrt{3}\epsilon_g \Sigma_b \Omega_K}, \tag{3.20}$$

where $\Sigma_b$ is the total surface density of solids, and $\epsilon_g$ is the dust growth efficiency through mutual sticking set to 0.5 Lambrechts et al. (2014). Then, we compute the Stokes number of pebbles as a function of their sizes Johansen et al. (2014):

$$\mathrm{St} = \begin{cases} \sqrt{2\pi}\dfrac{a_1 \rho_b}{\Sigma_g} \text{ If } a_1 \leq \dfrac{9}{4}\lambda \\ \dfrac{8}{9}\dfrac{a_1^2 \rho_b c_s}{\Sigma_g \nu} \text{ If } a_1 \geq \dfrac{9}{4}\lambda \end{cases}. \tag{3.21}$$

The top and bottom lines of Eq. 3.21 correspond to the Epstein and Stokes regimes, respectively. The limit between both regimes is fixed by the gas mean free path $\lambda = \sqrt{\pi/2} \cdot \nu / c_s$, computed by equating the two terms in Eq.(3.21). The term $\rho_b$ is the pebbles' mean bulk density:

$$\rho_b = \frac{\sum_i \Sigma_{b,i} \rho_{b,i}}{\sum_i \Sigma_{b,i}}, \tag{3.22}$$

computed as the average of each species' bulk density, $\rho_{b,i}$, weighted by their solid surface density, $\Sigma_{b,i}$.

Observations indicate that disks are rich in small dust and suggest that fragmentation is a dominant process Weidenschilling (2011). Based on this observation, our approach considers fragmentation and radial drift as the growth-limiting mechanisms. These mechanisms set an upper limit on the highest Stokes number that particles can achieve. The first limitation results from the fragmentation occurring when the relative speed between two pebbles due to turbulent motion exceeds the fragmentation velocity, $u_f$. This upper limit is given by Birnstiel et al. (2012):

$$\mathrm{St}_{\mathrm{frag}} = f_f \frac{1}{3\alpha} \frac{u_f^2}{c_s^2}, \tag{3.23}$$

where $u_f$ is set to $10\,\mathrm{m\,s^{-1}}$ and the factor $f_f = 0.37$ accounts for the fact that the representative size of the large population is smaller than the biggest size particles can achieve before they fragment.

A second limitation for dust growth is determined by the drift velocities of the different pebbles. When pebbles drift faster than they grow, this sets another upper limit for the Stokes number( Birnstiel et al. (2012)):

$$\mathrm{St}_{\mathrm{drift}} = f_d \frac{\Sigma_b v_K^2}{\Sigma_g c_s^2} \left| \frac{\mathrm{d} \ln P}{\mathrm{d} \ln r} \right|^{-1}, \tag{3.24}$$

where $P$ is the disk midplane pressure, $v_K$ the keplerian velocity, and $f_d = 0.55$ has the same origin as $f_f$.

When dust grains drift at a high velocity and collide with other particles on their path, they can fragment. This induces a third upper limit for the Stokes number Birnstiel et al. (2012), given by:

$$\mathrm{St}_{\mathrm{df}} = \frac{1}{1-N} \frac{u_f v_K}{c_s} \left( \frac{\mathrm{d}P}{\mathrm{d}r} \right)^{-1}, \tag{3.25}$$

where the factor $N = 0.5$ accounts for the fact that only larger grains fragment when colliding.

In the algorithm, all limiting Stokes numbers are computed and compared with the Stokes number derived from Eq. 3.21. At each time step, the smallest Stokes number found in this comparison becomes the reference Stokes number which, in turn, sets the value for the representative size, $a_1$, of the large population. The representative size of the small population is always $a_0$, and their Stokes number is always computed

in the Epstein regime (top line of Eq. 3.21).

Finally, the two-population algorithm of Birnstiel et al. (2012) introduces $f_m$ the fraction of the mass contained in the large population. Among the three size-limiting mechanisms, if particle drift is the most limiting one ($St_{drift} = \min(St_{frag}, St_{drift}, St_{df})$), then the fraction of the mass contained in the large population is $f_m = 0.97$. Otherwise, $f_m$ is set to 0.75 Birnstiel et al. (2012). The mean grain size $\bar{a}$ is then given by:

$$\bar{a} = f_m a_1 + (1 - f_m)\ a_0. \tag{3.26}$$

### 3.2.4. Sources and sinks of trace species

We follow the approach of Aguichine et al. (2020) to depict the sources and sinks for both the solid and vapor phases of the different species. A pure condensate of species $i$ undergoes sublimation if its partial pressure is lower than the corresponding equilibrium pressure. Sublimation results in a sink term for pure condensates during the time step, $\Delta t$ (Drążkowska et al. 2017):

$$\dot{Q}_{p,i} = -\min\left(\sqrt{\frac{8\pi\mu_i}{RT}}\frac{3}{\pi\bar{a}\bar{\rho}}P_{eq,i}\Sigma_{p,i}; \frac{\Sigma_{p,i}}{\Delta t}\right), \tag{3.27}$$

where $\mu_i$ is the molar mass of species $i$, $\bar{\rho}$ is the mean bulk density of grains, $P_{eq,i}$ is the equilibrium pressure, and $\bar{a}$ is the mean size of grains. The second part of the minimum function ensures that no more than the available quantity of pure condensate sublimates.

Conversely, a gas of species $i$ forms a pure condensate if its partial pressure is larger than the corresponding equilibrium pressure. The condensation rates results in a source term for pure condensates (Drążkowska et al. 2017):

$$\dot{Q}_{p,i} = \min\left((P_i - P_{eq,i})\frac{2H\mu_i}{RT\Delta t}; \frac{\Sigma_{v,i}}{\Delta t}\right). \tag{3.28}$$

To the model of Aguichine et al. (2020) we add the possibility of $NH_3$ monohydrate and clathrate hydrates crystallization in the PPD. To compute the source and sink of species clathrate hydrates and monohydrates, one use the same expression as for the condensation (Eq. 3.28) and vaporization (Eq. 3.27). As discussed in section 2.2, their formation is bounded to the presence of crystalline water. Consequently, the formation of clathrates and $NH_3$ monohydrate also requires the presence of a minimum amount of crystalline water, resulting in a limit for their source term $\dot{Q}_{c,i}$:

$$\dot{Q}_{c,i}\ \Delta t \leq \frac{\mu_i}{S_i\ \mu_{H_2O}}\left[\Sigma_{p,H_2O} - \sum_k \Sigma_{c,k}\frac{S_k\ \mu_{H_2O}}{\mu_k}\right]. \tag{3.29}$$

This expression takes the amount of available crystalline water $\Sigma_{p,H_2O}$ and subtracts the amount of water that is already used to trap currently existing clathrates. In this expression, $S_k$ is the stoichiometric ratio between the species $k$ and water. This ratio is set to 5.75, 5.66, and 1 in the cases of type I clathrate, type II clathrate, and $NH_3$

monohydrate, respectively. This condition sets an upper limit on the clathrate source term, that can be equal to 0 if all the crystalline water is already holding clathrates. If all conditions are met for a trace species to be able to form pure condensates, clathrates, and monohydrates, we prioritize the solid phase that has the greatest $P_i - P_{\mathrm{eq,i}}$ value. Prioritizing the largest $P_i - P_{\mathrm{eq,i}}$ value is equivalent to prioritizing the highest solidification rate. Such considerations are not taken into account when performing a prioritization test among clathrate formation and condensation of pure condensates, since clathrates only form when pure condensates are not stable.

# 4. Application to Giant planets

Formation models of giant planets suggest that their composition should mirror the composition of the protoplanetary disk (PPD) at their respective formation regions. The gas giants, Jupiter (317 $m_\oplus$) and Saturn (95 $m_\oplus$), accreted both solids and gas during their formation. In contrast, the ice giants, Uranus (14 $m_\oplus$) and Neptune (17 $m_\oplus$), primarily accreted solids due to their significantly lower final masses compared to the gas giants. In this chapter, we aim to assert the impact of hydrate and amorphous water ice on the radial distribution of volatile species and the impact on the putative formation location and periods of the giant planets.

## Table of Contents


4.1. Distribution of volatile species in the protoplanetary disk . . . . . 62
4.1.1. Model setup . . . . . 62
4.1.2. Volatile species radial distribution . . . . . 63
4.1.3. Water evolution in the PPD . . . . . 64
4.1.4. Initial delivery of pure condensates . . . . . 65
4.1.5. Initial delivery of species trapped in amorphous water ice . . . . 68
4.1.6. Variation of the model parameters . . . . . 70
4.2. Implications for Giant planets formation . . . . . 81
4.2.1. Jupiter . . . . . 81
4.2.2. Saturn . . . . . 83
4.2.3. Uranus and Neptune . . . . . 85


## 4.1. Distribution of volatile species in the protoplanetary disk

### 4.1.1. Model setup

We simulate the evolution of volatile species over a period of 1 Myr, following two scenarios. In the first scenario, referred to as *scenario 1*, the PPD is initially filled with volatile species in pure condensate and vapor phases. During the first time steps, hydrates form where they are stable according to their equation of states (see table 2.2). In the second scenario, referred to as *scenario 2*, volatile species are initially trapped within amorphous water ice and are released at the amorphous-to-crystalline

Table 4.1.: Model parameters used in nominal runs

| Parameter | Value | Reference |
|---|---|---|
| $M_{disk}$ | $10^{-1}$ $M_\odot$ | Hersant et al. (2004) |
| $a_0$ | $10^{-7}$ m | Birnstiel et al. (2012) |
| $\alpha$ | $10^{-3}$ | Shakura et al. (1973) |
| $\dot{M}_{acc,0}$ | $10^{-7.6}$ $M_\odot$ $yr^{-1}$ | Aguichine et al. (2020) |
| $\rho_{grains}$ | 0.5 | |
| $\mu_{gas}$ | 2.31 g $mol^{-1}$ | Aguichine et al. (2022) |

Table 4.2.: Initial molar abundances of the considered trace species.

| Trace species | $(X/H_2)_\odot$ | Trace species | $(X/H_2)_\odot$ |
|---|---|---|---|
| $H_2O$ | $5.479 \times 10^{-4}$ | $NH_3$ | $5.456 \times 10^{-5}$ |
| CO | $3.698 \times 10^{-4}$ | $PH_3$ | $6.368 \times 10^{-7}$ |
| $CO_2$ | $1.479 \times 10^{-4}$ | Ar | $7.150 \times 10^{-6}$ |
| $CH_4$ | $3.698 \times 10^{-5}$ | Kr | $4.310 \times 10^{-9}$ |
| $H_2S$ | $1.633 \times 10^{-5}$ | Xe | $4.210 \times 10^{-10}$ |
| $N_2$ | $5.456 \times 10^{-5}$ | | |

transition zone (ACTZ) of water ice, which occurs where the PPD temperature reaches 135 K (Bar-Nun et al. 2007).

We use a PPD mass of $10^{-1}$ $M_\odot$ (Hersant et al. 2004) and a viscosity parameter $\alpha = 10^{-3}$ (Shakura et al. 1973). We choose a grain density of 0.5, taking into account for the high porosity of grains aggregate and pebbles. Model parameters are presented in table 4.1.

### 4.1.2. Volatile species radial distribution

We use the elemental protosolar abundances from Lodders (2019). We assume that carbon is distributed between CO, $CO_2$ and $CH_4$, with the remaining oxygen $H_2O$. We assume CO:$CO_2$:$CH_4$ = 10:4:1 in the PPD gas phase, derived from ROSINA measurement of the comet 67P/Churyumov–Gerasimenko degassing composition. Specifically, CO:$CO_2$ ratio is deduced from measurements between August 2014 and September 2016 (Mousis et al. 2014) and CO:$CH_4$ ratio from the comet's production rates in its south hemisphere in October 2014 (Le Roy et al. 2015). Sulfur is assumed to be half trapped in $H_2S$ form and half in refractory sulfide components (Pasek et al. 2005). Finally, we assumed that $N_2$:$NH_3$ ratio is 1:1, predicted from thermochemical models (Fegley 2000; Mousis et al. 2009). We call *nominal abundances* abundances presented in table 4.2.

### 4.1.3. Water evolution in the PPD

Water is a particular species in our model as it is a carrier of other volatile species. Species are trapped by water to form clathrate hydrates in scenario 1 and carry volatile species in its amorphous form in scenario 2. Figure 4.1 shows the radial distribution of water in scenario 1 (top row) and scenario 2 (bottom row) at 10, 100 and 1000 kyr. It can be seen that the presence of amorphous water does not induce any significant variation in the water distribution. In both scenarios, after 100 kyr, the water condensation line at 2.8 AU shows a water enrichment of the order of 10 times the protosolar abundance. However, there is much less crystalline water available in scenario 2, where the water transition from amorphous to crystalline only occurs in the inner part of the PPD at about 4 AU.

Figure 4.1 shows that in scenario 1, the water ice distribution profile shows depleted regions located at 6.4 and 10 AU after 100 kyr of evolution, and at 3.9 and 8 AU after 1000 kyr of evolution. These depleted regions are caused by the accumulation of condensation lines in a narrow region, a mechanism discussed in more detail in section 4.1.4.

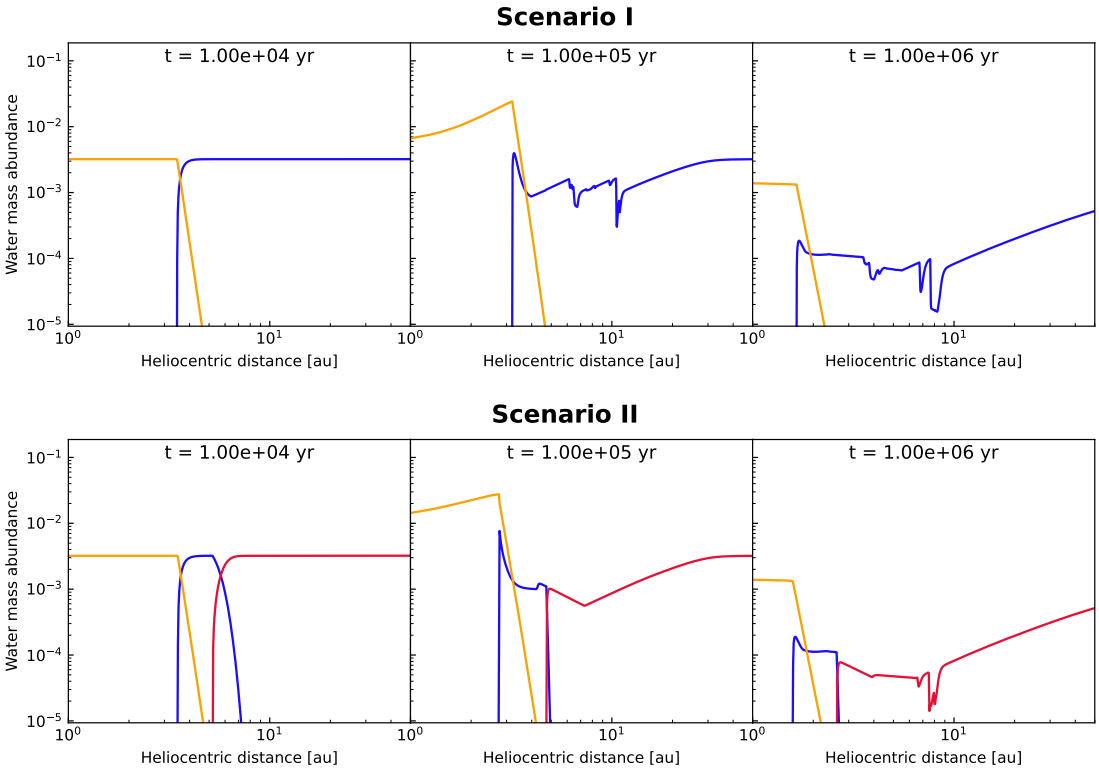


Figure 4.1.: Time and radial distribution of water mass abundance in vapor phase (orange line), crystalline ice (blue line) and amorphous ice (red line) in scenario 1 and 2 at $10^4$, $10^5$ and $10^6$ yr. Figure adapted from Schneeberger et al. (2023)

### 4.1.4. Initial delivery of pure condensates

The PPD is initially filled with either species vapor or pure condensate. During the first time steps, clathrate hydrate form where it is stable. Figure 4.2 represent the time and radial evolution of the abundances ratios, with respect to their initial abundances, of the different species. After 10 kyr of evolution, all species exists in all their possible form except for CO and $NH_3$ which never form their clathrate hydrate and monohydrate, respectively. Ac narrow region containing enclathrated species form between 7 and 12 AU, depending on the species considered. In this early stage, there is no significant enrichment for any species.

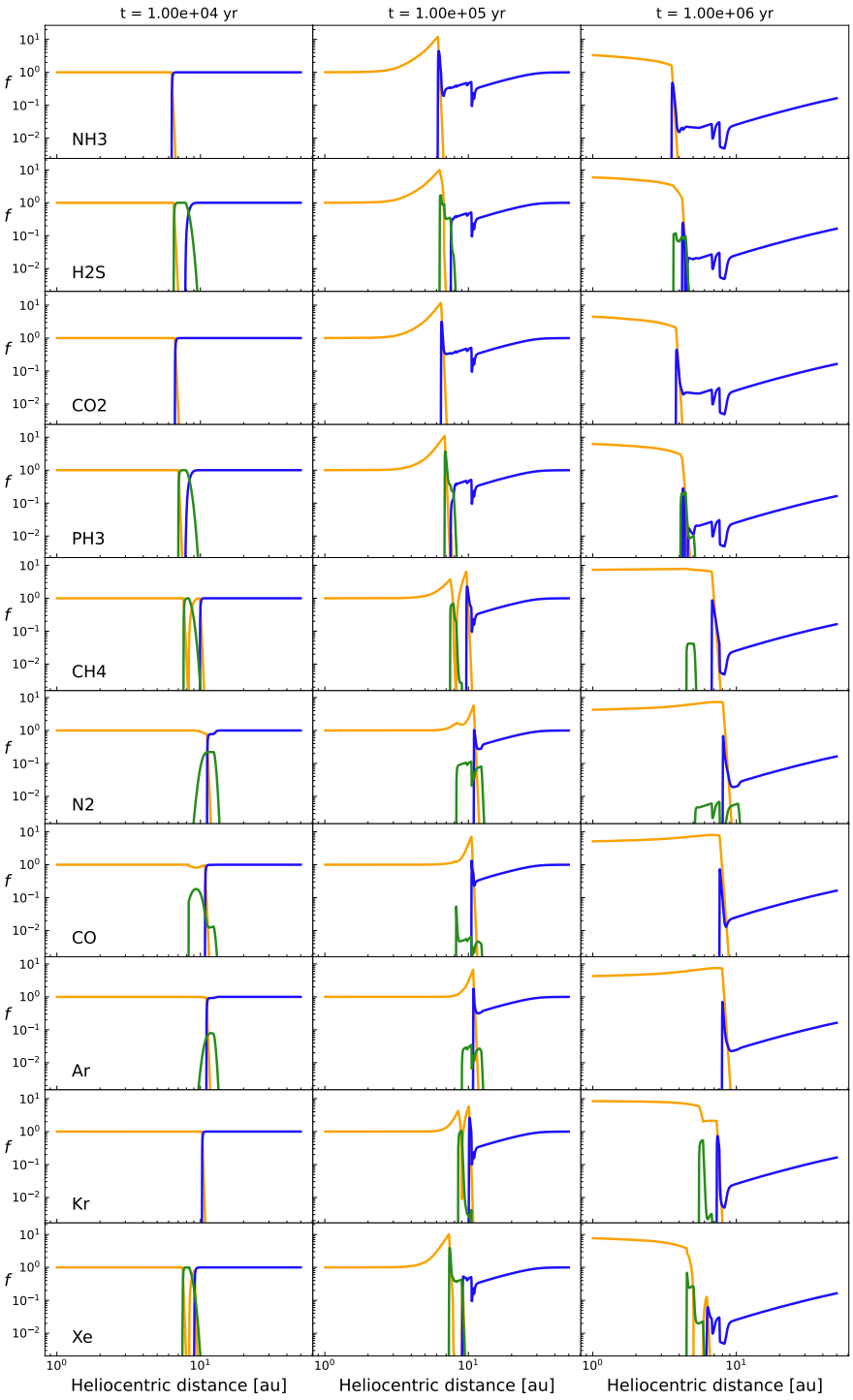


Figure 4.2.: Time and Radial distribution of volatile species mass abundances normalized to their initial values in gaseous phase (orange line), pure condensate (blue line) and clathrate (green line), at $10^4$, $10^5$ and $10^6$ yr in Scenario 1. Figure adapted from Schneeberger et al. (2023)

After 100 kyr of disk evolution, Figure 4.2 also shows that beyond 6 AU, clathrates

Table 4.3.: Heliocentric distance and value of the enrichment peak (relative to the initial abundance) for each species under consideration at $t$ = 0.1 Myr in the case of scenario 1 (middle column of Figure 4.2). Both vapor and solid forms are considered. Table adapted from Schneeberger et al. (2023)

| Element | Peak location (AU) | Peak value |
|---|---|---|
| H2O | 2.7 | 11.0 |
| CO | 10.4 | 8.1 |
| $CO_2$ | 6.0 | 16.0 |
| $CH_4$ | 7.1 | 4.7 |
| | 9.5 | 9.4 |
| $H_2S$ | 5.9 | 14.0 |
| $N_2$ | 10.9 | 5.6 |
| $NH_3$ | 5.6 | 17.2 |
| Ar | 10.7 | 7.3 |
| Kr | 8.2 | 9.12 |
| | 9.8 | 23.5 |
| Xe | 7.0 | 14.3 |
| $PH_3$ | 6.4 | 15.4 |

coexist with pure condensates and their abundances decrease steeply – except for $CO_2$ and $NH_3$, which that exist only as pure ices. A few AU beyond that, pure condensates become the only solid structures existing in the outer PPD. Depending on the PPD thermodynamic conditions and the availability of crystalline water, when the different species become fully enclathrated, their abundances form unique enrichment peaks located at their clathration lines, reaching up to ~15 times their initial values. On the other hand, if the budget of crystalline water is not high enough, then the species are only partly enclathrated. They then form two narrow enrichment peaks at their condensation and clathration lines, reaching ~5 and ~15 times their initial abundances, respectively. Table 4.3 displays the heliocentric distance and the value of the enrichment peak (relative to the initial abundance) for each species under consideration at $t$ = 0.1 Myr of the PPD evolution. Depending on the species considered, the enrichment peaks range between 2 and 18 times the protosolar values and are located in the 2–11 AU region. The closest and furthest peaks from the Sun are those of the water snow line at 2.8 AU and $N_2$ condensation line at 10.8 AU, respectively. Two enrichment peaks, located at the clathration and condensation line, are found in the cases of $CH_4$ and Kr.

In Figure 4.2, all species, except CO, $N_2$, and Ar, exhibit a dip in the surface densities of the pebbles of pure condensates around 10.5 AU. In this region, the total surface density of icy pebbles is increased due to the combined actions of CO, $N_2$, and Ar condensation lines located at 10.4, 10.9, and 10.7 AU, respectively. The condensations rate of CO, $N_2$, and Ar locally increase the surface density of solids, which are in excess compared with their loss rates via inward drift. On the other hand, because

the condensation lines of the other species are located closer to the Sun, their surface densities progressively decrease in this region, as a result of the inward drift of particles.

After 1 Myr of PPD evolution, all peaks are smoothed out in the gas phase. Because of the inward drift of pebbles, most of the species are in vapor form when the solids start to deplete. The total mass of solids has decreased by a factor of four compared to the beginning of the simulation. This effect is more significant in the case of clathrates forming at very low temperatures (less than 50 K), since the fraction of crystalline water used to form higher temperature clathrates increases with time.

### 4.1.5. Initial delivery of species trapped in amorphous water ice

Figure 4.3 represents the time and radial evolutions of the abundance ratios (with respect to the initial abundances) of the different species existing in various phases in the case of scenario 2. After 10 kyr of PPD evolution, with progressing heliocentric distance, first the different vapors are found, then an outer region that is only populated with amorphous ice. The budget of solid phase is dominated by species trapped in amorphous ice. Pure condensates only form when the vapors desorb from amorphous ice at the ACTZ (shown at ~5 AU), diffuse outward and cross a condensation line. Such a process is efficient only if the condensation line is close to the ACTZ, leading to very narrow regions with the presence of pure condensates only in the case of $NH_3$.

After 0.1 Myr of disk evolution, it is notable that only pure condensates of $NH_3$, $H_2S$, $CO_2$, and $PH_3$ form. Table 4.4 displays the heliocentric distance and the value of the enrichment peak (relative to the initial abundance) for each species under consideration at this epoch of the PPD evolution. All peaks are located in a much narrower region, centered at the location of the ACTZ, compared with the scenario 1, with values ranging from 7 to 10 times the initial abundances. The peak locations are influenced by the presence of narrow (less than 1 AU) regions filled with pure condensates. In those regions, corresponding to the condensation line, the abundance of pure condensates exceed that of amorphous ice, thus influencing the location of the enrichment peaks.

After 1 Myr of PPD evolution, as a result of pebble drift, all peaks have been smoothed and the volatile trapped in amorphous water ice phase are strongly depleted by factors reaching more than 100, compared with their gaseous abundances in the inner disk. The amount of pure condensates exceeds that of amorphous ice in some narrow regions, except in the cases of $H_2S$ and $PH_3$. For reasons identical to those invoked at the same epoch of PPD evolution in scenario 1, the surface density of solids is strongly decreased in the region centered at ~7 AU.

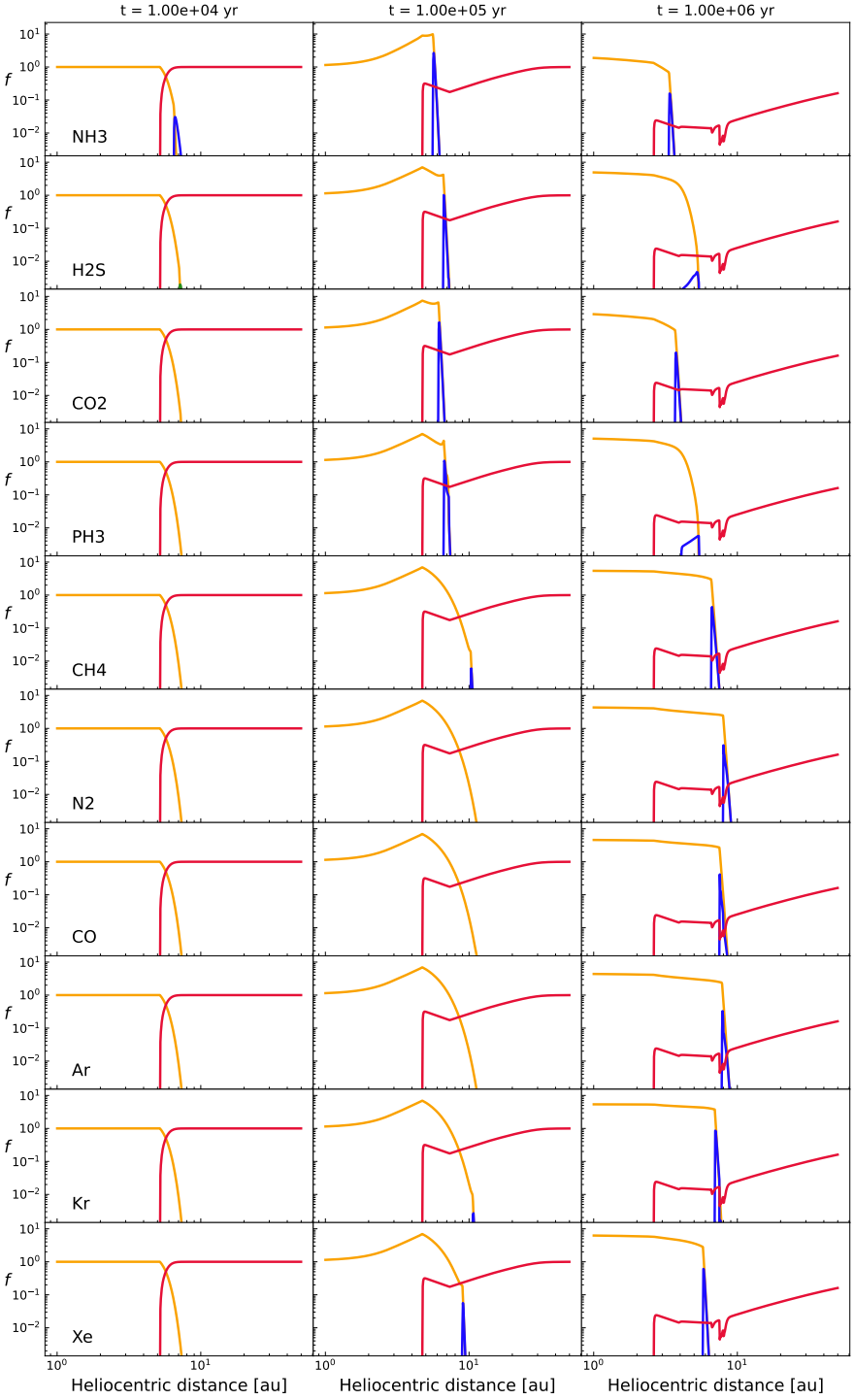


Figure 4.3.: Time and radial distribution of volatile species in gaseous phase (orange line), pure condensate (blue line) and amorphous line (red line), compared with their initial mass abundances, at $10^4$ , $10^5$ and $10^6$ yr in scenario 2. Figure adapted from Schneeberger et al. (2023)

Table 4.4.: Heliocentric distance and value of the enrichment peak (relative to the initial abundance) for each species under consideration at $t$ = 0.1 Myr in the case of scenario 2 (middle column of Figure 4.3.

| Element | Peak location (AU) | Peak value |
|---|---|---|
| H2O | 2.7 | 8.5 |
| CO | 4.8 | 7.0 |
| $CO_2$ | 4.7 | 7.5 |
| $CH_4$ | 4.7 | 7.0 |
| $H_2S$ | 4.7 | 7.1 |
| $N_2$ | 4.7 | 7.0 |
| $NH_3$ | 5.6 | 10.1 |
| Ar | 4.7 | 7.0 |
| Kr | 4.7 | 7.0 |
| Xe | 4.7 | 7.0 |
| $PH_3$ | 4.7 | 7.1 |

### 4.1.6. Variation of the model parameters

Radial profiles presented in sections 4.1.4 and 4.1.5 have to be modulated by the fact that it represent only one set of model parameters over a wide range of possibility. The PPD radial structure is most affected by variation of the viscous heating. This viscous heating is impacted by two main parameters, the parameter $\alpha$ from the viscosity equation (Eq. 3.6) and the initial mass of the disk. The initial disk mass constrain the initial surface density, the more massive the disk, the more dense and therefore the higher is viscous dissipation.

We explore also the variation of pebble density. At the studied scale, from $10^{-6}$ to $10^{-1}$ m, dust and pebbles are not compact and their porosity can greatly vary. Dust and pebble porosity will impact their density and therefore their coupling to the gas. The less dense the pebble is the more coupled it is and the slower is its drift speed.

**PPD initial mass** We vary the PPD mass from $10^{-1}$ $M_\odot$ to $1.5 \times 10^{-3}$ $M_\odot$. Since a mass of $10^{-1}$ $M_\odot$ is an upper limit of the sun's PPD mass. The direct consequence of the decrease of the PPD initial mass is the decrease of the viscous friction heating. Therefore, the PPD temperature decrease. Figure 4.4 show the comparison of the temperature, pressure, and surface density profiles of models with initial PPD mass of $10^{-1}$, $10^{-2}$ and $1.5 \times 10^{-3}$ $M_\odot$, after 10, 100 and 1000 kyr of evolution. It shows that after 10 kyr of evolution, the PPD temperature goes from 827 K at 1 AU with a PPD mass of $10^{-1}$ $M_\odot$ to 459 K and 210 K with PPD mass of $10^{-2}$ and $1.5 \times 10^{-3}$ $M_\odot$ respectively. Similarly, the midplane pressure and PPD surface density follow the same trend, the lower the mass, the lower are the midplane pressure and the surface density. After 10 kyr of evolution at 1 AU, the surface density and pressure go from $3.94 \times 10^4$ kg m$^{-3}$ and 5.3 Pa with a PPD mass of $10^{-1}$ $M_\odot$ to $1.95 \times 10^4$ kg m$^{-3}$ and 1.9 Pa with a PPD mass of $10^{-2}$ $M_\odot$ and finally down to $7.3 \times 10^3$ kg m$^{-3}$ and 0.5 Pa with a PPD mass of

$1.5 \times 10^{-3}$ $M_\odot$.

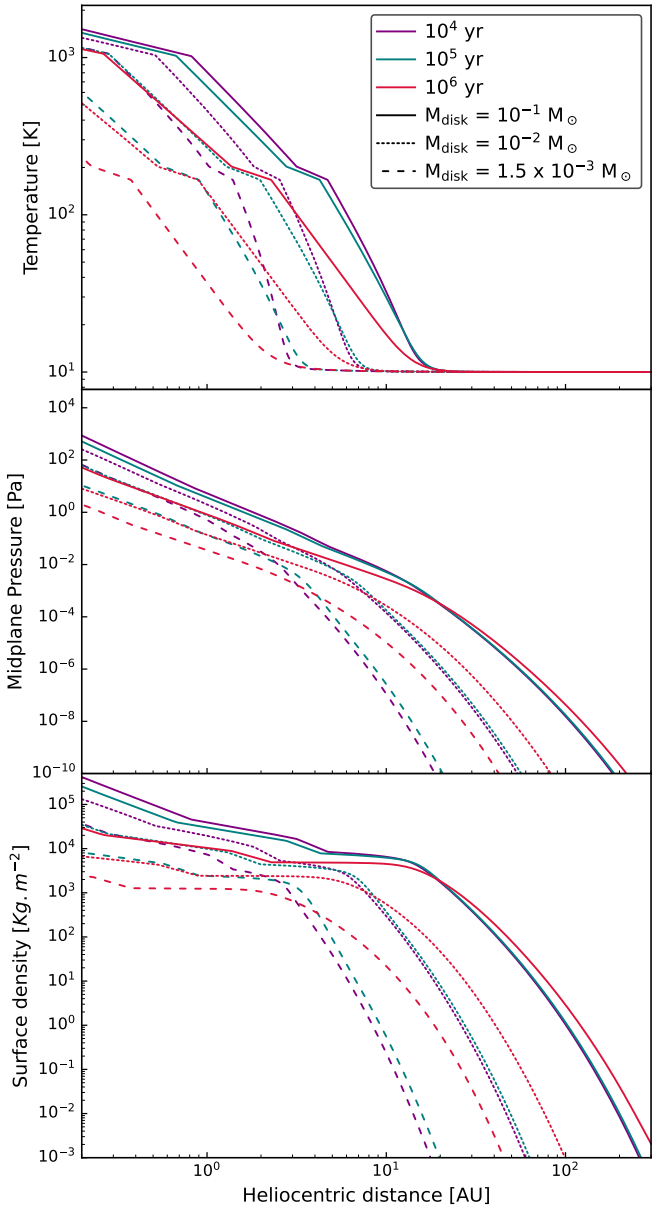


Figure 4.4.: Comparison of PPD temperature, pressure and surface density, from top to bottom panels, with an initial mass of $10^{-1}$ $M_\odot$ (plain line), $10^{-2}$ (dotted line ) and $1.5 \times 10^{-3}$ $M_\odot$ (dashed line). Profiles after 10, 100 and 1000 kyr of PPD evolutions are presented.

A lower temperature impact the position of the different lines. Examples of Xe and $CH_4$ distribution in scenario 1 with initial PPD mass of $10^{-2}$ and $1.5 \times 10^{-3}$ $M_\odot$ are displayed in figure 4.5 and 4.6. They show that the lower the PPD initial mass, the closer are clathration and condensation lines because of the colder PPD. The $CH_4$ condensation line goes from 4.3 to 2.0 AU after 100 kyr of evolution, and the

Xe condensation line goes from 4.2 to 1.8 when varying the PPD mass from $10^{-2}$ to $1.5 \times 10^{-3}$ $M_\odot$.

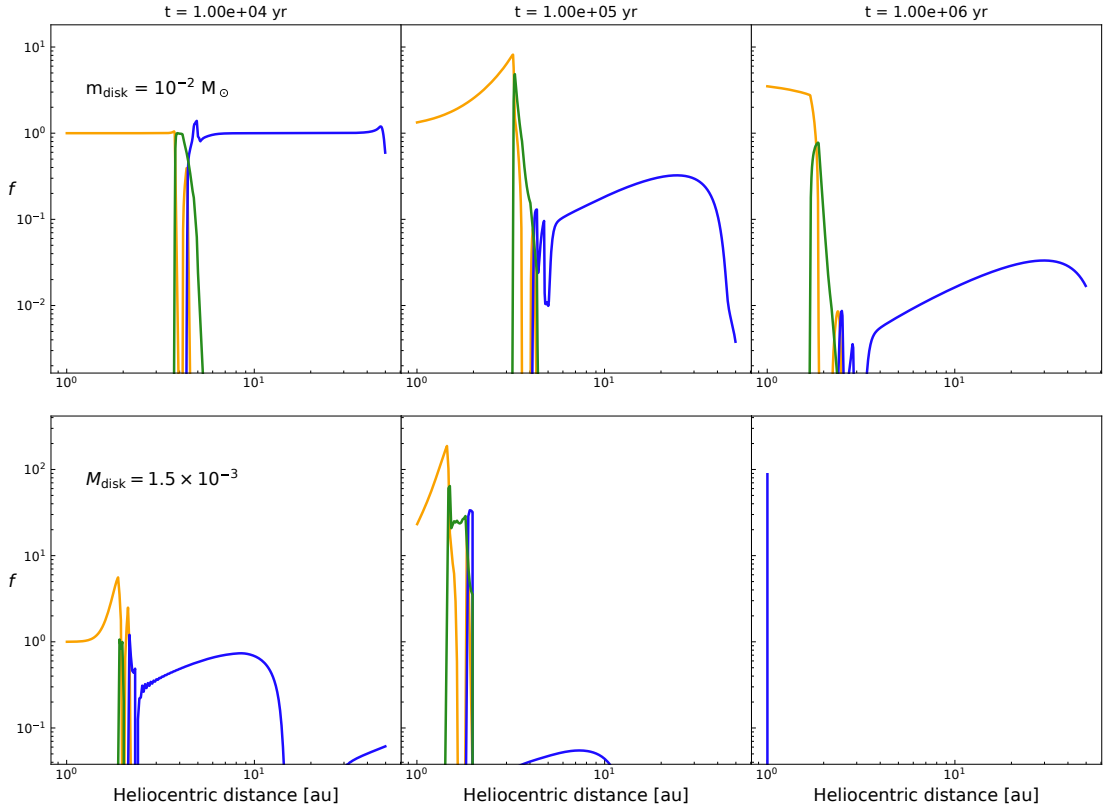


Figure 4.5.: Time and radial distribution of Xe mass abundance normalized to its initial value in gaseous phase (orange line), pure condensate (blue line) and clathrate (green line) in scenario 1, at $10^4$, $10^5$ and $10^6$ yr. Radial profiles with initial PPD mass of $10^{-2}$ $M_\odot$ (upper row) and $1.5 \times 10^{-3}$ $M_\odot$ (bottom row) are compared.

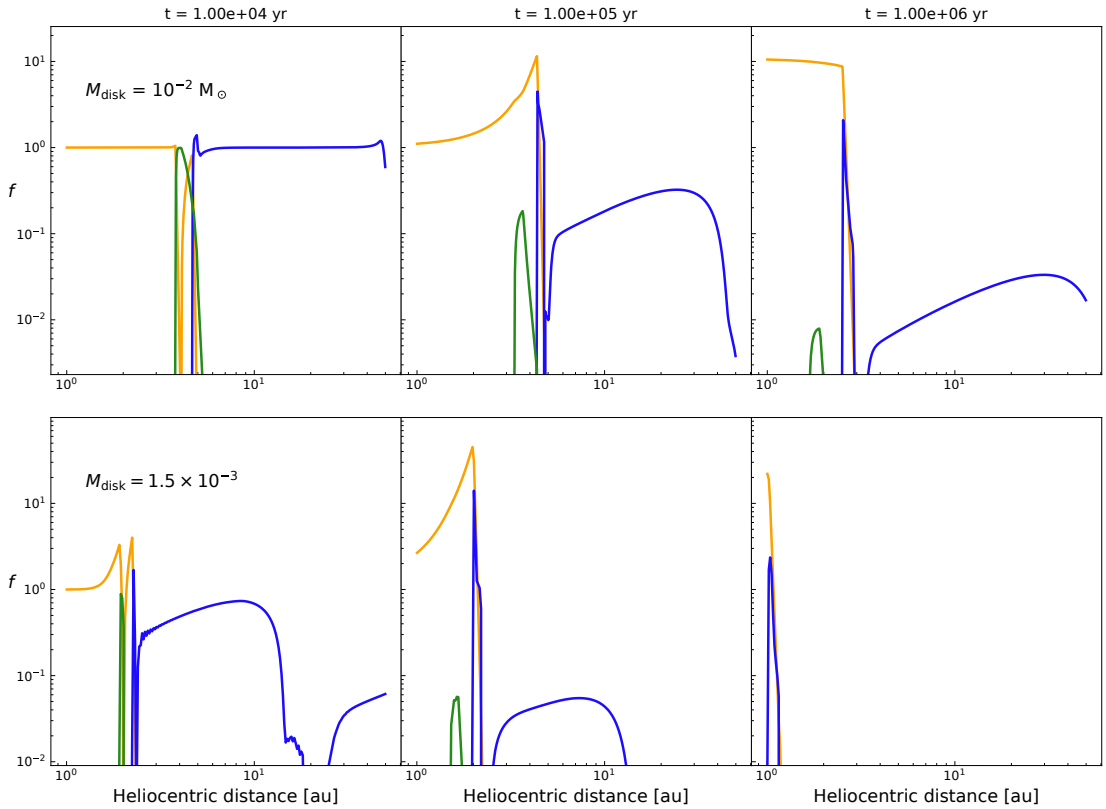


Figure 4.6.: Time and radial distribution of $CH_4$ mass abundance normalized to its initial value in gaseous phase (orange line), pure condensate (blue line) and clathrate (green line) in scenario 1, at $10^4$, $10^5$ and $10^6$ yr. Radial profiles with initial PPD mass of $10^{-2}$ $M_\odot$ (upper row) and $1.5 \times 10^{-3}$ $M_\odot$ (bottom row) are compared.

**$\alpha$-viscosity** We vary the viscous $\alpha$ parameter from $10^{-3}$ to $10^{-2}$. Figure 4.7 shows the pressure, temperature, and surface density for $\alpha$–parameters of $10^{-3}$ and $10^{-2}$. It shows that, because of the greater viscous diffusion of the PPD gas, that the outskirt of the PPD is denser and hotter with a larger $\alpha$, while the inner region of the PPD is cooler and less dense. The model with an $\alpha$ of $10^{-2}$ is hotter than the model with an $\alpha$ of $10^{-3}$ by ~30 K at 10 AU after 10 kyr of evolution. Whereas it is cooler by ~200 K at 1 AU. Therefore, the variation of $\alpha$ induce a variation of the position of the clathration line and the condensation line.

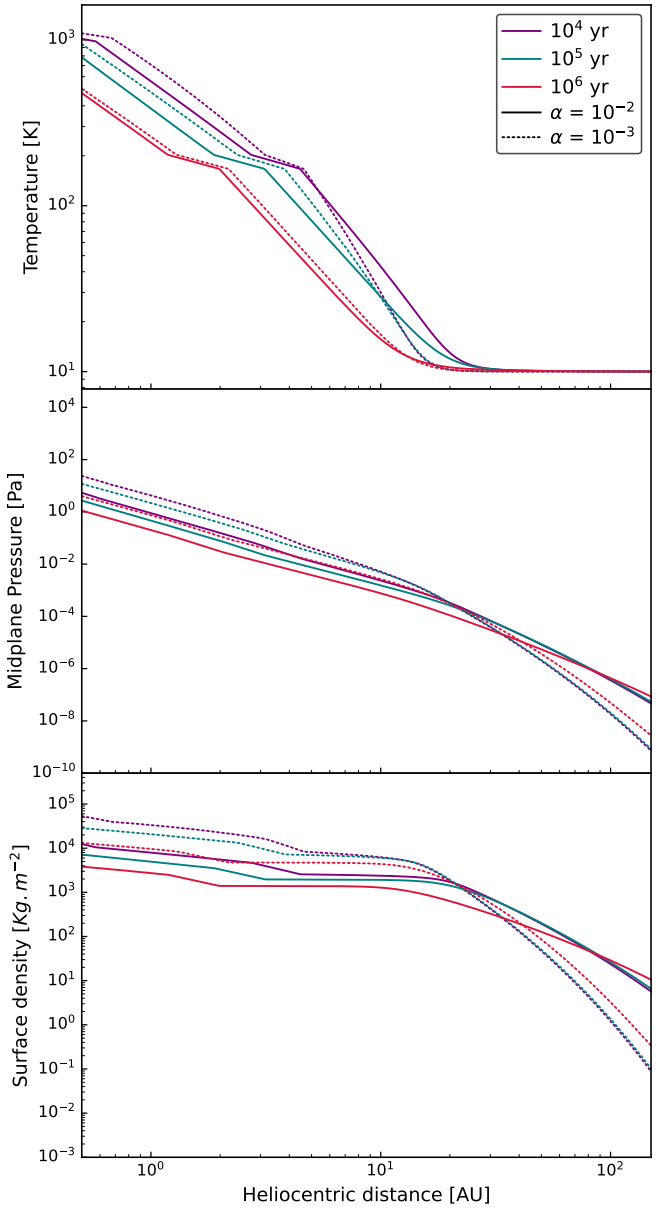


Figure 4.7.: Comparison of PPD temperature, pressure and surface density, from top to bottom panels, of models with $\alpha$ parameters of $10^{-2}$ (plain lines) and $10^{-3}$ (dotted line). Profiles after 10, 100 and 1000 kyr of evolution are presented.

Figures 4.8 and 4.9 show the variation of $CH_4$ and Xe in time and radial distribution respectively as the $\alpha$ parameter varies between $10^{-3}$ and $10^{-2}$. The lower the $\alpha$, the colder the PPD and the closer the different lines are. Varying $\alpha$ from $10^{-3}$ to $10^{-2}$ Xe condensation and clathration lines go from 9.1 to 12.5 AU and from 7.5 to 8.4 AU respectively after 10 kyr of evolution. Similarly, $CH_4$ condensation and clathration lines go from 10.1 to 12.6 AU and from 7.7 to 8.7 AU respectively.

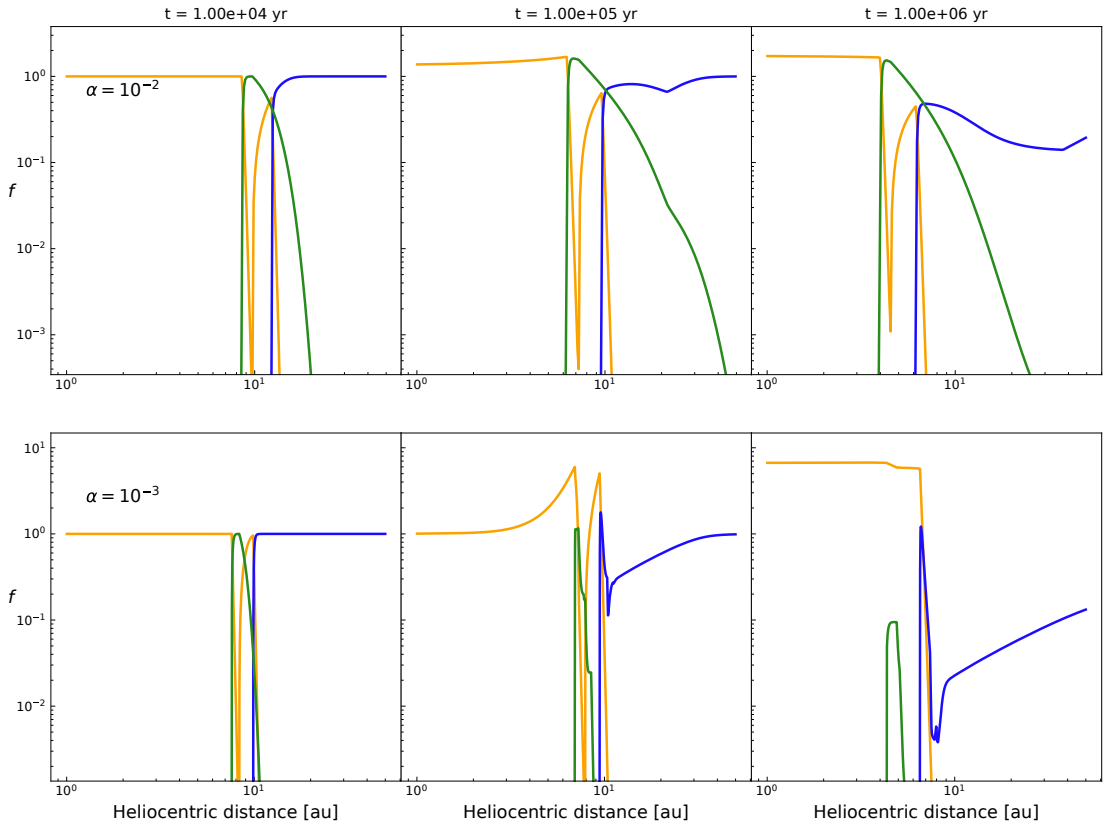


Figure 4.8.: Time and radial distribution of $CH_4$ mass abundance normalized to its initial value in gaseous phase (orange line), pure condensate (blue line) and clathrate (green line) in scenario 1, at $10^4$, $10^5$ and $10^6$ yr. Radial profiles with an $\alpha$-parameter of $10^{-2}$ (upper row) and $10^{-3}$ (bottom row) are compared.

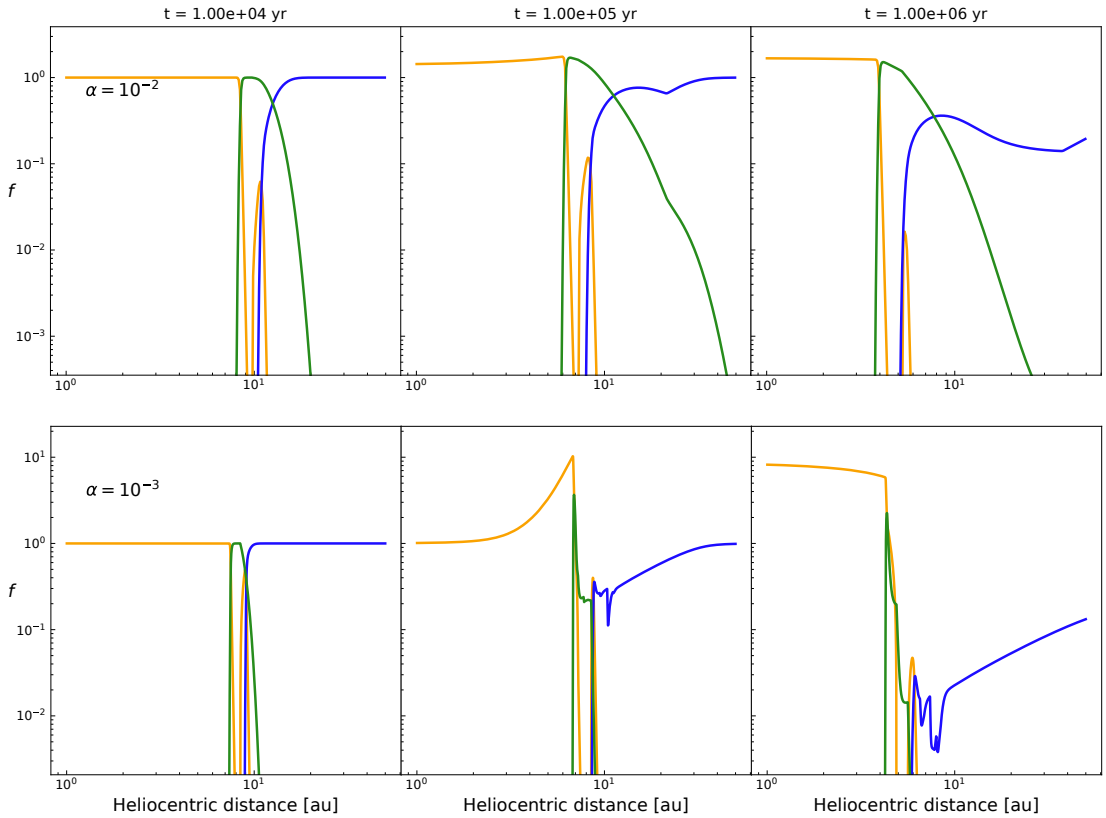


Figure 4.9.: Time and radial distribution of Xe mass abundance normalized to its initial value in gaseous phase (orange line), pure condensate (blue line) and clathrate (green line) in scenario 1, at $10^4$, $10^5$ and $10^6$ yr. Radial profiles with an $\alpha$-parameter of $10^{-2}$ (upper row) and $10^{-3}$ (bottom row) are compared.

Furthermore, the $\alpha$ parameter strongly influences the enrichment of the species mass abundances. The higher the $\alpha$, the greater the viscous diffusion and hence the broader but lower the enrichment peaks at the condensation and clathration lines. Therefore, after 100 kyr of evolution, the clathrate enrichment peak of Xe goes from 3.4 to 1.7 times the protosolar value and the $CH_4$ pure condensate enrichment peak goes from 1.8 to 0.6 times the protosolar value.

**Pebble density** We vary the pebble density between $5 \times 10^{-1}$ and $5 \times 10^{-2}$ to assess the variability of our pebble density results. Figures 4.10 and 4.11 show the variations of $CH_4$ and Xe in time and radial distribution respectively. Both figures show only marginal variations of the $CH_4$ and Xe radial distributions at their condensation and clathration lines. Since the average pebble size in our model is of the order of 10 cm, the pebbles are still strongly coupled to the gas and their density does not have a large effect.

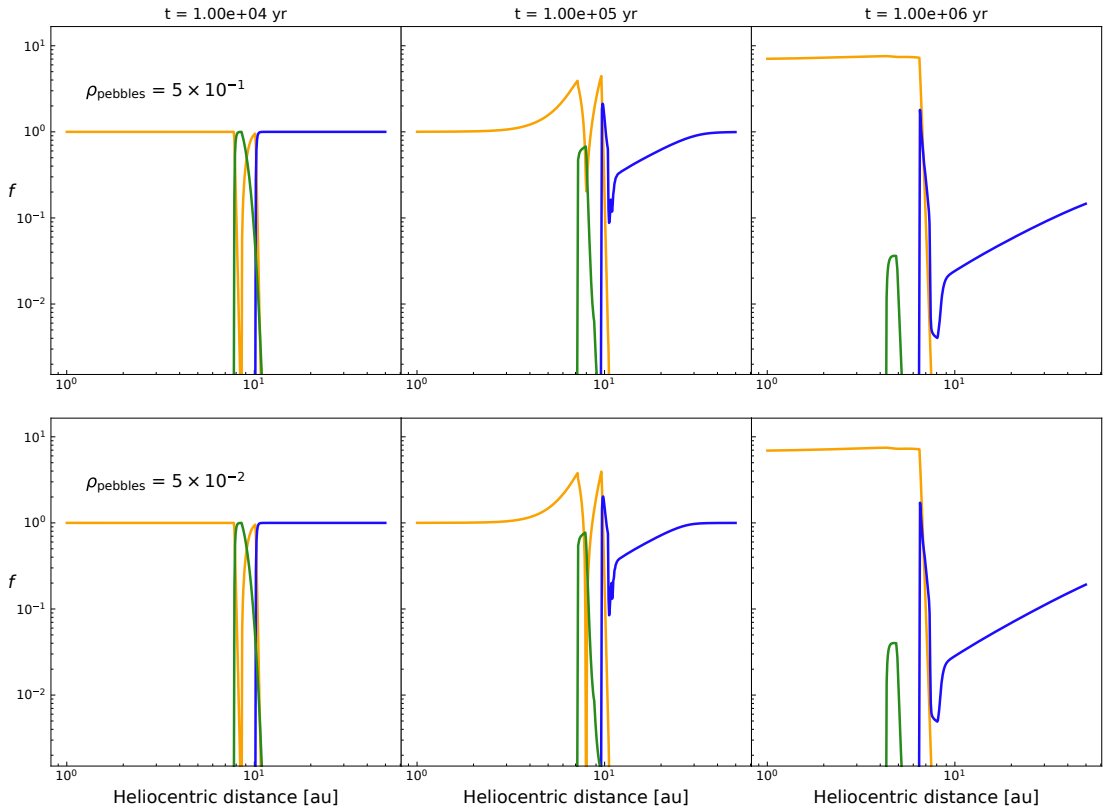


Figure 4.10.: Time and radial distribution of $CH_4$ mass abundance normalized to its initial value in gaseous phase (orange line), pure condensate (blue line) and clathrate (green line) in scenario 1, at $10^4$, $10^5$ and $10^6$ yr. Radial profiles with pebble density of $5 \times 10^{-1}$ (upper row) and $5 \times 10^{-2}$ (bottom row) are compared.

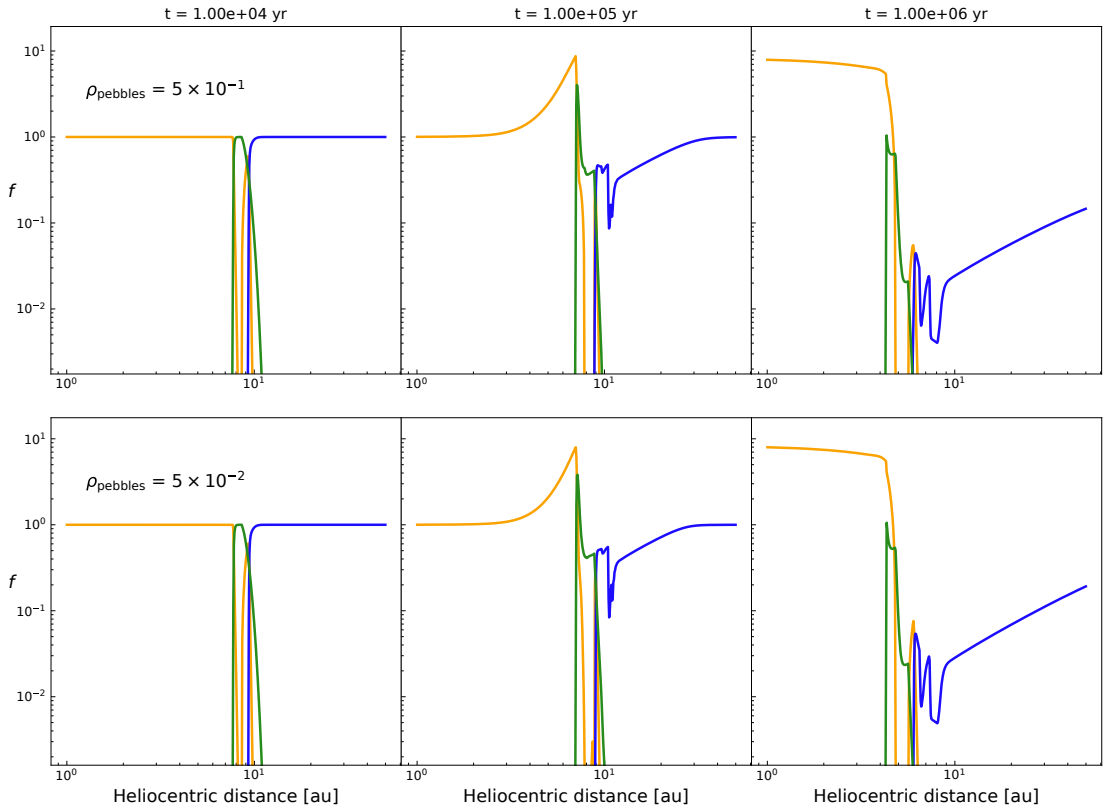


Figure 4.11.: Time and radial distribution of Xe mass abundance normalized to its initial value in gaseous phase (orange line), pure condensate (blue line) and clathrate (green line) in scenario 1, at $10^4$, $10^5$ and $10^6$ yr. Radial profiles with pebble density of $5 \times 10^{-1}$ (upper row) and $5 \times 10^{-2}$ (bottom row) are compared.

**Initial accretion rate** The initial accretion rate $\dot{M}_0$ plays a crucial role in the PPD structure, as it determines the initial surface density, and consequently, the thermal structure and positions of various lines. The accretion rate is varied between $10^{-8}$ and $10^{-6}$ $M_\odot$ $yr^{-1}$, with a constant PPD mass of $10^{-1}$ $M_\odot$. Figures 4.12 and 4.13 show the impact of varying accretion rates on the radial distributions of $CH_4$ and Xe, respectively. They demonstrate that higher initial accretion rates produce more significant enrichment peaks at the condensation and clathration lines. For $CH_4$, after 100 kyr of evolution, varying the initial accretion rate between $10^{-6}$ and $10^{-8}$ $M_\odot$ $yr^{-1}$ results in the enrichment peak at the condensation line decreasing from 18.6 times the protosolar value to 12.1 times, and from 99.1 to 12.7 after 1000 kyr of evolution. For Xe, after 100 kyr, the enrichment peak at its clathration line increases from 10.3 to 21 times the protosolar value when varying the initial accretion rate between $10^{-6}$ and $10^{-8}$ $M_\odot$ $yr^{-1}$, and from 150.5 to 13.1 after 1000 kyr.

These results indicate that before 100 kyr of evolution, the initial accretion rate does not establish a clear trend in the enrichment evolution of species. However, after 100 kyr and up to 1000 kyr, models with higher initial accretion rates produce

larger enrichment peaks at various lines, with differences of approximately an order of magnitude when the initial accretion rate is varied by a factor of 100.

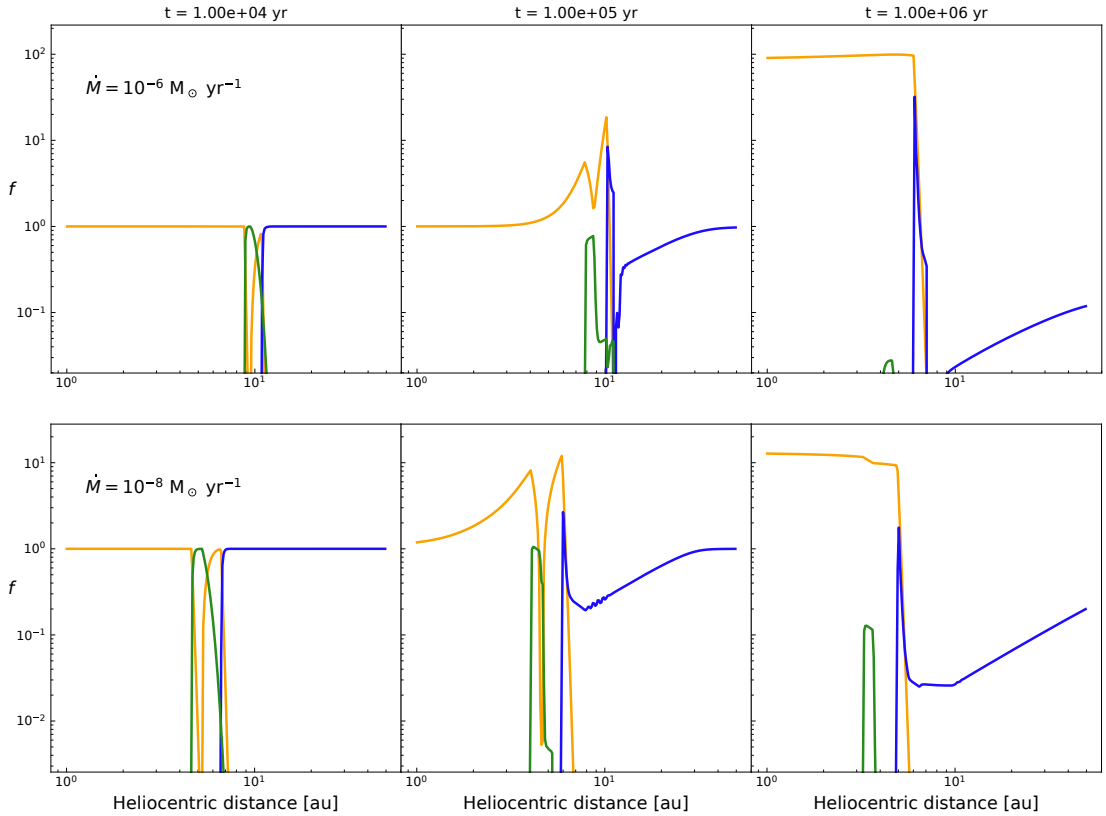


Figure 4.12.: Time and radial distribution of $CH_4$ mass abundance normalized to its initial value in gaseous phase (orange line), pure condensate (blue line) and clathrate (green line) in scenario 1, at $10^4$, $10^5$ and $10^6$ yr. Radial profiles with PPD initial accretions rates of $10^{-6}$ $M_\odot$ yr$^{-1}$ (upper row) and $10^{-8}$ $M_\odot$ yr$^{-1}$ are compared (bottom row).

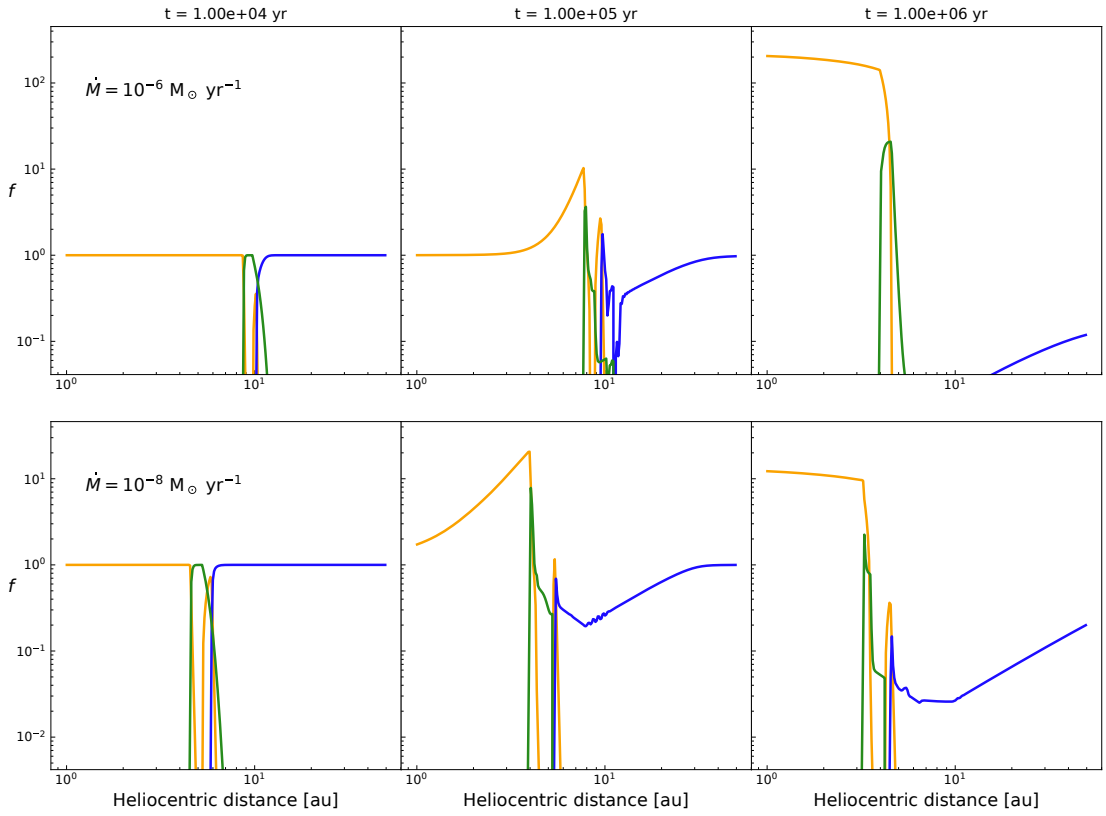


Figure 4.13.: Time and radial distribution of Xe mass abundance normalized to its initial value in gaseous phase (orange line), pure condensate (blue line) and clathrate (green line) in scenario 1, at $10^4$, $10^5$ and $10^6$ yr. Radial profiles with PPD initial accretions rates of $10^{-6}$ M$_\odot$ yr$^{-1}$ (upper row) and $10^{-8}$ M$_\odot$ yr$^{-1}$ are compared (bottom row).

The variation in the magnitude of enrichment peaks is attributed to changes in the radial velocity of gas and pebbles driven by the initial accretion rate. Higher initial accretion rates result in faster inward drift of gas and dust, causing more material to cross the different lines. This increased material flux at the lines, due to higher initial accretion rates, amplifies the recycling cycle at these lines and thereby further enriches the line's region.

**Summary** In this section we tested the sensitivity of the model to the variation of PPD mass ,pebble density, $\alpha$-viscosity factor, and initial accretion rates, we show that :

1. The PPD mass impact the position of the different lines. The higher the mass, the further the line position.

2. The $\alpha$-viscosity factor impact the diffusivity of the vapor. The higher the $\alpha$ the more diffusion the vapor undergoes and consequently the broader and the lower the enrichment peaks are.

3. The pebble density have only a minor impact on their evolution.

4. The initial accretion rates impact the radial velocity of vapor and pebbles. The larger the accretion rate, the higher the enrichment at the lines after 1 Myr.

## 4.2. Implications for Giant planets formation

In this section we explore implication of the two explored scenario on the formation of the Giant planets.

### 4.2.1. Jupiter

Jupiter's atmosphere present elemental enrichment's in the range between 1.6 and 6 times the protosolar abundances (Atreya et al. 2003; Wong et al. 2004; Mousis et al. 2018; Li et al. 2020). To explain this enrichment, it has been proposed that Jupiter formed from pebbles enriched in volatile species. Consequently, Jupiter's atmosphere would reflect the composition either made of pure condensate (Gautier et al. 2001; Gautier et al. 2005; Moraes et al. 2018), clathrate hydrates (Mousis et al. 2021a) or amorphous ice Owen et al. (1999).

Figure 4.14 shows the time evolution of the cumulative elemental enrichment of Carbon, Oxygen, Nitrogen, Phosphorus, Sulfur, Argon, Krypton, and Xenon in the PPD considering solids and vapor. Following the approach of Aguichine et al. (2022) we focused on the composition of solids and vapor at 4, 5 and 6 AU, possible locations of Jupiter's formation. In the vicinity of the water condensation line, the dust-to-gas ratio can become greater than 2 to 3 times the protosolar composition, which could ease the formation of a proto-Jupiter via streaming instability as proposed by Yang et al. (2017)

Figure 4.14 shows that in scenario 1 there is a period where all elemental enrichments match the enrichments measured in Jupiter's atmosphere only at 4 AU from 800 to 1000 kyr of PPD evolution, except for Krypton which has a higher enrichment of 8 times its protosolar abundance. There is no such period at 5 and 6 AU. In Scenario 1, elemental abundances vary drastically from one to another due to condensation and clathration lines of volatile species drifting inwards, enriching the corresponding element. Since the condensation and clathration lines are at a given distance at different times, the elemental enrichments never match at 5 and 6 AU, where all lines eventually pass.

In scenario 2, it exists periods where all species enrichments match the one measured at Jupiter. At 4 Au this period is from 50 to 100 kyr, at 5 AU between 20 and 50 kyr and at 6 AU between 50 and 90 kyr. Therefore, in the case where all volatile species are delivered to the PPD trapped in amorphous water ice, the period where enrichments match those of measured at Jupiter are very early in PPD evolution.

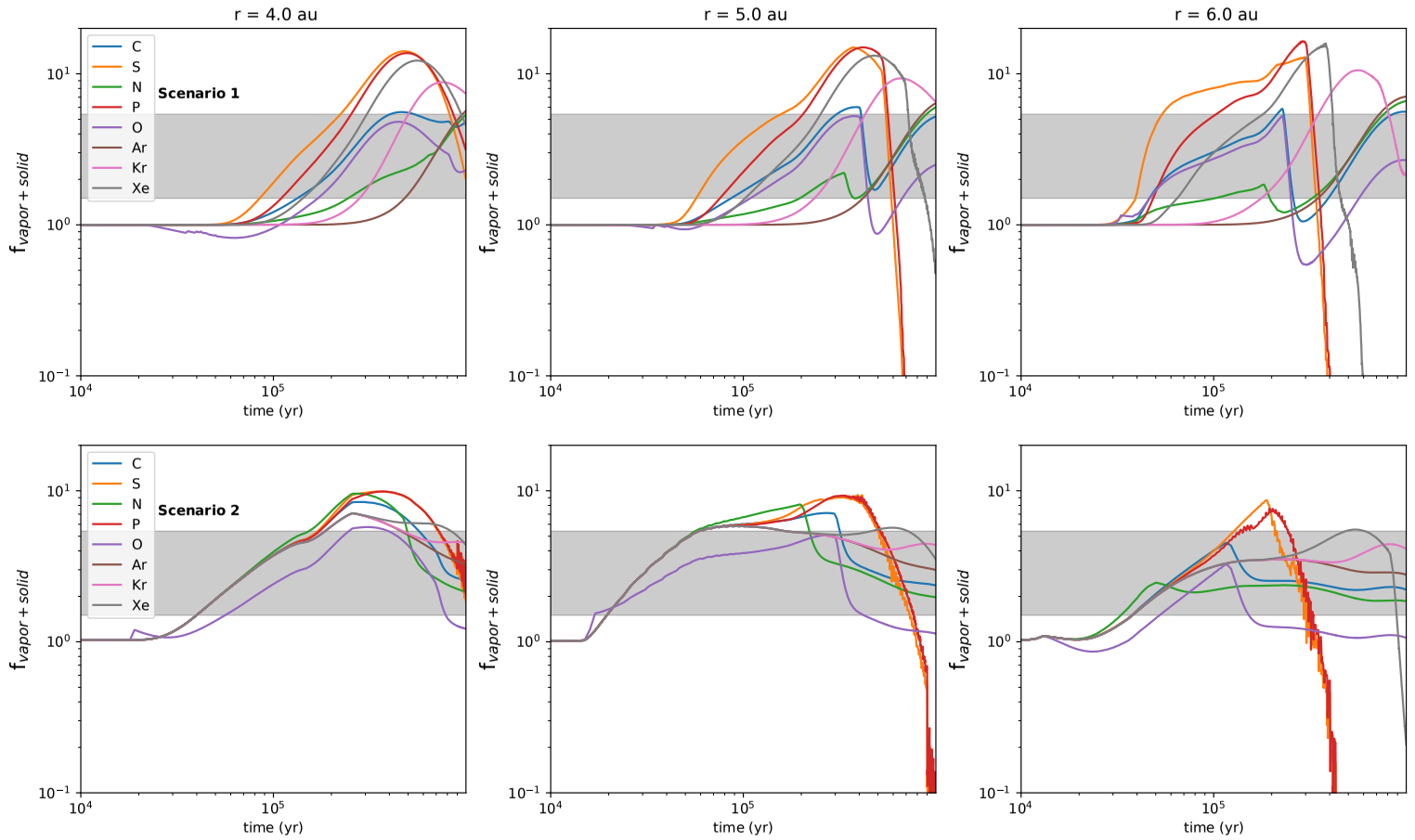


Figure 4.14.: Time evolution of elemental enrichment in vapor and pebbles of carbon, sulfur, nitrogen, phosphorus, oxygen, argon, krypton and xenon at 4, 5 and 6 AU from the sun in scenario 1 (upper row) and scenario 2 (lower row). With the gray bar being the range of elemental enrichment's measured in Jupiter's atmosphere, presented in figure 1.4.

### 4.2.2. Saturn

The elemental abundances in Saturn's atmosphere have been measured for carbon, nitrogen, sulfur, and phosphorus, showing enrichment levels between 3 and 13 times their protosolar values (Fletcher et al. 2009; Fletcher et al. 2011; Atreya et al. 2018). This indicates a higher metallicity in Saturn's atmosphere compared to Jupiter's. We do the hypothesis that Saturn formed near the $CO_2$ condensation line, where ices are enriched in carbon-bearing compounds. This line is located at approximately 6 AU in the model, close to Saturn's proposed formation region between 7 and 9 AU, according to the models of Batygin et al. (2010), Nesvorný (2011), Batygin et al. (2012), Nesvorný et al. (2012), and Morbidelli et al. (2020).

To compare the elemental enrichments predicted by scenarios 1 and 2 with the values observed in Saturn's atmosphere, we analyzed the elemental abundances near the $CO_2$ condensation line at 5, 6, and 7 AU. Figure 4.15, similarly to Figure 4.14, presents the elemental enrichment at these distances, with the gray bar representing the observed enrichment range in Saturn's atmosphere, between 3 and 13 times the protosolar values.

In Scenario 1, Figure 4.15 shows that there is no time period when the abundances of carbon, nitrogen, phosphorus, and sulfur simultaneously match the measured abundances in Saturn's atmosphere at any of the tested distances. However, in Scenario 2, a matching period occurs between 32 and 410 kyr at 5 AU. At greater distances, the enrichment does not reach sufficiently high levels. Although this matching period is long enough for a planetary core to form according to the pebble accretion model from Bitsch et al. (2015, 2019), the location at 5 AU is very close to Jupiter's proposed formation region in section 4.2.1 around 4 AU.

This result suggests that Saturn might have formed on the outer edge of Jupiter's gap, where the pressure bump acts as an efficient dust trap. Consequently, the accumulation of dust at the outer edge of Jupiter's gap could have triggered the formation of Saturn's core via streaming instability. However, the profiles presented in Figure 4.15 do not account for the gap formation at 4 AU and, therefore, do not reflect the potential modifications to elemental abundances caused by the presence of this inner gap.

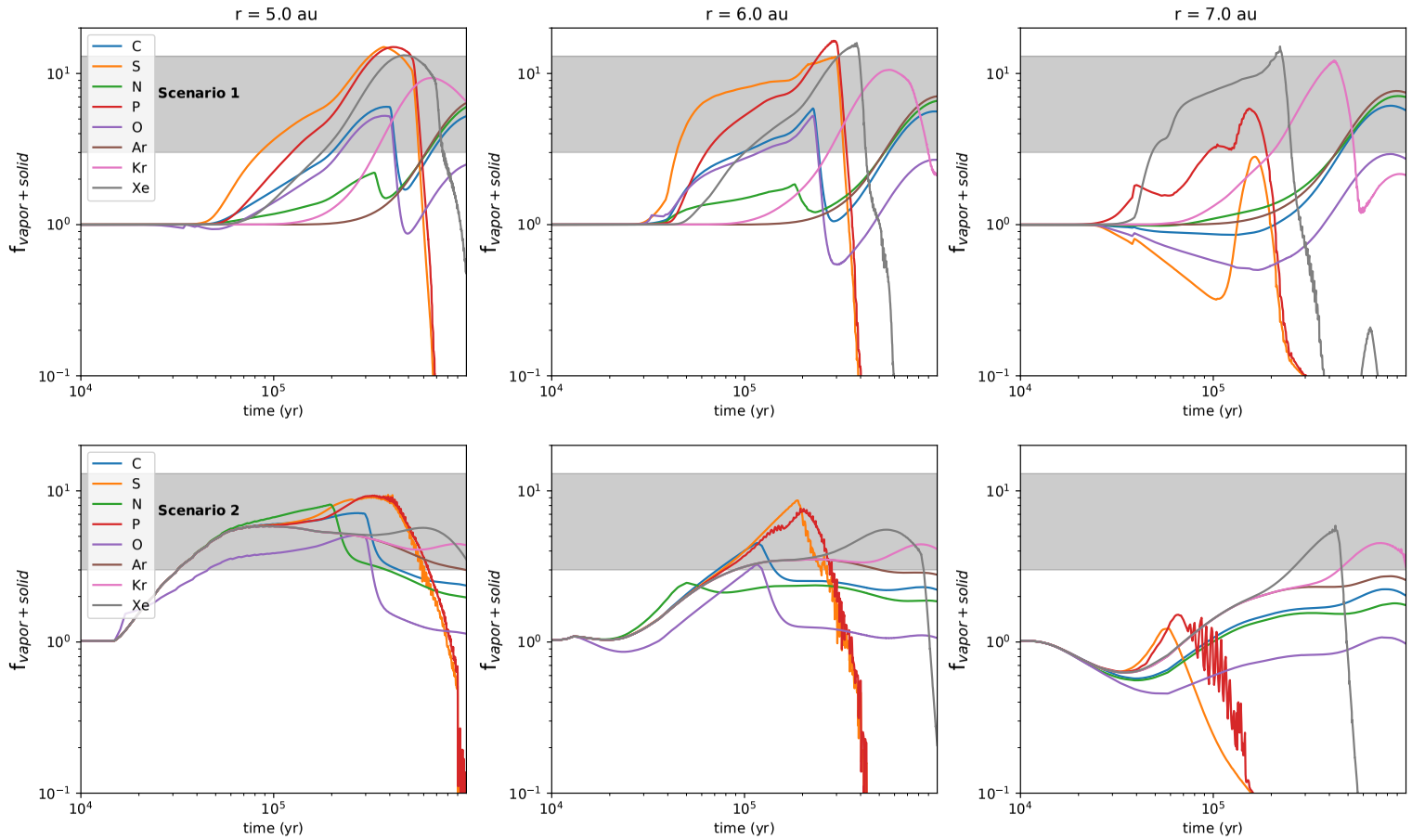


Figure 4.15.: Time evolution of elemental enrichment in vapor and pebbles of carbon, sulfur, nitrogen, phosphorus, oxygen, argon, krypton and xenon at 5, 6 and 7 AU from the sun in scenario 1 (upper row) and scenario 2 (lower row). With the gray bar being the range of elemental enrichment's measured in Saturn's atmosphere, presented in figure 1.4.

### 4.2.3. Uranus and Neptune

We compare known composition of Uranus and Neptune with the volatile species profiles. Little is known about their composition. One only have measurements from Voyager 2 and ground measurements. One can only rely on the C/N and C/S ratios which have been found to be equal or higher to ~ 175 and ~ 35 to compare observations with our model(Asplund et al. 2009; Karkoschka et al. 2009, 2011; Irwin et al. 2018, 2019a,b). The study of ice giants formation processes from constrain on their composition will be a primary scientific question thanks to the NASA initiative *Uranus Orbiter and Probe* (UOP). UOP is a mission concept that will be composed of an orbiter and an entry probe which will measure the deep composition of the Uranian atmosphere. As for Galileo at Jupiter, it will provide valuable constrains on the formation processes.

Figures 4.16 and 4.17 show the radial profiles of the C/S and C/N ratios in pebbles at 100, 500 and 1000 kyr of PPD evolution in scenarios 1 and 2, respectively. These ratios are compared with the minimum values measured in the troposphere of the two ice giants. Only in scenario 1 can these ratios reach the minimum values from the 9–10 AU region after 500 kyr to the 7–8 AU region after 1000 kyr of PPD evolution. This region is the location of the CO condensation line and the enrichment peak (see table 4.3). A secondary enrichment peak of C/S and C/N ratios is present in the 4–5 AU region after 500 kyr and in the 3–4 AU region after 1000 kyr. These secondary peaks, corresponding to the $CO_2$ condensation line, reach the minimum C/S and C/N values in scenario 1, but not in scenario 2, and are too close to be considered a suitable formation site for the ice giants, which according to the *NICE* model Batygin et al. (2010) should have formed in the 12–17 AU region.

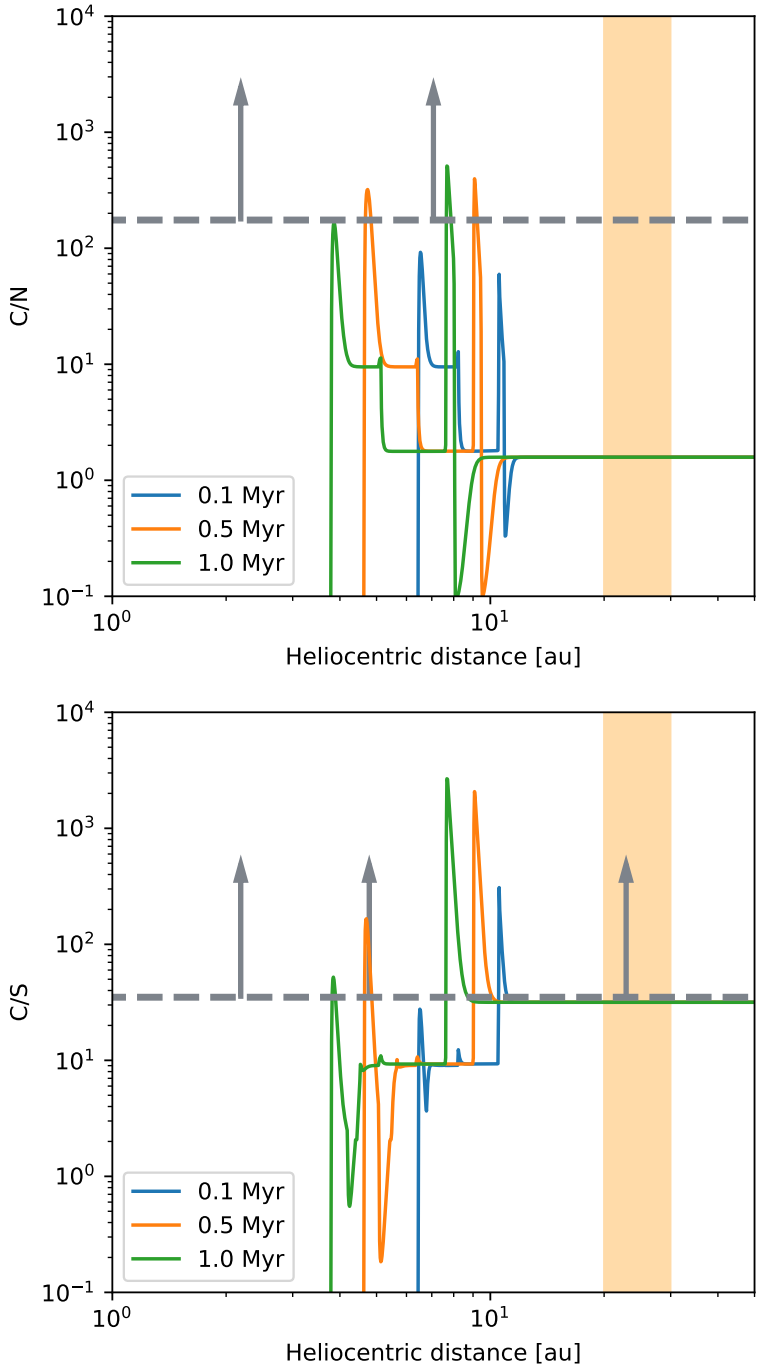


Figure 4.16.: Radial profiles of the C/N (top panel) and C/S (bottom panel) ratios calculated in pebbles at different epochs of the PPD evolution in the case of scenario 1. The horizontal dashed line represents the minimum ratio measured in the tropospheres of Uranus and Neptune. The orange area encompasses the current locations of the ice giants in the solar system

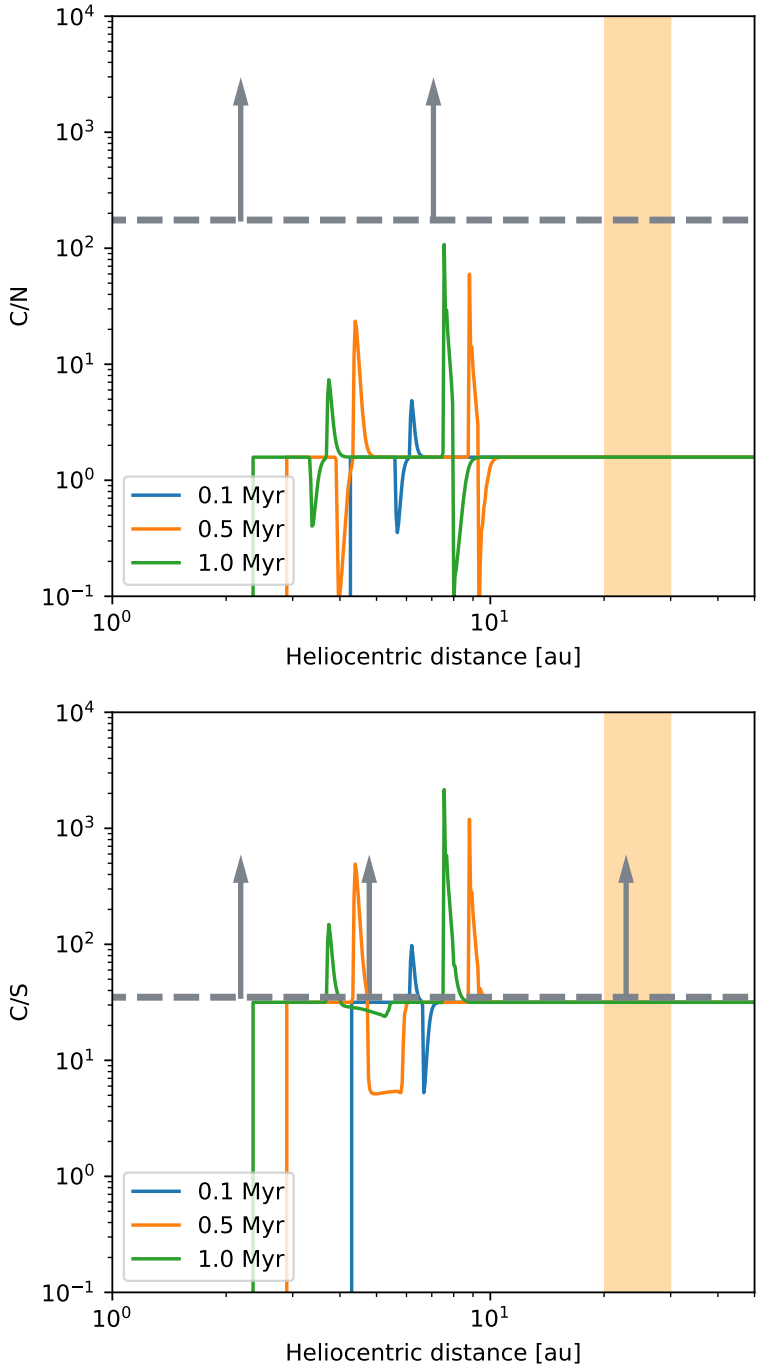


Figure 4.17.: Radial profiles of the C/N (top panel) and C/S (bottom panel) ratios calculated in pebbles at different epochs of the PPD evolution in the case of scenario 2. The horizontal dashed line represents the minimum ratio measured in the tropospheres of Uranus and Neptune. The orange area encompasses the current locations of the ice giants in the Solar System.

Those findings lead to the hypothesis that Uranus and Neptune formed in the

vicinity of the CO condensation line. We further explore this hypothesis by tracing elemental enrichment at the CO condensation line position. Since figure 4.17 show that the delivery of amorphous ice cannot reproduce the minimum values of the C/S and C/N ratios, in the following, we focus on the delivery of pure condensate to the PPD. Because we focus on the CO condensation line, to assert the variability of the presence of clathrate hydrate we use a model with only pure condensates and vapor as a reference model.

Figures 4.18 and 4.19 depict the temporal evolution of the elemental ratios Ar/C, N/C, O/C, Kr/C, S/C, P/C and Xe/C in the reference model and scenario 1 respectively. They show the ratios in pebbles only and the sum of the contribution of both pebbles and vapor. Figures 4.18 and 4.19 show that the CO condensation line gradually migrate inward from 10.7 AU to 7.2 AU from 10 kyr to 1000 kyr of evolution. In both models, P/C, S/C and Xe/C elemental ratios appear superimposed because elements are bound to single species ($H_2S$, $PH_3$ and Xe) which condensation lines are closer to the sun than the CO condensation line. As a comparison, after 100 kyr of evolution, when the CO condensation line is at 10.4 AU, $H_2S$, $PH_3$ and Xe are located at 5.9, 6.4 and 7 AU respectively, at least 3 AU closer. Therefore, their enrichments follow the same path governed by the pebble evolution in this region of the PPD. In both model, when considering the contribution of solid and vapor, the global Ar/C ratio rapidly evolve toward a plateau at 1.5 times the protosolar ratio, because of an enrichment of argon vapor at the CO condensation. Whereas, when considering the Ar/C ratio in only solids, it slowly decreases to 0.7 times the protosolar value in scenario 1. Interestingly, Ar/C ratio is heavily depleted at the CO condensation line in the reference model, with a ratio down to $10^{-25}$ times the protosolar value. This is due to the presence of clathrate hydrates of argon at the CO condensation line position in scenario 1, whereas in the reference model, argon is already in vapor phase at that distance from the sun.

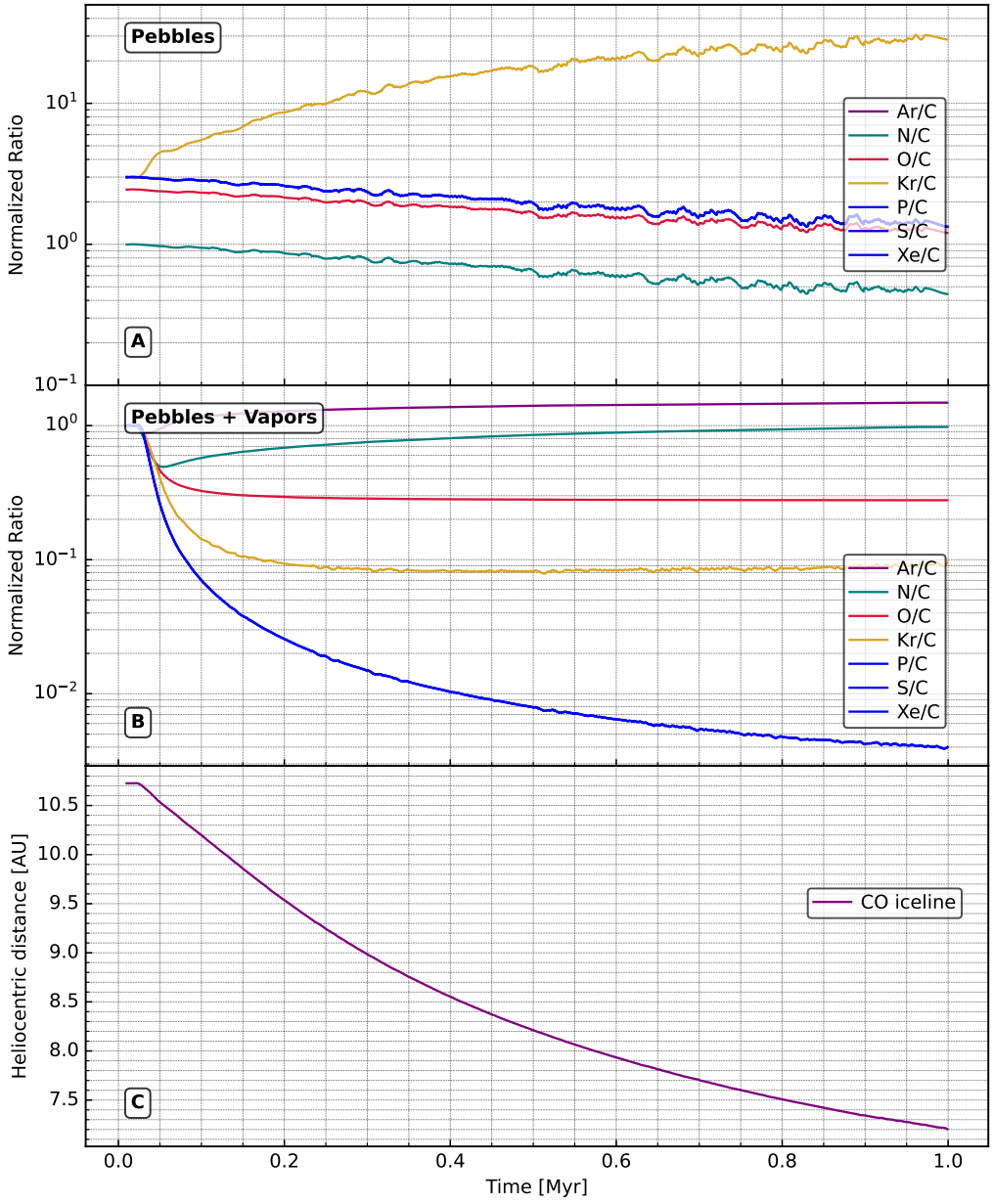


Figure 4.18.: Temporal evolution of elements ratios Ar/C, N/C, O/C, Kr/C, P/C and Xe/C in pebbles only (Panel A) and in pebbles and vapor (Panel B), calculated in the reference model with only pure condensate and vapor, at the CO condensation line position (Panel C). Figure reproduces from Mousis et al. (2024).

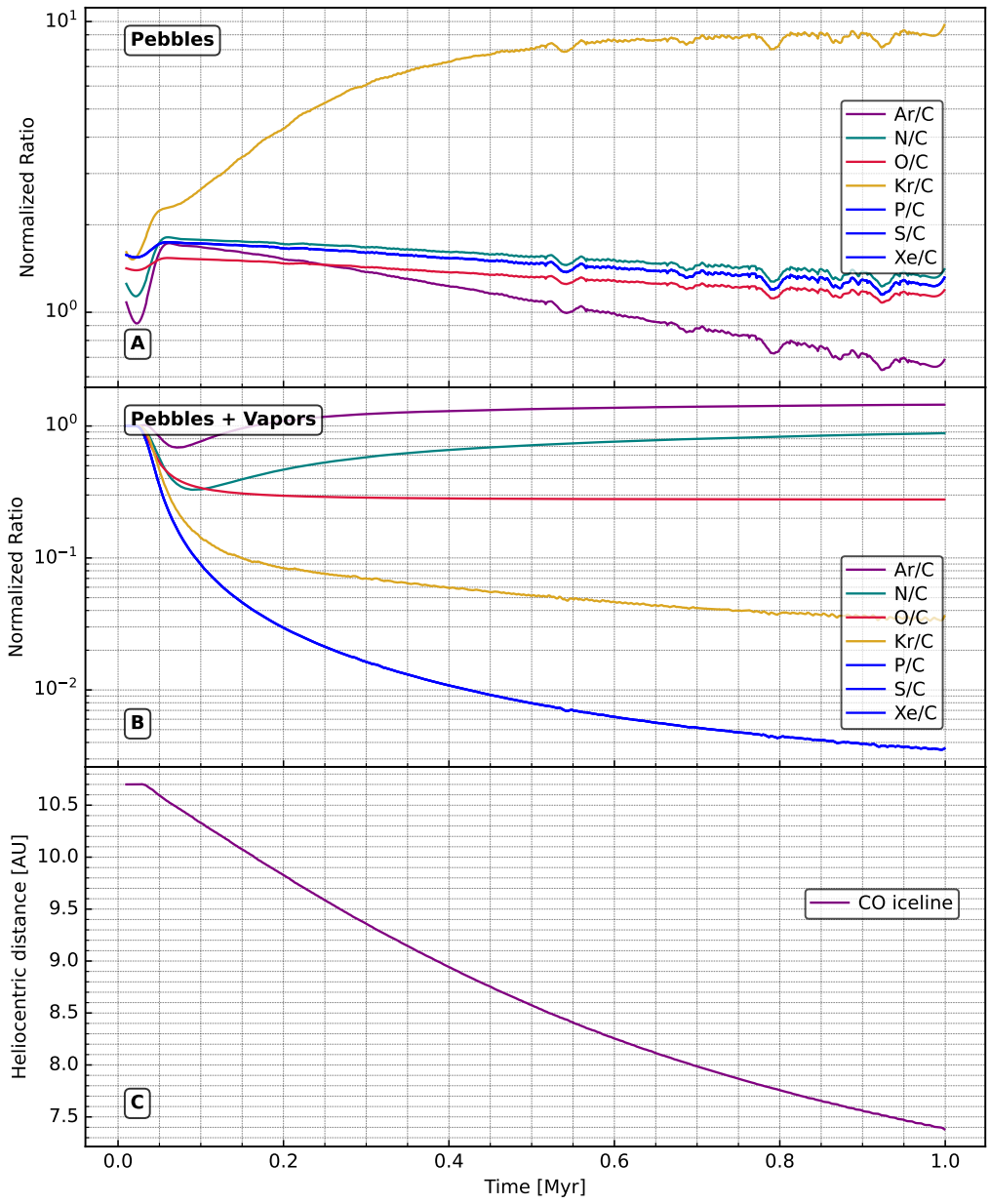


Figure 4.19.: Temporal evolution of elements ratios Ar/C, N/C, O/C, Kr/C, P/C and Xe/C in pebbles only (Panel A) and in pebbles and vapor (Panel B), calculated in scenario 1, with pure condensate, clathrate hydrates and and vapor, at the CO condensation line position (Panel C). Figure reproduces from Mousis et al. (2024).

From the predicted elemental ratios, we calculate predictions for bulk elemental

enrichments for Uranus and Neptune. The predicted bulk enrichments correspond to the scenario where the metallicity of the planets was primarily supplied by the accretion of solid material (Lambrechts et al. 2014; Helled et al. 2020), either from diluting their core or during the accretion process of the forming planets. Based on the abundance of carbon in the upper atmosphere of Uranus and Neptune derived from the $CH_4$ abundances (Sromovsky et al. 2011, 2014; Irwin et al. 2019a), we consider a carbon enrichment between 40 and 50 times the protosolar value for Uranus and between 68 and 104 times for Neptune.

Figures 4.20 and 4.21 illustrate the predicted bulk elemental enrichments for Uranus and Neptune in the reference model and scenario 1, respectively. All elemental enrichments of Uranus and Neptune in both models are presented in tables 4.5 and 4.6 respectively. They show that all elements have decreasing enrichment with the exception of krypton which abundance increase with time. This increase is due to the large krypton enrichment induced by its condensation line in the vicinity of the CO condensation line. The continuous decrease of the other elements enrichments is due to the depletion of pebble with time. Clathrate hydrates impact the elemental enrichments with the most notable difference being the enrichment of argon. When only considering the accretion of Uranus and Neptune from pure condensate, argon enrichments is close to 0, while when considering the delivery of argon by pure condensates and clathrate hydrates its enrichment jump to the ranges between 44–55 and 74.7–114.3 times the protosolar value for Uranus and Neptune, respectively, after 500 kyrs of evolution. This large divergence between the two models comes from the location of the argon (10.9–7.3 AU) condensation line, located further from the sun than the CO condensation line (10.7 – 7.2 AU). Whereas, the clathration line of argon is located closer than the CO condensation line between 9 and 5.4 AU.

Table 4.5.: Predicted elemental enrichment of Uranus after 500 and 1000 kyr of PPD evolution, assuming a carbon enrichment between 40 and 50 times the protosolar value.

| Epoch | Ar | Kr | Xe | N | O | P | S |
|---|---|---|---|---|---|---|---|
| Accretion of pure condensate | | | | | | | |
| 500 kyr | 0.0 | 729.7–912.2 | 78.7–98.4 | 26.2–32.8 | 67.2–84.0 | 78.7–98.4 | 78.7–98.4 |
| 1000 kyr | 0.0 | 1135.9–1419.8 | 53.2–66.6 | 17.7–22.2 | 48.2–60.3 | 53.2–66.6 | 53.2–66.6 |
| Accretion of pure condensate and clathrate hydrates | | | | | | | |
| 500 kyr | 44.0–55.0 | 323.8–404.7 | 59.0–73.7 | 62.3–77.8 | 53.0–66.2 | 59.0–73.7 | 59.0–73.7 |
| 1000 kyr | 27.4-34.3 | 389.2–486.6 | 52.6–65.8 | 56.2–70.3 | 47.7–59.6 | 52.6–65.8 | 52.6–65.8 |

Table 4.6.: Predicted elemental enrichment of Neptune after 500 and 1000 kyr of PPD evolution, assuming a carbon enrichment between 74.7 and 114.3 times the protosolar value.

| Epoch | Ar | Kr | Xe | N | O | P | S |
|---|---|---|---|---|---|---|---|
| | | | Accretion of pure condensate | | | | |
| 500 kyr | 0.0 | 1240.6–1897.3 | 133.8–204.6 | 44.6–68.2 | 114.3–174.8 | 133.8–204.6 | 133.8–204.6 |
| 1000 kyr | 0.0 | 1931.0–2953.3 | 90.5–138.4 | 30.2–46.1 | 82.0–125.4 | 90.5–138.4 | 90.5–138.4 |
| | | | Accretion of pure condensate and clathrate hydrates | | | | |
| 500 kyr | 74.7–114.3 | 550.4–841.8 | 100.3–153.3 | 105.8–161.9 | 90.0–137.7 | 100.3–153.3 | 100.3–153.3 |
| 1000 kyr | 46.7–71.4 | 661.7–1012.0 | 89.4–136.8 | 95.6–146.2 | 81.0–123.0 | 89.4–136.8 | 48.4–136.8 |

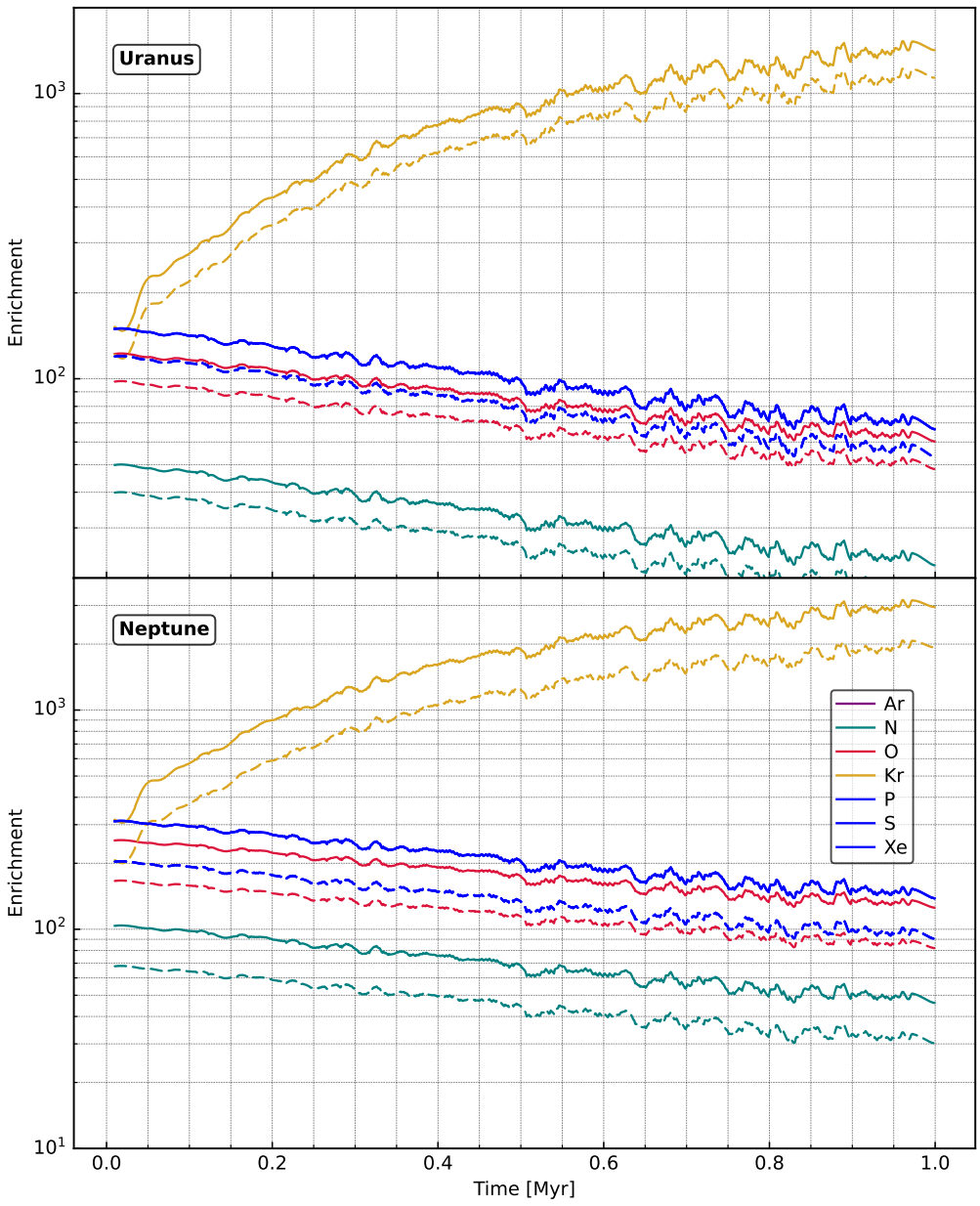


Figure 4.20.: Elemental enrichment with respect to protosolar abundances predicted in the envelope of Uranus (top panel) and Neptune (bottom panel) in the reference model, with pure condensate and vapor. It assumes a Uranus C enrichment between 40 and 50 times the protosolar value, and a Neptune C enrichment between 68 and 104 times the protosolar value. Dashed and solid lines correspond to the lower and upper bounds of the predicted elemental enrichments, respectively. Figure reproduces from Mousis et al. (2024).

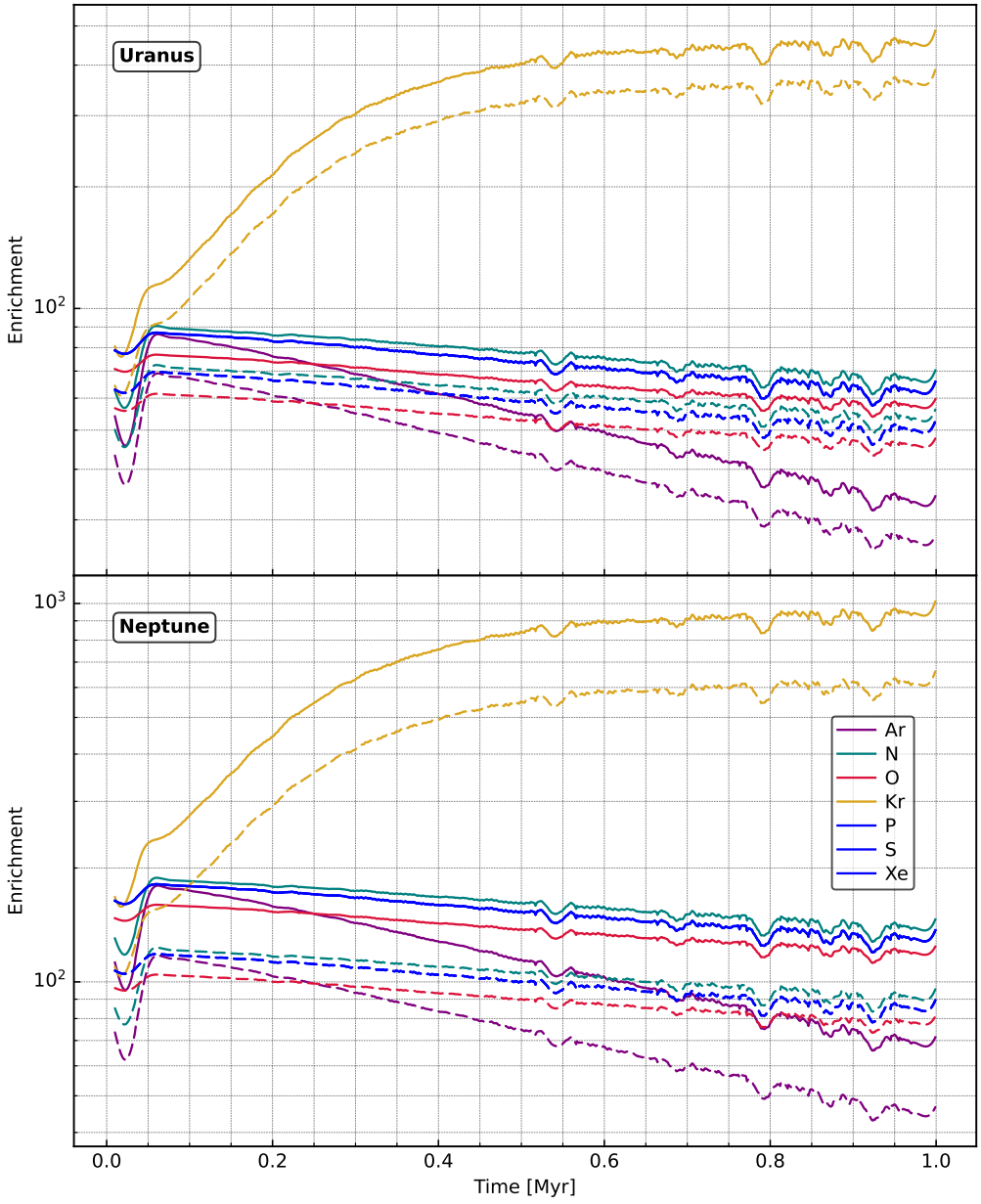


Figure 4.21.: Elemental enrichment with respect to protosolar abundances predicted in the envelope of Uranus (top panel) and Neptune (bottom panel) in scenario 1, with pure condensate, clathrate hydrate and vapor. It assumes a Uranus C enrichment between 40 and 50 times the protosolar value, and a Neptune C enrichment between 68 and 104 times the protosolar value. Dashed and solid lines correspond to the lower and upper bounds of the predicted elemental enrichments, respectively. Figure reproduces from Mousis et al. (2024).

Empirical interior models provide insight into the interior structure and possible bulk composition of the ice giants. Therefore, the observed depletion of $NH_3$ and $H_2S$, the main carriers of nitrogen and sulfur in the giant planets atmospheres, may not be representative of the bulk composition of Uranus and Neptune. A potential sink for $NH_3$ and $H_2S$ could be a deep liquid water ocean at 10 kilobar depth, or a super–ionic ocean at 100 kilobar depth (Atreya et al. 2005, 2020). The presence of such an ocean was first proposed by Ness et al. (1986) to explain the large intrinsic magnetic field of Uranus observed by Voyager 2, since metallic hydrogen, the main driver of Jupiter's magnetic field, is not expected to form at the depths of Uranus and Neptune. Therefore, the low N/C and S/C observed may not be representative of the bulk composition of the planet.

# 5. The Jovian Circumplanetary disk

Towards the end of its formation, Jupiter became surrounded by a disk of gas and dust, where the Galilean moons presumably formed. It is hypothesized that satellitesimals within this disk formed through streaming instability and grew by accreting pebbles.

## Table of Contents


5.1. Existing circumplanetary disk models . . . . . 97
5.1.1. Minimum mass circumplanetary disk model . . . . . 97
5.1.2. Gas starved disk model . . . . . 98
5.1.3. Insights from 3D hydrodynamic models . . . . . 98
5.2. An improved two-dimensional circumplanetary model . . . . . 99
5.2.1. Radial density profile . . . . . 100
5.2.2. Vertical structure . . . . . 101
5.2.3. Thermal Structure . . . . . 103
5.2.4. Self-shadowing . . . . . 105
5.2.5. Time evolution . . . . . 105
5.3. Numerical scheme . . . . . 106
5.3.1. Discretization . . . . . 106
5.3.2. Surface temperature Discretization . . . . . 109
5.3.3. Adiabatic to isothermal transition radius . . . . . 110
5.3.4. Jacobian Free Newton Krylov Method . . . . . 112


## 5.1. Existing circumplanetary disk models

After Jupiter's formation, the planet is surrounded by a circumplanetary planetary disk (CPD) constituted of gas, dust and ice (Lunine et al. 1982; Canup et al. 2002; Mousis et al. 2004; Canup et al. 2006; Coradini et al. 2010; Szulágyi et al. 2014, 2016; Szulágyi 2017; Li et al. 2020; Marleau et al. 2023). Here we review the different categories of CPD models.

### 5.1.1. Minimum mass circumplanetary disk model

A first model is to consider that its initial mass is equivalent to the mass of the moon system supplemented by additional gas to achieve a dust-to-gas ratio comparable to the one of the protoplanetary disk (Lunine et al. 1982; Mosqueira et al. 2003). Building a CPD disk in such a way lead to CPD mass as high as $10^{-2} M_{\rm J}$.

The mass of the CPD in the framework of the minimum mass CPD have two major consequences. The first one is the large viscous heating of the disk, warming the gas up to several thousand kelvin in disk region located at less than 30 $R_J$, which hinder the formation of water ice at the present day location of the Galilean Satellites (Canup et al. 2002). The second consequence of the large mass of the disk, is the rapid inward migration of forming satellites by type I migration induced by satellite-gas interaction (Ward 1997; Canup et al. 2002; Alibert et al. 2005). A forming satellite could fall onto Jupiter over a timescale approximately 0.1–10 kyr (Alibert et al. 2005). To encompass for the high temperature of this class of model, Lunine et al. (1982) considered an almost inviscid gas with a low upper limit viscosity to limit viscous heating and reach a temperature of 230 K at 10 $R_J$from the planet. This enables the formation of water ice at the present day location of Ganymede. Which ignore the possible contribution of the luminosity of the hot Jupiter after its formation. As Jupiter's surface temperature could be as high as 2000 K.

A major limitation of this model is the difficulty of forming such a massive CPD and maintaining this mass. This model could account for the early evolution of the CPD, during which the proto-Jupiter envelope undergoes significant growth, resulting in high accretion rate of order of $10^{-5}$ $M_J$ $yr^{-1}$ (Sasaki et al. 2010). Alternatively, such a massive could be formed from the outer parts of Jupiter's envelop left behind by the contracted planet, called a *"spin out disk"* (Korycansky et al. 1991).

### 5.1.2. Gas starved disk model

The gas starved model takes its root from CPD hydrodynamical simulation developments. They show that gas inflow from the PPD to the Jovian system, entering through the L1 and L2 Lagrange points in the planet's hill sphere, form a wide CPD around the planets (Lubow et al. 1999; D'Angelo et al. 2002). Due to the pressure gradient surrounding the gap, only gas and dust situated several scale heights above the midplane could be drawn onto the CPD (Lambrechts et al. 2012; Zhu et al. 2012). Consequently, the net inflow of gas and dust sustaining the sub–disk is limited, resulting in the formation of cold CPDs characterized by low accretion rates, typically on the order of $\sim 10^{-7}$ $M_J$ $yr^{-1}$(Canup et al. 2002, 2006; Sasaki et al. 2010; Anderson et al. 2021). Consequently, the gas starved CPD is lighter and cooler than the Minimum mass CPD, enabling the formation of water ice at distances from Jupiter equivalent to the present day Ganymede semi-major axis.

### 5.1.3. Insights from 3D hydrodynamic models

Recent advances in global three-dimensional hydrodynamic simulations, through increased grid resolution and more accurate radiative transfer model enabled by the increased computational power available, point out that runaway gas accretion results in a planet with an exceptionally high surface temperature, reaching several thousand kelvin (Szulágyi et al. 2016; Szulágyi 2017). Furthermore, the integration of a third dimension in the those simulations has pointed out the major role of material

meridional circulation patterns in the planet hill sphere. It facilitates the exchange of material between the CPD and the PPD through intricate streams of gas flowing in both directions Morbidelli et al. (2014) and Szulágyi et al. (2014). This meridional circulation has profound implications for our comprehension of CPD formation and replenishment processes. By establishing a dynamic physical connection between the PPD and the CPD, it initiates intricate feedback mechanisms that regulate the accretion rate onto the CPD. Consequently, these mechanisms impose constraints on Jupiter's growth during the gas runaway accretion phase Szulágyi et al. (2014). Furthermore, it has been suggested that meridional circulation can uplift dust from the midplane of the PPD, thereby enriching the accreted material with dust–to–gas ratios that surpass those estimated for the PPD Szulágyi et al. (2022). This contrasts with previous arguments proposing significant dust depletion in the accreting material Canup et al. (2006), Lambrechts et al. (2012), and Zhu et al. (2012).

Three-dimensional simulations also underscore the significance of the opacity regime prescription. In the context of a fully optically thick CPD, studies have demonstrated that its temperature profile can escalate to 4500 K, with a centrifugal radius extending up to one-third of the Hill radius Ayliffe et al. (2009), significantly beyond the extent proposed by the gas-starved model, which posits only a few percent of the Hill radius Canup et al. (2002, 2006). In the most extreme scenario, Fung et al. (2019) and Krapp et al. (2024) showed that the gas surrounding Jupiter might be thermally supported, leading to the formation of a circumplanetary shell rather than a CPD. Conversely, when the CPD is assumed to be optically thin and locally isothermal, cooling becomes considerably more efficient, resulting in the formation of a massive CPD Fung et al. (2019).

## 5.2. An improved two-dimensional circumplanetary model

In the following section, we present the two-dimensional circumplanetary disk model depicted by figure 5.1. This CPD model is divided into two distinct areas, an outer optically thin and vertically isotherm, and an inner optically thick and adiabatic inner area. Both areas are separated by the adiabatic–to–isothermal transition radius, where the CPD becomes optically thin. The heating of the CPD by Jupiter's radiative heating occurs at its photosurface, where the medium becomes optically thick. This heat is subsequently propagated to the midplane using a gray atmosphere radiative transfer model. Furthermore, we account for the projection of shadows cast by the optically thick region onto the optically thin region.

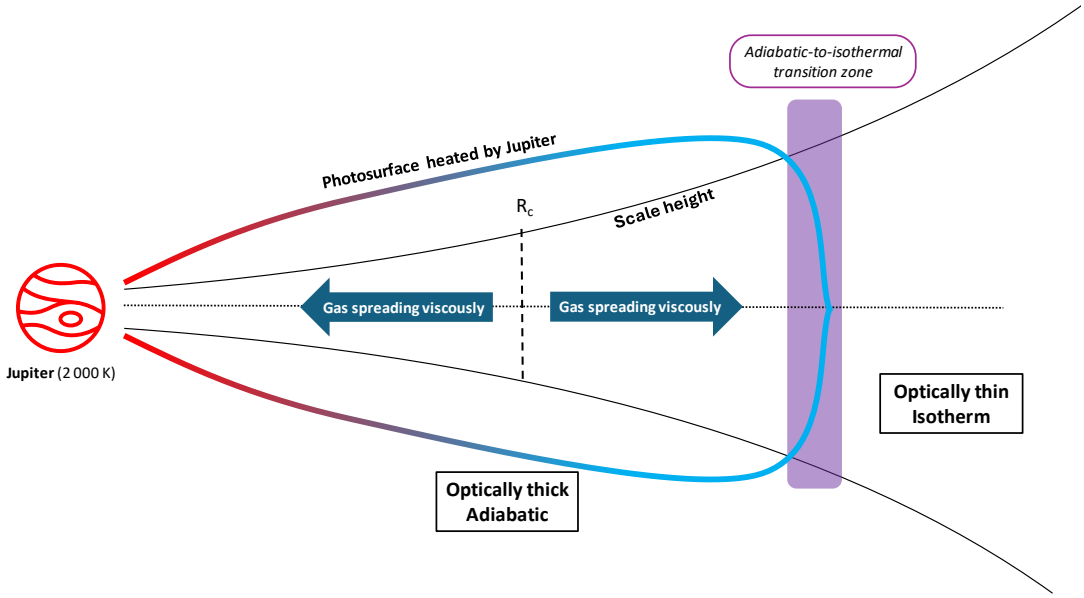


Figure 5.1.: Diagram illustrating the structure of the circumplanetary disk model, and delimited into two distinct zones. The first zone, situated closer to Jupiter, is optically thick, characterized by an optical depth $\tau$ exceeding 2/3 in the midplane. The second zone, located farther from Jupiter, is optically thin, with $\tau$ below 2/3 in the midplane. The altitude at $\tau = 2/3$ defines the photosurface. Within the optically thick region, bold lines on the diagram depict this photosurface, indicating a temperature gradient ranging from hot (red) to cold (blue) regions. These regions are demarcated by the adiabatic–to–isothermal transition zone (purple box), where the photosurface ceases to exist. Material is uniformly accreted onto the CPD at distances closer to the centrifugal radius ($R_c$).

### 5.2.1. Radial density profile

The CPD is axisymetric and at hydrostatic equilibrium. We adopt the viscous accretion model of Canup et al. (2002) and Canup et al. (2006) , where the viscosity is parameterized by the $\alpha$–turbulence viscosity of Shakura et al. (1973). The surface density is defined as (Canup et al. 2002) :

$$\Sigma_g = \frac{\dot{M}}{3\pi\nu}\frac{\Lambda}{l}, \tag{5.1}$$

where $\dot{M}$ is the accretion rate of matter onto the planet. The factors $\Lambda$ and $l$ are derived from the gas surface density continuity equation (Canup et al. 2002; Makalkin et al. 2014). When considering distances shorter than $R_c$, the following relation holds:

$$\Lambda(r) = 1 - \frac{1}{5}\left(\frac{r}{R_c}\right)^2 - \sqrt{\frac{R_p}{r}} - \frac{4}{5}\sqrt{\frac{R_c}{r_d}} + \frac{4}{5}\frac{R_p R_c}{r_d r} + \frac{1}{5}\sqrt{\frac{R_p}{r_d}}\left(\frac{r}{R_c}\right)^2, \tag{5.2}$$

while at distance greater than $R_c$

$$\Lambda(r) = \frac{4}{5}\sqrt{\frac{R_c}{r}} - \frac{R_p}{r} - \frac{4}{5}\frac{R_c}{r_d} + \sqrt{\frac{R_p}{r_d}}, \tag{5.3}$$

with $R_p$ representing the radius of the planet. Finally, one have:

$$l = 1 - \sqrt{\frac{R_p}{r_d}}, \tag{5.4}$$

with $r_d$ denoting the size of the disk.

At the centrifugal radius location, the centrifugal force of an object with a specific angular momentum compensates for the gravitational force. Closer than this radius, the CPD's gas will drift inward toward the planet, while at greater distances, it flows outward, merging with the meridional flow within the Hill sphere of the planet (Szulágyi et al. 2016; Szulágyi 2017; Batygin et al. 2020). Therefore, the centrifugal distance is defined as:

$$R_c = \frac{j^2}{GM_p}, \tag{5.5}$$

where $j$ represents the specific angular momentum of falling gas from the Hill sphere, $G$ denotes the universal gravitational constant, and $M_p$ stands for the mass of the planet. The centrifugal radius exhibits significant variability, contingent upon the value of the specific angular momentum parameter $j$. The centrifugal radius can then be treated as an input parameter in the model, allowing for the exploration of different scenarios and configurations.

## 5.2.2. Vertical structure

Assuming a CPD at hydrostatic equilibrium, the vertical density profile follows a Gaussian distribution:

$$\rho(r,z) = \rho_0(r)\exp\left\{\left(-\frac{z^2}{2h(r)^2}\right)\right\}, \tag{5.6}$$

where $\rho_0$ represents the gas density at the disk midplane. $h$ denotes the disk scale height, given by:

$$h = \frac{C_s}{\Omega_K}. \tag{5.7}$$

By definition, the surface density $\Sigma_g(r)$ is given as the integral of the density $\rho(z,r)$ over all vertical heights:

$$\Sigma_g(r) = \int_{-\infty}^{+\infty} \rho(z,r)\,dz. \tag{5.8}$$

one can thus deduce the midplane density by combining this equation with the vertical density profile:

$$\rho_0(r) = \sqrt{\frac{2}{\pi}} \frac{\Sigma_g}{2h}, \tag{5.9}$$

which depends solely on the distance to the planet.

The CPD is divided into two regions: an adiabatic, optically thick zone where the optical depth $\tau$ in the midplane exceeds the standard value of 2/3, and a vertically isothermal, optically thin zone where $\tau$ is less than 2/3 in the midplane (see Fig. **??**). $\tau$ is defined as:

$$\tau(z) = \int_z^{+\infty} \rho(r,z')\kappa_{\mathrm{R}}(r,z')dz', \tag{5.10}$$

where $\kappa_{\mathrm{R}}$ represents the mean Roseland opacity of the medium. In this study, we use the opacity experimental data compiled by Makalkin et al. (1995). These data define the different opacity regimes induced by the vaporization (condensation) of various ices and refractory elements as the temperature increases (decreases).

The optically thick region is heated by the planet's radiation at the CPD photosurface level, corresponding to $\tau = 2/3$. By combining the density profile equation with the definition of optical depth, one can determine the altitude of the photosurface, $z_s$, by solving:

$$\frac{2}{3} = \int_{z_s}^{\infty} \rho(r,z')\kappa_{\mathrm{R}}(r,z')dz'. \tag{5.11}$$

Since the region above the photosurface is vertically isothermal, the opacity is constant above the photosurface. This allows for computing $z_s$ by combining Eqs. 5.6,5.9,5.11:

$$z_s(r) = \mathrm{erf}^{-1}\left(1 - \frac{4}{3}\frac{1}{\Sigma_g(r)\kappa_R(r,z_s)}\right)\sqrt{2}h(r), \tag{5.12}$$

where $\kappa_p(r,z_s)$ denotes the opacity at the photospheric location.

The photosurface exists only if $z_s$ is positive, leading to the condition:

$$\begin{aligned} &\mathrm{erf}^{-1}\left(1 - \frac{4}{3}\frac{1}{\Sigma_g(r)\kappa_p(r,z_s)}\right) > 0 \\ &\iff \Sigma_g(r)\kappa_p(r,z_s) > \frac{4}{3}. \end{aligned} \tag{5.13}$$

From this condition, the radial position of the transition zone between an optically thick CPD and a fully optically thin CPD can be determined. The CPD is optically thin if:

$$\Sigma_g(r)\kappa_p(r,0) < \frac{4}{3}, \tag{5.14}$$

where $\kappa_p(r,0)$ represents the opacity at the CPD midplane location.

### 5.2.3. Thermal Structure

In the optically thick region, the temperature at the photosurface altitude, referred to as the surface temperature, follows the semi-analytical model Makalkin et al. (1995, 2014):

$$T_s^4(r) = \frac{1+\left(2\kappa_p(r,z_s)\Sigma_g(r)\right)^{-1}}{\sigma_{\rm SB}} \times \left(F_{\rm vis}+F_{\rm acc}+k_s F_{\rm p}\right)+T_{\rm neb}^4. \tag{5.15}$$

where $\sigma_{\rm SB}$ represents the Stefan-Boltzmann constant, $T_{\rm neb}^4$ denotes the temperature of the surrounding PPD, and $F_{\rm vis}$, $F_{\rm acc}$, and $F_{\rm p}$ are the heat fluxes produced by viscous stress, accretion of material onto the CPD, and Jupiter's radiative heating, respectively. Additionally, $k_s$ is a factor between 0 and 1 defining the fraction of Jupiter's light absorbed, with the remainder either reflected or scattered. We use the value $k_s = 0.2$ Makalkin et al. (1995). The expressions for the heat fluxes are then Makalkin et al. (2014):

$$F_{\rm vis} = \frac{3}{8\pi}\frac{\Lambda}{l}\dot{M}\Omega_{\rm K}^2, \tag{5.16}$$

$$F_{\rm acc} = \frac{X_d \chi G M_p \dot{M}}{4\pi R_c^2 r}\exp\left\{\left(-\frac{r^2}{R_c^2}\right)\right\}, \tag{5.17}$$

$$F_{\rm p} = L_{\rm p}\frac{\sin(\zeta+\eta)}{8\pi(r^2+z_s^2)}. \tag{5.18}$$

Here, $X_d$ represents the metallicity of the PPD, and $\chi$ is the metallicity enrichment factor between the PPD and the CPD, associated with dust enrichment. In the expression for Jupiter's surface heating flux, $L_p$ denotes the planet's luminosity, while $\zeta$ and $\eta$ are angles expressing the disk's geometry, defined as follows:

$$\zeta = \arctan\left(\frac{4}{3\pi}\frac{R_p}{\sqrt{r^2+z_s^2}}\right), \tag{5.19}$$

$$\eta = \arctan\left(\frac{dz_s}{dr}\right) - \arctan\left(\frac{z_s}{r}\right). \tag{5.20}$$

From the surface temperature, we determine the vertical temperature structure using the Eddington approximation Makalkin et al. (1995). By utilizing the first and second moments of the radiative transfer equation and considering that Jupiter's light does not penetrate the optically thick region, we arrive at:

$$\frac{dT^4}{dq} = -\frac{27}{64\pi}\nu(q)\Sigma_g^2\Omega_K^2\kappa_R(q)q, \tag{5.21}$$

where $q$ represents the vertical mass coordinate given by:

$$q(z) = 2\int_0^z \rho(z')dz'. \tag{5.22}$$

Normalizing the mass coordinate in Eq. 5.21 by the mass coordinate of the photosurface $q_s$, we obtain:

$$\frac{dT^4}{dq'} = -\frac{27}{64\pi}\nu(q')\Sigma_g^2\Omega_K^2\kappa_R(q')q'q_s^2, \tag{5.23}$$

where

$$q' = \frac{q}{q_s}. \tag{5.24}$$

Here, the normalized mass coordinate $q' = 1$ corresponds to the altitude of the photosurface, implying:

$$T(q' = 1) = T_s. \tag{5.25}$$

We assume that the disk is vertically symmetric with respect to the midplane, implying that the vertical temperature profile attains a maximum value at the midplane altitude:

$$\left.\frac{dT}{dq'}\right|_{q'=0} = 0. \tag{5.26}$$

In the aforementioned equation system, the viscosity $\nu$, the surface density $\Sigma_g$, and the mean Roseland opacity $\kappa_R$ depend on the temperature itself. Furthermore, the surface temperature depends on the derivative of the photosurface altitude, which itself depends on the midplane temperature. We employ an iterative solving method based on the Jacobian-Free-Newton-Krylov method (JFNK) Knoll et al. (1993, 2004) and Zhou et al. (2022) to solve Eq. 5.23 in the $(r, q')$ parameter space. Subsequently, we use a spline cubic interpolation method to transform the solution from $(r, q')$ space to $(r, z)$ space.

When the disk is vertically isothermal, the disk surface temperature given by Eq. 5.15 becomes its effective temperature. However, in the absence of a well-defined photosurface, a smaller fraction of Jupiter's incident radiation is absorbed by the medium within the CPD. Hence, we define an absorption factor based on the midplane optical depth:

$$\tau(r, z = 0) = \int_0^\infty \rho(r, z')\kappa_R(r, z')dz'. \tag{5.27}$$

Given that we are operating in the optically thin region, and assuming a vertically isothermal temperature profile, $\kappa_R$ remains constant with respect to the vertical coor-

dinate, $z'$. Thus, we have:

$$\tau(r, z=0) = \frac{\kappa_R \Sigma_g}{2}. \tag{5.28}$$

As a result, only a fraction of Jupiter's light is absorbed by the disk. We employ a simple Beer-Lambert law approximation:

$$F_\mathrm{a} = F_\mathrm{p} e^{-\tau}, \tag{5.29}$$

where $F_\mathrm{a}$ represents the absorbed flux. The effective temperature is then computed using Eq. 5.15, with the planetary flux $F_\mathrm{p}$ replaced by the absorbed flux $F_\mathrm{a}$.

### 5.2.4. Self-shadowing

The photosurface, being completely opaque, can cast a shadow onto part of the CPD, either onto the photosurface itself or onto the optically thin area. Particularly at the frontier between the optically thick and optically thin regions, the photospheric altitude decreases, forming an opaque wall in this region. Materials close to the wall are then plunged into its shadow. When a part of the disk is in shadow, it is no longer heated by Jupiter's light, resulting in significantly colder temperatures compared to its surroundings.

A part of the disk is considered to be shadowed if it fulfills the following condition:

$$z_s(r) > R_\mathrm{J} + \frac{z_s(r' - R_\mathrm{J})}{r'} r, \quad \forall r' < r. \tag{5.30}$$

Here, $z_s(r)$ is equal to 0 when the model is operating in an optically thin region.

### 5.2.5. Time evolution

The model operates as a quasi-static framework, assuming hydrostatic equilibrium at each time step. Consequently, the properties of the CPD, including its mass and thermodynamic characteristics, depend solely on the time-varying CPD accretion rate and the planet's luminosity. We adopt a Jupiter accretion model from Mordasini et al. (2012) and Mordasini (2013), which model the accretion process by considering a known PPD density profile and gap formation around Jupiter. From this model, we derive a simple parametric fit:

$$\dot{M}(t) = \exp\left(-61.5 \times \frac{t}{10^6 \mathrm{yr}} - 12.0\right) M_\mathrm{J}/\mathrm{yr} \tag{5.31}$$

and

$$L_p(t) = \frac{1}{79285.7 \frac{t}{10^6 \mathrm{yr}} - 12.442} L_\odot, \tag{5.32}$$

where $t$ is the time elapsed since the end of the runaway gas accretion, which is

assumed to be the time of formation of the CPD. At each time step, the thermodynamic properties of the CPD are computed based on the corresponding accretion rate and luminosity.

## 5.3. Numerical scheme

To resolve the thermal structure of the CPD, a numerical scheme has been developed, which is detailed in this section.

### 5.3.1. Discretization

The CPD structure calculation is divided into two areas. Close to the star, the optically thick and adiabatic region thermal structure is calculated using a two-dimensional grid. Whereas, the optically thick and isothermal thermal structure is calculated using a one-dimensional grid. Both computation grids are linked by the innermost cell of the one-dimensional grid, which act as a ghost cell for the two-dimensional grid.

The two-dimensional grid lies in the $(q',r)$ space. Where $q'$ is the normalized mass coordinate, with $q'=0$ is the midplane mass coordinate and $q'=1$ is the photosurface mass coordinate. The grid is constructed such that the $r$ dimension is a logarithmic grid, while the $q'$ dimension is a chebichev grid :

$$r_i = r_{\rm min}\exp\left\{\left[\frac{i-1}{N_r-1}\log\left(\frac{r_{\rm iso}}{r_{\rm min}}\right)\right]\right\}, \tag{5.33}$$

$$q'_i = \frac{r_{\rm min}+r_{\rm max}}{2} + \frac{r_{\rm min}-r_{\rm max}}{2}\cos\theta_i, \tag{5.34}$$

where $\theta_i$ is the linear grid of angles between 0 and $\pi$, $r_{\rm min}$ is the inner edge of the CPD and $r_{\rm iso}$ is the adiabatic-to-isothermal transition radius, the distance at which the CPD become optically thin and vertically isothermal.

Recalling the radiative transfer equation 5.23, one have:

$$\frac{dT^4}{dq'} = -\frac{27}{64\pi}\nu(q')\Sigma_g^2\Omega_{\rm K}^2\kappa_{\rm R}(q')q'q_s, \tag{5.35}$$

By expanding the derivative

$$\frac{dT^4}{dq'} = 4T^3\frac{dT}{dq'}, \tag{5.36}$$

we can rewrite the radiative transfer equation as

$$4T^3\frac{dT}{dq'} + \frac{27}{64\pi}\nu(q')\Sigma_g^2\Omega_{\rm K}^2\kappa_{\rm R}(q')q'q_s^2 = 0. \tag{5.37}$$

The vertical derivative of temperature at point $(r_i,q'_j)$, $\left.\frac{dT}{dq'}\right|_{r_i,q'_j}$ can be discretized

as:

$$\left.\frac{dT}{dq'}\right|_{r_i,q'_j} = \frac{T_{i,j+1/2} - T_{i,j-1/2}}{q'_{j+1/2} - q'_{j+1/2}} \tag{5.38}$$

Therefore, one have the discretized radiative transfer equation at point $q'_j$

$$4T_{i,j}^3 \frac{T_{i,j+1/2} - T_{i,j-1/2}}{q'_{j+1/2} - q'_{j+1/2}} + \frac{27}{64\pi}\nu(r_i, q'_j)\Sigma_g(r_i)^2\Omega_{\rm K}(r_i)^2\kappa_{\rm R}(r_i, q'_j)q'_j q_s(r_i) = 0, \tag{5.39}$$

where $\nu(r_i, q'_j)$, $\Sigma_g(r_i)$, $\kappa_{\rm R}(r_i, q'_j)$ and $q_s(r_i)$ are only dependent on the temperature and $\Omega_{\rm K}(r_i)$ is constant with the CPD temperature and only dependent on the radius $r_i$ and considered constant.

To solve numerically equation 5.39, one need to determine the value of *in between cells* temperatures $T_{i,j+1/2}$ and $T_{i,j-1/2}$ and coordinates $q_{j+1/2}$ and $q_{j-1/2}$. An intuitive method would be to consider a mean value:

$$\begin{cases} q'_{j+1/2} = \frac{q'_j + q'_{j+1}}{2}, \\ q'_{j-1/2} = \frac{q'_j + q'_{j-1}}{2}, \\ T_{i,j+1/2} = \frac{T_{i,j} + T_{i,j+1}}{2}, \\ T_{i,j-1/2} = \frac{T_{i,j} + T_{i,j-1}}{2}, \end{cases} \tag{5.40}$$

Therefore, the derivative would be:

$$\begin{aligned} \left.\frac{dT}{dq'}\right|_{r_i,q'_j} &= \frac{T_{i,j+1/2} - T_{i,j-1/2}}{q'_{j+1/2} - q'_{j+1/2}} \\ &= \frac{\frac{T_{i,j}+T_{i,j+1}}{2} - \frac{T_{i,j}+T_{i,j-1}}{2}}{\frac{q'_j+q'_{j+1}}{2} - \frac{q'_j+q'_{j-1}}{2}} \\ &= \frac{T_{i,j+1} - T_{i,j-1}}{q'_{i,j+1} - q'_{i,j-1}}. \end{aligned} \tag{5.41}$$

This formulation lead to the well known centered derivative, which in our case has proven to be not stable and to lead to large instabilities.

Other interpolations methods are the first order up– and down-wind interpolation schemes. When having to compute a quantity linked to the propagation of a flux, here the temperature linked to the propagation of the heat flux, to get the value of the quantity between two cells, one can simply use the quantity of the cell which is upstream of the flux. Because Jupiter's heat flux propagate from the upper layers to the bottom layers of the disk, one have:

$$\begin{cases} T_{i,j-1/2} = T_{i,j}, \\ T_{i,j+1/2} = T_{i,j}. \end{cases} \tag{5.42}$$

Using the values of $q'_{i,j+1/2}$ and $q'_{i,j-1/2}$ from equation 5.40 one have:

$$\left.\frac{dT}{dq'}\right|_{r_i,q'_j} = 2\frac{T_{i,j+1} - T_{i,j}}{q'_{j+1} - q'_{j-1}} \tag{5.43}$$

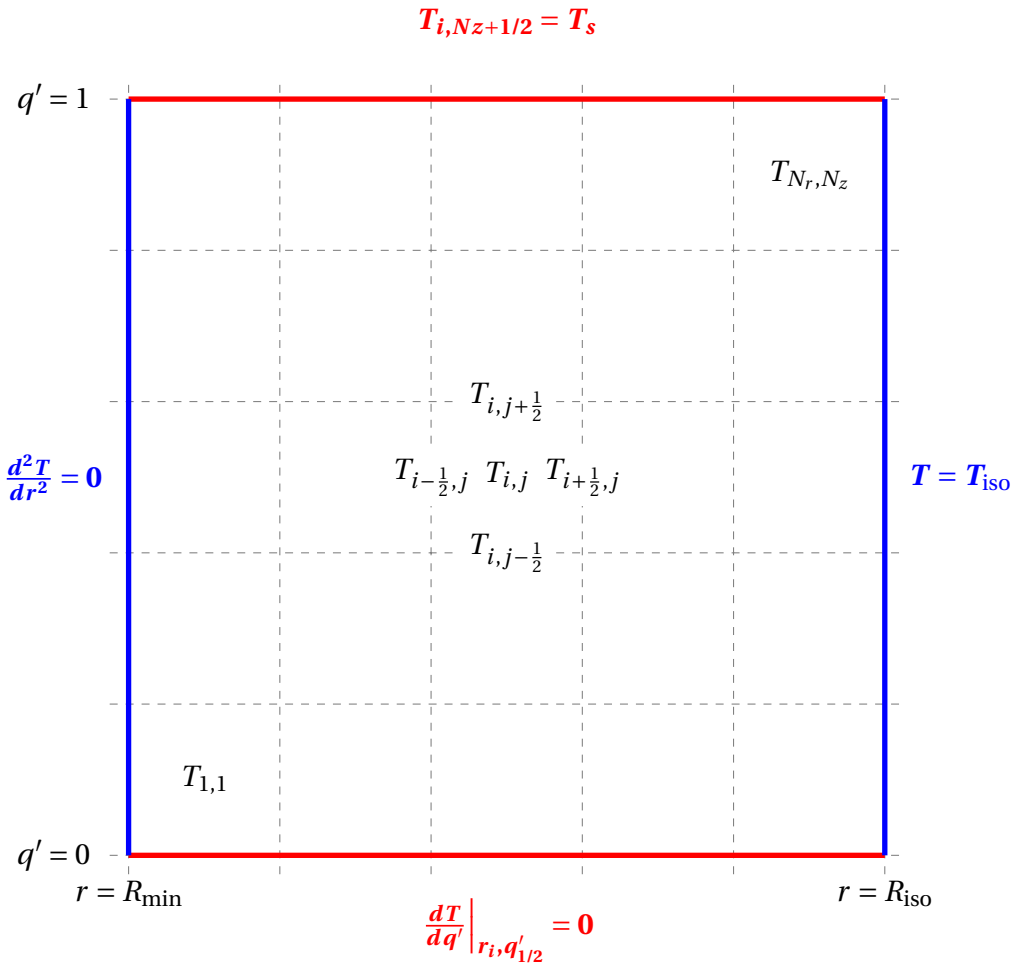


Figure 5.2.: Sketch of the computational grid used to determine the thermal structure of the optically thick and adiabatic region of the CPD. Blue borders denote the radial inner and outer boundaries which conditions are $\frac{d^2T}{dr^2} = 0$ and $T = T_{\rm iso}$ respectively. While the red borders denote the lower and upper boundaries, which conditions are $\frac{dT}{dz} = 0$ and $T = T_s$.

At the photosurface level, the temperature is the surface temperature governed by equation 5.15. Therefore, the upper boundary condition is simply:

$$T_{i,N_z+1/2} = T_s(r_i). \tag{5.44}$$

At the midplane level, the temperature is maximum, leading to the boundary condi-

tion:

$$\left.\frac{dT}{dq'}\right|_{r_i,1} = 0 \tag{5.45}$$

Using the upwind interpolation, one have

$$\begin{aligned}\left.\frac{dT}{dq'}\right|_{r_i,q'_1} &= \frac{T_3/2 - T_1/2}{q'_3/2 - q'_1/2} \\ &= \frac{T_2 - T_1}{\frac{q'_2+q'_1}{2} - q'_{1/2}}\end{aligned} \tag{5.46}$$

By posing that $q'_{1/2} = 0$ :

$$\left.\frac{dT}{dq'}\right|_{r_i,q'_1} = 2\frac{T_2 - T_1}{q'_2 + q'_1} = 0 \tag{5.47}$$

Leading to the midplane boundary conditions

$$T_1 = T_2. \tag{5.48}$$

### 5.3.2. Surface temperature Discretization

We recall the surface temperature equation at distance $r_i$ from the planet:

$$\begin{aligned}T_s^4(r_i) = &\frac{1 + \left(2\kappa_p(r_i, z_s)\Sigma_g(r_i)\right)^{-1}}{\sigma_{\rm SB}} \\ &\times \left(F_{\rm vis}(r_i) + F_{\rm acc}(r_i) + k_s F_{\rm p}(r_i)\right) + T_{\rm neb}^4.\end{aligned} \tag{5.49}$$

Because the surface temperature is an energy balance between, viscous heating, accretion heating and radiative heating, the surface temperature is dependent on the midplane temperature. Therefore, the upper boundary condition is itself dependent on the CPD thermal structure.

More specifically, the radiative heating of the planet $F_{\rm p}$ is dependent on the derivative of the photosurface altitude $z_s$. We express this derivative as a function of the photosurface mass coordinate using equations 5.12 :

$$\frac{dz_s}{dr} = \sqrt{2\pi}h\exp\left\{\frac{1}{\sqrt{2}}\,\mathrm{erf}^{-1}\,q_s\right\}\frac{dq_s}{dr} + \sqrt{2}\,\mathrm{erf}^{-1}\,q_s\frac{dh}{dr}, \tag{5.50}$$

where the derivative is computed using a centered derivative scheme:

$$\left.\frac{dq_s}{dr}\right|_{r_i} = \frac{q_{s,i+1} - q_{s,i-1}}{r_{i+1} - r_{i-1}} \tag{5.51}$$

and

$$\left.\frac{dh}{dr}\right|_{r_i} = \frac{h_{i+1} - h_{i-1}}{r_{i+1} - r_{-1}} \tag{5.52}$$

Therefore, one have

$$\left.\frac{dz_s}{dr}\right|_{r_i} = \sqrt{2\pi} h_i \exp\left\{\frac{1}{\sqrt{2}}\mathrm{erf}^{-1}(q_{s,i})\right\}\frac{q_{s,i+1}-q_{s,i-1}}{r_{i+1}-r_{i-1}} + \sqrt{2}\,\mathrm{erf}^{-1}(q_{s,i})\frac{h_{i+1}-h_{i-1}}{r_{i+1}-r_{-1}}. \tag{5.53}$$

With outer boundary conditions being

$$T_{Nr,j} = T_{\mathrm{iso}}\ \forall\, j, \tag{5.54}$$

where $T_{\mathrm{iso}}$ is the temperature of at the adiabatic-to-isothermal transition radius. The outer boundary condition is built such that the second derivative of the temperature is null:

$$\left.\frac{d^2T}{dr^2}\right|_{r_1} = 0. \tag{5.55}$$

Which is equivalent to do a linear interpolation of the temperature to compute a temperature $T_{0,j}$ in the inner ghost cells at the virtual radial coordinate $r_0$:

$$\begin{aligned} &\frac{T_{2,j}+T_{0,j}-2T_1}{2(r_2-r_1)^2} = 0 \\ \Longleftrightarrow\ &T_{0,j} = 2T_{1,j} - T_{2,j}. \end{aligned} \tag{5.56}$$

Since the surface temperature and the two-dimensional thermal structure of the disc are interdependent, they are calculated iteratively. We first compute the surface temperature from a first estimate of the thermal structure of the optically thick region. The surface temperature is then estimated again from the new thermal structure, which is used to compute the new thermal structure. The iteration is repeated until convergence is reached.

### 5.3.3. Adiabatic to isothermal transition radius

The computational grid is divided into two zones. Close to the planet, the CPD is optically thick and adiabatic, whereas the outer region of the CPD is optically thin and isothermal. Both regions are separated by the Adiabatic-to-isothermal transition radius. At this location, the photosurface altitude is null, in other word, the midplane optical depth is equal to 2/3. Using the definition of the midplane optical depth in the optically thin region :

$$\tau(r = r_{\mathrm{iso}}, z = 0) = \frac{\kappa_R(r)\Sigma_g(r)}{2} = \frac{2}{3}. \tag{5.57}$$

Where $r_{\mathrm{iso}}$ is the adiabatic-to-isothermal transition radius. Since $\Sigma_g$ and $\kappa_{\mathrm{R}}$ are dependent on the temperature, we cannot solve analytically this equation. We use a binary search algorithm to retrieve $r_{\mathrm{iso}}$. The algorithm initialize with a first guess $r_0$ between $r_{\mathrm{min}}$ and $r_{\mathrm{max}}$, the inner and outer edges of the CPD respectively. At $r_0$, the optical depth $\tau$ is evaluated. If $\tau$ is larger than 2/3, $r_0$ is too small and the solution is between

$r_0$ and $r_{\max}$. Conversely, if $\tau$ is smaller than 2/3 , $r_0$ is too large and the solution is between $r_{\min}$ and $r_0$. At the next iteration, a new guess is chosen such that :

$$r_1 = \begin{cases} \frac{r_0+r_{\max}}{2} \text{ if } \tau > \frac{2}{3} \\ \frac{r_{\min}+r_0}{2} \text{ if } \tau < \frac{2}{3} \end{cases} \tag{5.58}$$

And the search domain is updated such that :

$$\begin{cases} r_0 \rightarrow r_{\min} \text{ if } \tau > \frac{2}{3}, \\ r_0 \rightarrow r_{\max} \text{ if } \tau < \frac{2}{3}, \end{cases} \tag{5.59}$$

and the iteration goes on until the search domain is small enough

$$r_{\max} - r_{\min} < \text{tol}_{\text{bin}}. \tag{5.60}$$

At each iteration of the binary search, the evaluation of the optical depth imply the computation of the midplane temperature, assuming that we are in the optically thin and vertically isothermal region of the CPD. Therefore, at each iteration need to solve equation 5.49 at a specific distance $r_i$ from the planet and assuming there is no photosurface ($z_s = 0$). Assuming that there is no photosurface simplify greatly the equation 5.49 because there is no need to calculate $\frac{dz_s}{dr}$ which depends on the neighbor cells, the temperature at a distance $r_i$ is calculated independently. Consequently, we use a simple secant method to calculate the temperature. We manipulate equation 5.49 to be of the form

$$f(T, r_i) = 0 \tag{5.61}$$

where $f(T, r_i)$ is

$$\begin{aligned} f(T, r_i) = T^4 - \frac{1 + \left(2\kappa_p(T)\Sigma_g(T)\right)^{-1}}{\sigma_{\text{SB}}} \\ \times \left(F_{\text{vis}}(r_i) + F_{\text{acc}}(r_i) + k_s F_{\text{p}}(r_i)\right) - T_{\text{neb}}^4. \end{aligned} \tag{5.62}$$

At iteration k of the secant algorithm, the k+1-th estimation of the temperature is :

$$T^{k+1} = T^k + f(T^k, r_i)\frac{T^k - T^{k-1}}{f(T^k, r_i) - f(T^{k-1}, r_i)}. \tag{5.63}$$

Since iteration $k+1$ is dependent on iterations $k$ and $k-1$, therefore, the first iteration of the algorithm need two first guesses of the temperature $T^0$ and $T^1$ of value of 200 K and 210 K respectively. The iteration goes on until the function $f(T^k, r_i)$ is small enough :

$$\left|f(T, r_i)\right| < \text{tol}_{\text{res}} \tag{5.64}$$

In the model it possible that the optically thick and adiabatic region does not exist, in which case $r_{\text{iso}}$ will not converge, or converge toward a null value.

### 5.3.4. Jacobian Free Newton Krylov Method

Combining equations 5.39 and 5.49, form an equation system, of the form

$$\vec{F}\left[\vec{X}\right] = 0. \tag{5.65}$$

To solve the system, one can first do a first order Taylor expansion of the system on a short step :

$$\vec{F}\left[\vec{X}_{k+1}\right] = \vec{F}\left[\vec{X}_k\right] + \boldsymbol{J}\left[\vec{X}_k\right] \cdot \left(\vec{X}_{k+1} - \vec{X}_k\right) + O(\vec{X}^2). \tag{5.66}$$

Where $\boldsymbol{J}\left[\vec{X}^k\right]$ is the Jacobian of the equation system at point $\vec{X}_k$:

$$\boldsymbol{J}^{i,j}\left[\vec{X}_k\right] = \frac{\partial \vec{F}^i\left[\vec{X}_k\right]}{\partial X_k^j} \tag{5.67}$$

Where $X_k^i$ is the i-th components of the vector $\vec{X}_k$. Setting the right-hand side of equation 5.66 to zero and solving for $\vec{X}_{k+1}$ yields to a strict newton method,

$$\vec{X}_{k+1} = -\boldsymbol{J}^{-1}\left[\vec{X}_k\right] \cdot F\left[\vec{X}_k\right] + X_k. \tag{5.68}$$

By doing so, $\vec{X}_{k+1}$ is an approximation of the solution of the equation system. Because it is only a first order approximation, the vector $\vec{X}_{k+1}$ can still be far from the solution, therefore, to get a good approximation of the solution, one need to iterate as much as needed. The iteration stop based on the required drop of the residual

$$\frac{\|F[\vec{X}_k]\|}{\|F[\vec{X}_0]\|} < \text{tol}_{\text{res}}, \tag{5.69}$$

or a sufficiently small Newton step

$$\frac{\|\delta\vec{X}_k\|}{\|\vec{X}_k\|} < \text{tol}_{\text{step}} \tag{5.70}$$

Where $\vec{X}_0$ is the solution initial guess used for the first Newton-Raphson iteration and $\delta\vec{X}_k$ being the step $\vec{X}_{k+1} - \vec{X}_k$.

The Newton-Raphson method, although simple in its theory, needs the calculation of the inverse of the system's Jacobian. The Jacobian can be non-trivial and computationally heavy. Consequently, it can be faster to use a *Jacobian-free* method. More specifically, we use a Jacobian Free Newton Krylov method (JFNK). In such methods, the Jacobian is not explicitly computed, only the dot product of the jacobian with a vector V. The dot product with a vector $\vec{V}$ at the point $\vec{X}_k$ is

$$\boldsymbol{J} \cdot \vec{V} = \frac{F[\vec{X}_k + \epsilon\vec{V}] - F[\vec{X}_k]}{\epsilon}. \tag{5.71}$$

Where the value $\epsilon$ is a value sufficiently small of order of the machine precision. By

rewriting equation 5.68 one have :

$$F\left[\vec{X}_k\right] + \boldsymbol{J}\left[\vec{X}_k\right] \cdot \delta\vec{X}_k = 0, \tag{5.72}$$

The advantage of this approach is that the convergence of the iterative method is Newton–like, but without storing and inverting the system's Jacobian. However, we end up with a new equation system to solve to compute the Newton step $\delta\vec{X}_k$.

To solve this equation we use the iterative method Generalised Minimal RESidual Algorithm (GMRES), a Krylov space method (Saad et al. 1986). Consequently, we have nested iterations to solve the system. The outer iteration method is the Newton-Raphson iteration and the inner iteration method is the GMRES algorithm to determine the Newton step by solving the equation 5.72.

The lack of convergence robustness of the Newton-Raphson method can lead to stagnation. There are two correction which can be applied to the GMRES algorithm and to the Newton steps, which are preconditioning and globalization respectively (Knoll et al. 2004). Globalization act on the newton step $\delta\vec{X}_k$ such that the step direction and magnitude follow the function gradient toward its global minimum. It exists numerous strategy to perform this globalization, in this study we performed globalization by simply applying a factor $\lambda$ to the step vector $\delta\vec{X}_k$ such that:

$$\vec{X}_{k+1} = \vec{X}_k + \lambda\delta\vec{X}_k \tag{5.73}$$

the residual $F[\vec{X}_{k+1}]$ is minimized (Knoll et al. 1993). The simplest method is to linearly search for a factor $\lambda$ such that :

$$\|F[\vec{X}_k + \lambda\delta\vec{X}_k]\| < \|F[\vec{X}_k]\|. \tag{5.74}$$

Where $\lambda$ is between a minimum value, a free parameter of the resolution method, and 1. However, by enforcing a strict decrease of the residual, the newton iteration cannot go out of a local minimum in the solution space. Therefore, one need a globalization method that allow the residual to go through local minimum to find the global minimum. Furthermore, the linear search does not prevent the apparition of negative values in the vector $\vec{X}_k$. Therefore, during the resolution of the thermal structure of the CPD, this method allows the apparition of non physic negative temperatures. Consequently, we use another strategy which limit the step size based on current state of $\vec{X}_k$:

$$\lambda = \mathrm{Min}\left(1; \mathrm{Min}_i\left(\frac{\beta X_k^i}{\delta X_k^i}\right)\right). \tag{5.75}$$

With this search parameter, the quantity $X_k^i$ is not allowed to change more than a fraction $\beta$ . Therefore, the closer to zero $X_k^i$ is, the smaller $\lambda$ is. Consequently, $X_k^i$ is never null.

# 6. Circumplanetary disk structure implication on its volatile composition and Trappist-1 protoplanetary disk

This chapter present the application of the CPD model to constrain its structure and composition, as well as implication to the analogous exoplanet system Trappist-1. We first present the characteristics of the model developed in the precedent chapter and effects of the shadow cast onto the CPD, the composition of the CPD using the volatile evolution method presented in chapter 5. Finally, using a simpler one-dimensional gas starved model, we present the hypothesis of the formation of the moons in a water ice and vapor depleted environment and its implication of the Trappist-1 system formation history.

## Table of Contents


6.1. Impact of self shadowing on the Thermal structure . . . . . 115
6.1.1. Model Setup . . . . . 115
6.1.2. Depletion timescale of the disk . . . . . 116
6.1.3. Thermal profile . . . . . 117
6.1.4. Effect of Jupiter's radiative heating . . . . . 121
6.1.5. Effect of CPD metallicity Variations . . . . . 124
6.1.6. Effect of accretion timescale Variations . . . . . 126
6.2. Condensation lines location . . . . . 128
6.3. volatile species evolution . . . . . 131
6.4. Delivery of phyllosilicates to a one-dimensional circumplanetary disk . 135
6.4.1. Gas starved CPD model . . . . . 135
6.4.2. Impact of phyllosilicate grains on the water radial distribution . 138
6.4.3. Putative Galilean moons formation sequence . . . . . 140
6.5. Application to the Trappist-1 System . . . . . 141
6.5.1. Trappist-1 planets characteristics . . . . . 141
6.5.2. Delivery of water to the Trappist-1 PPD . . . . . 143
6.5.3. Variation of phyllosilicate dehydration temperature . . . . . 149
6.5.4. Consequence on Trappist-1 planet formation locations . . . . . 152

Table 6.1.: Nominal model parameters

| Parameter | Value | References |
|---|---|---|
| $M_p$ | 0.95 $M_J$ | Mordasini (2013) |
| $R_p$ | 1.1 $R_J$ | Mordasini (2013) |
| $a_p$ | 5 AU | |
| $t_{initial}$ | $3 \times 10^4$ yr | |
| $t_{final}$ | $4 \times 10^5$ yr | |
| $X_d$ | $2.45 \times 10^{-2}$ | Lodders (2019) |
| $\chi$ | $10^{-1} - 10$ | |
| $k_s$ | 0.2 | Makalkin et al. (1995) |
| $\alpha$ | $10^{-3}$ | Lynden-Bell et al. (1974) |
| $T_{amb}$ | 40 K | Aguichine et al. (2020) |
| $\mu_g$ | $2.341 \times 10^{-3}$ | Lodders (2019) |
| $R_c$ | 50 $R_J$ | |

## 6.1. Impact of self shadowing on the Thermal structure

We present in this section the impact on CPD structure of the projected shadow onto the CPD.

### 6.1.1. Model Setup

Simulations were conducted spanning a time range from 30 kyr to 400 kyr following the formation of the CPD. We first present the results for the nominal case, where the CPD metallicity is set to 0.1 times the protosolar value. This subsolar metallicity factor is motivated by the observations from hydrodynamic models, which suggest that the gas feeding the CPD has a subsolar metal content Canup et al. (2002), Lambrechts et al. (2012), and Zhu et al. (2012). We then compare these results with cases of larger metallicities, 1 and 10 times the protosolar value, to explore scenarios where dust pileup occurs in the CPD, as proposed by Drążkowska et al. (2018) and Batygin et al. (2020).

We assume that Jupiter's formation occurred 1 Myr after the formation of calcium-aluminum-rich inclusions (CAIs) Mordasini (2013). In our study, we do not account for Jupiter's post-formation migration and keep the planet at its present-day distance of 5 AU from the Sun. Finally, we set the minimum temperature of the CPD to 40 K, which corresponds to the surrounding PPD temperature after 1 Myr following CAI formation, according to Aguichine et al. (2020). Detailed specifications of all model parameters are provided in Table 6.1.

### 6.1.2. Depletion timescale of the disk

Figure 6.1 illustrates the temporal evolution of both the CPD mass and Jupiter's accretion rate over a time span of 30 kyr to 400 kyr following the formation of the CPD. The figure vividly portrays the rapid depletion of the CPD, with the accretion rate ranging from $8.4 \times 10^{-7}$ $M_J.yr^{-1}$ to $1.3 \times 10^{-16}$ $M_J.yr^{-1}$, encompassing a remarkable nine orders of magnitude. Concurrently, the CPD mass undergoes a dramatic reduction from an initial value of $1.26 \times 10^{-4}$ $M_J$ to a final value of $6.46 \times 10^{-11}$ $M_J$, spanning seven orders of magnitude.

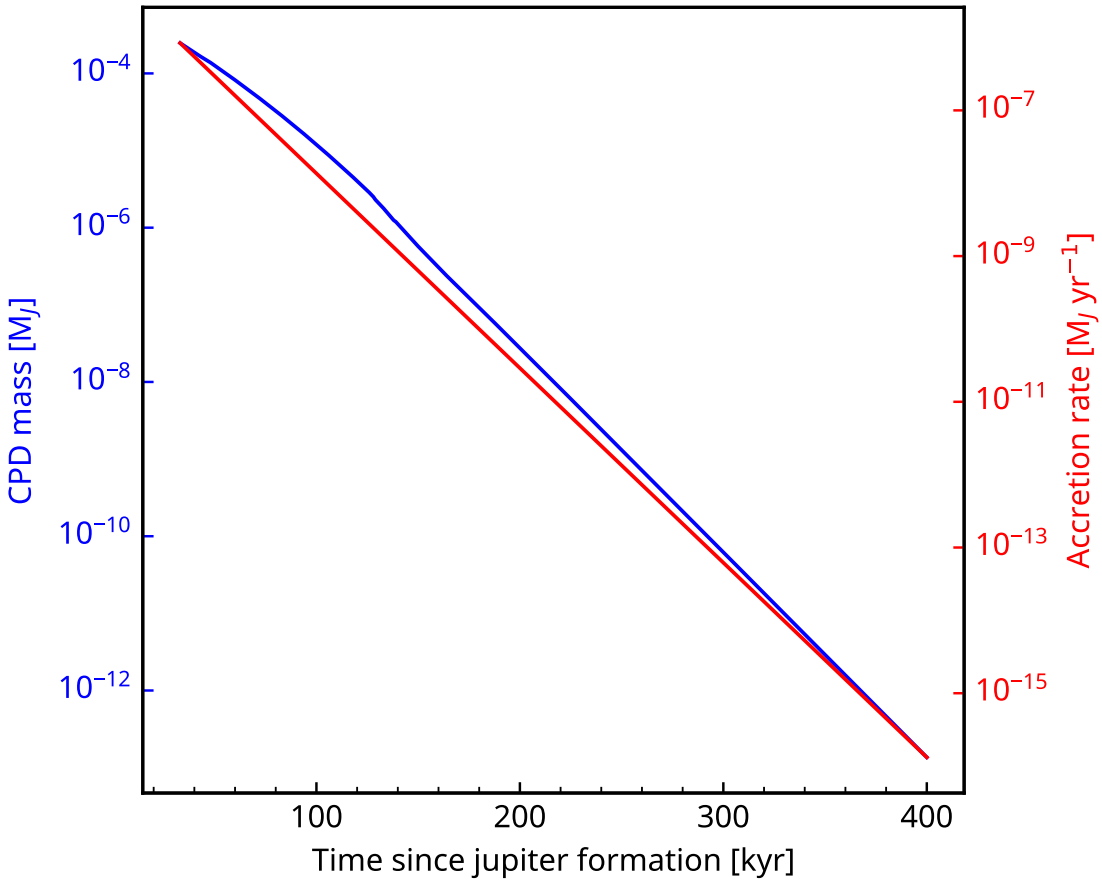


Figure 6.1.: CPD mass (blue curve) and accretion rate (red curve) evolution from 30 kyr to 400 kyr after the formation of the CPD.

Timescale of CPD depletion has an impact on the amount of solid the CPD accrete. As we start the evolution of the CPD when Jupiter reached 95% of its final mass. In both the rapid and the slow depleting CPD cases, the disk mass is at most $10^{-4}$ $M_J$, accounting for solid and gas, which is about half the mass of the Galilean system. Therefore, in the model there is not enough mass at a given time to form the moon, regardless of the dust-to-gas ratio.

However, the cumulative mass of accreted material, including both gas and dust, throughout a simulation period of 400 kyr, amounts to $1.5 \times 10^{-2}$ $M_J$, a much higher

value than the total mass of the four Galilean moons ($\sim 2.07 \times 10^{-4}\ M_J$). Consequently, if it is assumed that the solid material required for the formation of the moons originates from the accreted material, a dust-to-gas ratio exceeding $1.4 \times 10^{-2}$ is necessary for the accumulation of sufficient solid material onto the CPD in order to enable the formation of the Galilean moons, based on the premise of a short-lived CPD. Under this assumption, the accreted gas would present at minimum a protosolar metallicity. However, this finding contradicts outcomes from three-dimensional hydrodynamic simulations that trace the destiny of dust and grains in the vicinity of Jupiter's formation. These models reveal a significant depletion of grain and dust material, reduced by a factor of 100 compared to the PPD Lambrechts et al. (2012) and Zhu et al. (2012). Implementing this depletion factor into our model suggests that only $1.4 \times 10^{-4}\ M_J$ of dust and grains would be assimilated by the CPD, over the course of the simulation. It would then prevent the formation of the moons over a decent timescale. In contrast, alternative three-dimensional hydrodynamic simulations suggest that meridional circulation effectively transports dust from the midplane of the PPD to the CPD Szulágyi et al. (2022). This mechanism results in the accreted material displaying a dust-to-gas ratio exceeding that of the PPD. In light of these conditions, there would be ample material available for the formation of the Galilean moons.

### 6.1.3. Thermal profile

Figure 3.1 presents the surface density, midplane temperature, and midplane pressure profiles of the CPD at 33, 50, 100, 150, and 200 kyr after CPD formation. It showcases the rapid depletion of the CPD, with the surface density diminishing from a range between $1.3 \times 10^3$ and $10^2$ g.cm$^{-2}$ 33 kyr, to a range between $2 \times 10^{-1}$ and $3.6 \times 10^{-4}$ g.cm$^{-2}$ 200 kyr, after Jupiter's formation. Concurrently, the CPD's temperature experiences a decline from a peak of 2270 K at 33 kyr to approximately 440 K at 200 kyr. Consequently, over the same time span, the midplane pressure diminishes by a factor of $10^4$, consistent with the rapid CPD depletion depicted in Figure 6.1.

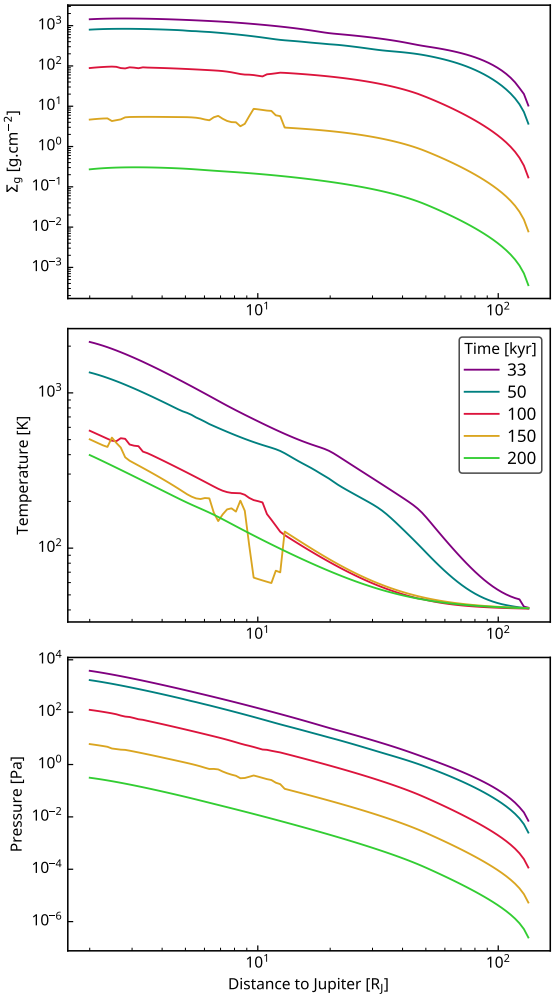


Figure 6.2.: From top to bottom: CPD's surface density, midplane temperature and midplane pressure profiles, represented at $t$ = 33, 50, 100, 150 and 200 kyr of the CPD evolution.

Before 100 kyr, the primary sources of heating in the CPD are the viscous and accretion processes. However, following 100 kyr, as a result of the rapid depletion of the CPD, radiative heating from Jupiter's hot surface becomes predominant. This transition is explored in Sec. 5.2.3, where the dependence of the disk's heating on the slope of the photosurface, due to Jupiter's illumination, is emphasized. Figure 3.1 further illustrates that beyond 100 kyr, the temperature distribution does not exhibit a monotonic decrease with distance from Jupiter. At around 150 kyr post-Jupiter's formation, a narrow region centered around 2.5 $R_J$ exhibits a temperature 50 K higher than its surroundings, persisting for approximately 10 kyr. Conversely, a region between 9 and 15 $R_J$appears to be 100 K colder than its surroundings, lasting for about 60 kyr, spanning from 100 kyr to 160 kyr after the CPD's formation.

Figure 6.3 provides a visual representation of the two-dimensional temperature and pressure profiles of the CPD at $t$ = 50, 100, 150, and 200 kyr of its evolution. At

100 kyr of CPD evolution, the temperature difference between the photosurface and the midplane remains small, typically within 1 K. This suggests that the disk is nearly vertically isothermal, emphasizing the dominance of Jupiter's radiative heating at the photosurface altitude over viscous and accretion heating mechanisms. At 150 kyr of CPD evolution, an optically thin region forms in the inner part of the CPD, specifically in regions closer than 3 $R_J$. In these regions, where the temperature exceeds 700 K, the partial evaporation of the most abundant dust components, such as Mg-silicates and iron, leads to a sudden drop in opacity from the experimental data used in our model. This phenomenon induces a decrease in the photosurface altitude at the evaporation front, eventually causing the photosurface to vanish in the inner part of the disk when the density reaches sufficiently low levels. The photosurface has entirely vanished after 200 kyr of CPD evolution, resulting in the partial absorption of Jupiter's radiation. Consequently, in the absence of shadows causing cold regions or flaring inducing hot regions, the temperature profile exhibits a monotonic decrease with distance from Jupiter.

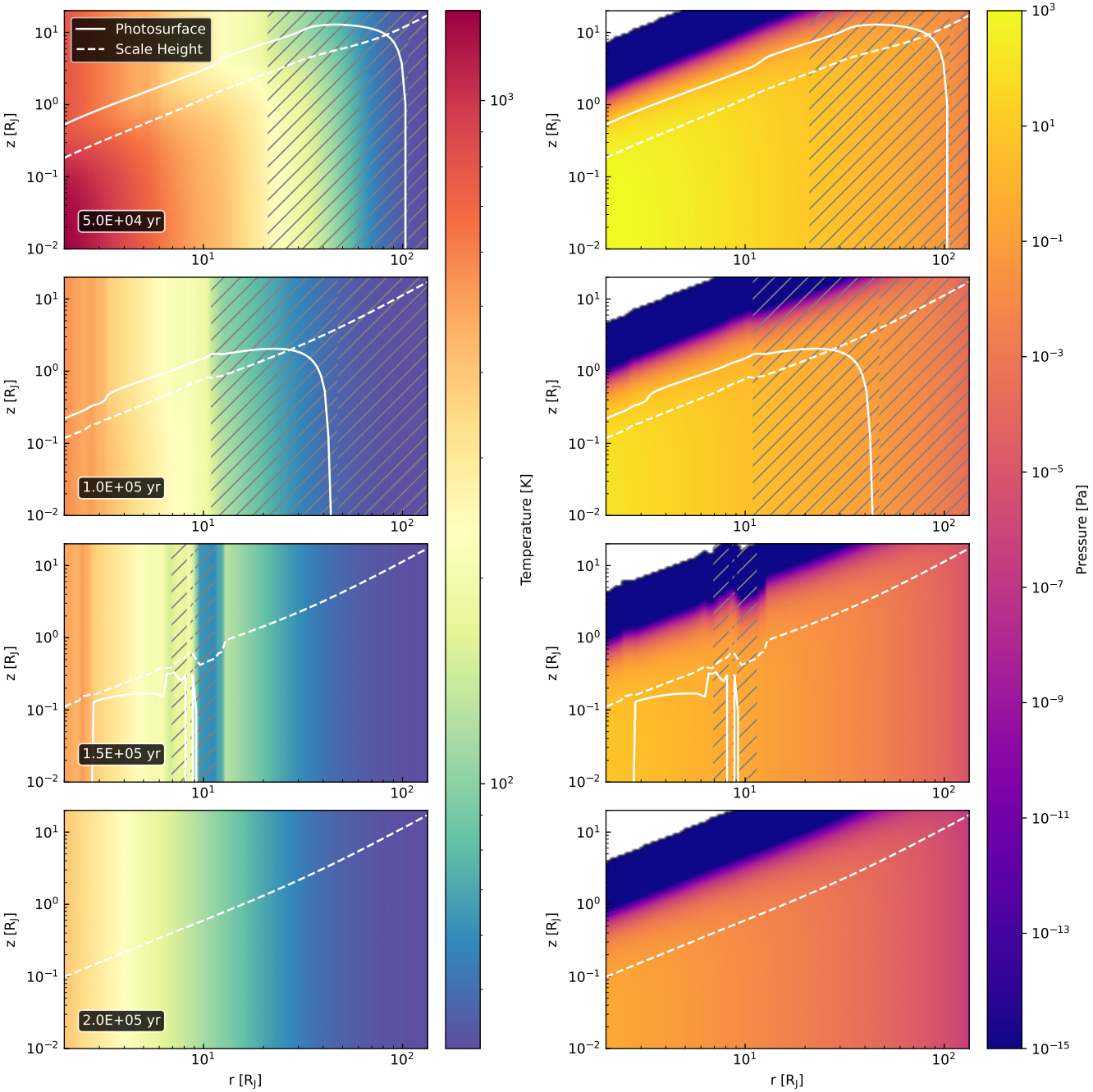


Figure 6.3.: Temperature (left panels) and pressure (right panels) profiles of the CPD at $t$ = 50, 100, 150, and 200 kyr of the CPD evolution. The photosurface and the CPD's scale height are presented by the white plain and dashed lines, respectively. . If the photosurface is not explicitly shown or represented in a given panel, it indicates its absence. The hatched area is located within the shadow cast by the CPD.

### 6.1.4. Effect of Jupiter's radiative heating

To assert the effect of Jupiter's radiation on the thermal, we compare the presented results with a simulation where Jupiter's radiation is disabled, hereafter refereed as the *cold model*. Figure 6.4 show the two-dimensional temperature and pressure profiles of the CPD model after 80, 100, 150 and 200 kyr of CPD evolution. It shows that the optically thick region exist for a longer period than in the model accounting for Jupiter's radiative heating, hereafter refereed as the *hot model*.

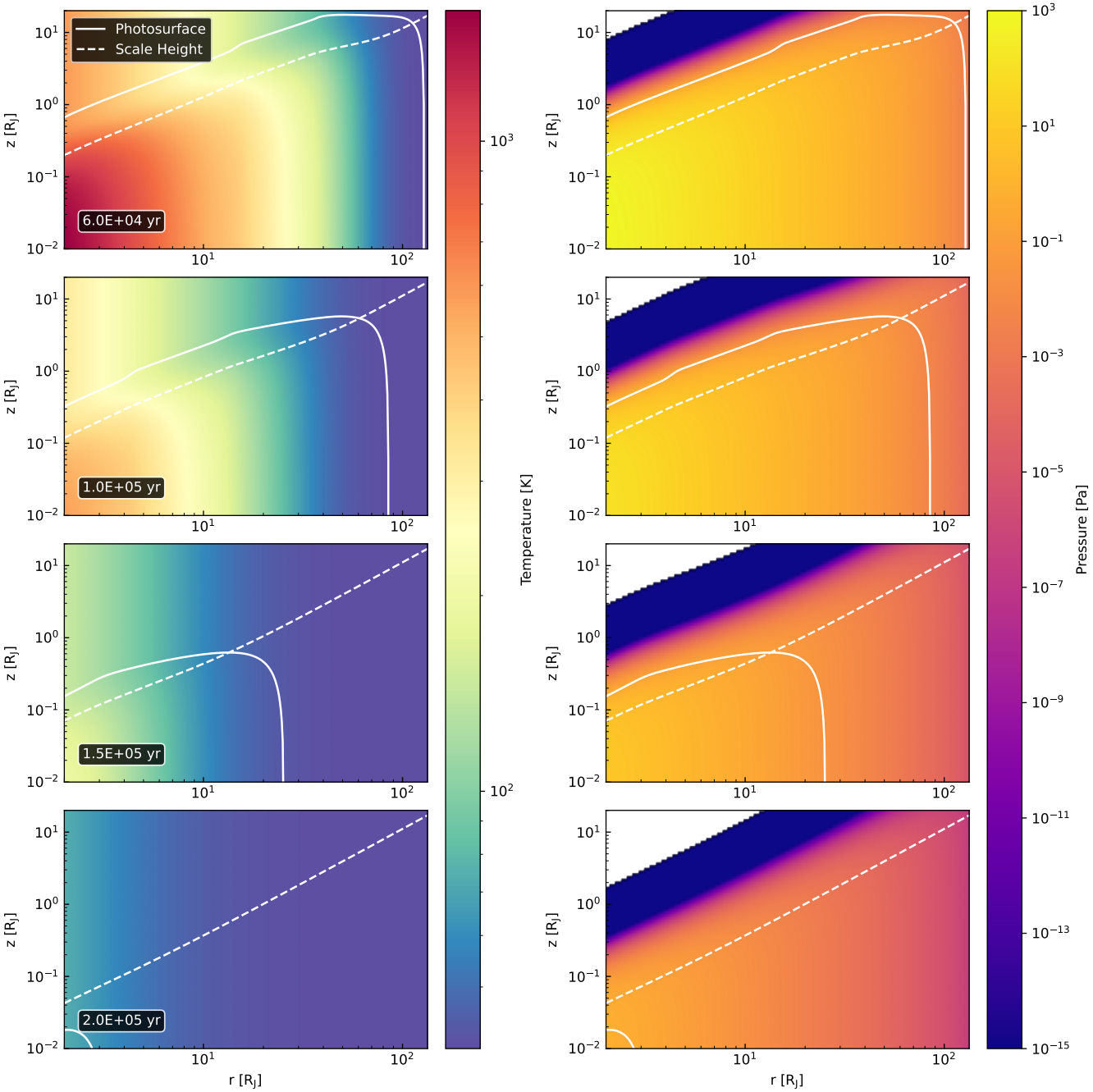


Figure 6.4.: Temperature (left panels) and pressure (right panels) profiles of the CPD model where Jupiter's radiative heating is deactivated, at $t$ = 80, 100, 150, and 200 kyr of the CPD evolution. The photosurface and the CPD's scale height are presented by the white plain and dashed lines, respectively. If the photosurface is not explicitly shown or represented in a given panel, it indicates its absence.

Figure 6.5 shows the comparison of the CPD surface temperature, midplane temperature, and midplane pressure profiles between the hot model and the cold model. It

shows that at epochs earlier than 100 kyr, the cold model is hotter and denser than the hot model at distances closer than 14 $R_J$to Jupiter. Where the cold model is up to 90 K hotter than the hot model. Conversely, at distances larger than 14 $R_J$the hot model is hotter up to 30 K than the cold model. At epochs after 100 kyr the hot model is hotter at all distances than the cold mode, excepted in the shadowed region of the hot model where it is colder by 4 K than the cold model. However, it still exists an inner region denser in the cold model than in the cold model at distances closer than 24 $R_J$.

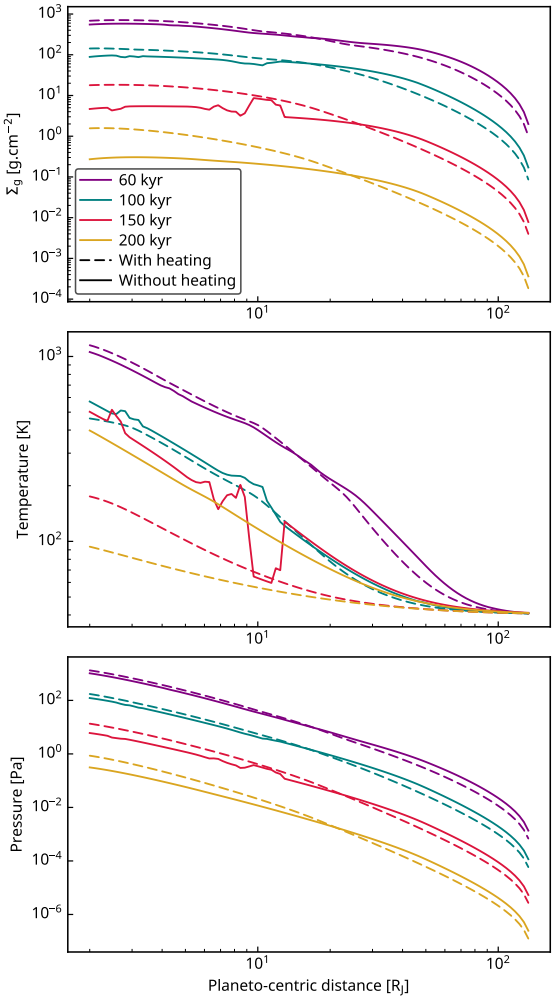


Figure 6.5.: Evolution of the CPD surface density (top panel), midplane temperature (central panel), and midplane pressure (bottom panel) when the CPD is subjected to Jupiter's irradiation (plain lines) and not subjected to Jupiter's irradiation (dashed lines). The evolution is presented at 60, 100, 150, and 200 kyr after CPD formation

The existence of an inner region where the cold model is denser than the hot model can be explained by the temperature of the upper layer of the CPD, which is heated by Jupiter's irradiation in the hot model. Figure 6.6 depicts the gas density and

temperature at the photosurface level of both the hot and cold models. It shows that the surface temperature of the hot model is consistently higher than that of the cold model, except in the shadowed area at $t$ = 150 kyr. The gas density follows a more complex trend. Before 150 kyr, the gas densities of the hot and cold models differ by a factor of 2 at most. However, after 150 kyr, within distances closer than 24 $R_J$, the photosurface of the cold model becomes up to ten times denser than that of the hot model. This indicates that due to Jupiter's heating, which becomes the dominant heat source in the CPD after 150 kyr, the upper layers of the CPD in the hot model are less dense. Consequently, the total surface density diminishes due to the heating.

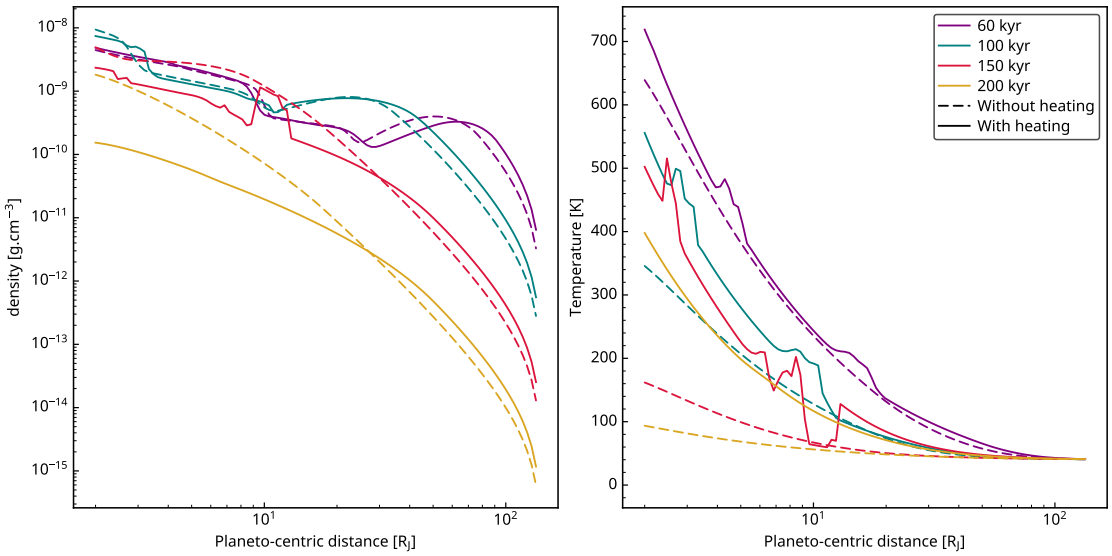


Figure 6.6.: CPD photosurface density (left panel) and photosurface temperature (right panel) in the hot model (plain line) and the cold model (dashed line) after 60, 100, 150 and 200 kyr of CPD evolution.

Therefore, Jupiter's radiative heating impacts the upper layer density once its heating becomes dominant. Radiative heating increases the CPD scale height, thereby reducing the photosurface density and, consequently, the overall surface density.

### 6.1.5. Effect of CPD metallicity Variations

Figure 6.7 represents three snapshots of the CPD at $t$ = 100, 150, and 200 kyr of its evolution. The three simulations represented in the figure differ in their metallicity enrichment levels, corresponding to 0.1, 1, and 10 times the protosolar metallicity ($Z/H = 2.45 \times 10^{-2}$; Lodders (2019)). The figure demonstrates that an increase in metallicity corresponds to higher opacity within the CPD, consequently leading to an enlarged adiabatic zone relative to cases with lower metallicity levels. In the nominal simulation, with a metallicity 0.1 times protosolar, the adiabatic–isothermal transition zone is located at 46.5 $R_J$ and 12.9 $R_J$ after 100 and 150 kyr of CPD evolution, respectively. However, this transition disappears after 200 kyr. For simulations with

protosolar metallicity, the adiabatic–isothermal transition occurs at distances of 88.2 $R_J$ and 34.5 $R_J$ after 100 and 150 kyr of CPD evolution, respectively. In the scenario where the CPD exhibits a metallicity ten times higher than the protosolar value, this transition is observed at distances of 127.7 $R_J$, 71.9 $R_J$, and 25.2 $R_J$ after 100, 150, and 200 kyr of CPD evolution, respectively. Furthermore, the adiabatic zone vanishes after 161 kyr, 197 kyr and 230 kyr following the CPD formation, for a metallicity of 0.1, 1 and 10 times the protosolar value respectively.

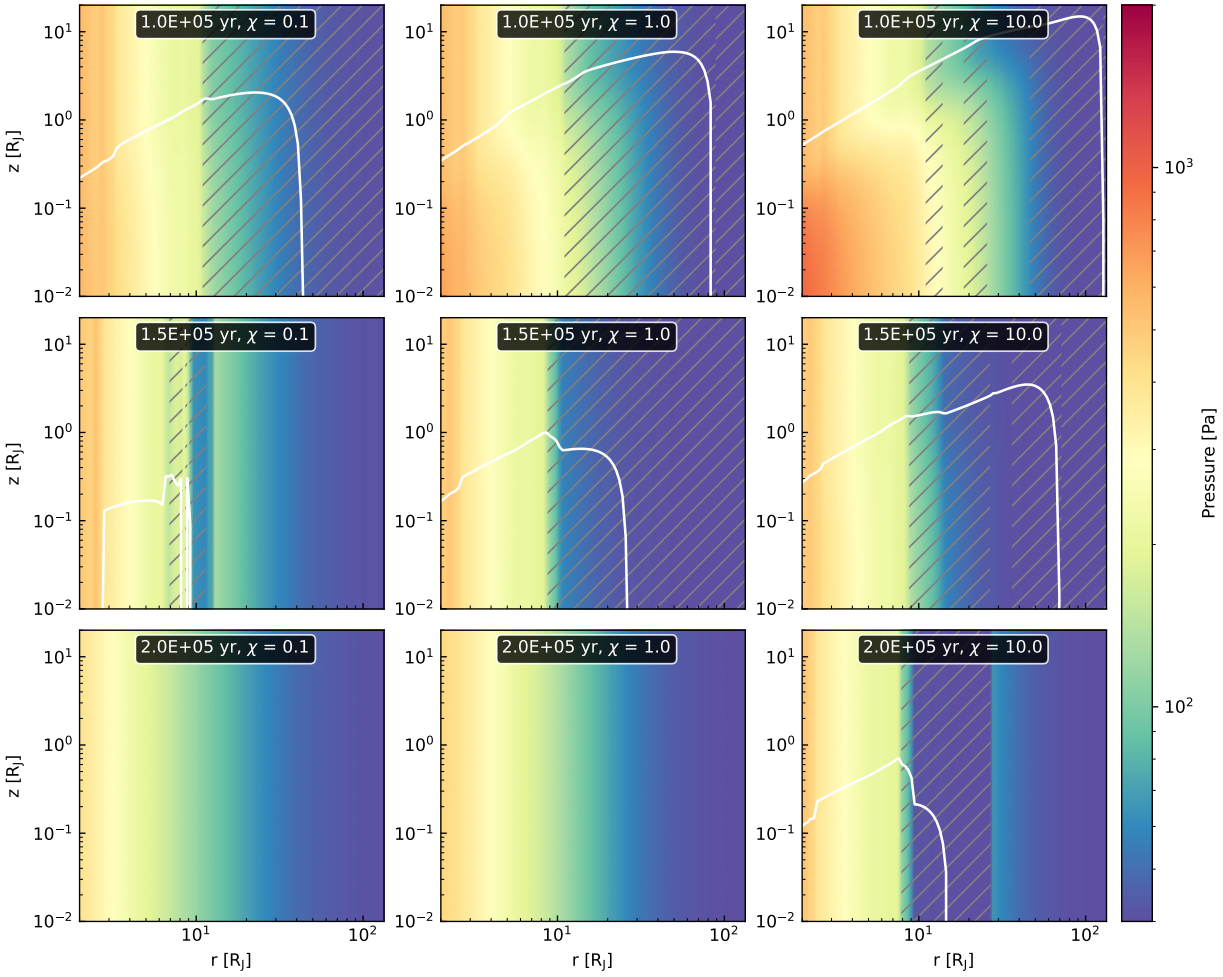


Figure 6.7.: CPD temperature profiles with dust enrichment levels (from left to right columns) corresponding to 0.1, 1, and 10 times the protosolar value, depicted at $t$ = 100, 150, and 200 kyr of the CPD evolution (from top to bottom rows). The solid white line represents the altitude of the photosurface. If the photosurface is not explicitly shown or represented in a given panel, it indicates its absence. The hatched areas are located within the shadow cast by the CPD.

The increased opacity leads to two primary consequences. First, it results in an elevated photosurface altitude, allowing it to cast shadows further into the CPD. For

instance, after 150 kyr of CPD evolution, a shadow extends from 9 to 15 $R_J$ in the nominal simulation, with a metallicity 0.1 times the protosolar value, disappearing after 161 kyr of CPD evolution. In contrast, for one and tenfold enrichments, shadows extend from 10 to 133 $R_J$ and from 9.2$R_J$ to 133 $R_J$, respectively, after 150 kyr of CPD evolution. In the scenario with a tenfold enrichment in metallicity, the photosurface exhibits a remarkably prolonged existence compared to the other cases. It casts a shadow from 9.5 $R_J$ to the outer edge of the disk until 196 kyr of CPD evolution, persisting until it ultimately dissipates after 230 kyr. Second, the augmented opacity results in a substantial escalation of temperatures. After 100 kyr of CPD evolution, the maximum midplane temperatures attain values of 700, 720, and 1009 K for simulations with metallicity enrichments of 0.1, 1, and 10 times the protosolar value, respectively.

### 6.1.6. Effect of accretion timescale Variations

The accretion rate decay timescale used in our model is significantly shorter than the one typically used in most CPD models Lunine et al. (1982), Canup et al. (2002), Mousis (2002), Mousis et al. (2004), Sasaki et al. (2010), Anderson et al. (2021), and Mousis et al. (2023). Several alternative models Anderson et al. (2021) and Mousis et al. (2023) are based on the hypothesis presented in Sasaki et al. (2010) that the CPD dissipation timescale is equivalent to the protoplanetary disk dissipation timescale. To account for this major difference, we conducted tests using a slower accretion decay rate, specifically employing a CPD depletion timescale of 1 Myr as proposed by Sasaki et al. (2010). The time evolution of the accretion rate is given by:

$$\dot{M}(t) = \dot{M}_0 \exp\left\{\left(\frac{-t}{10^6 \mathrm{yr}}\right)\right\} \tag{6.1}$$

With $\dot{M}_0 = 5 \times 10^{-7}\ M_J\ \mathrm{yr}^{-1}$ the accretion rate at initialization.

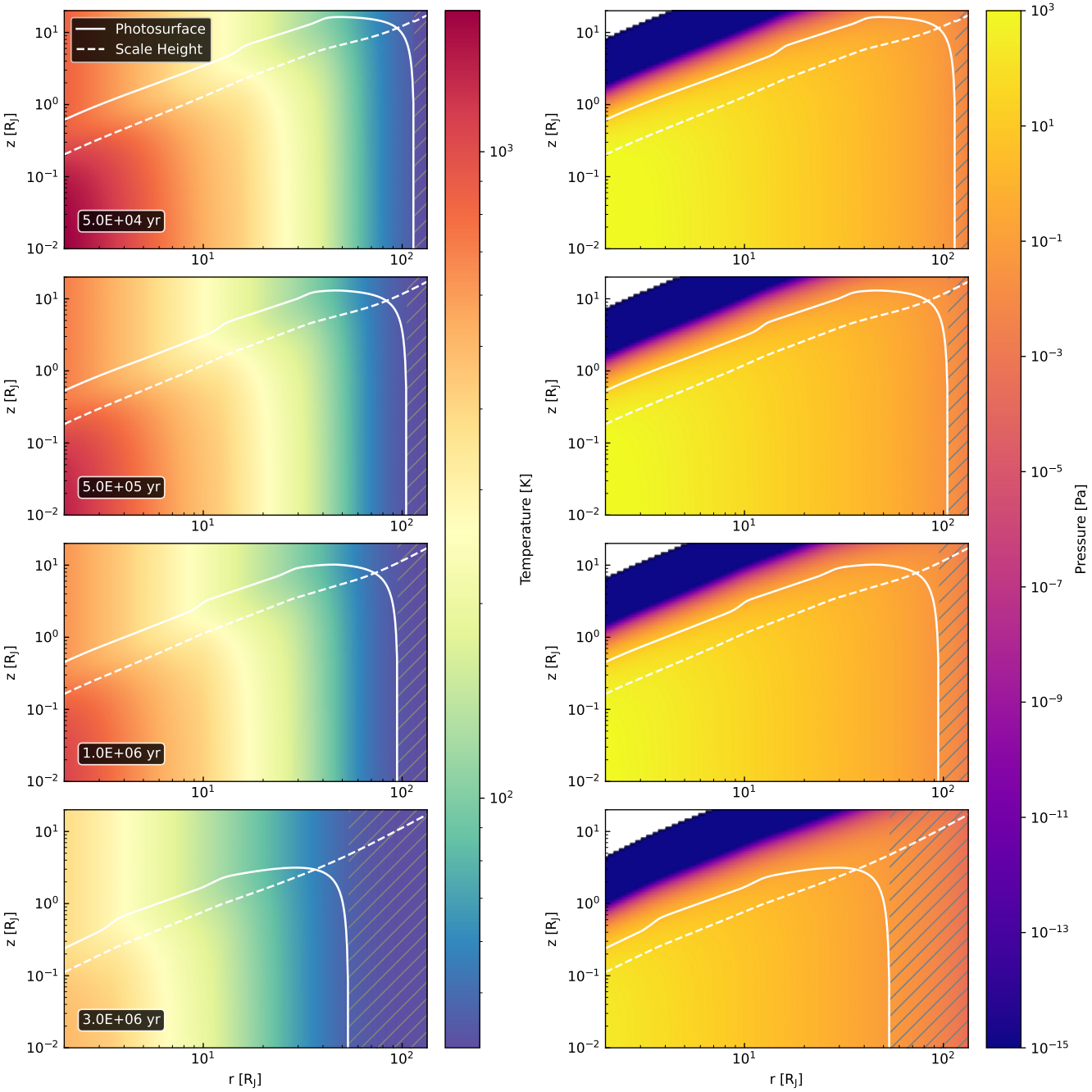


Figure 6.8.: Temperature and pressure profiles within the CPD after $t$ = 50, 500, 1000, and 3000 kyr of evolution, using the accretion rate prescription from Sasaki et al. (2010), and a metallicity 0.1 times the protosolar one. The photosurface and the CPD's scale height are represented by the white plain and dashed lines, respectively. The hatched area is located within the shadow cast by the CPD.

Figure 6.8 illustrates the temperature (left panels) and pressure (right panels) profiles at various time intervals (50, 500, 1000, and 3000 kyr) during the CPD evolution, with

a metallicity 0.1 times the protosolar one. It demonstrates the slow depletion of the CPD over a period of 3000 kyr. Consequently, the CPD remains hotter after 3000 kyr of its evolution than the nominal case described in Section **??** after 200 kyr. This highlights the significant dependence of our results on the accretion rate evolution. Since accretion and viscous heating dominate over the planet's heating, the shadowed areas (hatched areas) do not exhibit significant temperature drops. Therefore, the consequences of CPD self-shadowing presented in Section **??** only exist for a rapidly decreasing accretion rate after Jupiter's formation.

## 6.2. Condensation lines location

Furthermore, the launch of the James Webb Space Telescope (JWST) has enabled extensive observations and studies of the surface composition of the Galilean moons. The most notable observation so far is the putative detection of $CO_2$ ice on Europa's surface, which is believed to originate from the internal oceans of the moons Trumbo et al. (2023).

Our model can be used to trace the evolution of volatile species within the CPD. We examine the positions of the condensation lines for a large set of volatile species $H_2O$, CO, $CO_2$, $CH_4$, $H_2S$, $N_2$, $NH_3$, Ar, Kr, Xe, and $PH_3$. Out of the eleven volatile species examined, only five ($H_2O$, $NH_3$, $CO_2$, $H_2S$, and $PH_3$) have condensation temperatures higher than the minimum temperature of 40 K in our CPD model. Figure 6.9 shows the positions of the condensation lines for these four volatile species at 40, 150, and 200 kyr of the CPD evolution. The black dashed lines in the figure represent the condensation lines for the various volatile species within the CPD. At 40 kyr after the formation of the CPD, the disk is still hot and massive, leading to the condensation lines being located far from Jupiter. In the disk midplane, the condensation lines are positioned at 34.5 $R_J$, 58.2 $R_J$, 64.4 $R_J$, 70.2 $R_J$, and 91.2 $R_J$for $H_2O$, $NH_3$, $CO_2$, $H_2S$ and $PH_3$ respectively. In contrast, at 200 kyr, when the CPD has become much colder, the condensation lines have moved significantly inward, to 5.2 $R_J$, 14.6 $R_J$, 18.6 $R_J$, 23.3 $R_J$and 44.2 $R_J$for $H_2O$, $NH_3$, $CO_2$, $H_2S$ and $PH_3$ respectively. Between these two extremes, disk self-shadowing comes into play, and produces a cold area centered around 10 $R_J$. At 150 kyr of CPD evolution, this shadowed region acts as a cold trap for the volatile species. Within the 9 $R_J$ to 12 $R_J$ range, $H_2O$, $NH_3$, $CO_2$, and $H_2S$ can form ices at distances closer than their respective condensation lines, which are located at 18 $R_J$, 21.5 $R_J$, and 25.5 $R_J$ for $NH_3$, $CO_2$, and $H_2S$, respectively. This cold trap exists at epochs between 127 and 160 kyr after the CPD formation, and could have consequences on the composition of the grains within the disk.

The analysis of the volatile condensation lines within the CPD suggests that disk self-shadowing could play a key role in understanding the early icy grain composition and, consequently, the composition of the building blocks of the Galilean moons. While this analysis is qualitative rather than quantitative, it demonstrates that the cold trap created by the self-shadowed region of the disk could lead to the formation of ices for various volatile species, such as $H_2O$, $NH_3$, $CO_2$, and $H_2S$, at distances

closer to Jupiter than their respective condensation lines. This effect on the icy grain composition within the disk could be significant, as the volatile species would be able to condense and accrete onto the grains at closer distances to the planet. This, in turn, could influence the overall composition of the material that eventually forms the Galilean moons.

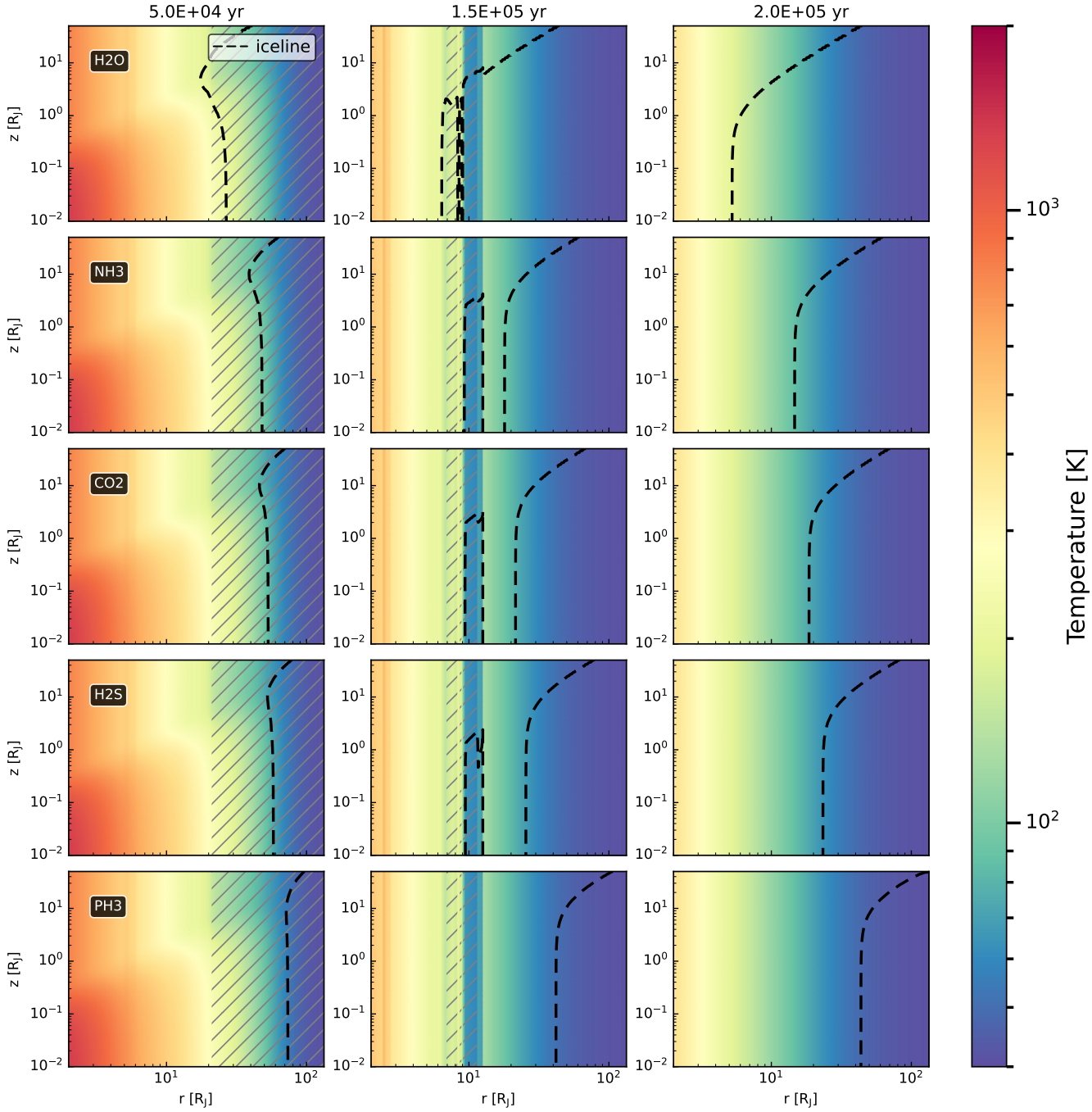


Figure 6.9.: From top to bottom: shapes of the $H_2O$, $NH_3$, $CO_2$, $H_2S$ and $PH_3$ condensation lines (black dashed lines) at $t$ = 50, 150 and 200 kyr of the CPD evolution. The hatched areas are located within the shadow cast by the CPD. We use the nominal model depicted in table 6.1, with a metallicity 0.1 times protosolar.

## 6.3. volatile species evolution

We transpose the volatile evolution model used in the PPD to study the volatile composition of the CPD. The working principle of the model is the same as for chapter 3. A new source therm is added to the advection-diffusion equation 3.13:

$$\frac{\partial \Sigma_i}{\partial t} + \frac{1}{r}\frac{\partial}{\partial r}\left[r\left(\Sigma_i v_i - D_i \Sigma_g \frac{\partial}{\partial r}\left(\frac{\Sigma_i}{\Sigma_g}\right)\right)\right] - \dot{Q}_i - \dot{Q}_{acc} = 0, \tag{6.2}$$

where $\dot{Q}_{acc}$ is the quantity of species $i$ incorporated to the CPD by accretion from the PPD. The accreted material is assumed to have a protosolar composition:

$$\dot{Q}_{acc}(r) = x_i \dot{F}(r) \tag{6.3}$$

with the accretion flux being :

$$\dot{F}(r) = \begin{cases} \frac{\dot{M}}{2\pi r} \text{ if } r > R_c \\ 0 \text{ if } r > R_c \end{cases} \tag{6.4}$$

We use the initial abundances presented in table 4.2

We show preliminary results of this study, which is still ongoing. We show volatile distribution in CPD models without the formation of shadows in the CPD, because of numerical instabilities that develop on the edge of the shadowed area. Therefore, to cover end-member scenarios, we first show the volatile evolution, assuming the slowly depleting and hot CPD presented from section 6.1.6 in figure 6.10. It assumes the accretion rate from Sasaki et al. (2010) described in Eq. 6.1. Secondly, we present the volatile distribution in the cold cpd model discussed in section 6.1.4, assuming a cold Jupiter, in figure 6.11.

Figure 6.10 shows the abundance profile of volatile species, considering only pure condensate and vapor phases, after 51, 100, 150 and 190 kyr of evolution. Because the CPD minimum temperature of the nominal model is set to 40 K, only species with condensation temperature higher than 40 K can condense, namely $H_2O$, $CO_2$, $NH_3$, $H_2S$ and $PH_3$. The centrifugal radius is set to 50 $R_J$, at a distance closer than the condensation lines of all the condensing species except for $H_2O$. Therefore, following equation 6.4 the delivered ices of $CO_2$, $NH_3$, $H_2S$ and $PH_3$, vaporize. Consequently, the pure condensate phase of those species is not replenished with incoming material, combined as the inward drift of the dust and pebbles result in the depletion of the pure condensate phase at distances larger than the condensation line.

After 51 kyr of CPD evolution, it shows that, because of a rapid inward drift of the pebbles and a rapid viscous diffusion of the vapor within the CPD, the water ice enrichment peak at its condensation line hardly goes over unity, with a pure condensate enrichment of 1.33 times the initial abundance at 31 $R_J$from the planet. Because the pure condensate phase of the other presented species are not replenished, their pure condensate enrichment are below unity, with values of 0.25, 0.67, 0.38 and 0.38 for $CO_2$, $NH_3$, $H_2S$ and $PH_3$, respectively.

With time, the situation worsens, the volatile species with their condensation lines further than the centrifugal radius deplete and become negligible, while the water abundance remain almost constant. The quasi observed steady states over 140 kyr comes from the slowly evolving CPD, which depletion timescale is 3 Myr.

This model would suggest that Io, which contain no water, could have formed inner to 31 $R_J$, the water condensation line, while the water rich Europa, Ganymede, and Callisto should have formed further. Furthermore, the formed moons should have a very low volatile content.

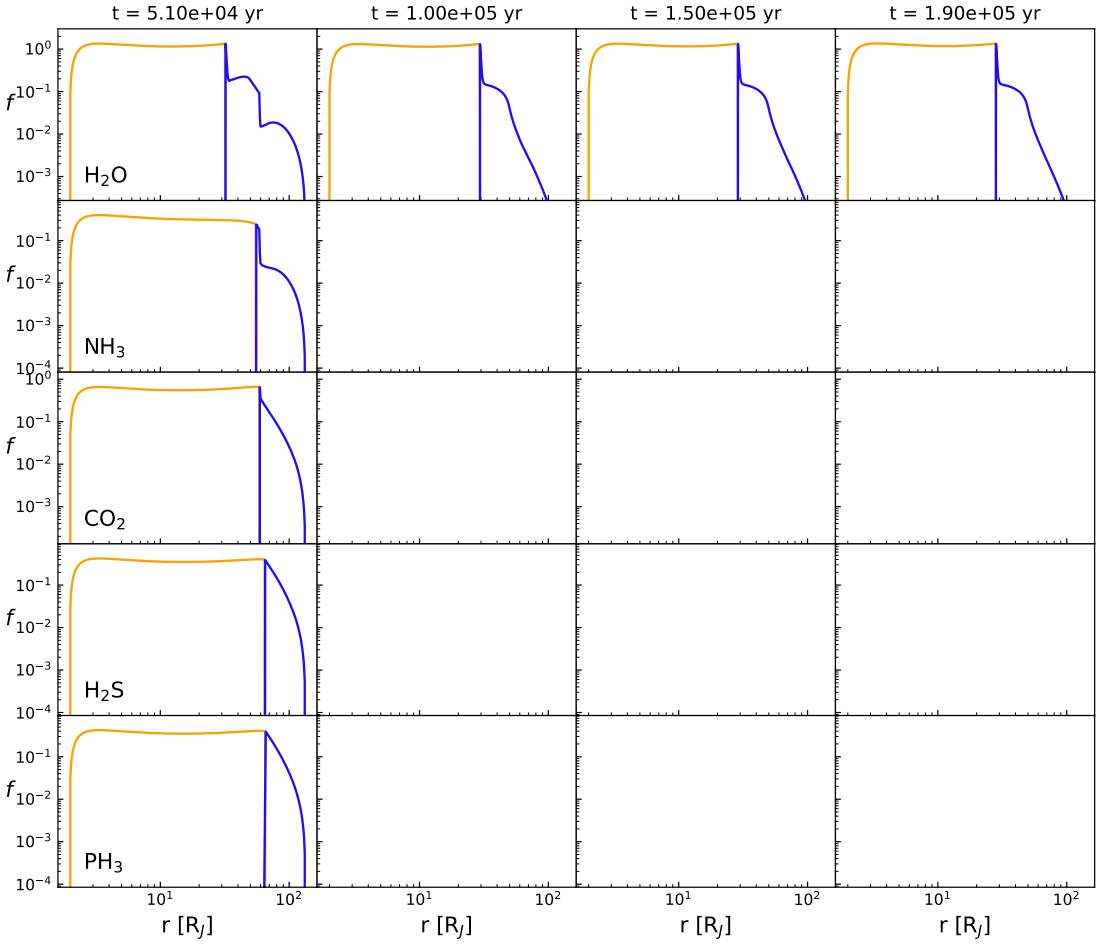


Figure 6.10.: Radial profiles of the condensing volatile species, from top to bottom, $H_2O$, $CO_2$, $NH_3$, $H_2S$ and $PH_3$, abundances within the CPD expressed as function of the initial protosolar abundance. Vapor (orange) and Ice (blue) radial profile are represented after 51, 100, 150 and 190 kyr of CPD evolution, from left to right column. The underlying CPD model uses the slowly decreasing accretion rate of Sasaki et al. (2010).

The second extreme member scenario, without Jupiter's heating and the rapidly decreasing accretion rate of Mordasini (2013), is presented in figure 6.11. Contrarily

to the hot and massive model presented above, it shows that the volatile species condensation lines are closer than the centrifugal radius to Jupiter, therefore species' pure condensate phases are replenished, avoiding large depletion of $CO_2$, $H_2S$, $NH_3$ and $PH_3$.

Although the pure condensate phase is replenished, species' abundances depletes over times. Starting from 1.2, 0.37, 0.94, 0.44 and 0.41 times the initial abundances after 51 kyr of evolution for $H_2O$, $CO_2$, $NH_3$, $H_2S$ and $PH_3$, respectively, down to 0.2, $1.2 \times 10^{-3}$, $1.1 \times 10^{-3}$ and $5.2 \times 10^{-3}$ times the initial abundances. This depletion is the result of the rapid decrease of the CPD accretion rates, and consequently, the rapid decrease of the accretion of volatile species. Combined to the rapid pebbles' inward drift and vapor viscous diffusion, the volatile species abundance depleted over the CPD lifetime.

Because the CPD is not heated by Jupiter, the condensation lines become very close to the planet, even closer than the inner boundary of our computational grid, located at 2 $R_J$, in the cases of $H_2O$, $CO_2$ and $NH_3$. Therefore, in such a case, the CPD composition is dominated by species' pure condensates. As a consequence, the resulting Galilean moons could be rich in volatile species. In such a case, Io can not form dry, it has to be water rich at its formation. Therefore, according to this model, Io should have lost its hydrosphere after its formation.

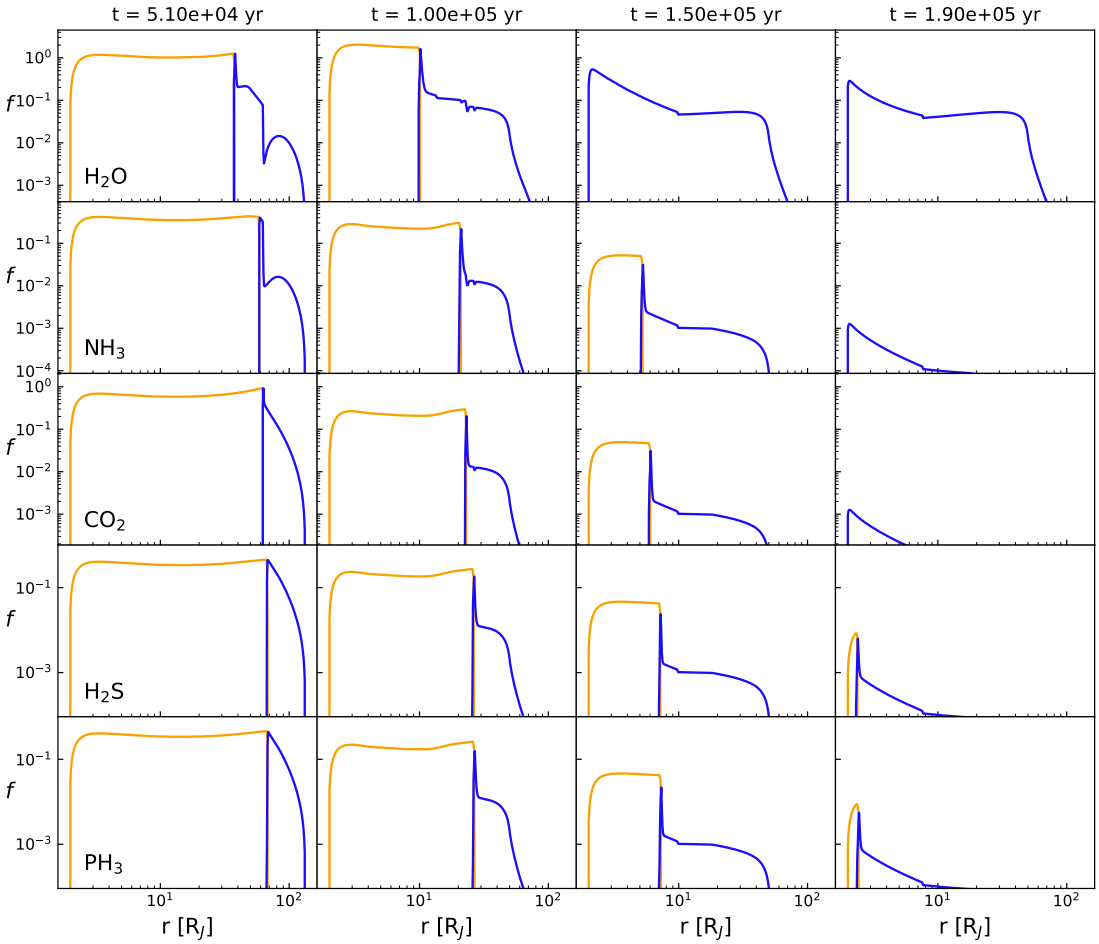


Figure 6.11.: Radial profiles of the condensing volatile species, from top to bottom,$H_2O$, $CO_2$, $NH_3$, $H_2S$ and $PH_3$, abundances within the CPD expressed as function of the initial protosolar abundance. Vapor (orange) and Ice (blue) radial profile are represented after 51, 100, 150 and 190 kyr of CPD evolution, from left to right column. The underlying CPD model uses the cold model, without Jupiter's heating, described in section 6.1.4

Both extreme members cases show radically different outcomes, showing the dependence on the accretion rate evolution and Jupiter's surface temperature of the CPD volatile content. Consequently, it shows that CPD properties greatly influence the composition of the solids within the disk, which must be imprinted in the moons' bulk composition.

## 6.4. Delivery of phyllosilicates to a one-dimensional circumplanetary disk

Here, we present a model to test the effect of phyllosilicate delivery to the CPD on the radial distribution of water in the CPD. The Juno measurements do not rule out the possibility of a low oxygen abundance in Jupiter's atmosphere, which may be as low as 0 at the 2–$\sigma$ confidence level (Li et al. 2020). In the hypothesis of high oxygen depletion in Jupiter's atmosphere, this would indicate that Jupiter and its subsequent CPD would not have accreted solids that were no more water-rich than carbonaceous chondrites. This hypothesis would be supported by the work of Melwani Daswani et al. (2021), who suggests that Europa's ocean could have been formed by the devolatilization of carbonates and phyllosilicates. Europa would have been hot enough, as it is likely to have an iron core (Anderson et al. 1998; Schubert et al. 2009), indicating that temperatures within Europa would have reached at least 1250 K. Therefore, this high temperature would have been sufficient to release volatile species from the rocks and form today's hydrosphere, which accounts for 8 wt%.

### 6.4.1. Gas starved CPD model

In this section, by using the simple gas-starved model developed by Sasaki et al. (2010) , Anderson et al. (2021) and Mousis et al. (2023), we assess the impact of phyllosilicates dehydration on the Galilean moons' building block composition.

The gas starved model used is based on the model presented by Canup et al. (2002) and Canup et al. (2006), it is a simple one-dimensional CPD. In this model, the CPD is fed by a uniform flux of gas and dust in centrifugally supported orbits, located at distances shorter than the so-called centrifugal radius $R_c$. At a distance larger than the centrifugal radius, falling material is ejected back to the PPD and does not accrete onto the CPD. The surface density is obtained by solving the continuity equation for the falling gas (Canup et al. 2002):

$$\Sigma_{\rm g} = \frac{4F_{\rm p}}{15\pi\nu}\lambda(r) \tag{6.5}$$

where $F_{\rm p}$ is the total infall rate and $\nu$ is the $\alpha$–viscosity. The coefficient $\lambda(r)$ is defined as :

$$\lambda(r) = \begin{cases} \frac{5}{4} - \sqrt{\frac{R_c}{r_d}} - \frac{1}{4}\frac{r^2}{R_c^2} & \text{if} \quad r < R_c, \\ \sqrt{\frac{R_c}{r}} - \sqrt{\frac{R_c}{r_d}} & \text{if} \quad r > R_c. \end{cases} \tag{6.6}$$

With the value of $R_c$ set to 30 $R_{\rm J}$(Sasaki et al. 2010). The total infall rate follows an exponential decay :

$$F_p = F_{p,0}\exp\left(\frac{-t}{\tau_{\rm d}}\right), \tag{6.7}$$

with $\tau_{\rm d}$ is the surrounding PPD depletion timescale of order of 3 Myr (Sasaki et al. 2010)

and $F_{p,0}$ is the initial steady accretion rate from the PPD set to $5 \times 10^{-7}$ $M_{\rm J}$ yr$^{-1}$. A CPD depletion timescale of 3 Myr is a very slow CPD evolution and allow for the existence of the CPD up to the total dissipation of the PPD. In this model, one only consider the viscous dissipation as the main source of heat, where initial CPD temperature is :

$$T_0^4(r) = \frac{3\Omega_{\rm K}^2}{10\pi\sigma_{\rm sb}} F_{p,0}\lambda(r) \tag{6.8}$$

and evolve following an exponential low:

$$T = T_0 \exp\left(\frac{-t}{4\tau_{\rm d}}\right). \tag{6.9}$$

Where $\sigma_{\rm sb}$ is the Stefan-Boltzmann constant.

Figure 6.12 illustrates the temperature, pressure, and surface density profiles of the CPD after 10 kyr, 100 kyr, and 1 Myr of evolution. The vertical blue and brown rectangles indicate the inward migration of the phyllosilicate dehydration line and the water condensation line, respectively. Given the relatively long depletion timescale of 3 Myr, the temperature, pressure, and surface density exhibit small evolutions over the course of 1 Myr, as the water condensation line remains in the 23.6–25.9 $R_{\rm J}$region over 1 Myr. Which is a region located between the present positions Ganymede and Callisto.

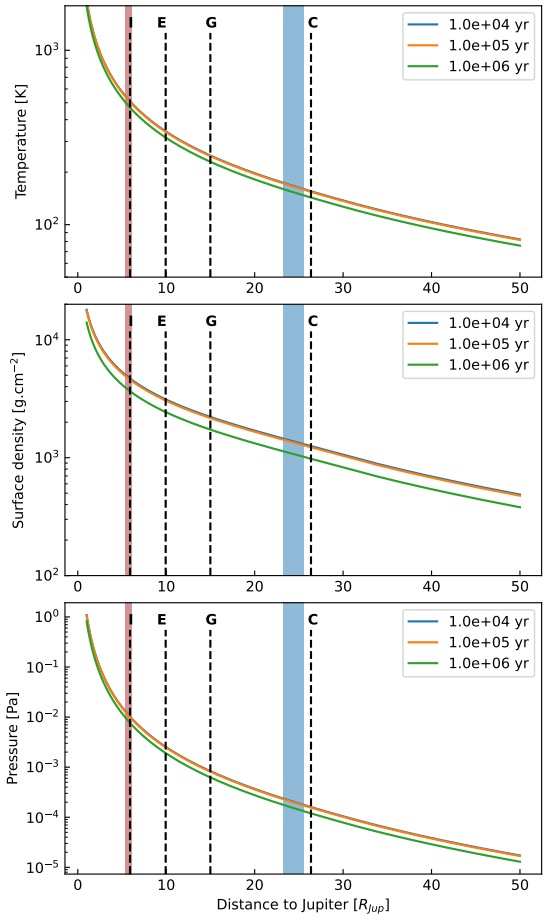


Figure 6.12.: Temperature, surface density and pressure profiles in the CPD at 10, 100 and 1000 kyr, using the model adapted from Anderson et al. (2021). The vertical bars designated by the letters I, E, G and C correspond to the current orbits of Io, Europa, Ganymede and Callisto, respectively. The vertical brow and blue rectangles correspond to the time evolution of the phyllosilicate dehydration line and water condensation line over 1000 kyr in the CPD, respectively. A dehydration temperature of 500 K is assumed in this figure. Figure adapted from Mousis et al. (2023)

Water and phyllosilicates evolution is treated using the same method as for the Sun and Trappist-1 PPDs. With the only difference of the constant supply of grains within the centrifugal radius:

$$\dot{\Sigma}_{\text{phyllo}} = \begin{cases} \frac{f F_p}{\pi R_c^2} & \text{if} \quad r < R_c \\ 0 & \text{if} \quad r > R_c \end{cases} \tag{6.10}$$

where $f$ is the solid–to–gas ratio in our CPD model, here assumed to be $3 \times 10^{-3}$ in mass fraction, based on the abundance of silicates and other rocky material (Lodders 2003).

### 6.4.2. Impact of phyllosilicate grains on the water radial distribution

Figure 6.13 shows the evolution over 1 Myr of the water vapor and ice abundance profiles in the CPD, normalized to the initial abundance in the phyllosilicate–bearing solids (10 wt% in this model). Phyllosilicate–rich grains drift inward and cross the phyllosilicate dehydration line, and when they cross the dehydration line, water vapor is released and diffuses into the CPD. A small portion of the water vapor crosses the water condensation line and condenses on the phyllosilicate-rich grains. As in the Trappist-1 study, we consider three phyllosilicate dehydration temperatures, 400 K, 500 K, and 600 K.

Figure 6.13 shows that the phyllosilicate dehydration line is initially located at 8.2, 6.1, and 4.9 $R_J$for the respective dehydration temperatures of 400, 500, and 600 K. The phyllosilicate dehydration line then drifts inward toward the planet as the CPD cools. After 1 Myr of evolution, it is located at 4.2, 5.7, and 7.8 $R_J$, respectively.

The system rapidly evolves toward high water ice enrichment at the condensation line, with enrichment peaks of 12, 2.3, and 1.5 times the initial water mass abundances in phyllosilicate crystals at dehydration temperatures of 400, 500, and 600 K, respectively, after only 10 kyr. Enrichments that increase to 13.3, 9.3, and 7.0 times the initial water abundance after 100 kyr and slowly decrease to 12.6, 9.2, and 6.7 times the initial water abundance after 1 Myr of evolution. As in the case of the Trappist-1 system study, lower dehydration implies a larger water ice enrichment peak at the water condensation line, because the phyllosilicate dehydration line is closer to the water condensation line, therefore more water vapor crosses the condensation line and condensates onto grains and pebbles.

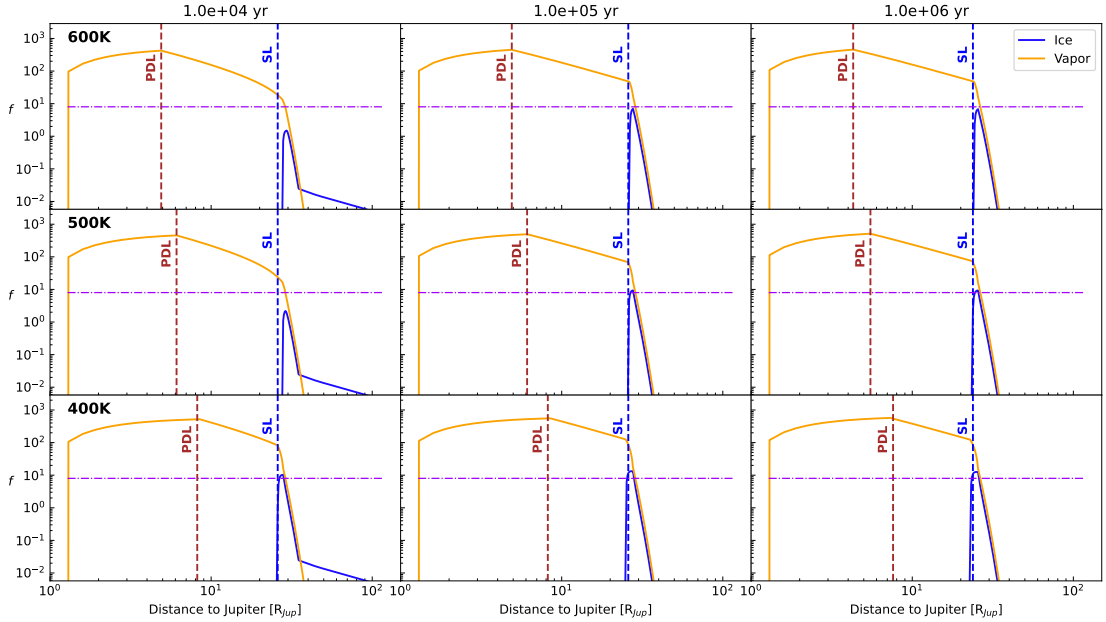


Figure 6.13.: Radial profiles of the water abundances within the CPD expressed as function of the initial abundance in phyllosilicate–rich grains. Water vapor (orange) and ice (blue) radial profile are represented after 10, 100 and 1000 kyr of evolution (from left to right column), assuming phyllosilicate dehydration temperatures of 600 K (top row), 500 K (middle row) and 400 K (bottom row). The horizontal dashed line denotes the threshold at which the amount of condensed water, onto grains, is sufficient to account for that in Ganymede and Callisto. The blue and brown vertical dashed lines correspond to the Phyllosilicate dehydration line and the water condensation line positions. Figure adapted from Mousis et al. (2023).

The water mass fraction is defined as:

$$\mathrm{WMF} = \frac{M_{\mathrm{Water}}}{M_{\mathrm{Water}} + M_{\mathrm{Rock}}} \tag{6.11}$$

Reformulating $M_{\mathrm{Water}}$ and $M_{\mathrm{rock}}$ in terms of water ice enrichment compared to the initial water mass fraction of the phyllosilicate–rich grains ($f_{\mathrm{ice}}$) and phyllosilicate water mass fraction $\mathrm{WMF_p}$, one have :

$$\mathrm{WMF} = \frac{f_{\mathrm{ice}} + 1}{f_{\mathrm{ice}} + \mathrm{WMF_p}} \tag{6.12}$$

Solving equation 6.12 show that a water mass fraction of 50% correspond to a water ice enrichment of 8 times the initial water abundance. Therefore, a pebble water mass fraction corresponding to those of Ganymede and Callisto require a water ice enrichment of 8 times the initial water abundance, denoted by the vertical purple line.

After 100 kyr of evolution and later enrichment of water ice reach values higher than eight times the initial enrichment only for dehydration temperatures of 400 K and 500 K. Conversely, a dehydration temperature of 600 K does not allow the formation of pebble with water mass fraction of 50%.

### 6.4.3. Putative Galilean moons formation sequence

The formation scenario of the Galilean moons in a water-rich scenario proposes that the Galilean moons formed in a water-rich CPD followed by their drift towards the inner part of the CPD until the three inner moons, Io, Europa and Ganymede, were trapped in a mean motion resonance chain as proposed by Canup et al. (2002), Sasaki et al. (2010), Oberg et al. (2020), and Madeira et al. (2021). In this scenario, Callisto could have formed later and stopped its migration outside the mean motion resonance due to CPD dissipation. Or Callisto could have been trapped in the mean motion resonance chain but later ejected from it by tidal forces (Madeira et al. 2021). The large water mass fractions of Ganymede and Callisto are indicative of their formation outside the water condensation lines, assuming that the CPD is fed by material with an ice-to-rock ratio. Io and Europa would have accreted the same material, but devolatilized while drifting in the hotter region of the CPD, inside the water condensation line (Canup et al. 2002; Sasaki et al. 2010; Ronnet et al. 2017).

In the water-poor environment proposed in this section, Ganymede and Callisto would have formed from material derived from the water condensation line. While Europa would have formed from phyllosilicate-rich grains and Io from dehydrated silicate from within the phyllosilicate dehydration line. Europa's hydrosphere would result from the dehydration of phyllosilicate minerals (Melwani Daswani et al. 2021). If Io formed from the same material as Europa, it would have lost its hydrosphere by hydrodynamic escape, as suggested by Bierson et al. (2020).

The possibility of this scenario can be tested observationally by measuring the deuterium to hydrogen ratio (D/H) in the moon's water. If the Galilean moons accreted water-rich material, they should have a supersolar D/H ratio close to that measured in comets (Horner et al. 2008; Waite et al. 2009). Conversely, if the moons were formed from ice-free solids, meaning that they formed in a warm and dense PPD environment, they would have a D/H ratio close to the protosolar value proposed by Horner et al. (2008). In the case that Europa lost part of its hydrosphere by hydrodynamic escape, it should have a D/H ratio on the order of 10–100 times higher than that measured on Ganymede and Callisto (Bierson et al. 2020). Finally, in the case of accretion of exclusively chondritic material, as proposed in this section, the moons should have a D/H ratio close to that measured in carbonaceous chondrites. There could be a slight difference between the D/H ratio in Europa and the D/H ratio in Ganymede and Callisto, which could be slightly lower because of the isotopic exchange between water vapor and $H_2$ during its diffusion from the phyllosilicate dehydration line to the water condensation line.

## 6.5. Application to the Trappist-1 System

The Trappist-1 system contains seven exoplanets in a resonance chain, three of which are within the habitable zone (Gillon et al. 2016, 2017) with semi-major axis ranging between 0.015 and 0.063 AU (Luger et al. 2017; Agol et al. 2021). This resonance chain could be a sign of a past inward drift of the whole system before orbital capture (Ormel et al. 2017; Bitsch et al. 2019; Coleman et al. 2019; Izidoro et al. 2021; Madeira et al. 2021). Furthermore, Trappist-1 is an M dwarf star only 20 % larger than Jupiter but 80 times more massive than the Jupiter. Trappist-1 h, the outermost planet of the system, is only 5 times further from the Trappist-1 star than Callisto is from the Jupiter. As for the Galilean system, the Trappist-1 planets display a density gradient. Those characteristics make the Trappist-1 system the closest analogue to the well-characterized Galilean moon system.

### 6.5.1. Trappist-1 planets characteristics

The measured densities of the Trappist-1 planets are among the most accurate ones available for an exoplanetary system Luger et al. (2017). These densities have been used by Acuña et al. (2021) to assess their interiors and compositions. The authors show evidence for an increasing water mass fraction (WMF) of the planets with increasing distance from the host star, as shown by 6.14. The planets can be separated into two groups, with planets b–c containing little to zero water, and planets d–h presenting significant amounts of water (see Table 6.2). Recent observations from the James Webb Space Telescope of planets Trappist-1 b and c showed that they probably are only bare rocks, or surrounded by a thin atmosphere dominated by $O_2$ or by $CO_2$ (Greene et al. 2023; Zieba et al. 2023). Confirming predictions from interior models.

The significant amount of water estimated in the five outermost planets has been interpreted as a sign that they formed beyond the position of the water condensation line, within the water-rich PPD, prior to their inward migration Ormel et al. (2017) and Johansen et al. (2022). Such a mechanism requires a rapid growth of the planets, which could be eased by the formation of planetesimals via streaming instability triggered by a solid-to-gas ratio above unity at the water condensation line due to ice enrichment Ormel et al. (2017), similarly to Jupiter in the sun's PPD.

Table 6.2.: Estimated masses and WMFs for Trappist-1 planets Acuña et al. (2021).

| Planet | Mass ($M_\oplus$) | WMF |
|---|---|---|
| b | $1.375 \pm 0.041$ | $(3.1^{+0.5}_{-3.1}) \times 10^{-5}$ |
| c | $1.300 \pm 0.036$ | $(0.0^{+4.4}_{-0.0}) \times 10^{-6}$ |
| d | $0.388 \pm 0.007$ | $0.084 \pm 0.071$ |
| e | $0.699 \pm 0.013$ | $0.094 \pm 0.067$ |
| f | $1.043 \pm 0.019$ | $0.105 \pm 0.073$ |
| g | $1.327 \pm 0.024$ | $0.119 \pm 0.080$ |
| h | $0.327 \pm 0.012$ | $0.081^{+0.059}_{-0.081}$ |

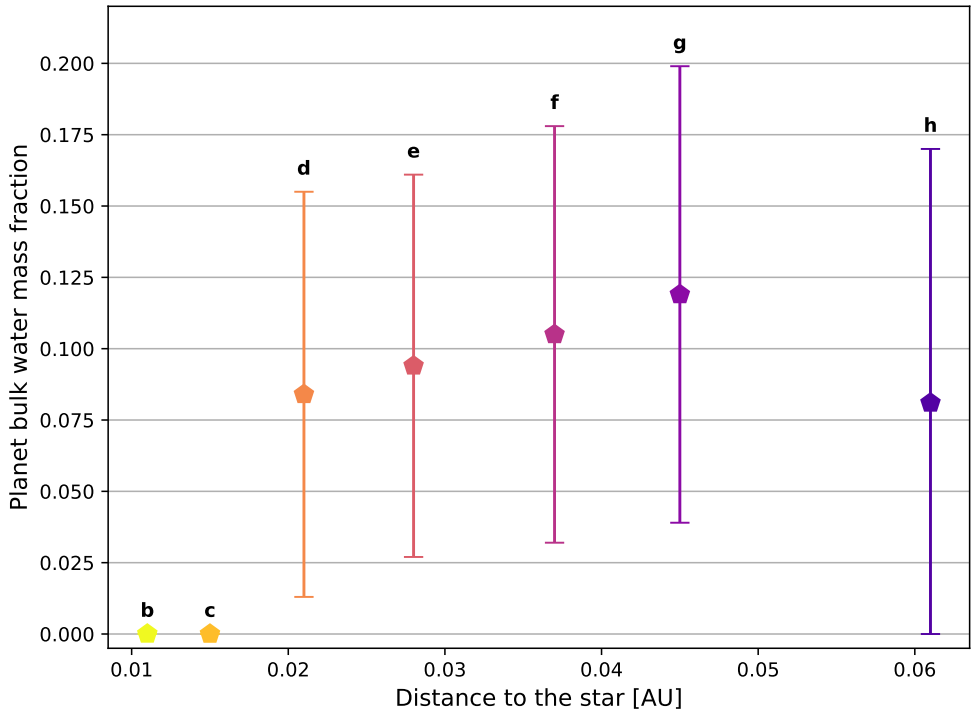


Figure 6.14.: Water mass fraction of the Trappist-1 planets as function of their distance to the star, derived from Acuña et al. (2021) with their respective 1-$\sigma$ error bar.

However, red dwarfs produce far-ultraviolet (FUV) and extreme-ultraviolet (XUV) irradiation during their early evolution (Shkolnik et al. 2014). This can cause the photolytic destruction of the water present in the PPD or in the material originating from the interstellar medium and accreted by the PPD (Shkolnik et al. 2014; Parke Loyd et al. 2018; Youngblood et al. 2021). Furthermore, repeated episodes of accretional

outbursts by Trappist-1 could have produced rapid temperature rises in the PPD that would dehydrate pebbles (Houge et al. 2023). Finally, sequestration of oxygen in rock- and metal-forming species must be considered when the carbon-to-oxygen (C/O) ratio exceeds the solar value (0.55; Lodders (2021)) in the PPD. When the C/O ratio reaches or exceeds 0.8, the depletion of oxygen is severe; it is bound up in rock, metal oxides, CO, and $CO_2$, hindering the production of water (Pekmezci et al. 2019).

### 6.5.2. Delivery of water to the Trappist-1 PPD

In the case of a water depleted PPD, water would be delivered by phyllosilicates to the inner Trappist-1 PPD, following the scenario described in section 2.4. Figure 6.15 shows the studied scenario, including the putative formation site of the Trappist-1 planets. Trappist-1 b and c would have formed closer to the star than the phyllosilicate dehydration line, while Trappist-1 c through h would have formed near or beyond the water condensation line.

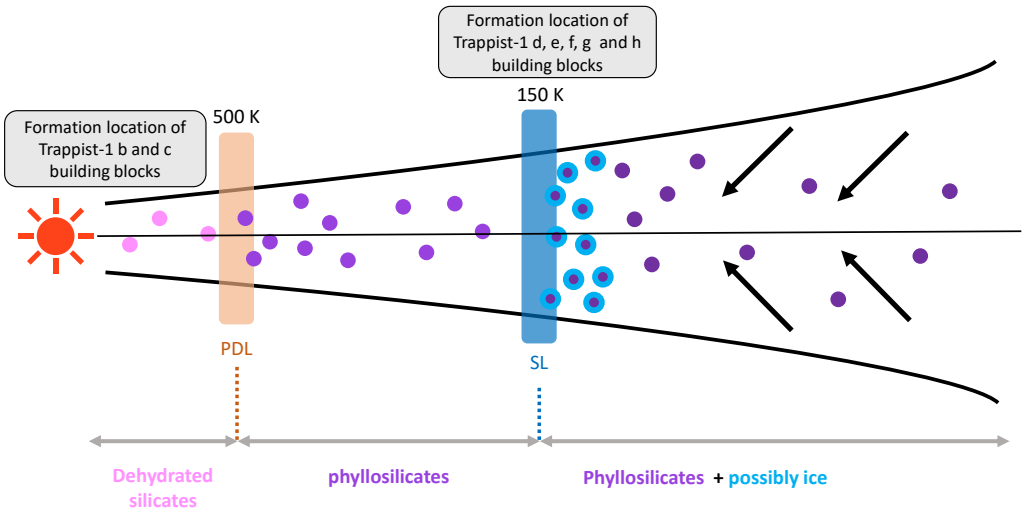


Figure 6.15.: Sketch of the delivery of water by phyllosilicate–rich grains to the inner regions of Trappist-1 regions and puttative formation location of the Trappist-1 planet in this scenario. The figure reproduce figures 2.6 supplemented with Trappist-1 planet location formation.

To study the formation of the Trappist-1 planets in the PPD, we study only the outcome of water in the PPD of the system. Since the Trappist-1 star is much less massive than the Sun, one must scale down the initial mass and accretion rate of the PPD. In the previous sections, we assumed a PPD mass centered around $10^{-1}$ $M_\odot$ and an accretion rate centered around $10^{-7.6}$ $M_\odot$ $yr^{-1}$ following the studies of (Hartmann et al. 1998, 2016). There are immense uncertainties in the mass and accretion rates

of PPDs as a function of their host star mass and age. Therefore, we assume a simple linear scaling from a mass and accretion rate of $10^{-1}$ $M_\odot$ and $10^{-7.6}$ $M_\odot$ $yr^{-1}$ for the PPD of the Sun to a mass and accretion rate of $10^{-1}$ $M_\star$ and $10^{-7.6}$ $M_\star$ $yr^{-1}$ for the PPD of Trappist-1, where $M_\star$ is the mass of Trappist-1.

Figure 6.16 shows the comparison between Trappist-1 and the Sun's PPD midplane temperature, pressure, and surface density profiles at 10, 100, and 1000 kyr. It shows that the Trappist-1 PPD is cooler and less dense than the Sun's PPD by a factor of 5–10 in the 0.5–10 AU region. Consequently, the PPD midplane pressure is also 30–70 times lower than the solar PPD pressure.

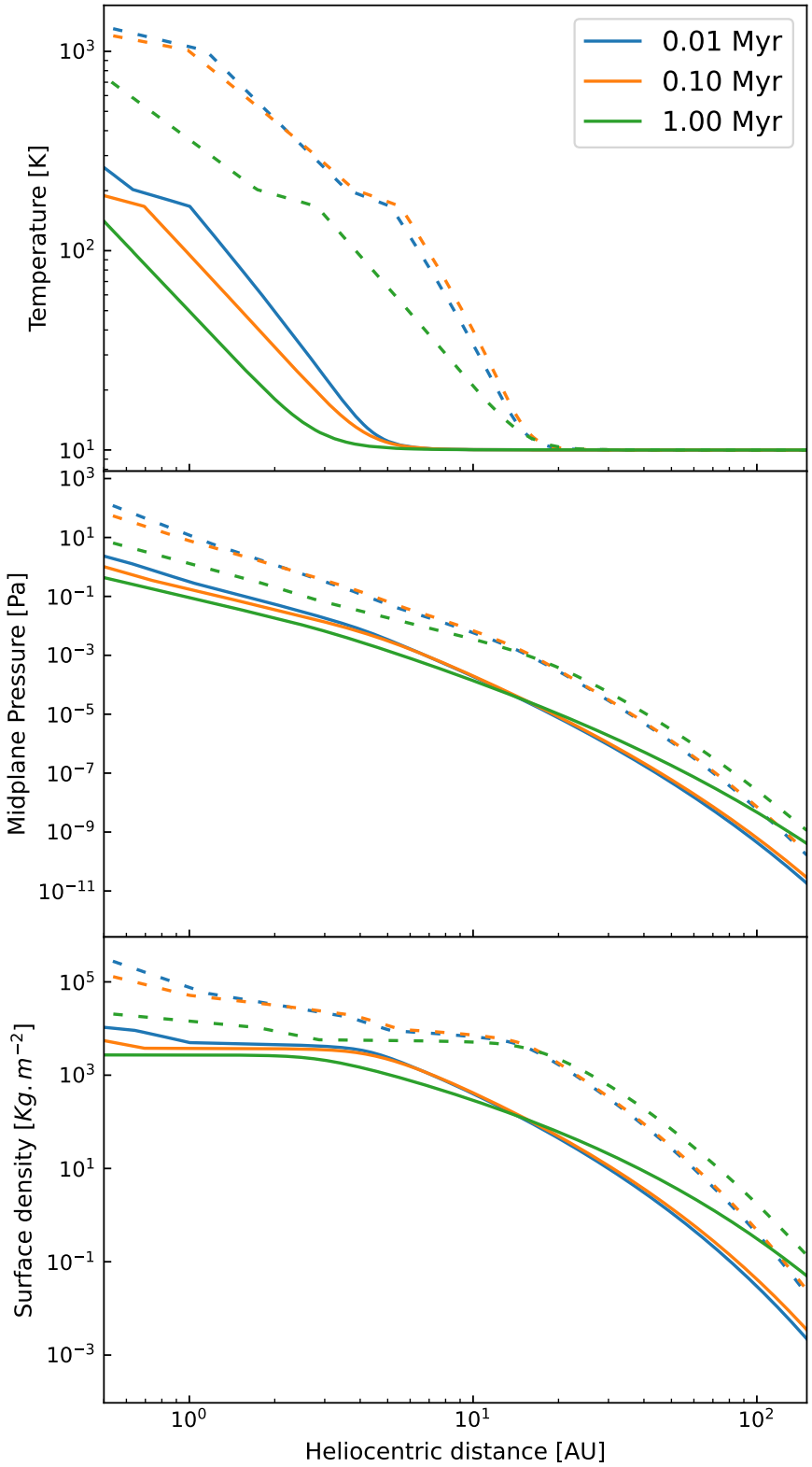


Figure 6.16.: From top to bottom: Temperature, pressure, and surface density profiles of the Trappist-1 PPD (solid lines) superimposed onto those of the PPD taken figure 3.1 (dashed lines) after 10, 100, and 1000 kyr of evolution.

As for previous sections, we use an $\alpha$–viscosity parameter of $10^{-3}$, as well as a phyllosilicate dehydration temperature in the range between 400 and 600 K. The pebble density is 0.5, accounting for the great porosity of pebbles in the PPD. Finally, the mass abundance of silicate in the PPD is taken from (Lodders 2019) with a value of $3.212 \times 10^{-3}$. The phyllosilicate-rich grain water mass fraction is varied between 1% and 10% of water mass fraction, accounting for the different phyllosilicate minerals production mechanisms and rates leading to different hydration rate of the grains.

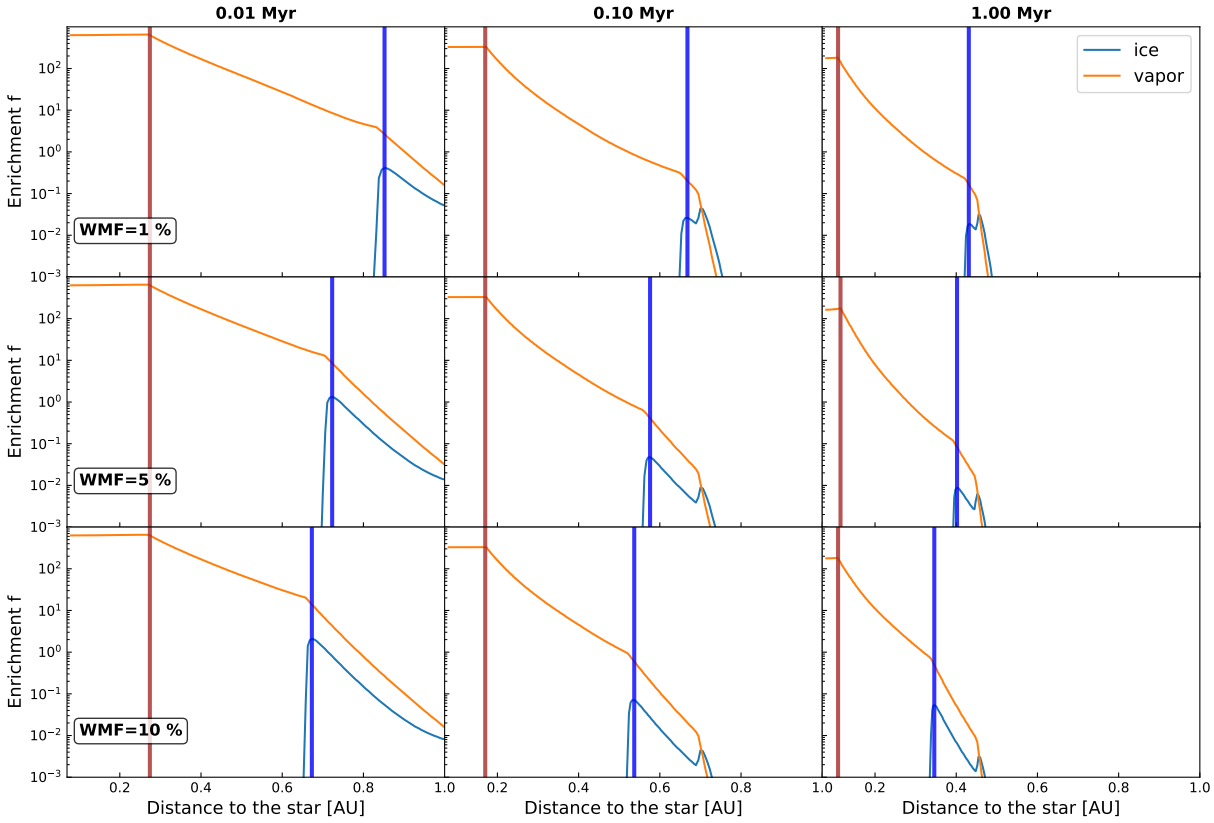


Figure 6.17.: From left to right: Enrichment profiles of water vapor (orange lines) and ice (blue lines) normalized with the initial abundance of water in phyllosilicates at $t$ = 0.01, 0.1, and 1 Myr. The initial WMFs in phyllosilicates here are 1%, 5%, and 10%. The PDL and SL are represented as brown and blue bars, respectively.

Figure 6.17 displays water ice and vapor enrichment profiles in the PPD, with respect to the initial water abundance, after 10, 100 and 1000 kyr of PPD evolution. The initial water abundance is defined as

$$x^0_{H_2O} = \mathrm{WMF}_{\mathrm{phyllo}}\, x^0_{\mathrm{p}}. \tag{6.13}$$

Since the disk only contains phyllosilicate at $t$ = 0, the starting water abundance only depends on the water contained in phyllosilicate particles. $\mathrm{WMF}_{\mathrm{phyllo}}$ of 1%,

5%, and 10% were used in the simulations. The distance between the SL and the central star increases from 0.67 to 0.85 AU, 0.53 to 0.66 AU, and 0.35 to 0.43 AU when the $WMF_{phyllo}$ value is ranged between 1% and 10% at 0.01, 0.1, and 1 Myr of PPD evolution, respectively.

The increase in this distance range is the direct consequence of the decrease in the amount of water vapor released from the pebbles into the PPD. Vapor accumulates at the PDL because its diffusion rate in the PPD is much lower than its production rate. A fraction of this vapor diffuses outward and crosses the SL.

Figure 6.17 shows that the water ice enrichment reach maximums of 0.4, 1.3 and 2 times the initial water abundance after 10 kyr of evolution. Between 10 and 100 kyr of evolution, the water enrichment decreases by a factor 20–30 down to 0.02, 0.04 and 0.07 times the initial water mass abundance. After 100 kyr, the enrichment remains constant up to 1000 kyr, the end of the simulation.

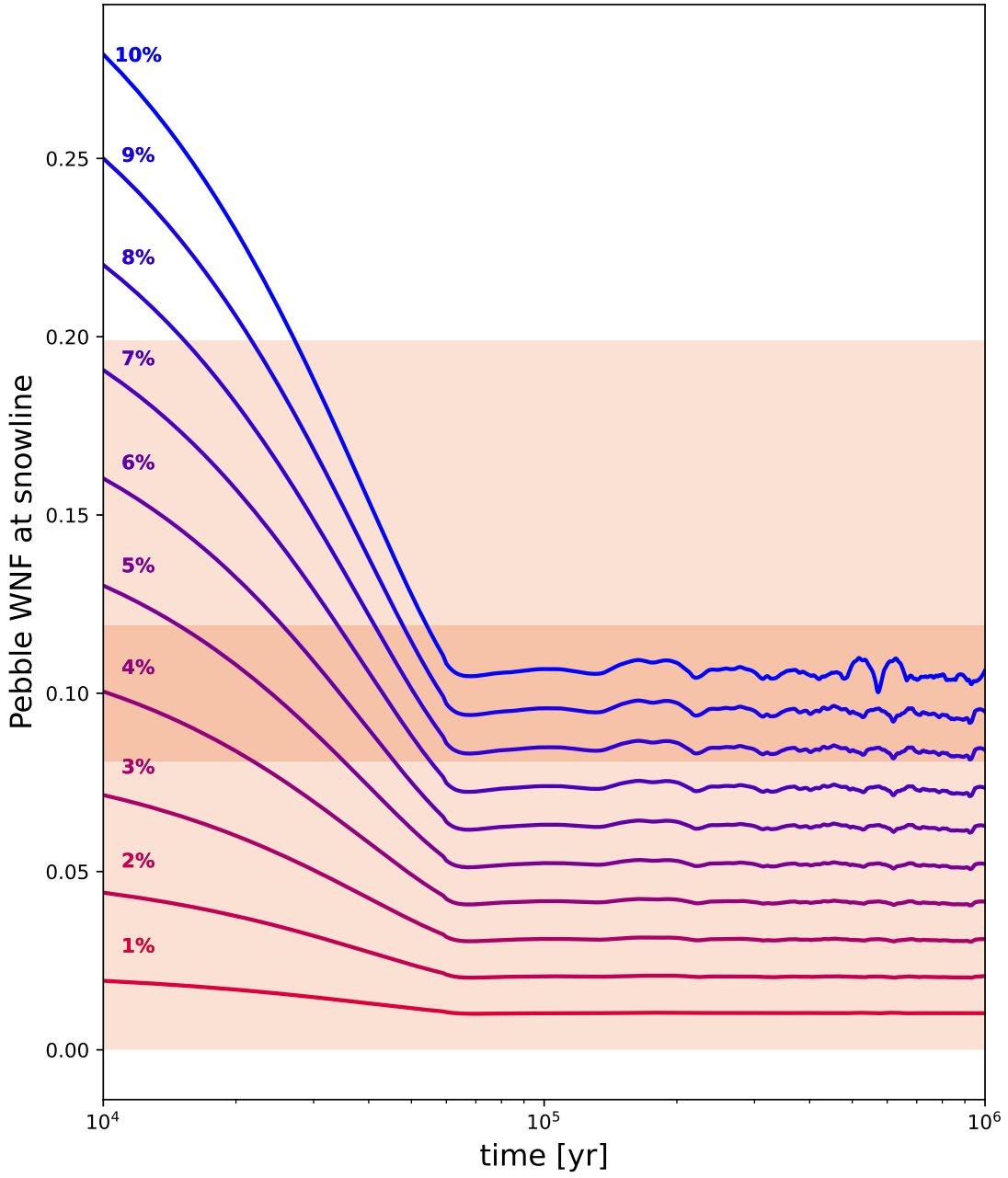


Figure 6.18.: Time evolution of the pebbles' WMFs at the SL location for a phyllosilicate dehydration temperature of 500 K. The phyllosilicate WMF is varied between 1 and 10%. The range of the WMF central values of the different Trappist-1 planets is bracketed by the dark orange box (Acuña et al. 2021), and the $1\sigma$ errors are shown in light orange.

The evolution of the water mass fraction as a function of time at the location of the water condensation line when the initial grain water mass fraction is varied between 1% and 10% is shown in figure 6.18. where the grain mass fraction is calculated such

that:

$$\mathrm{WMF} = \frac{\mathrm{WMF}_{\mathrm{phyllo}}\Sigma_{\mathrm{p}} + \Sigma_{\mathrm{ice}}}{\Sigma_{\mathrm{p}} + \Sigma_{\mathrm{ice}}}, \tag{6.14}$$

where $\Sigma_{\mathrm{p}}$ is the phyllosilicate-rich grain surface density, and $\Sigma_{\mathrm{ice}}$ is the water ice surface density.

Figure 6.18 show that, even in the absence of water at initialization, the grains' water mass fraction is of the order of 2 to 3 times the initial value at the condensation line location. After only 10 kyr of evolution, the grains' water mass fraction reach 28% when starting with a grains' water mass fraction 10%. On the other hand with the lowest initial grains water mass fractions of 1%, after 10 kyr of evolution, the grains water mass fraction reach 2%.

As the PPD depletes, the amount of water vapor released from phyllosilicates decreases, therefore reducing the amount of water ice condensing at the water condensation line. This leads to the rapid decrease of the water enrichment at water condensation line location, therefore the grains WMF converge toward the initial grains water mass fraction after only 70 kyr. It implies that only cases with $\mathrm{WMF}_{\mathrm{phyllo}}$ in the 8–10% range match the water mass fraction of planets d through h before 70 kyr of PPD evolution. After this epoch, water ice is too depleted.

### 6.5.3. Variation of phyllosilicate dehydration temperature

As discussed in section 2.2, the phyllosilicate dehydration temperature has been calculated to be around 200 K (Mousis et al. 2023), although we choose a dehydration temperature of 500 K, we test dehydration temperature between 400 and 600 K.

Figures 6.19 and 6.20 shows the evolution of grains' water mass fraction at the water condensation line location for phyllosilicate dehydration temperatures of 400 K and 600 K respectively. They show that the lower the dehydration temperature, the higher is the water mass fractions of grains at the water condensation line location. The water mass fraction reach 73% and 16% with a $\mathrm{WMF}_{\mathrm{phyllo}}$ of 10% when the phyllosilicate dehydration temperature is varied between 400 K and 600 K. The increase of grains' WMF when the phyllosilicate dehydration temperature is lowered is due to the PDL location closer to water condensation line. The closer the PDL to the condensation line, the more water vapor can diffuse passed the condensation line, and therefore the more water ice condense onto grains in the vicinity of the water condensation line.

Even though the water ice enrichment at the water condensation line changes dramatically with the dehydration temperature of the phyllosilicate, the enrichment depletion timescale does not vary, with grain WMFs converging to a plateau after 70 kyr of PPD evolution. At a dehydration temperature of 400 K, the WMFs converge to a value between 1.5–2 times the initial grain water mass fraction. On the other hand, at a phyllosilicate dehydration temperature of 600 K, grain WMFs converge to the initial grain WMF.

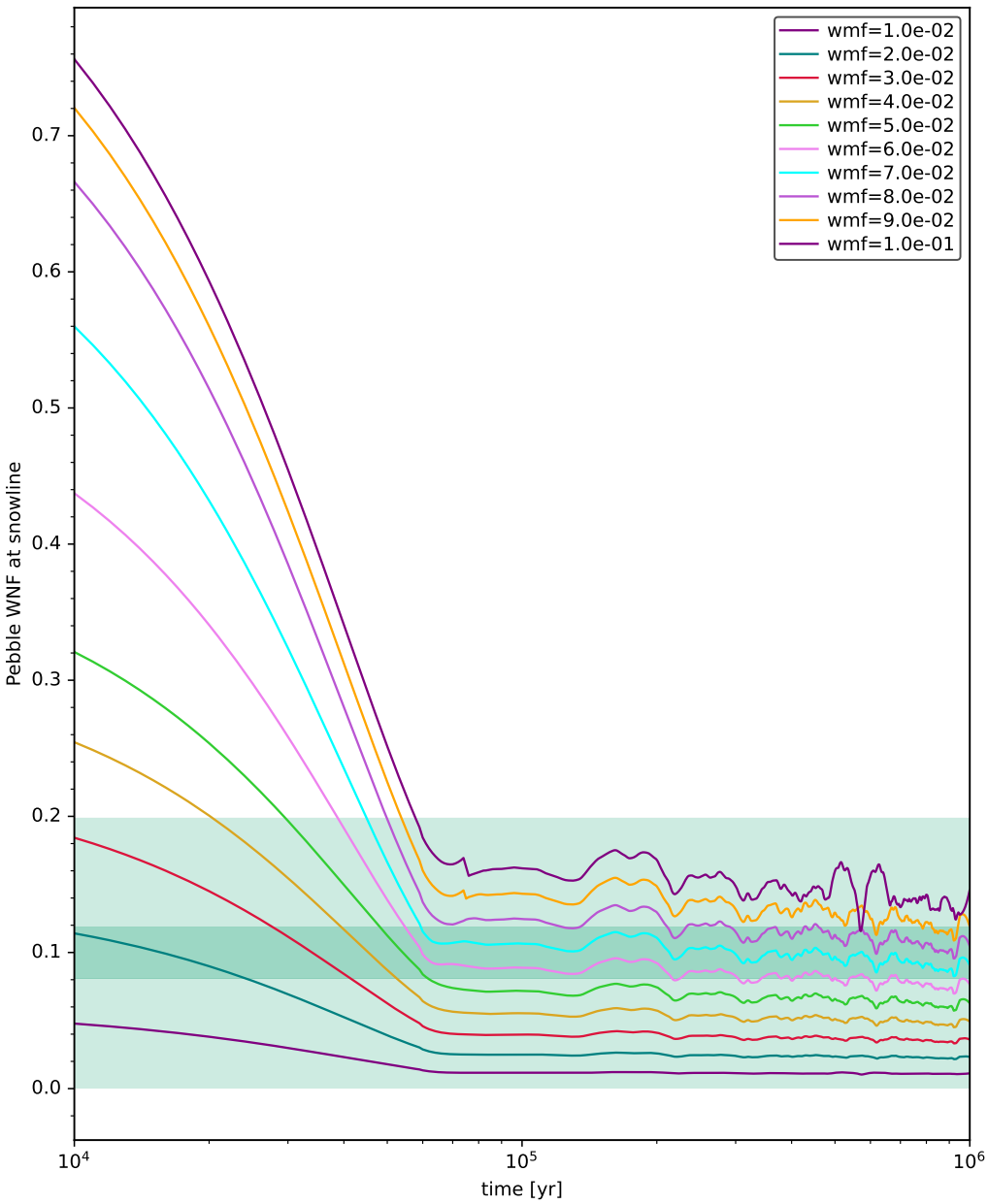


Figure 6.19.: Time evolution of the pebbles' WMFs at the SL location for a phyllosilicate dehydration temperature of 400 K. The phyllosilicate WMF is varied between 1 and 10%. The range of the WMF central values of the different Trappist-1 planets is bracketed by the dark green box (Acuña et al. 2021), and the $1\sigma$ errors are shown in light green.

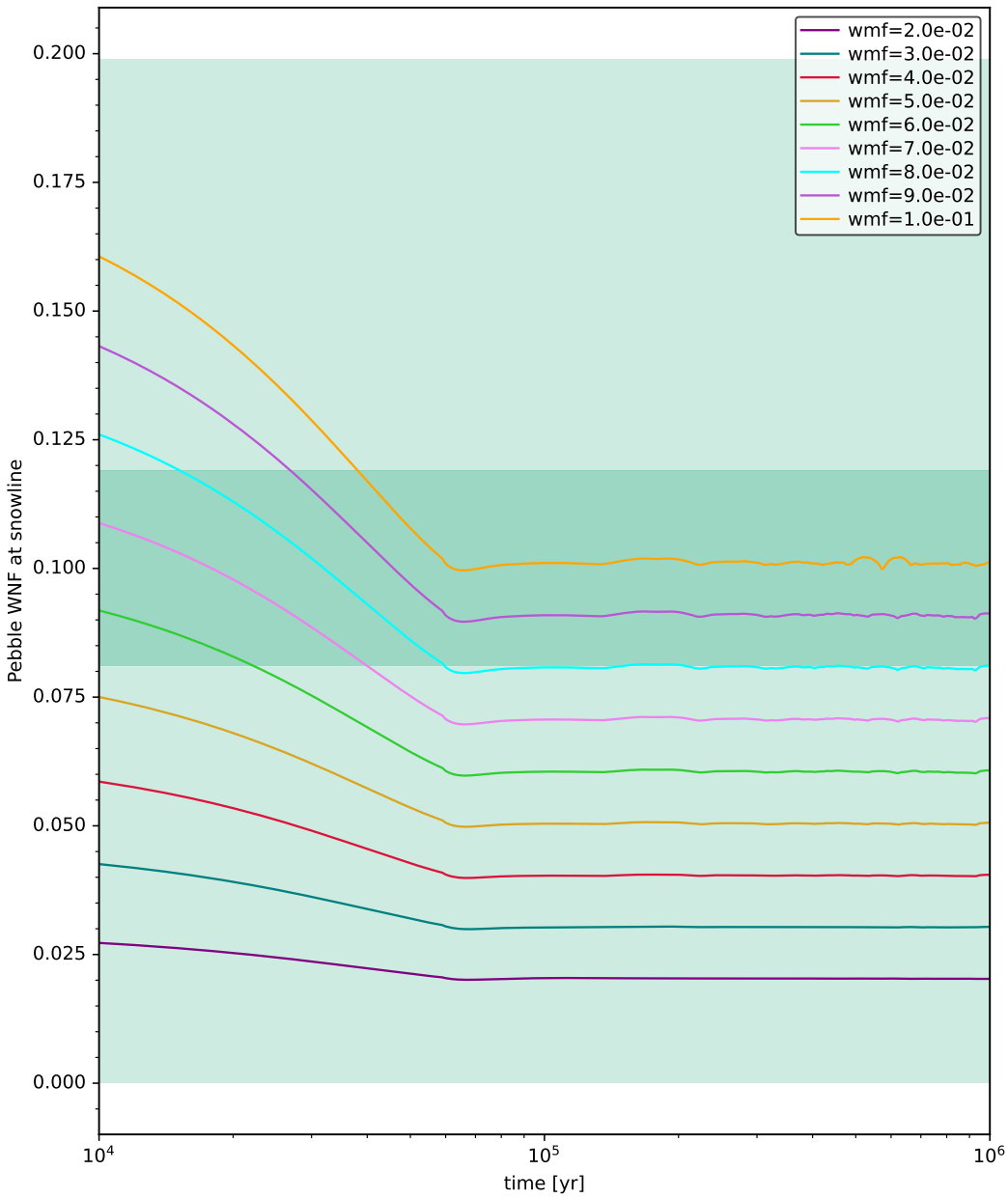


Figure 6.20.: Time evolution of the pebbles' WMFs at the SL location for a phyllosilicate dehydration temperature of 600 K. The phyllosilicate WMF is varied between 1 and 10%. The range of the WMF central values of the different Trappist-1 planets is bracketed by the dark green box (Acuña et al. 2021), and the $1\sigma$ errors are shown in light green.

Varying the phyllosilicate dehydration temperature consequently changes the range

of initial $WMF_{phyllo}$ at which the planet's d to h WMFs are reproduced. When the phyllosilicate dehydration temperature is 400 K, initial $WMF_{phyllo}$ between 6% and 8% reproduce the planet's WMF. On the other hand, if the phyllosilicate dehydration temperature is 600 K, initial $WMF_{phyllo}$ between 8% and 10% will reproduce the planet's WMF.

### 6.5.4. Consequence on Trappist-1 planet formation locations

In this scenario, the PPD is divided into three regions. An inner region interior to the PDL, in which pebbles and grains are made of dehydrated silicate, devoid of water. Then an intermediary region located between the PDL and the water condensation line, populated with pebble made of phyllosilicate–rich material, with WMFs up to 10%. Finally, an outer region located beyond the water condensation line, populated with phyllosilicate–rich grains coated with water ice.

In this scenario, the building blocks of planets b and c come from the dry inner regions. While planets d though h would either have formed from phyllosilicate–rich building blocks from the intermediary region between the PDL and the water condensation line, or from building blocks from the outer region beyond the condensation line, phyllosilicate–rich pebbles coated with water ice.

Therefore, planets b and c could have formed at their present locations at $1.154 \times 10^{-2}$ and $1.580 \times 10^{-2}$ AU, respectively. On the other hand, planets d–h whose present-day locations are closer than the PDL, between $2.227 \times 10^{-2}$ and $6.189 \times 10^{-2}$ AU, must have formed further away (Ormel et al. 2017; Coleman et al. 2019; Huang et al. 2022; Ogihara et al. 2022). Furthermore, a sequential formation of the planets followed by an inward migration could have led to the observed mean motion resonance chain formed by the seven planets (Ormel et al. 2017; Bitsch et al. 2019; Coleman et al. 2019; Izidoro et al. 2021).

A major limit of this works comes from the initial assumption of the initial water loss driven by photolysis driven by FUV/XUV radiation from the young Trappist-1 star, whose intensity and time evolution remain unknown. Consequently, if the FUV/XUV levels were very low, it is likely that primordial water ice would remain abundant in the PPD. On the other hand, an extreme FUV/XUV radiation episode of sufficient duration would destroy the vapor released by phyllosilicate grains and pebbles, thereby preventing any ice formation at the condensation line.

# 7. Application of a chemical network to the CPD

In the previous chapter, we focused on the composition of ice and vapor by considering only vaporization and condensation processes. In this chapter, we aim to extend the model by incorporating a chemical reaction network to better characterize the chemical tracers within the formation environments of the Galilean moons. Our goal is to develop a model that accounts for out-of-equilibrium chemistry. We first present the chemical composition of the CPD at thermochemical equilibrium, followed by a detailed explanation of the methods used to study out-of-equilibrium chemistry.

## Table of Contents


7.1. Thermochemical equilibrium . . . 153
7.1.1. Method : ACE software . . . 154
7.1.2. Composition of the CPD at thermochemical equilibrium . . . 154
7.1.3. Limits of the approach . . . 161
7.2. Non-equilibrium chemistry . . . 162
7.2.1. Continuity equation . . . 162
7.2.2. Description of the chemical network . . . 162
7.2.3. Flux of species . . . 165
7.3. Numerical scheme . . . 166
7.3.1. Discretization . . . 166
7.3.2. Backward Differentiation Formula integration Scheme . . . 167
7.3.3. Jacobian matrix construction and inversion . . . 169
7.3.4. Boundary conditions . . . 172
7.4. Resolution instabilities . . . 173


## 7.1. Thermochemical equilibrium

In this section, we present the thermochemical equilibrium model and the resulting CPD composition. The composition obtained with this model is then used as the initial condition of the out-of-equilibrium model that will be presented in section 7.2.

### 7.1.1. Method : ACE software

We use the model ACE developed by Agúndez et al. (2012) and Al-Refaie et al. (2021, 2022). One consider a closed system with $N_c$ species. It is based on the minimization of the system's Gibbs energy :

$$G = \sum_{l}^{N_c} \bar{g}_l n_l \tag{7.1}$$

where $N_c$ is the total number of species, $\bar{g}_l$ the partial free energy of species $l$ and $n_l$ is the number of moles of species $l$. The partial Gibbs energy of a species in an ideal gas is expressed as:

$$\bar{g}_l = g_l(T,P) + RT \ln n_l. \tag{7.2}$$

With $g_l(T,P)$ is the free Gibbs energy of species l and $R$ the perfect gas constant. The free Gibbs energy is defined as:

$$g_l(T,P) = h_l^0(T) - Ts_l^0(T) + RT \ln\left(\frac{P}{P^0}\right) \tag{7.3}$$

where $h_l^0(T)$ and $s_l^0(T)$ are the standard-state enthalpy and entropy of species $l$, respectively, and pressure $P^0 = 101325$ Pa is the standard state pressure . The standard enthalpy and entropy are expressed as polynomial coefficients from McBride et al. (1993) :

$$\frac{h_l^0(T)}{RT} = a_1 + a_2 T + a_3 T^2 + a_4 T^3 + a_4 T^4, \tag{7.4}$$

and,

$$\frac{s_l^0(T)}{RT} = a_1 \ln T + a_2 T + a_3 \frac{T^2}{2} + a_4 \frac{T^3}{3} + a_5 \frac{T^4}{4} + a_7, \tag{7.5}$$

where coefficient $a_1$ through $a_7$ are the numerical NASA coefficients for the polynomial form of the standard enthalpy and entropy. As explained by Venot et al. (2012), coefficients for most species are taken from McBride et al. (1993), however when needed coefficients are estimated using THERGAS developed **muller1995**. The minimization is performed using an iterative method, detailed in Agúndez et al. (2012).

### 7.1.2. Composition of the CPD at thermochemical equilibrium

In this section, we present the composition of the CPD at thermochemical equilibrium, from the Gibbs energy minimization method. The energy minimization is performed starting with protosolar elemental abundances of Hydrogen, Helium, Oxygen, Nitrogen, and Carbon. The used chemical network does not contain Sulfur bearing compound, therefore Sulfur is not considered in the following. Over the 935 chemical species of the network, we present only the main carriers of carbon, oxygen, and nitrogen which are namely CO, $CO_2$, $CH_4$, $N_2$, $NH_3$ and $H_20$. As an example of minor species, we also present abundances profiles of HCN, CN and $C_2H_2$.

Table 7.1.: Nominal model parameters

| Parameter | Value | References |
|---|---|---|
| $M_p$ | 0.95 $M_J$ | Mordasini (2013) |
| $R_p$ | 1.1 $R_J$ | Mordasini (2013) |
| $a_p$ | 5 AU | |
| $t_{initial}$ | $3 \times 10^4$ yr | |
| $t_{final}$ | $4 \times 10^5$ yr | |
| $X_d$ | $2.45 \times 10^{-2}$ | Lodders (2021) |
| $\chi$ | $10^{-1} - 10$ | |
| $k_s$ | 0.2 | Makalkin et al. (1995) |
| $\alpha$ | $10^{-3}$ | Lynden-Bell et al. (1974) |
| $T_{amb}$ | 40 K | Aguichine et al. (2020) |
| $\mu_g$ | $2.341 \times 10^{-3}$ | Lodders (2021) |
| $R_c$ | 50 $R_J$ | |
| $X_H$ | 12 | Lodders (2021) |
| $X_{He}$ | 10.99 | Lodders (2021) |
| $X_C$ | 8.56 | Lodders (2021) |
| $X_N$ | 7.94 | Lodders (2021) |
| $X_O$ | 8.82 | Lodders (2021) |

The CPD temporal evolution is provided by the model presented in chapter 5. CPD parameters are presented in table 7.1. Elemental abundances of hydrogen, helium, carbon, nitrogen, and oxygen are set to their protosolar values of 12, 10.99, 8.56, 7.94 and 8.82 DEX (Lodders 2021). With the molar abundance of each species linked to the DEX abundance such that:

$$\frac{x_i}{H} = 10^{X_i - 12}. \tag{7.6}$$

Where $x_i / H$ is the molar abundance of species $i$ and $X_i$ is the abundance expressed in DEX.

Figure 7.1 show the abundance of CO, $CO_2$, and $CH_4$ in the gas phase of the CPD at 60, 100, and 150 kyr of evolution. After 60 kyr, CO and $CO_2$ are present only within 9 $R_J$ from the planet in the gas phase, while $CH_4$ is less abundant within 4 $R_J$ but dominates the carbon budget at greater distances. The vertical abundance profiles of CO and $CO_2$ show a decrease in abundance up to the altitude of the photosurface, where the CPD becomes vertically isotherm, followed by an increase in their abundances. This results in the formation of a CO and $CO_2$ layer in the upper layer of the CPD, at altitudes between ~1 and 7 $R_J$ within 9 $R_J$ of the planet. Conversely, $CH_4$ is depleted in this region, with no $CH_4$ present in the uppermost layers closer than 9 $R_J$ to the planet.

After 100 and 150 kyr of evolution, CO and $CO_2$ become confined to the uppermost layers of the CPD, at altitudes between 0.3 and 3 $R_J$ in the region interior to 7 $R_J$ from the planet. Within this region, the abundances of CO and $CO_2$ are anti-correlated. As the distance from the planet increases, the abundance of CO decreases from $4 \times 10^{-4}$

to $9 \times 10^{-6}$, while the $CO_2$ abundance increases from $7.2 \times 10^{-8}$ to $1.3 \times 10^{-4}$ at 3 and 6 $R_J$, after 100 kyr of CPD evolution. Conversely, $CH_4$ is most abundant in the CPD midplane and is depleted in the uppermost regions of the inner CPD, particularly within 9 $R_J$. This pattern highlights the competition between the formation of CO and $CO_2$ and the formation of $CH_4$ within the CPD.

The shadow cast over the outer region of the CPD impacts the abundances of CO and $CO_2$, as a decrease in midplane temperature leads to an abrupt drop in their midplane abundances. Conversely, in a region hotter than its surroundings at 2.8 $R_J$from the planet, the abundances of CO and $CO_2$ increase from $2.8 \times 10^{-11}$ to $2.7 \times 10^{-10}$ and from $4.5 \times 10^{-12}$ to $3.7 \times 10^{-11}$, respectively, after 100 kyr of evolution.

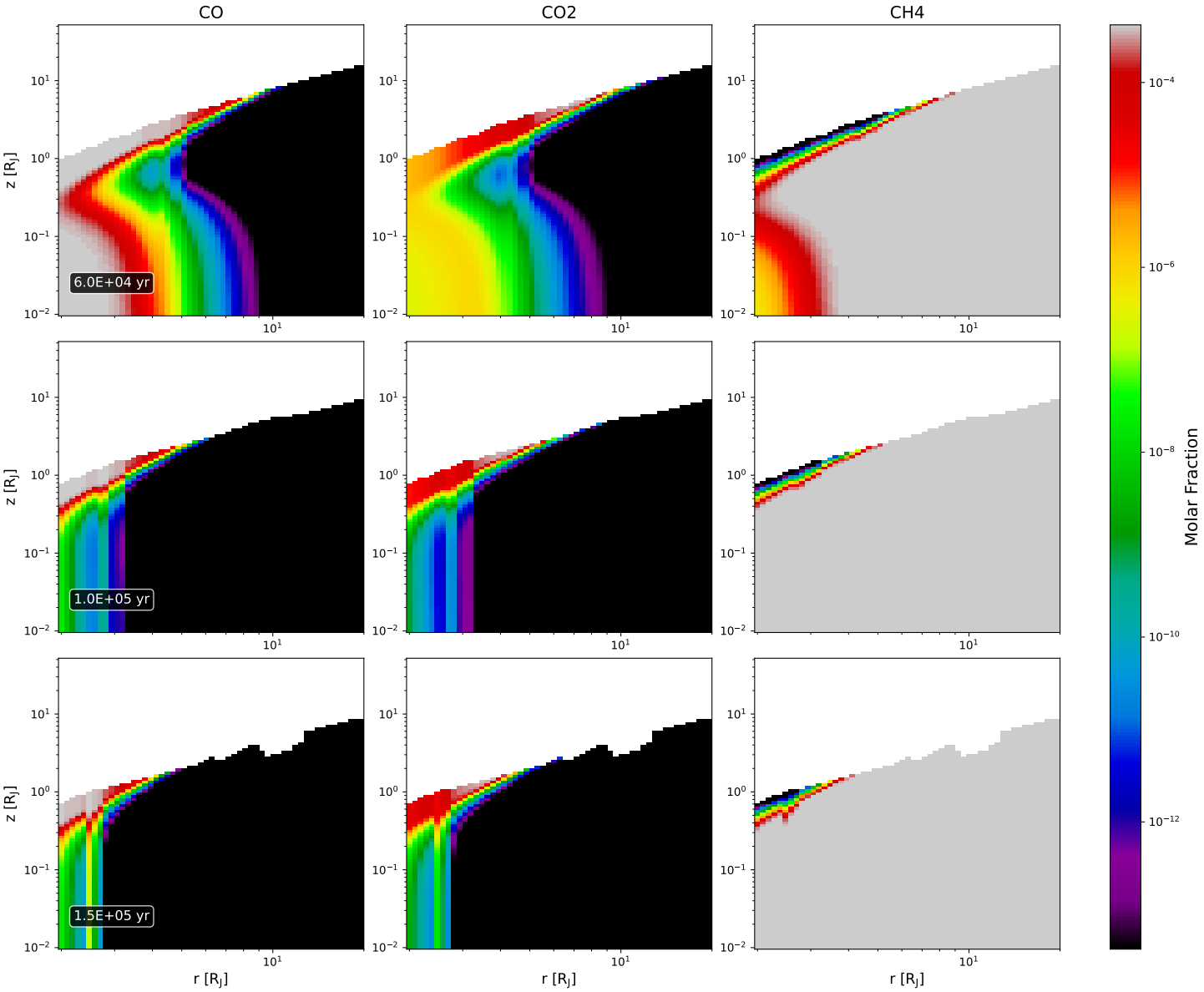


Figure 7.1.: Molar fractions of the three main carbon-bearing species, CO, $CO_2$ and $CH_4$ (from left to right) at thermochemical equilibrium after, 60, 100 and 150 kyr (from top to bottom) following the formation of the CPD. Where the thermochemical equilibrium did not converge, no data is represented.

Figure 7.2 shows the abundances of $N_2$ and $NH_3$, the main nitrogen-bearing species, after 60, 100, and 150 kyr of evolution. After 60 kyr, the inner disk is dominated by $N_2$ up to a distance of 15 $R_J$from the planet, while $NH_3$ becomes more abundant beyond 15 $R_J$. As altitude increases, the abundance of $N_2$ decreases until it reaches a minimum at the photosurface; beyond this point, at constant temperature and decreasing pressure, the $N_2$ abundance increases again. Conversely, the abundance of $NH_3$ increases with altitude, reaching a maximum at the photosurface, and then

decreases.

After 100 kyr of evolution, $N_2$ becomes highly depleted at distances greater than 6 $R_J$, while $NH_3$ dominates closer to the planet, within 2 $R_J$. A region hotter than its surroundings at 1.8 $R_J$in the CPD causes a depletion of $NH_3$ by a factor of approximately 100, however it does not impact the $N_2$ abundance. Conversely, in the shadowed region beyond 10 $R_J$, the $N_2$ abundance drops by a factor of about 100, with minimal impact on $NH_3$ abundance.

Finally, after 150 kyr of evolution, the shadowed region is confined to between 7 and 11 $R_J$, limiting the $N_2$ abundance drop to this region. The variation in $N_2$ abundance between 8 and 9 $R_J$, where differences of up to $10^4$ occur between adjacent columns, may be due to numerical instabilities.

Figure 7.2 therefore indicates that the CPD nitrogen budget is dominated by $N_2$ in the inner region, up to 15 $R_J$after 60 kyr, which rapidly shrinks to 5 $R_J$after 150 kyr. Meanwhile, $NH_3$ dominates the budget in the outer region, from beyond 15 $R_J$down to 5 $R_J$between 60 and 150 kyr.

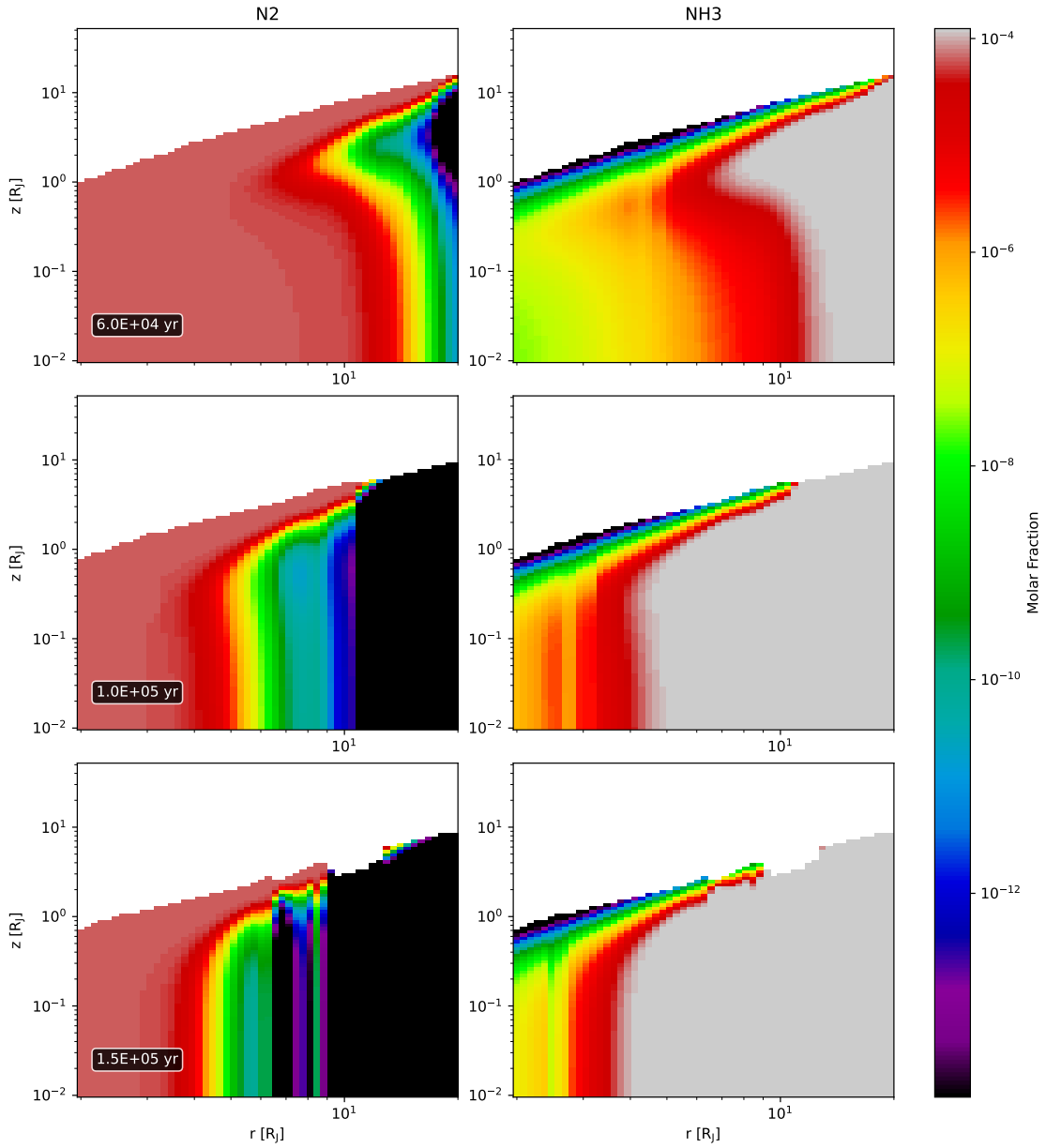


Figure 7.2.: Molar fractions of the two main nitrogen-bearing species, $N_2$ (left column) and $NH_3$ (right column) at thermochemical equilibrium after 60, 100 and 150 kyr (from top to bottom) following the formation of the CPD.

In addition to the main carbon- and nitrogen-bearing species, we investigate the distribution of minor species typically used as tracers of protoplanetary disk properties, particularly in planet-forming regions. Figure 7.3 shows the spatial distribution of HCN, CN, and $C_2H_2$ molecules. HCN and CN are tracers for understanding the inheritance state of nitrogen chemistry and complex organic chemistry, as they are precursors to prebiotic compounds (Dutrey et al. 2014; Öberg et al. 2021; Anderson et al. 2024). The small organic molecule $C_2H_2$ is also a tracer of organic chemistry

within the CPD (Oberg et al. 2023).

Figure 7.3 illustrates that HCN, CN, and $C_2H_2$ are most abundant in the inner regions of the CPD. After 60 kyr of evolution, HCN reaches its maximum abundance within the inner 3 $R_J$of the CPD, with midplane abundances on the order of $10^{-11}$. CN, however, has a much lower abundance, around $10^{-19}$, concentrated within the inner 2 $R_J$. $C_2H_2$ is found within the region closer than 3 $R_J$, with abundances of $10^{-15}$. At higher altitudes, a distinct layer of HCN molecules is present between 0.6 and 2 $R_J$, with an abundance approximately one order of magnitude lower than in the midplane ($\sim 10^{-12}$), while CN abundance decreases with altitude. The vertical abundance profile of $C_2H_2$ resembles that of HCN, with a layer of molecules between 0.6 and 2 $R_J$at altitudes, where abundances range from $10^{-18}$ to $10^{-15}$.

As the CPD cools over time, the midplane abundance of HCN decreases to around $10^{-19}$ within 2 $R_J$of the planet after 100 kyr and 150 kyr of evolution. HCN remains abundant at higher altitudes, between 0.4 and 1.4 $R_J$, with abundances of $10^{-15}$. Meanwhile, the abundances of CN and $C_2H_2$ drop to below $10^{-21}$ after 100 and 150 kyr of evolution, effectively indicating the near absence of these molecules in the CPD.

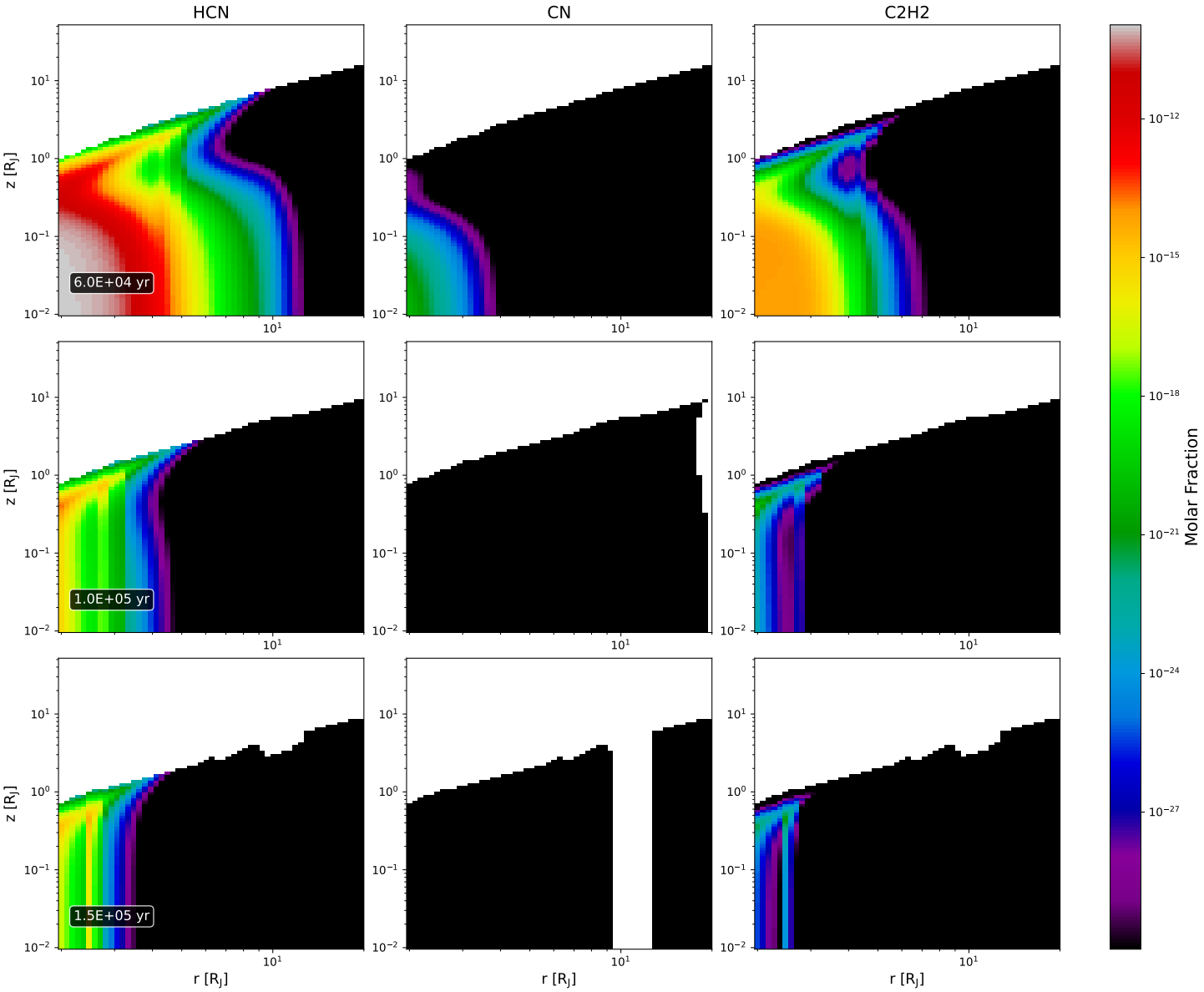


Figure 7.3.: Molar fractions of the tracer species of planet forming regions observed in PPD. HCN (left column), CN (middle column) and $C_2H_2$ (right column) at thermochemical equilibrium after 60, 100 and 150 kyr (from top to bottom) following the formation of the CPD.

### 7.1.3. Limits of the approach

When considering thermochemical equilibrium, the chemical profile of the CPD is structured into vertical layers dominated by different species. This analysis reveals that CO and $CO_2$ are most abundant in the upper layers of the CPD, while $CH_4$ is confined to the midplane. Similarly, HCN and $C_2H_2$ are also concentrated in the uppermost layers of the CPD. This results in a CO distribution that is consistent with

the structure of modeled PPDs as described by Woitke et al. (2022), Woitke (2023), and Woitke et al. (2023). However, the distribution of HCN and $C_2H_2$ in our model diverges from these studies, where these molecules are typically confined to the PPD midplane.

This divergence highlights the limitations of the thermochemical equilibrium approach. While it provides a good first-order estimate of species distribution, it does not account for processes such as mixing, photo-dissociation, and the heating and cooling effects induced by endothermic and exothermic reactions. The lack of consideration for photo-dissociation is particularly impact-full in the optically thin regions of the CPD, specifically in the uppermost layers and the outer regions. After 200 kyr of evolution in the nominal model, the CPD becomes fully optically thin and therefore should be significantly affected by photo-dissociation.

Another limitation of this approach, is the consideration of non-equilibrium states in the colder regions of the CPD. At low temperature and density characteristic of the CPD outer regions, reaction timescale becomes larger than the viscous diffusion and accretion timescale. Consequently, in this region, the system cannot reach equilibrium and the thermochemical equilibrium does not describe the composition of this region.

## 7.2. Non-equilibrium chemistry

In this section, we present the time–dependent continuity equation which drive the evolution of the chemical species of the network.

### 7.2.1. Continuity equation

The evolution of the chemical species through time is given by the following diffusion equation (Venot et al. 2012; Hue et al. 2015; Cavalié et al. 2017) :

$$\frac{dn_l}{dt} = L_l + P_l - \nabla \cdot \phi_l \tag{7.7}$$

where $n_l$ is the number density of species $i$ expressed in $cm^{-3}$, $L_l$ and $P_l$ are the destruction and production rates of species $l$ due to chemical reactions expressed in $cm^{-3}\ s^{-1}$, and $\phi_l$ is the flux of species $l$, expressed in $cm^{-2}\ s^{-1}$. The initial condition of the continuity equation is the composition at thermochemical equilibrium found in section 7.1.2, which is supposed to be not far from the equilibrium between the chemical reactions production rates and the species' mixing by viscous diffusion.

### 7.2.2. Description of the chemical network

The used chemical network used is the one presented by Venot et al. (2012), it based itself on combustion experiments of carbonaceous species from $C_0$ to $C_2$ length. It also includes N–bearing species, which reactions originates from Konnov et al. (2000) and Konnov (2009) and Coppens et al. (2007). In the following, we summarize the

working principle of the chemical network. Originally intended for the study of the Jupiter's atmosphere composition (e.g. hot temperature and high pressure).

Let's consider a reversible reaction of the form :

$$\sum_{l=1}^{N_{\text{species}}} \nu_l X_l \rightleftharpoons \sum_{l=1}^{N_{\text{species}}} \nu'_l X_l \tag{7.8}$$

where $\nu_l$ and $\nu'_l$ are the direct and indirect reactions stoichiometric factors of species $X_l$. Because of the conservation of the matter, what is destroyed on the left hand-side of the reactions must create on the right hand-side :

$$-\frac{1}{\nu_l}\frac{d[X_l]}{dt} = \frac{1}{\nu'_l}\frac{d[X_l]}{dt} = v \tag{7.9}$$

where $[X_l]$ is the concentration of species $X_l$ , and $v$ is the reaction rate expressed in mol $s^{-1}$. The reaction rates depend on both, the species' concentration and temperature, following Van't Hoff law :

$$v = k(T) \prod_{l=0}^{N_{\text{species}}} [X_l]^{\nu_l} \tag{7.10}$$

with $K(T)$ the reaction constants, dependent on temperature. One can use the empirical modified Arrhenius law to determine the reaction constant:

$$K(T) = AT^n \exp\left(-\frac{E_a}{RT}\right) \tag{7.11}$$

where A is the pre-exponential factor and, $T^n$ to account for the dependence of the pre-exponential factor on the temperature where $n$ is determined empirically, $E_a$ is the reaction activation energy. By default, the constant $K(T)$ correspond to the forward reaction constant, from the left hand-side to the right hand-side of the reaction equation. In the case of reversible reaction, one have to calculate the reversed reaction constant, from the right hand-side to the left hand-side of the reaction equation. Which is calculated from the reaction equilibrium constant $K_{\text{eq}}$ :

$$K_r = \frac{K_f}{K_{\text{eq}}} \tag{7.12}$$

with the equilibrium constant being deduced from the NASA coefficients (Venot 2012), and $K_f$ and $K_r$ the forward and reversed reactions constants.

In the case of three–body reactions, the reaction constant is also dependent on the environment pressure. This is due to the nature of the reaction, consisting in a first reaction between two species resulting in an exited product :

$$A + B \rightarrow AB^*, \tag{7.13}$$

The excited product $AB^*$ is unstable and will decompose to form the reactants. In

order to conserve a stable $AB$ species, another molecule $M$ has to collide with $AB^*$ to deexcite and stabilize the species :

$$AB^* + M \rightarrow AB + M \tag{7.14}$$

Molecule M can can be any other species present in the disk, hence the pressure dependence of the reaction constant of the reaction. If the pressure is high enough, the collision of any molecule $M$ the collision has a probability of one, and the reaction is equivalent to the bi-molecular reaction

$$A + B \rightarrow AB. \tag{7.15}$$

with its reaction rate being :

$$\upsilon_\infty = K_\infty[A][B]. \tag{7.16}$$

Conversely, if the pressure is low enough, the collision rate of any species $M$ is the limiting factor to the formation of $AB$, therefore in that case, the reaction is equivalent to a simple trimolecular reaction :

$$A + B + M \rightarrow AB + M, \tag{7.17}$$

with the corresponding reaction rate

$$\upsilon_0 = K_0[A][B][M]. \tag{7.18}$$

$K_\infty$ and $K_0$ are the reaction constant determined at high and low pressure respectively, similarly $\upsilon_0$ and $\upsilon_\infty$ are the reactions rates at low and high pressure. $[M]$ is the concentration of the third bodies computed from combined species concentrations and their respective efficacy

$$[M] = \sum_{l=0}^{N_{\text{species}}} [X_l]\alpha_{m,l}. \tag{7.19}$$

where $\alpha_{m,l}$ is the efficiency of species $X_l$ on reaction $m$.

Between both extreme conditions, lies a pressure region where the reaction constant becomes dependent on the concentration [M. This pressure region is called the fall–off region, typically met in the inner region of the CPD. One have the general formulation of the reaction constant :

$$K([M], T) = K_\infty \left( \frac{P_r}{1 + P_r} \right) F([M], T), \tag{7.20}$$

where $P_r$ is the reduced pressure :

$$P_r = \frac{K_0[M]}{K_\infty}, \tag{7.21}$$

with F being the augmentation factor function, which translate the transition be-

tween high to low pressure regime. It exists several formulations of this function to describe the fall-off region of the reaction. The KIDA chemical network uses the Troe formulation :

$$\log F = \frac{\log\left(F_{\text{cent}}\right)}{1+\left[\frac{\log(P_r)+c}{N-d\left(\log(P_r)+c\right)}\right]} \tag{7.22}$$

with d a constant of value 0.14,

$$c = -0.4 - 0.67\log\left(F_{\text{cent}}\right), \tag{7.23}$$

and

$$N = 0.75 - 1.27\log\left(F_{\text{cent}}\right). \tag{7.24}$$

finally $F_{\text{cent}}$ is the central augmentation factor :

$$F_{\text{cent}} = a\exp\left(-\frac{T}{T_1}\right) + \exp\left(-\frac{T_2}{T}\right) + (1-a)\exp\left(-\frac{T}{T_3}\right), \tag{7.25}$$

where $a$, $T_1$, $T_2$, $T_3$ are the Troe coefficients of the reaction.

By combining the Van't Hoff law of all reaction affecting a given species $l$ in a grid cell $i$n productions and loss terms of the transport equation wan be written as :

$$P_l(y_{i,l}) = \sum_{m=1}^{N_{\text{reactions}}}\left[K^m(T_i)\prod_{l'=1}^{N_c}\left(y_{i,l'}n_i\right)\right] \tag{7.26}$$

and

$$L_l(y_{i,l}) = -\sum_{m=1}^{N_{\text{reactions}}}\left[K^m(T_i)\prod_{l'=1}^{N_c}\left(y_{i,l'}n_i\right)\right]. \tag{7.27}$$

Where $N_{\text{reaction}}$ is the number of reaction producing (destroying) species $l$ , and $N_c$ the number of species reacting in reaction $m$.

## 7.2.3. Flux of species

The flux of species is expressed as

$$\phi_l = K_{\text{rr}}n\frac{\partial}{\partial r}\left(\frac{n_l}{n}\right) \tag{7.28}$$

with $n$ being the total gas molecule number density and with $K_{rr}$ the diffusion coefficient in the radial direction in the CPD, expressed as

$$K_{\text{rr}} = \alpha h C_s. \tag{7.29}$$

The molecular flux can be described in terms of molar fraction $y_i = n_i/n$,

$$\phi_l = K_{\text{rr}}n\frac{\partial y_l}{\partial r}. \tag{7.30}$$

Assuming a perfect gas law, the total gas molecule number density is

$$n = \frac{P}{k_B T} \tag{7.31}$$

where $P$ is the CPD midplane pressure and $k_B$ is the Boltzmann constant.

## 7.3. Numerical scheme

We present the different numerical schemes tested to solve the continuity equation in CPD conditions. The principal difficulty comes from the radically different environment between the current application of `KIDA` to determine giant planets' atmosphere vertical composition profile (Venot et al. 2012).

By reformulating equation 7.7 using the molar fraction $y_l = n_l/n$, of species $l$ :

$$\frac{dy_l}{dt} = \frac{1}{n}\left(P_l + L_l - \nabla\cdot\phi_i\right). \tag{7.32}$$

where $n$ is only dependent on the pre-computed CPD model presented in chapter **??**.

### 7.3.1. Discretization

One can discretize equation 7.32 for a species $l$ in a grid cell $i$ . We express the discretized divergence of the flux $\nabla\cdot\phi$ such as :

$$\begin{aligned}\nabla\cdot\phi_{i,l} &= \frac{1}{r}\frac{\partial r\phi}{\partial r}\bigg|_{r_i} \\ &= \frac{r_{i+1/2}\phi_{i+1/2} - r_{i-1/2}\phi_{i-1/2}}{r_i\left(r_{i+1/2} - r_{i-1/2}\right)}\end{aligned} \tag{7.33}$$

Were $\phi_{i-1/2}$ and $\phi_{i+1/2}$ are expressed as :

$$\begin{cases}\phi_{i+1/2} = K_{\mathrm{rr},i+1/2}\, n_{i+1/2}\, \frac{y_{i+1}-y_i}{r_{i+1}-r_i} \\ \phi_{i-1/2} = K_{\mathrm{rr},i-1/2}\, n_{i-1/2}\, \frac{y_k-y_{i-1}}{r_k-r_{i-1}}\end{cases} \tag{7.34}$$

By combining equations 7.7 and 7.34 one have

$$\begin{aligned}\nabla\cdot\phi^i = &\frac{2}{r_i r_{i+1} - r_i r_{i-1}}\Bigg(r_{i+1/2}K_{\mathrm{rr},i+1/2}\, n_{i+1/2}\frac{y_{i+1}-y_i}{r_{i+1}-r_i} \\ &- r_{i-1/2}K_{\mathrm{rr},i-1/2}\, n_{i-1/2}\frac{y_i - y_{i-1}}{r_i - r_{i-1}}\Bigg).\end{aligned} \tag{7.35}$$

The quantities $K_{\mathrm{rr},i+1/2}$, $K_{\mathrm{rr},i-1/2}$, $n_{i+1/2}$ and $n_{i-1/2}$ are calculated at the interface

between two cells using a simple mean between the two cells :

$$\begin{cases} K_{\mathrm{rr},i+1/2} = \frac{K_{\mathrm{rr},i}+K_{\mathrm{rr},i+1}}{2}, \\ K_{\mathrm{rr},i-1/2} = \frac{K_{\mathrm{rr},i-1}+K_{\mathrm{rr},i}}{2}, \\ n_{i+1/2} = \frac{n_{i+1}+n_k}{2}, \\ n_{i-1/2} = \frac{n_k+n_{i-1}}{2} \end{cases} \tag{7.36}$$

## 7.3.2. Backward Differentiation Formula integration Scheme

Within the equation system formed by the continuity equation, all the unknown molar fractions are highly coupled together by the chemical productions ($P^n_{i,l}$) and losses ($L^n_{i,l}$) terms of the equation. Therefore, one can not use a simple explicit Euler scheme of the form

$$y^{n+1}_{i,l} = y^n_{i,l} + \Delta t \left( P^n_{i,l} + L^n_{i,l} - \nabla \cdot \phi^n_{i,l} \right). \tag{7.37}$$

This scheme is unstable and diverge toward non-physical values after a few time steps. To stabilize the scheme it would require a very small time step of order of $10^{-6}$ s, leading to computation times of several months to only do an evolution over a few thousand years. Consequently, one need an implicit integration scheme. We use the backward Euler integration scheme of the form

$$y^{n+1}_{i,l} = y^n_{i,l} + \Delta t \left( P^{n+1}_{i,l} + L^{n+1}_{i,l} - \nabla \cdot \phi^{n+1}_{i,l} \right). \tag{7.38}$$

Where the $P^{n+1}_{i,l}$, $L^{n+1}_{i,l}$, and $\phi^{n+1}_{i,l}$ are dependent on the molar fraction, $y^{n+1}_{i,l}$ which is an unknown of the equation. Equation 7.38 is a nonlinear equation that can be solved using iterative methods. We tested several methods of solving, firstly the Newton-Raphson method, secondly the JFNK method used to produce the CPD's thermal profiles (see Sec. 5.3.4) and lastly the FORTRAN subroutine `DLSODE` from the `ODEPACK` software (Radhakrishnan 1993) used in the works of Venot et al. (2012), Hue et al. (2015), and Cavalié et al. (2017).

To solve equation 7.38 one have to use an iterative method, such as the Newton-Raphson method or the JFNK method described in section 5.3.4. The JFNK does not require either the explicit computation and the inversion of the Jacobian matrix of the system, while the Newton-Raphson require its computation and inversion. In the following, we will detail the Newton-Raphson method used to solve equation 7.38.

We recall the $k+1$ iteration of the Newton-Raphson method to approximate solution vector $\vec{Y}^{n+1}$ contains the values $y^{n+1}_{i,l}$ for each compound ($l \in [1, N_c]$) and each cell ($i \in [1, N_r]$) at time iteration $n+1$. With $N_r$ and $N_c$ being the number of grid cells and compounds, respectively.

$$\vec{Y}^{n+1}_{k+1} = -\mathbf{J}^{-1}\left[\vec{Y}^{n+1}_k\right] \cdot F\left[\vec{Y}^{n+1}_k\right] + \vec{Y}^{n+1}_k \tag{7.39}$$

The vector $\vec{Y}^{n+1}$ is of dimension $N = N_c \times N_r$ and constructed such that

$$\vec{Y}^{n+1} = \begin{bmatrix} y_{1,1}^{n+1} \\ y_{1,2}^{n+1} \\ \vdots \\ y_{1,N_c}^{n+1} \\ y_{2,1}^{n+1} \\ y_{2,2}^{n+1} \\ \vdots \\ y_{i,l}^{n+1} \\ \vdots \\ y_{N_r,N_c}^{n+1} \end{bmatrix} \tag{7.40}$$

Similarly, we define the vector $\vec{F}^{n+1} = F\left[\vec{Y}^{n+1}\right]$ with components $f_{i,l}^{n+1}$ values of the function defined as :

$$\begin{aligned} f_{i,l}^{n+1} = & -y_{i,l}^{n} + y_{i,l}^{n+1} \\ & + \frac{\Delta t}{n_{i,l}}\left(P\left(y_{i,l}^{n+1}\right) + L\left(y_{i,l}^{n+1}\right)\right. \\ & - \frac{2}{r_i r_{i+1} - r_i r_{i-1}}\Big[ r_{i+1/2} K_{\mathrm{rr},i+1/2,l}\, n_{i+1/2,l} \frac{y_{i+1,l}^{n+1} - y_{i,l}^{n+1}}{r_{i+1} - r_i} \\ & \left. - r_{i-1/2} K_{\mathrm{rr},i-1/2,l}\, n_{i-1/2,l} \frac{y_{i,l}^{n+1} - y_{i-1,l}^{n+1}}{r_i - r_{i-1}} \Big]\right), \end{aligned} \tag{7.41}$$

where elements $y_{i,l}^{n}$ are the current values of the molar fractions and considered as constants. The vector $\vec{F}^{n+1}$ is then constructed as :

$$\vec{F}^{n+1} = \begin{bmatrix} f_{1,1}^{n+1} \\ f_{1,2}^{n+1} \\ \vdots \\ f_{1,N_c}^{n+1} \\ f_{2,1}^{n+1} \\ f_{2,2}^{n+1} \\ \vdots \\ f_{i,l}^{n+1} \\ \vdots \\ f_{N_r,N_c}^{n+1} \end{bmatrix} \tag{7.42}$$

### 7.3.3. Jacobian matrix construction and inversion

To perform the Newton-Raphson step from equation 7.39, one have to construct and invert the Jacobian matrix. The jacobian of the equation system 7.38 is defined as :

$$J^{p,q} = \frac{\partial F_p^{n+1}}{\partial Y_q^{n+1}} \tag{7.43}$$

where $F_p$ and $Y_q$ are the pth and qth elements of vectors $\vec{F}$ and $\vec{Y}$ such that :

$$\begin{cases} F_p^{n+1} = F_{I+N_c(L-1)}^{n+1} = f_{I,L}^{n+1}, \\ Y_q^{n+1} = Y_{i'+N_c(l'-1)}^{n+1} = y_{i',l'}^{n+1}. \end{cases} \tag{7.44}$$

Because of the architecture of vectors $\vec{F}$ and $\vec{Y}$, the resulting jacobian is a bloc matrix. Each submatrice having a size $(N_c \times N_c)$.

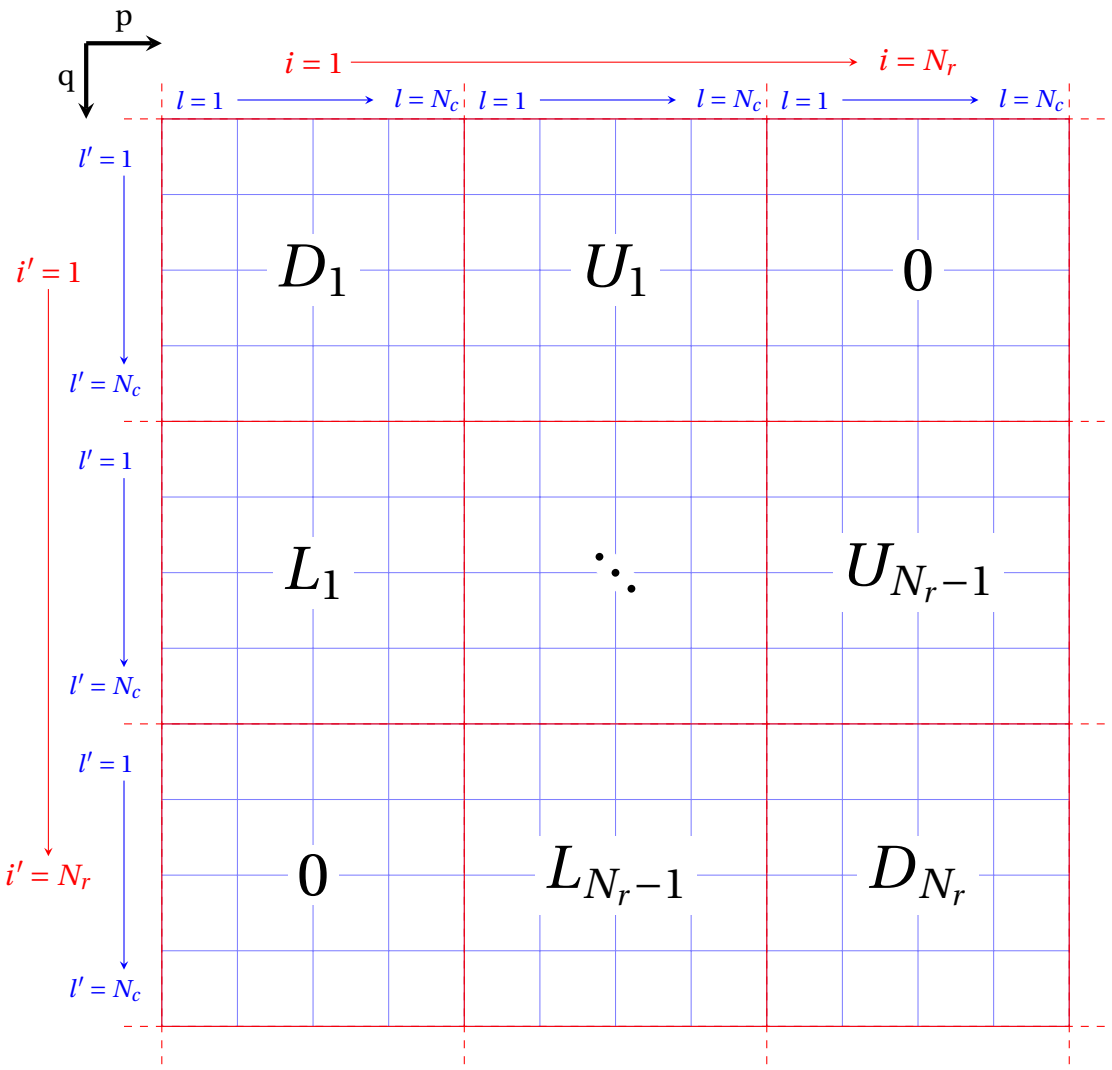


Figure 7.4.: Sketch of the structure of the jacobian matrix of the equation 7.38, defined as $J^{p,q} = \frac{\partial F_p}{\partial Y_p}$, expressed by the equation 7.45, where the indices $p$ and $q$ are in the range between 1 and $N_r \times N_c$. The Jacobian matrix is a tridiagonal block matrix with submatrices of size $(N_c \times N_c)$. The submatrices $\{D_1, \ldots, D_{N_r}\}$ are the diagonal matrices whose elements are defined by the equation 7.47 The submatrices $\{U_1, \ldots, U_{N_r-1}\}$ and $\{L_1, \ldots, L_{N_r-1}\}$ are the super- and subdiagonal submatrices. The super- and subdiagonal submatrices are diagonal matrices whose diagonal elements are defined by the equations 7.48 and 7.49. The rest of the submatrices are null and filled only with null elements.

By combining equations 7.41, 7.43 and 7.44, we rewrite the jacobian elements as :

$$
\begin{aligned}
J^{p,q} =& \delta_{q,p} + \frac{\Delta t}{n_i}\Bigg[\frac{\partial P\left(Y_p^{n+1}\right)}{\partial Y_q^{n+1}} + \frac{\partial L\left(Y_p^{n+1}\right)}{\partial Y_q^{n+1}} \\
& \frac{2\delta_{l,l'}}{r_i r_{i+1} - r_i r_{i-1}}\Bigg(\frac{r_{i+1/2} K_{\mathrm{rr},i+1/2,l} n_{i+1/2,l}}{r_{i+1} - r_i}\left(\delta_{i+1,i'} - \delta_{i,i'}\right) \\
& - \frac{r_{i-1/2} K_{\mathrm{rr},i-1/2,l} n_{i-1/2,l}}{r_i - r_{i-1}}\left(\delta_{i,i'} - \delta_{i-1,i'}\right)\Bigg)\Bigg]
\end{aligned}
\tag{7.45}
$$

with $\delta$ being the Kronecker delta.

$$
\delta_{i,j} = \begin{cases} 1 & \text{if} \quad i = j \\ 0 & \text{if} \quad i \neq j \end{cases} \quad . \tag{7.46}
$$

The structure of the jacobian matrix is depicted in figure 7.4, which show that the resulting matrix is a tridiagonal block matrix composed of diagonal sub-matrices :

$$
\begin{aligned}
D_{l,l'} =& \delta_{l,l'} + \frac{\Delta t}{n_i}\Bigg[\frac{\partial P\left(y_{i,l}^{n+1}\right)}{\partial y_{i,l'}^{n+1}} + \frac{\partial L\left(y_{i,l}^{n+1}\right)}{\partial y_{i,l'}^{n+1}} \\
& + \frac{2\delta_{l,l'}}{r_i r_{i+1} - r_i r_{i-1}}\left(\frac{r_{i+1/2} K_{\mathrm{rr},i+1/2,l} n_{i+1/2,l}}{r_{i+1} - r_i} + \frac{r_{i-1/2} K_{\mathrm{rr},i-1/2,l} n_{i-1/2,l}}{r_i - r_{i-1}}\right),
\end{aligned}
\tag{7.47}
$$

super-diagonal submatrices of the form :

$$
U_{l,l'} = \frac{-\Delta t}{n_i}\frac{2}{r_i r_{i+1} - r_i r_i i - 1}\frac{r_i K_{\mathrm{rr},i+1/2} n_{i+1/2}}{r_{i+1} - r_i}\delta_{l,l'}, \tag{7.48}
$$

and sub-diagonal submatrices of the form :

$$
L_{l,l'} = \frac{-\Delta t}{n_i}\frac{2}{r_i r_{i+1} - r_i r_i i - 1}\frac{r_i K_{\mathrm{rr},i-1/2} n_{i-1/2}}{r_i - r_{i-1}}\delta_{l,l'}. \tag{7.49}
$$

Both super– and sub-diagonal submatrices ($U_i$ and $L_i$) are diagonal matrices, while the diagonal submatrices ($D_i$) have non-diagonal elements determined by the chemical network productions and losses which derivatives are expressed as :

$$
\frac{\partial P\left(y_{i,l}^{n+1}\right)}{\partial y_{i,l'}^{n+1}} = \frac{1}{y_{i,l'}^{n+1}}\sum_{m}^{N_{\mathrm{reactions}}}\left(K^m \prod_{l}^{N_s} y_{i,l}^{n+1} n_i\right), \tag{7.50}
$$

and

$$
\frac{\partial L\left(y_{i,l}^{n+1}\right)}{\partial y_{i,l'}^{n+1}} = \frac{-1}{y_{i,l'}^{n+1}}\sum_{m}^{N_{\mathrm{reactions}}}\left(K^m \prod_{l}^{N_s} y_{i,l}^{n+1} n_i\right). \tag{7.51}
$$

with $N_{\mathrm{reactions}}$ the number of reactions producing or destroying species $l$ and $N_s$ the number of species reacting in reaction $m$.

The Jacobian inversion can be done efficiently with a back-substitution algorithm that allows the Newton-Raphson step to be computed. The most computationally intensive calculation of the algorithm is the inversion of the diagonal submatrices $D_i$. Due to the large amplitude of species production and destruction at a given time step $n$, the diagonal matrices are ill-conditioned. Therefore, a naive numerical inversion of these submatrices leads to large numerical errors.

To avoid those large numerical errors, one can proceed to a regularized Newton-Raphson method :

$$\delta \vec{Y}_k = -\left(\mathbf{J}\mathbf{J}^T + \lambda \mathbb{1}\right)^{-1} \mathbf{J}^T \cdot F\left[\vec{Y}_k\right], \tag{7.52}$$

where $\lambda$ is the regularization factor, which is a free parameter of the method for order of the trace of the jacobian matrix. The matrix $\mathbf{J}\mathbf{J}^T$ is better conditioned and have the same architecture as the jacobian matrix, $\mathbf{J}$ and can be efficiently inverted using the back-substitution method. The better conditioning of the matrix to invert come with the cost of a slower convergence of the Newton-Raphson method and consequently a longer computation time.

Another strategy is to suppress the Jacobian elements that cause bad conditioning. Very low production or destruction rate of a species is a cause of bad conditioning, so if a species production or destruction rate is less than one molecule of species $l$ per year, it is nullified:

$$\begin{cases} P\left(y_{i,l}\right) = 0 & \text{if} \quad P\left(y_{i,l}\right) < 3.17 \times 10^{-8}, \\ L\left(y_{i,l}\right) = 0 & \text{if} \quad L\left(y_{i,l}\right) < 3.17 \times 10^{-8}. \end{cases} \tag{7.53}$$

## 7.3.4. Boundary conditions

The inner and outer boundary conditions are built such that the second derivative of the molar fraction is null:

$$\left.\frac{d^2 y}{dr^2}\right|_{r=r_0} = 0 \tag{7.54}$$

and

$$\left.\frac{d^2 y}{dr^2}\right|_{r=r_{N_r}} = 0 \tag{7.55}$$

which lead to the following boundary conditions:

$$\begin{cases} y_{0,l} = 2y_{1,l} - y_{2,l}, \\ y_{N_r+1,l} = 2y_{N_r,l} - y_{N_r-1,l}. \end{cases} \tag{7.56}$$

Where $y_{0,l}$ and $y_{N_r+1,l}$ are the molar fractions of species $l$ in the inner and outer ghost cells located at distances $r_0$ and $r_{N_r+1}$:

$$\begin{cases} r_0 = 2r_1 - r_2, \\ r_{N_r+1} = 2r_{N_r} - r_{N_r-1}. \end{cases} \tag{7.57}$$

This boundary condition is equivalent to a simple linear interpolation of the quantities $y_{i,l}$ in the inner and outer ghost cells, and therefore sensitive to numerical error produced by the integration scheme.

## 7.4. Resolution instabilities

We present, in the following sections, encountered numerical instabilities using different stiff non-linear equation solver. We rapport results from the DLSODE solver, the Newton-Raphson method described in section 7.3 and the Jacobian-Free Newton-Krylov described in section 5.3.4.

**DLSODE** The DLSODE method used in the original works of Venot et al. (2012), Hue et al. (2015), and Cavalié et al. (2017) is based is a backward Euler integration scheme. The method require the computation of the Jacobian, calculated in 7.3.3 . Although the method is efficient to solve stiff non-linear differential equation, its resolution speed pose a huge problem. Because of the ill-conditioning of the system, the first time steps of the systems' evolution must be of order of $10^{-3}$ s with a time step resolution time of a few hours the required computation times is unrealistic. Such large computation time comes from the very slow convergence of the internal iterative resolution method. Even by filtering species production and destruction by chemical reaction lower than one molecule per year per cm$^3$ ( $3.17^{-8}$ cm$^{-3}$ s$^{-1}$), do not significantly reduce the computation time. Because we use the thermochemical equilibrium as a starting point, it is a possibility that this equilibrium is very far from the dynamic equilibrium, therefore producing huge variations during the first time steps to reach equilibrium.

**Newton-Raphson** The resolution of the backward Euler step using the Newton-Raphson method, presented in section 7.3, is faster than the DLSODE method, typically a few minutes, however it still faces an instability which grow from the inner and outer boundaries of the grid and explode after a few tens of time steps. The propagation of boundaries instabilities can be the sign of the bad boundary conditions or grid too coarse near the boundaries. Here we present actions taken to stabilize the scheme. A first hypothesis of the instability of the scheme was the ill-conditioning of the system due to the wide range of the pressure and temperature profiles used for the numerical tests, which span up to five and two orders of magnitude, respectively. We therefore constrained the computation box to a smaller outer region of the CPD, between 10 and 30 $R_\mathrm{J}$. Although it stabilizes the scheme, boundary instabilities still appear.

By performing a simple numerical in an experiment where the chemistry is deactivated, leaving only the advection–diffusion part of the equation, show a stable

evolution of the species' molar fraction. Therefore, narrowing the instabilities toward the chemical network.

**JFNK method** Finally, we tested to solve the time step using the JFNK method used to resolve the CPD structure and depicted in section 5.3.4. This method is much slower, but is of use to assert the validity of the Jacobian matrix we constructed, since this method does not require an explicit jacobian, if it does not converge one can rule out a possible error in the jacobian construction.

It shows the same behavior as for the Newton-Raphson method. The advection diffusion resolution alone gives coherent results, while the resolution of the chemical reaction lead to numerical instabilities after a few time steps.

**Future works** Future investigation on the evolution of chemical species in the CPD involve refining the numerical method presented above. Firstly, the development of a preconditioner is an ongoing work for both the JFNK and the Newton-Raphson methods. A preconditioner matrix modify the equation system such that :

$$\mathbf{P}^{-1}\mathbf{A}\vec{x} = \mathbf{M}^{-1}\vec{b} \tag{7.58}$$

where $\mathbf{P}$ is the preconditioner matrix which, in our case, should approximate the value of the Jacobian matrix, be non-singular and eigenvalues of $\mathbf{P}^{-1}\mathbf{A}$ should be clustered around 1. The use of a preconditioner should help to solve the stiff non-linear equation and better manage the large difference in production and losses of each species, ill conditioning the jacobian matrix.

# Conclusion

This work explores the origins of the solar system, focusing on the formation of giant planets within the PPD and the Galilean moons within the circumplanetary disk CPD of Jupiter. It serves as a foundation for constructing a coherent history of the Jovian system, with the goal of supporting the scientific objectives of the ESA/JUICE and NASA/Europa Clipper missions.

The study is twofold. The first part is dedicated to the formation of the giant planets Jupiter, Saturn, Uranus, and Neptune. Building upon the work of Aguichine et al. (2022), we investigate the impact of volatile species trapped in clathrate hydrates and amorphous water ice on the distribution of these species within a 1+1D $\alpha$- viscous accretion disk. We demonstrate that clathrate hydrates bring volatile species in solid form closer to the Sun than when considering only pure condensates. This results in enrichment peaks at the clathration lines, up to 2 AU closer to the Sun than the corresponding condensation lines. Volatile species trapped in amorphous water ice, on the other hand, are only released at the amorphous-to-crystalline transition zone (ACTZ), creating a distinct enrichment peak centered around 5 AU.

Using these models, we compare the composition of the PPD with the observed atmospheric compositions of the giant planets. In a PPD devoid of amorphous water ice, Jupiter's atmospheric composition matches the PPD's composition in a region around 4 AU after 0.8 to 1 Myr of evolution. However, if amorphous ice is considered, this period shortens to between 20 and 100 kyr in a region between 4 and 6 AU. For Saturn, in a disk without amorphous ice, no matching period exists in the region between 5 and 7 AU. In contrast, when amorphous ice is included, a matching period emerges between 30 and 400 kyr of PPD evolution.

Comparing the PPD model with estimates of the carbon enrichment in Uranus and Neptune suggests that the ice giants could have formed between 7 and 9 AU over a period of 0.5 to 1 Myr, but only in the absence of amorphous ice. This location is near the CO condensation line in our model, prompting further investigation. Our analysis predicts that if the gas giants formed in the vicinity of the CO condensation line, it would result in noble gazes enrichment at this location, up to a thousand times protosolar values.

While this approach provides a preliminary estimate of the giant planets' building block compositions based on their atmospheric data, the available measurement, especially for Saturn, Uranus, and Neptune, remain limited. Thus, the analysis is

constrained by the precision of existing in-situ measurements. To refine our model and better understand the origins of the giant planets, further measurements of their deep atmospheric compositions are necessary, possibly using re-entry probes similar to the Galileo probe at Jupiter. Although the *ESA/Hera* mission, which would have provided insight into Saturn's deep composition (Mousis et al. 2016b), was ultimately not selected, NASA's decadal survey has emphasized the importance of exploring the ice giants. The proposed *Uranus Orbiter and Probe* mission would offer a deeper understanding of the ice giants' compositions, for which we currently only know that they are carbon-rich (Simons et al. 2021).

Another limitation of our model is that it does not consider planetesimal formation, focusing only on pebble accretion. Depending on the formation process, the planet's building blocks may originate from different regions of the PPD, which would affect our analysis. However, the timescales we propose, under 1 Myr, are consistent with the pebble accretion formation model (Bitsch et al. 2015; Alibert et al. 2018; Armitage et al. 2019; Bitsch et al. 2019; Venturini et al. 2020) and the observed carbonaceous chondrite dichotomy (Kleine et al. 2020). Additionally, we do not account for planetary migration, assuming in-situ formation. A migrating planetary core would accrete material from different regions of the PPD (Masset et al. 2003; Schneider et al. 2021), which could influence our findings. While planetary migration may contradict in-situ formation, recent 3D hydrodynamic simulations suggest that type I and II migrations could be slower than previously thought (Chrenko et al. 2020; Lega et al. 2021; Chametla et al. 2022).

To disentangle between the two cases, a better understanding of the clathrate cages formation is needed. This work use theoretical equation of states, fitted over data that has been taken a pressures orders of magnitude higher than the one in our PPD model. Furthermore, the presence of clathrate has yet to be confirmed within the icy solar system's bodies. Clathrate hydrate cages have been invoked to explain the release of $O_2$ by the comet 67P/Churyumov–Gerasimenko (Mousis et al. 2016a) , to explain the composition of Titan atmosphere (Mousis et al. 2009). However, direct observation of clathrate on the outer solar system bodies, such as comets and trans-Neptunian objects are yet to be done. Study of Dartois et al. (2021) show that the kinetic at low temperature show that the clathration could be significant only in big bodies such a planets or satellites.

In conclusion, our model shows that the known compositions of the giant planets can be reproduced both with and without the presence of amorphous water ice in the PPD, leaving the question of its presence unresolved.

The second part of this work focuses on the structure and evolution of Jupiter's CPD. We developed a 2D CPD model, that demonstrate the significance of Jupiter's heating, which can raise CPD temperatures to as high as 2000 K. This heating notably affects the inner regions of the CPD, when the disk becomes less massive and more diffuse.

If the CPD's lifetime is less than 1 Myr, during the transitional phase from a dense to a sparse disk, shadows are cast from the inner regions onto the outskirts of the CPD. These shadows significantly influence the disk's structure, causing a temperature drop of up to 100 K and a pressure increase by a factor of approximately two.

We tested the robustness of our result by varying the CPD lifetime. We show that when we consider a CPD depleting over a timescale of 3 Myr, the CPD remain hot for over 1 Myr. Over this period of time, the planet cools down significantly. As a consequence, Jupiter's heating is never stronger than the viscous heating over the simulation period. For this reason, shadowed regions are not cooler than their surrounding in this case.

Moreover, we showed that the CPD's material metallicity, which translates into dust-to-gas ratio in the model, has a major impact on the extent and duration of the shadows across the CPD. With a material metallicity of 0.1 times the protosolar value, the shadows vanish from the CPD after 160 kyr, while when we consider a metallicity 10 times the protosolar value, the shadows vanish after 230 kyr of CPD evolution, a major difference of 70 kyr.

In addition, we showed that cold traps have an impact on the volatile species distribution within the CPD. We first did a simple computation of the position of the condensation lines, using protosolar abundances as a reference. We show that the cold traps could indeed induce the condensation of $H_2O$, $NH_3$, $CO_2$ and $H_2S$. Therefore, motivating a detailed study of the volatile distribution within the CPD.

We then studied the evolution of volatiles within the CPD, considering only their pure condensate and vapor phases. In this part of the study, we were not able to consider the model versions that contained cold traps because of persisting numerical instabilities on their edges. However, we considered two cases, the first case is the model version where the CPD last for 3 Myr, where Jupiter's heating and shadows are considered but without the formation of cold traps. According to that case, the condensation lines of all considered species are beyond the centrifugal radius of the CPD located at 50 $R_J$except for $H_2O$. The direct consequence of this situation is the rapid depletion of those species under 10 kyr of evolution. After 200 kyr of evolution, only $H_2O$ remains, with an enrichment peak at its condensation line of 1.2 times its initial abundance. The second case is the model where the CPD last for 1 Myr, but without considering Jupiter's heating. This result in a cold CPD where the condensation lines of the species are all located within the centrifugal radius. This lead to volatile species enrichment between 0.1 and 1.2 times their initial abundances, below unity. Thus showing that because of the rapid dynamic of the CPD, in this model, a large enrichment peak can not be sustained. Because both cases lead to radically different results, it motivates the ongoing study of the cold traps, which could show radical differences from the two cases.

This first approach of the study of the evolution of volatile species within the CPD, because of the radically different composition profiles, shows that the CPD properties could imprint a compositional signature within the Galilean moon's bulk composition. A *hot* CPD model would lead to volatile–poor moons, while a *cold* CPD model would lead to volatile–rich moons.

In addition to the 2D CPD model, we explored the hypothesis of a "dry" CPD, where water is primarily supplied by hydrated minerals. This investigation was motivated by oxygen abundance measurements from the JUNO mission, which, at a 2-$\sigma$ confidence level, do not rule out the possibility of subsolar oxygen abundance in Jupiter's atmosphere (Li et al. 2020). If this high oxygen depletion hypothesis holds, it would suggest that both Jupiter and its CPD accreted solids that were water-depleted. We propose that chondritic material, rich in phyllosilicate minerals, was delivered to the Jovian system. Phyllosilicates can retain up to 13 wt% of water, making them a potential significant source of water in a "dry" CPD scenario.

For this, we adapted the 1D model developed by Anderson et al. (2021) to the Jovian system, focusing on phyllosilicates minerals evolution. Our findings show that hydrated minerals alone can account for building blocks with water mass fractions as high as 50 wt%, demonstrating that hydrated minerals could be a viable source of water in the CPD. However, the dehydration temperature of the hydrated mineral in the low-pressure environment of the CPD is highly uncertain. Results would vary greatly with the dehydration temperature, the higher the dehydration temperature, the lower the final building blocks water mass fraction becomes.

According to this hypothesis, Io would have formed from dry silicate, leftover of the phyllosilicate dehydration and Europa from chondritic material within the water condensation line. Ganymede and Callisto would have formed from material originating from the water condensation line, composed of phyllosilicate grains coated with water ice.

Inspired by these results, we tested the hypothesis of a dry disk in the context of the exoplanetary system TRAPPIST-1, where planets exhibit structures and water mass fractions similar to those of the Galilean moons (Acuña et al. 2021). Adapting the PPD model from the first part of this work to the TRAPPIST-1 system, we showed that, if its PPD contained only hydrated minerals, we could form building blocks with water mass fractions consistent with the estimates by Acuña et al. (2021) . While the TRAPPIST-1 PPD may not have been entirely dry, this suggests that hydrated minerals may have played a role in the distribution of water within both PPDs and CPDs.

The third part of this work involved developing a self-consistent chemical model to study the gas-phase chemical composition of the CPD, building upon the models of Venot et al. (2012), Cavalié et al. (2017), and Cavalié et al. (2023). This is a first step toward modeling the chemical composition of the solids in the CPD. We present results for thermochemical equilibrium within the 2D CPD model, revealing vertical

compositional layering consistent with expectations (Woitke et al. 2016). Furthermore, we showed the impact of the shadow on the composition of the CPD at thermochemical equilibrium, with sudden drops or increase in molecule abundances in the gas phase.

However, while thermochemical equilibrium is a good approximation for the hot midplane of the CPD, where chemical timescales are shorter than viscous timescales, it does not accurately represent the chemical composition of the cold midplane or the upper layers of the CPD, where the viscous timescale is shorter than the chemical timescale. We presented the numerical developments and the challenge we are facing. The chemical evolution, combined to the viscous diffusion of the molecule, produce an ill-conditioned system of equation that remain numerically unstable. This ongoing study has showed promising results at thermochemical equilibrium and will be pursued in the future.

In conclusion, this research represents the first step toward a self-consistent understanding of the origin of the Jovian system, from Jupiter's formation in the PPD to the formation of the Galilean moons in the CPD. However, much development remains to be done. This includes understanding the impact of Jupiter's formation on the distribution of volatile in its neighborhood, determining the timing and mechanism of the Galilean moons' formation, and comprehending the formation and evolution of the CPD, including the accretion mechanisms and their effects on the composition of the accreted material. Future work will focus on improving the chemical model of the CPD to create a self-consistent model of the composition of the solids within the CPD. This will help us understand the accretion mechanisms of the moons and study the alteration of their initial building block compositions.

This theoretical work relies on the discoveries to be made by future missions such as ESA/JUICE and NASA/Europa Clipper, which will enhance our understanding of the structure and bulk composition of the Jovian system. Finally, it highlights the need for the probing of the atmospheres of the giant planets to understand and disentangle the existing hypothesis on the planet's formation sequence.

# Bibliography


ACUÑA et al., 2021. Characterisation of the Hydrospheres of TRAPPIST-1 Planets. *Astronomy and Astrophysics*. Vol. 647, A53. ISSN 0004-6361. Available from DOI: 10.1051/0004-6361/202039885 (cit. on pp. 15, 141, 142, 148, 150, 151, 178).

AGOL et al., 2021. Refining the Transit-timing and Photometric Analysis of TRAPPIST-1: Masses, Radii, Densities, Dynamics, and Ephemerides. *The Planetary Science Journal*. Vol. 2, p. 1. ISSN 2632-3338. Available from DOI: 10.3847/PSJ/abd022 (cit. on p. 141).

AGUICHINE, 2022. *Retracer Le Parcours de Composés Volatils : Des Disques Circumstellaires Aux Intérieurs Planétaires*. Available also from: https://theses.fr/2022AIXM0422. These de doctorat. Aix-Marseille (cit. on pp. 10, 33, 53, 56, 57).

AGUICHINE; MOUSIS; DEVOUARD; RONNET, 2020. Rocklines as Cradles for Refractory Solids in the Protosolar Nebula. *The Astrophysical Journal*. Vol. 901, no. 2, p. 97. ISSN 1538-4357. Available from DOI: 10.3847/1538-4357/abaf47 (cit. on pp. 53, 57, 60, 63, 115, 155).

AGUICHINE; MOUSIS; LUNINE, 2022. The Possible Formation of Jupiter from Supersolar Gas. *The Planetary Science Journal*. Vol. 3, no. 6, p. 141. ISSN 2632-3338. Available from DOI: 10.3847/PSJ/ac6bf1 (cit. on pp. 8, 9, 11, 33, 39, 41, 42, 53, 57, 63, 81, 175).

AGÚNDEZ et al., 2012. The Impact of Atmospheric Circulation on the Chemistry of the Hot Jupiter HD 209458b. *Astronomy and Astrophysics*. Vol. 548, A73. ISSN 0004-6361. Available from DOI: 10.1051/0004-6361/201220365 (cit. on pp. 15, 154).

ALEXANDER, 2019. Quantitative Models for the Elemental and Isotopic Fractionations in the Chondrites: The Non-Carbonaceous Chondrites. *Geochimica et Cosmochimica Acta*. Vol. 254, pp. 246–276. ISSN 0016-7037. Available from DOI: 10.1016/j.gca.2019.01.026 (cit. on pp. 10, 46).

ALIBERT; MOUSIS; BENZ, 2005. Modeling the Jovian Subnebula: I. Thermodynamic Conditions and Migration of Proto-Satellites. *Astronomy & Astrophysics*. Vol. 439, no. 3, pp. 1205–1213. ISSN 0004-6361, ISSN 1432-0746. Available from DOI: 10.1051/0004-6361:20052841 (cit. on p. 98).

ALIBERT et al., 2018. The Formation of Jupiter by Hybrid Pebble–Planetesimal Accretion. *Nature Astronomy*. Vol. 2, no. 11, pp. 873–877. ISSN 2397-3366. Available from DOI: 10.1038/s41550-018-0557-2 (cit. on p. 176).

ANDERSON et al., 2024. Molecular Gas Tracers in Young and Old Protoplanetary Disks. *The Astrophysical Journal*. Vol. 966, no. 1, p. 84. ISSN 0004-637X, ISSN 1538-4357. Available from DOI: 10.3847/1538-4357/ad2fa2 (cit. on p. 159).

ANDERSON; LAU; SJOGREN; SCHUBERT; MOORE, 1996. Gravitational Constraints on the Internal Structure of Ganymede. *Nature*. Vol. 384, no. 6609, pp. 541–543. ISSN 1476-4687. Available from DOI: 10.1038/384541a0 (cit. on p. 37).

ANDERSON et al., 1998. Europa's Differentiated Internal Structure: Inferences from Four Galileo Encounters. *Science*. Vol. 281, p. 2019. ISSN 0036-8075. Available from DOI: 10.1126/science.281.5385.2019 (cit. on pp. 37, 135).

ANDERSON; MOUSIS; RONNET, 2021. Formation Conditions of Titan's and Enceladus's Building Blocks in Saturn's Circumplanetary Disk. *The Planetary Science Journal*. Vol. 2, no. 2, p. 50. ISSN 2632-3338. Available from DOI: 10.3847/PSJ/abe0ba (cit. on pp. 14, 39, 98, 126, 135, 137, 178).

ARMITAGE; KLEY, 2019. *From Protoplanetary Disks to Planet Formation: Saas-Fee Advanced Course 45. Swiss Society for Astrophysics and Astronomy*. Vol. 45. Ed. by AUDARD; MEYER; ALIBERT. Berlin, Heidelberg: Springer Berlin Heidelberg. Saas-Fee Advanced Course. Available from DOI: 10.1007/978-3-662-58687-7_1 (cit. on pp. 54, 176).

ASPLUND; GREVESSE; SAUVAL; SCOTT, 2009. The Chemical Composition of the Sun. *Annual Review of Astronomy and Astrophysics*. Vol. 47, no. 1, pp. 481–522. ISSN 0066-4146, ISSN 1545-4282. Available from DOI: 10.1146/annurev.astro.46.060407.145222 (cit. on p. 85).

ATREYA; MAHAFFY; NIEMANN; WONG; OWEN, 2003. Composition and Origin of the Atmosphere of Jupiter—an Update, and Implications for the Extrasolar Giant Planets. *Planetary and Space Science*. Vol. 51, no. 2, pp. 105–112. ISSN 00320633. Available from DOI: 10.1016/S0032-0633(02)00144-7 (cit. on p. 81).

ATREYA; WONG, 2005. Coupled Clouds and Chemistry of the Giant Planets— A Case for Multiprobes. *Space Science Reviews*. Vol. 116, pp. 121–136. ISSN 0038-6308. Available from DOI: 10.1007/s11214-005-1951-5 (cit. on p. 96).

ATREYA et al., 2018. The Origin and Evolution of Saturn, with Exoplanet Perspective. In: BAINES; FLASAR; KRUPP; STALLARD (eds.). *Saturn in the 21st Century*. 1st ed. Cambridge University Press, pp. 5–43. ISBN 978-1-316-22722-0 978-1-107-10677-2 978-1-107-51446-1. Available from DOI: 10.1017/9781316227220.002 (cit. on p. 83).

ATREYA et al., 2020. Deep Atmosphere Composition, Structure, Origin, and Exploration, with Particular Focus on Critical in Situ Science at the Icy Giants. *Space Science Reviews*. Vol. 216, p. 18. ISSN 0038-6308. Available from DOI: 10.1007/s11214-020-0640-8 (cit. on p. 96).

AVENHAUS et al., 2018. Disks ARound TTauri Stars with Sphere (DARTTS-S) I: Sphere / IRDIS Polarimetric Imaging of 8 Prominent TTauri Disks. *The Astrophysical Journal*. Vol. 863, no. 1, p. 44. ISSN 0004-637X, ISSN 1538-4357. Available from DOI: 10.3847/1538-4357/aab846 (cit. on p. 29).

AYLIFFE; BATE, 2009. *Circumplanetary Disc Properties Obtained from Radiation Hydrodynamical Simulations of Gas Accretion by Protoplanets*. Vol. 397. No. 2. Available from DOI: 10.1111/j.1365-2966.2009.15002.x (cit. on p. 99).

BAR-NUN; NOTESCO; OWEN, 2007. Trapping of N2, CO and Ar in Amorphous Ice—Application to Comets. *Icarus*. Vol. 190, no. 2, pp. 655–659. ISSN 00191035. Available from DOI: 10.1016/j.icarus.2007.03.021 (cit. on pp. 10, 28, 45, 63).

BATYGIN; BROWN, 2010. Early Dynamical Evolution Of The Solar System: Pinning Down The Initial Conditions Of The Nice Model. *The Astrophysical Journal*. Vol. 716, no. 2, pp. 1323–1331. ISSN 0004-637X, ISSN 1538-4357. Available from DOI: 10.1088/0004-637X/716/2/1323 (cit. on pp. 83, 85).

BATYGIN; BROWN; BETTS, 2012. Instability-Driven Dynamical Evolution Model Of A Primordially Five-Planet Outer Solar System. *The Astrophysical Journal*. Vol. 744, no. 1, p. L3. ISSN 2041-8205, ISSN 2041-8213. Available from DOI: 10.1088/2041-8205/744/1/L3 (cit. on p. 83).

BATYGIN; MORBIDELLI, 2020. Formation of Giant Planet Satellites. *The Astrophysical Journal*. Vol. 894, no. 2, p. 143. ISSN 1538-4357. Available from DOI: 10.3847/1538-4357/ab8937 (cit. on pp. 101, 115).

BECK et al., 2010. Hydrous Mineralogy of CM and CI Chondrites from Infrared Spectroscopy and Their Relationship with Low Albedo Asteroids. *Geochimica et Cosmochimica Acta*. Vol. 74, pp. 4881–4892. ISSN 0016-7037. Available from DOI: 10.1016/j.gca.2010.05.020 (cit. on pp. 10, 46).

BECK et al., 2014. Transmission Infrared Spectra (2-25 $\mu$m) of Carbonaceous Chondrites (CI, CM, CV-CK, CR, C2 Ungrouped): Mineralogy, Water, and Asteroidal Processes. *Icarus*. Vol. 229, pp. 263–277. ISSN 0019-1035. Available from DOI: 10.1016/j.icarus.2013.10.019 (cit. on pp. 10, 46).

BELL; LIN, 1994. Using FU Orionis Outbursts to Constrain Self-Regulated Protostellar Disk Models. *The Astrophysical Journal*. Vol. 427, p. 987. ISSN 0004-637X, ISSN 1538-4357. Available from DOI: 10.1086/174206 (cit. on p. 55).

BENISTY et al., 2021. *A Circumplanetary Disk around PDS70c*. Vol. 916. No. L2. Available from DOI: 10.3847/2041-8213/ac0f83 (cit. on pp. 34, 38).

BERTAUX; BELTON, 1979. Evidence of SO2 on Io from UV Observations. *Nature*. Vol. 282, pp. 813–815. ISSN 0028-0836. Available from DOI: 10.1038/282813a0 (cit. on p. 36).

BIERSON; NIMMO, 2020. Explaining the Galilean Satellites' Density Gradient by Hydrodynamic Escape. *The Astrophysical Journal*. Vol. 897, p. L43. ISSN 0004-637X. Available from DOI: 10.3847/2041-8213/aba11a (cit. on p. 140).

BIRNSTIEL; KLAHR; ERCOLANO, 2012. A Simple Model for the Evolution of the Dust Population in Protoplanetary Disks. *Astronomy & Astrophysics*. Vol. 539, A148. ISSN 0004-6361, ISSN 1432-0746. Available from DOI: 10.1051/0004-6361/201118136 (cit. on pp. 11, 54, 57–60, 63).

BISCHOFF, 1998. Aqueous Alteration of Carbonaceous Chondrites: Evidence for Preaccretionary Alteration. A Review. *Meteoritics and Planetary Science*. Vol. 33, pp. 1113–1122. ISSN 1086-9379. Available from DOI: 10.1111/j.1945-5100.1998.tb01716.x (cit. on p. 46).

BITSCH; LAMBRECHTS; JOHANSEN, 2015. The Growth of Planets by Pebble Accretion in Evolving Protoplanetary Discs. *Astronomy and Astrophysics*. Vol. 582, A112. ISSN 0004-6361. Available from DOI: 10.1051/0004-6361/201526463 (cit. on pp. 83, 176).

BITSCH; RAYMOND; IZIDORO, 2019. Rocky Super-Earths or Waterworlds: The Interplay of Planet Migration, Pebble Accretion, and Disc Evolution. *Astronomy & Astrophysics*. Vol. 624, A109. ISSN 0004-6361, ISSN 1432-0746. Available from DOI: 10.1051/0004-6361/201935007 (cit. on pp. 83, 141, 152, 176).

BLAKELY et al., 2024. *The James Webb Interferometer: Space-based Interferometric Detections of PDS 70 b and c at 4.8 $\mu$m*. 2024-04-19. Available from arXiv: 2404.13032 [astro-ph] (cit. on p. 34).

BOOTH; CLARKE; MADHUSUDHAN; ILEE, 2017. Chemical Enrichment of Giant Planets and Discs Due to Pebble Drift. *Monthly Notices of the Royal Astronomical Society*. Vol. 469, no. 4, pp. 3994–4011. ISSN 0035-8711, ISSN 1365-2966. Available from DOI: 10.1093/mnras/stx1103 (cit. on pp. 9, 41).

BREARLEY, 2006. *The Action of Water*. Available also from: https://ui.adsabs.harvard.edu/abs/2006mess.book..584B (cit. on p. 47).

BRUDERER, 2013. Survival of Molecular Gas in Cavities of Transition Disks - I. CO. *Astronomy & Astrophysics*. Vol. 559, A46. ISSN 0004-6361, ISSN 1432-0746. Available from DOI: 10.1051/0004-6361/201321171 (cit. on p. 38).

BURKHARDT et al., 2019. Modeling C-shock Chemistry in Isolated Molecular Outflows. *The Astrophysical Journal*. Vol. 881, no. 1, p. 32. ISSN 1538-4357. Available from DOI: 10.3847/1538-4357/ab2be8 (cit. on pp. 28, 46).

CANUP; WARD, 2002. Formation of the Galilean Satellites: Conditions of Accretion. *The Astronomical Journal*. Vol. 124, no. 6, pp. 3404–3423. ISSN 00046256, ISSN 15383881. Available from DOI: 10.1086/344684 (cit. on pp. 12, 97–100, 115, 126, 135, 140).

CANUP; WARD, 2006. A Common Mass Scaling for Satellite Systems of Gaseous Planets. *Nature*. Vol. 441, no. 7095, pp. 834–839. ISSN 0028-0836, ISSN 1476-4687. Available from DOI: 10.1038/nature04860 (cit. on pp. 12, 97–100, 135).

CAVALIÉ; LUNINE; MOUSIS, 2023. A Subsolar Oxygen Abundance or a Radiative Region Deep in Jupiter Revealed by Thermochemical Modelling. *Nature Astronomy*. Vol. 7, pp. 678–683. ISSN 2397-3366. Available from DOI: 10.1038/s41550-023-01928-8 (cit. on pp. 33, 178).

CAVALIÉ et al., 2017. Thermochemistry and Vertical Mixing in the Tropospheres of Uranus and Neptune: How Convection Inhibition Can Affect the Derivation of Deep Oxygen Abundances. *Icarus*. Vol. 291, pp. 1–16. ISSN 00191035. Available from DOI: 10.1016/j.icarus.2017.03.015 (cit. on pp. 15, 162, 167, 173, 178).

CHAMETLA; CHRENKO, 2022. Spreading Pressure Bumps in Gas-Dust Discs Can Stall Planet Migration via Planet-Vortex Interactions. *Monthly Notices of the Royal Astronomical Society*. Vol. 512, pp. 2189–2201. ISSN 0035-8711. Available from DOI: 10.1093/mnras/stac611 (cit. on p. 176).

CHRENKO; NESVORNÝ, 2020. Migration of Gap-Opening Planets in 3D Stellar-Irradiated Accretion Disks. *Astronomy and Astrophysics*. Vol. 642, A219. ISSN 0004-6361. Available from DOI: 10.1051/0004-6361/202038988 (cit. on p. 176).

CHRISTIAENS et al., 2019. *Evidence for a Circumplanetary Disk around Protoplanet PDS 70 b*. Vol. 877. No. L33. Available from DOI: 10.3847/2041-8213/ab212b (cit. on pp. 34, 38).

CIESLA; LAURETTA; COHEN; HOOD, 2003. A Nebular Origin for Chondritic Fine-Grained Phyllosilicates. *Science*. Vol. 299, no. 5606, pp. 549–552. Available from DOI: 10.1126/science.1079427 (cit. on p. 46).

CLOUTIS et al., 2008. Spectral Reflectance Properties of Minerals Exposed to Simulated Mars Surface Conditions. *Icarus*. Vol. 195, no. 1, pp. 140–168. ISSN 00191035. Available from DOI: 10.1016/j.icarus.2007.10.028 (cit. on pp. 10, 47).

CLOUTIS et al., 2007. Stability of Hydrated Minerals on Mars. *Geophysical Research Letters*. Vol. 34, no. 20, p. L20202. ISSN 0094-8276. Available from DOI: 10.1029/2007GL031267 (cit. on pp. 10, 47).

COLEMAN; LELEU; ALIBERT; BENZ, 2019. Pebbles versus Planetesimals: The Case of Trappist-1. *Astronomy & Astrophysics*. Vol. 631, A7. ISSN 0004-6361, ISSN 1432-0746. Available from DOI: 10.1051/0004-6361/201935922 (cit. on pp. 141, 152).

COLLINS et al., 2022. Episodic Plate Tectonics on Europa: Evidence for Widespread Patches of Mobile-Lid Behavior in the Antijovian Hemisphere. *Journal of Geophysical Research: Planets*. Vol. 127, no. 11, e2022JE007492. ISSN 2169-9100. Available from DOI: 10.1029/2022JE007492 (cit. on p. 36).

COPPENS; DE RUYCK; KONNOV, 2007. The Effects of Composition on Burning Velocity and Nitric Oxide Formation in Laminar Premixed Flames of CH4 + H2 + O2 + N2. *Combustion and Flame*. Vol. 149, no. 4, pp. 409–417. ISSN 0010-2180. Available from DOI: 10.1016/j.combustflame.2007.02.004 (cit. on p. 162).

CORADINI; MAGNI; TURRINI, 2010. From Gas to Satellitesimals: Disk Formation and Evolution. *Space Science Reviews*. Vol. 153, pp. 411–429. ISSN 0038-6308. Available from DOI: 10.1007/s11214-009-9611-9 (cit. on p. 97).

D'ANGELO; HENNING; KLEY, 2002. Nested-Grid Calculations of Disk-Planet Interaction. *Astronomy and Astrophysics*. Vol. 385, pp. 647–670. ISSN 0004-6361. Available from DOI: 10.1051/0004-6361:20020173 (cit. on p. 98).

D'ANGELO; CAZAUX; KAMP; THI; WOITKE, 2019. Water Delivery in the Inner Solar Nebula. Monte Carlo Simulations of Forsterite Hydration. *Astronomy and Astrophysics*. Vol. 622, A208. ISSN 0004-6361. Available from DOI: 10.1051/0004-6361/201833715 (cit. on p. 46).

DARTOIS; LANGLET, 2021. Carbon Dioxide Clathrate Hydrate Formation at Low Temperature: Diffusion-limited Kinetics Growth as Monitored by FTIR. *Astronomy & Astrophysics*. Vol. 652, A74. ISSN 0004-6361, ISSN 1432-0746. Available from DOI: 10.1051/0004-6361/202140858 (cit. on p. 176).

DAVIES; PERRY; WILLIAMS; NELSON, 2024. Io's Polar Volcanic Thermal Emission Indicative of Magma Ocean and Shallow Tidal Heating Models. *Nature Astronomy*. Vol. 8, no. 1, pp. 94–100. ISSN 2397-3366. Available from DOI: 10.1038/s41550-023-02123-5 (cit. on p. 36).

De la VILLARMOIS et al., 2022. Physical Properties of Accretion Shocks toward the Class I Protostellar System Oph-IRS 44. *Astronomy & Astrophysics*. Vol. 667, A20. ISSN 0004-6361, ISSN 1432-0746. Available from DOI: 10.1051/0004-6361/202244312 (cit. on p. 28).

DEBRAS; CHABRIER, 2019. New Models of Jupiter in the Context of Juno and Galileo. *The Astrophysical Journal*. Vol. 872, p. 100. ISSN 0004-637X. Available from DOI: 10.3847/1538-4357/aaff65 (cit. on p. 33).

DESCH; ESTRADA; KALYAAN; CUZZI, 2017. Formulas for Radial Transport in Protoplanetary Disks. *The Astrophysical Journal*. Vol. 840, no. 2, p. 86. ISSN 1538-4357. Available from DOI: 10.3847/1538-4357/aa6bfb (cit. on p. 57).

DRĄŻKOWSKA; ALIBERT, 2017. Planetesimal Formation Starts at the Snow Line. *Astronomy & Astrophysics*. Vol. 608, A92. ISSN 0004-6361, ISSN 1432-0746. Available from DOI: 10.1051/0004-6361/201731491 (cit. on pp. 54, 60).

DRĄŻKOWSKA; SZULÁGYI, 2018. *Dust Evolution and Satellitesimal Formation in Circumplanetary Disks*. Vol. 866. No. 142. Available from DOI: 10.3847/1538-4357/aae0fd (cit. on p. 115).

DUTREY et al., 2014. Physical and Chemical Structure of Planet-Forming Disks Probed by Millimeter Observations and Modeling. In: BEUTHER; KLESSEN; DULLEMOND; HENNING (eds.). *Protostars and Planets VI*, pp. 317–338. Available from DOI: 10.2458/azu_uapress_9780816531240-ch014 (cit. on p. 159).

FANALE; BROWN; CRUIKSHANK; CLAKE, 1979. Significance of Absorption Features in Io's IR Reflectance Spectrum. *Nature*. Vol. 280, pp. 761–763. ISSN 0028-0836. Available from DOI: 10.1038/280761a0 (cit. on p. 36).

FEGLEY, 2000. Kinetics of Gas-Grain Reactions in the Solar Nebula. *Space Science Reviews*. Vol. 92, pp. 177–200. ISSN 0038-6308. Available from DOI: 10.1023/A:1005286910756 (cit. on pp. 47, 63).

FIGUEREDO; GREELEY, 2004. Resurfacing History of Europa from Pole-to-Pole Geological Mapping. *Icarus*. Vol. 167, no. 2, pp. 287–312. ISSN 0019-1035. Available from DOI: 10.1016/j.icarus.2003.09.016 (cit. on p. 36).

FLETCHER; ORTON; TEANBY; IRWIN, 2009. Phosphine on Jupiter and Saturn from Cassini/CIRS. *Icarus*. Vol. 202, pp. 543–564. ISSN 0019-1035. Available from DOI: 10.1016/j.icarus.2009.03.023 (cit. on pp. 8, 32, 33, 83).

FLETCHER et al., 2011. Saturn's Tropospheric Composition and Clouds from Cassini/VIMS 4.6–5.1 $\mu$m Nightside Spectroscopy. *Icarus*. Vol. 214, no. 2, pp. 510–533. ISSN 0019-1035. Available from DOI: 10.1016/j.icarus.2011.06.006 (cit. on pp. 33, 83).

FRAY; SCHMITT, 2009. Sublimation of Ices of Astrophysical Interest: A Bibliographic Review. *Planetary and Space Science*. Vol. 57, no. 14-15, pp. 2053–2080. ISSN 00320633. Available from DOI: 10.1016/j.pss.2009.09.011 (cit. on p. 50).

FUNG; ZHU; CHIANG, 2019. *Circumplanetary Disk Dynamics in the Isothermal and Adiabatic Limits*. Vol. 887. No. 152. Available from DOI: 10.3847/1538-4357/ab53da (cit. on p. 99).

GAUTIER; HERSANT; MOUSIS; LUNINE, 2001. Enrichments in Volatiles in Jupiter: A New Interpretation of the Galileo Measurements. *The Astrophysical Journal*. Vol. 550, no. 2, pp. L227–L230. ISSN 0004637X. Available from DOI: 10.1086/319648 (cit. on p. 81).

GAUTIER; HERSANT, 2005. Formation and Composition of Planetesimals: Trapping Volatiles by Clathration. *Space Science Reviews*. Vol. 116, no. 1-2, pp. 25–52. ISSN 0038-6308, ISSN 1572-9672. Available from DOI: 10.1007/s11214-005-1946-2 (cit. on pp. 42, 54, 81).

GIBB; WHITTET; BOOGERT; TIELENS, 2004. Interstellar Ice: The Infrared Space Observatory Legacy. *The Astrophysical Journal Supplement Series*. Vol. 151, no. 1, pp. 35–73. ISSN 0067-0049, ISSN 1538-4365. Available from DOI: 10.1086/381182 (cit. on pp. 10, 28, 45).

GILLON et al., 2016. Temperate Earth-sized Planets Transiting a Nearby Ultracool Dwarf Star. *Nature*. Vol. 533, pp. 221–224. ISSN 0028-0836. Available from DOI: 10.1038/nature17448 (cit. on p. 141).

GILLON et al., 2017. Seven Temperate Terrestrial Planets around the Nearby Ultracool Dwarf Star TRAPPIST-1. *Nature*. Vol. 542, pp. 456–460. ISSN 0028-0836. Available from DOI: 10.1038/nature21360 (cit. on p. 141).

GREENE et al., 2023. *Thermal Emission from the Earth-sized Exoplanet TRAPPIST-1 b Using JWST*. 2023-03-26. Available from arXiv: 2303.14849 [astro-ph] (cit. on p. 141).

GURNETT; KURTH; ROUX; BOLTON; KENNEL, 1996. Evidence for a Magnetosphere at Ganymede from Plasma-Wave Observations by the Galileo Spacecraft. *Nature*. Vol. 384, pp. 535–537. ISSN 0028-0836. Available from DOI: 10.1038/384535a0 (cit. on p. 37).

HARTMANN; CALVET; GULLBRING; D'ALESSIO, 1998. Accretion and the Evolution of T Tauri Disks. *The Astrophysical Journal*. Vol. 495, no. 1, pp. 385–400. ISSN 0004-637X, ISSN 1538-4357. Available from DOI: 10.1086/305277 (cit. on pp. 54, 55, 143).

HARTMANN; HERCZEG; CALVET, 2016. Accretion onto Pre-Main-Sequence Stars. *Annual Review of Astronomy and Astrophysics*. Vol. 54, no. 1, pp. 135–180. ISSN 0066-4146, ISSN 1545-4282. Available from DOI: 10.1146/annurev-astro-081915-023347 (cit. on p. 143).

HELLED; FORTNEY, 2020. The Interiors of Uranus and Neptune: Current Understanding and Open Questions. *Philosophical Transactions of the Royal Society A: Mathematical, Physical and Engineering Sciences*. Vol. 378, no. 2187, p. 20190474. ISSN 1364-503X, ISSN 1471-2962. Available from DOI: 10.1098/rsta.2019.0474 (cit. on p. 91).

HELLER, 2015. Water Ice Lines and the Formation of Giant Moons around Super Jovian Planets. *The Astrophysical Journal*, p. 9 (cit. on p. 12).

HERSANT; GAUTIER; LUNINE, 2004. Enrichment in Volatiles in the Giant Planets of the Solar System. *Planetary and Space Science*. Vol. 52, pp. 623–641. ISSN 0032-0633. Available from DOI: 10.1016/j.pss.2003.12.011 (cit. on pp. 52, 54, 63).

HOLDER; ZETTS; PRADHAN, 1988. Phase Behavior in Systems Containing Clathrate Hydrates: A Review. *Reviews in Chemical Engineering*. Vol. 5, no. 1-4, pp. 1–70. ISSN 2191-0235. Available from DOI: 10.1515/REVCE.1988.5.1-4.1 (cit. on p. 42).

HORNER; MOUSIS; ALIBERT; LUNINE; BLANC, 2008. Constraints from Deuterium on the Formation of Icy Bodies in the Jovian System and Beyond. *Planetary and Space Science*. Vol. 56, pp. 1585–1595. ISSN 0032-0633. Available from DOI: 10.1016/j.pss.2008.04.010 (cit. on p. 140).

HOUGE; KRIJT, 2023. Collisional Evolution of Dust and Water Ice in Protoplanetary Discs during and after an Accretion Outburst. *Monthly Notices of the Royal Astronomical Society*. Vol. 521, no. 4, pp. 5826–5845. ISSN 0035-8711, ISSN 1365-2966. Available from DOI: 10.1093/mnras/stad866 (cit. on p. 143).

HUANG; ORMEL, 2022. The Dynamics of the TRAPPIST-1 System in the Context of Its Formation. *Monthly Notices of the Royal Astronomical Society*. Vol. 511, no. 3, pp. 3814–3831. ISSN 0035-8711, ISSN 1365-2966. Available from DOI: 10.1093/mnras/stac288 (cit. on p. 152).

HUE; CAVALIÉ; DOBRIJEVIC; HERSANT; GREATHOUSE, 2015. 2D Photochemical Modeling of Saturn's Stratosphere. Part I: Seasonal Variation of Atmospheric Composition without Meridional Transport. *Icarus*. Vol. 257, pp. 163–184. ISSN 00191035. Available from DOI: 10.1016/j.icarus.2015.04.001 (cit. on pp. 162, 167, 173).

HUESO; GUILLOT, 2005. Evolution of Protoplanetary Disks: Constraints from DM Tauri and GM Aurigae. *Astronomy & Astrophysics*. Vol. 442, no. 2, pp. 703–725. ISSN 0004-6361, ISSN 1432-0746. Available from DOI: 10.1051/0004-6361:20041905 (cit. on pp. 54, 55).

IRWIN et al., 2018. Detection of Hydrogen Sulfide above the Clouds in Uranus's Atmosphere. *Nature Astronomy*. Vol. 2, no. 5, pp. 420–427. ISSN 2397-3366. Available from DOI: 10.1038/s41550-018-0432-1 (cit. on p. 85).

IRWIN et al., 2019a. Latitudinal Variation in the Abundance of Methane (CH4) above the Clouds in Neptune's Atmosphere from VLT/MUSE Narrow Field Mode Observations. *Icarus*. Vol. 331, pp. 69–82. ISSN 00191035. Available from DOI: 10.1016/j.icarus.2019.05.011 (cit. on pp. 85, 91).

IRWIN et al., 2019b. Probable Detection of Hydrogen Sulphide (H2S) in Neptune's Atmosphere. *Icarus*. Vol. 321, pp. 550–563. ISSN 00191035. Available from DOI: 10.1016/j.icarus.2018.12.014 (cit. on p. 85).

IZIDORO et al., 2021. Formation of Planetary Systems by Pebble Accretion and Migration: Hot Super-Earth Systems from Breaking Compact Resonant Chains. *Astronomy & Astrophysics*. Vol. 650, A152. ISSN 0004-6361, ISSN 1432-0746. Available from DOI: 10.1051/0004-6361/201935336 (cit. on pp. 141, 152).

JENNISKENS; BLAKE; WILSON; POHORILLE, 1995. High-Density Amorphous Ice, the Frost on Interstellar Grains. *The Astrophysical Journal*. Vol. 455, p. 389. ISSN 0004-637X, ISSN 1538-4357. Available from DOI: 10.1086/176585 (cit. on pp. 28, 45).

JOHANSEN; RONNET; SCHILLER; DENG; BIZZARRO, 2022. *Anatomy of Rocky Planets Formed by Rapid Pebble Accretion I. How Icy Pebbles Determine the Core Fraction and FeO Contents*. 2022-07-20. Available from arXiv: 2207.09795 [astro-ph] (cit. on p. 141).

JOHANSEN et al., 2014. The Multifaceted Planetesimal Formation Process. In: available from DOI: 10.2458/azu_uapress_9780816531240-ch024 (cit. on p. 58).

JOHNSON; OELKERS; HELGESON, 1992. SUPCRT92: A Software Package for Calculating the Standard Molal Thermodynamic Properties of Minerals, Gases, Aqueous Species, and Reactions from 1 to 5000 Bar and 0 to 1000°C. *Computers and Geosciences*. Vol. 18, pp. 899–947. ISSN 0098-3004. Available from DOI: 10.1016/0098-3004(92)90029-Q (cit. on p. 47).

KARKOSCHKA; TOMASKO, 2009. The Haze and Methane Distributions on Uranus from HST-STIS Spectroscopy. *Icarus*. Vol. 202, no. 1, pp. 287–309. ISSN 00191035. Available from DOI: 10.1016/j.icarus.2009.02.010 (cit. on pp. 33, 85).

KARKOSCHKA; TOMASKO, 2011. The Haze and Methane Distributions on Neptune from HST–STIS Spectroscopy. *Icarus*. Vol. 211, no. 1, pp. 780–797. ISSN 00191035. Available from DOI: 10.1016/j.icarus.2010.08.013 (cit. on p. 85).

KESZTHELYI; MCEWEN, 1997. Magmatic Differentiation of Io. *ıcarus*. Vol. 130, no. 2, pp. 437–448. Available from DOI: 10.1006/icar.1997.5837 (cit. on p. 36).

KIVELSON et al., 1996. Discovery of Ganymede's Magnetic Field by the Galileo Spacecraft. *Nature*. Vol. 384, pp. 537–541. ISSN 0028-0836. Available from DOI: 10.1038/384537a0 (cit. on p. 37).

KLEINE et al., 2020. The Non-carbonaceous–Carbonaceous Meteorite Dichotomy. *Space Science Reviews*. Vol. 216, no. 4, p. 55. ISSN 0038-6308, ISSN 1572-9672. Available from DOI: 10.1007/s11214-020-00675-w (cit. on p. 176).

KNOLL; PRINJA; CAMPBELL, 1993. A Directe Newton Solver for the Two-Dimensional Tokamak Edge Plasma Fluid Equation. *Journal of Computational Physics*. No. 104, pp. 418–126. Available also from: https://api-istex-fr.insu.bib.cnrs.fr/ark:/67375/6H6-VRJ5TT56-K/fulltext.pdf?auth=ip%2Cfede&sid=ebsco%2Cistex-view (cit. on pp. 13, 104, 113).

KNOLL; KEYES, 2004. Jacobian-Free Newton–Krylov Methods: A Survey of Approaches and Applications. *Journal of Computational Physics*. Vol. 193, no. 2, pp. 357–397. ISSN 00219991. Available from DOI: 10.1016/j.jcp.2003.08.010 (cit. on pp. 104, 113).

KONNOV, 2009. Implementation of the NCN Pathway of Prompt-NO Formation in the Detailed Reaction Mechanism. *Combustion and Flame*. Vol. 156, no. 11, pp. 2093–2105. ISSN 0010-2180. Available from DOI: 10.1016/j.combustflame.2009.03.016 (cit. on p. 162).

KONNOV; RUYCK, 2000. Kinetic Modeling of the Thermal Decomposition of Ammonia. *Combustion Science and Technology*. Vol. 152, no. 1, pp. 23–37. ISSN 0010-2202. Available from DOI: 10.1080/00102200008952125 (cit. on p. 162).

KORYCANSKY; BODENHEIMER; POLLACK, 1991. Numerical Models of Giant Planet Formation with Rotation. *Icarus*. Vol. 92, pp. 234–251. ISSN 0019-1035. Available from DOI: 10.1016/0019-1035(91)90048-X (cit. on p. 98).

KOYAMA; INAYOSHI; IWASAWA; TAKEBE, 1983. Reflectance Spectra of SO2 Frosts Contaminated by Sodium and Their Implication on Io. *Publications of the Astronomical Society of Japan*. Vol. 35, pp. 143–154. ISSN 0004-6264. Available also from: https://ui.adsabs.harvard.edu/abs/1983PASJ...35..143K (cit. on p. 36).

KRAPP et al., 2024. *A Thermodynamic Criterion for the Formation of Circumplanetary Disks*. 2024-02-26. Available from arXiv: 2402.14638 [astro-ph] (cit. on p. 99).

KUSKOV; KRONROD, 2005. Internal Structure of Europa and Callisto. *ıcarus*. Vol. 177, no. 2, pp. 550–569. Available from DOI: 10.1016/j.icarus.2005.04.014 (cit. on p. 37).

LAMBRECHTS; JOHANSEN, 2012. Rapid Growth of Gas-Giant Cores by Pebble Accretion. *Astronomy and Astrophysics*. Vol. 544, A32. ISSN 0004-6361. Available from DOI: 10.1051/0004-6361/201219127 (cit. on pp. 98, 99, 115, 117).

LAMBRECHTS; JOHANSEN, 2014. Forming the Cores of Giant Planets from the Radial Pebble Flux in Protoplanetary Discs. *Astronomy & Astrophysics*. Vol. 572, A107. ISSN 0004-6361, ISSN 1432-0746. Available from DOI: 10.1051/0004-6361/201424343 (cit. on pp. 58, 91).

LANGE; AHRENS, 1982. Impact Induced Dehydration of Serpentine and the Evolution of Planetary Atmospheres. *Journal of Geophysical Research*. Vol. 87, no. S01, A451. ISSN 0148-0227. Available from DOI: 10.1029/JB087iS01p0A451 (cit. on pp. 10, 47).

LAURETTA et al., 2024. Asteroid (101955) Bennu in the Laboratory: Properties of the Sample Collected by OSIRIS-REx. *Meteoritics & Planetary Science*. Vol. n/a, no. n/a. ISSN 1945-5100. Available from DOI: 10.1111/maps.14227 (cit. on p. 46).

LE ROY et al., 2015. Inventory of the Volatiles on Comet 67P/Churyumov-Gerasimenko from Rosetta/ROSINA. *Astronomy & Astrophysics*. Vol. 583, A1. ISSN 0004-6361, ISSN 1432-0746. Available from DOI: 10.1051/0004-6361/201526450 (cit. on p. 63).

LEGA et al., 2021. Migration of Jupiter-mass Planets in Low-Viscosity Discs. *Astronomy and Astrophysics*. Vol. 646, A166. ISSN 0004-6361. Available from DOI: 10.1051/0004-6361/202039520 (cit. on p. 176).

LESAGE; SCHMIDT; ANDRIEU; MASSOL, 2021. Constraints on Effusive Cryovolcanic Eruptions on Europa Using Topography Obtained from Galileo Images. *Icarus*. Vol. 361, p. 114373. ISSN 0019-1035. Available from DOI: 10.1016/j.icarus.2021.114373 (cit. on p. 36).

LI et al., 2020. The Water Abundance in Jupiter's Equatorial Zone. *Nature Astronomy*. Vol. 4, no. 6, pp. 609–616. ISSN 2397-3366. Available from DOI: 10.1038/s41550-020-1009-3 (cit. on pp. 14, 32, 33, 81, 97, 135, 178).

LI et al., 2024. Super-Adiabatic Temperature Gradient at Jupiter's Equatorial Zone and Implications for the Water Abundance. *Icarus*. Vol. 414, p. 116028. ISSN 0019-1035. Available from DOI: 10.1016/j.icarus.2024.116028 (cit. on p. 32).

LIANG; LIU; MEI, 2022. In Situ Study on Dehydration and Phase Transformation of Antigorite. *Minerals*. Vol. 12, no. 5, p. 567. ISSN 2075-163X. Available from DOI: 10.3390/min12050567 (cit. on pp. 10, 47).

LIN; PAPALOIZOU, 1985. *On the Dynamical Origin of the Solar System*. Available also from: https://ui.adsabs.harvard.edu/abs/1985prpl.conf..981L (cit. on p. 54).

LINDAL et al., 1987. The Atmosphere of Uranus: Results of Radio Occultation Measurements with Voyager 2. *Journal of Geophysical Research: Space Physics*. Vol. 92, no. A13, pp. 14987–15001. ISSN 0148-0227, ISSN 2156-2202. Available from DOI: 10.1029/JA092iA13p14987 (cit. on p. 33).

LINDAL et al., 1990. The Atmosphere of Neptune: Results of Radio Occultation Measurements with the Voyager 2 Spacecraft. *Geophysical Research Letters*. Vol. 17, no. 10, pp. 1733–1736. ISSN 00948276. Available from DOI: 10.1029/GL017i010p01733 (cit. on p. 33).

LINDAL, 1992. The Atmosphere of Neptune: An Analysis of Radio Occultation Data Acquired with Voyager 2. *The Astronomical Journal*. Vol. 103, p. 967. ISSN 0004-6256. Available from DOI: 10.1086/116119 (cit. on p. 33).

LODDERS, 2003. Solar System Abundances and Condensation Temperatures of the Elements. *The Astrophysical Journal*. Vol. 591, pp. 1220–1247. ISSN 0004-637X. Available from DOI: 10.1086/375492 (cit. on pp. 8, 28, 137).

LODDERS, 2019. *Solar Elemental Abundances*. arXiv e-prints, 2019-12-01. Available from DOI: 10.48550/arXiv.1912.00844 (cit. on pp. 8, 28, 63, 115, 124, 146).

LODDERS, 2021. Relative Atomic Solar System Abundances, Mass Fractions, and Atomic Masses of the Elements and Their Isotopes, Composition of the Solar Photosphere, and Compositions of the Major Chondritic Meteorite Groups. *Space Science Reviews*. Vol. 217, no. 3, p. 44. ISSN 0038-6308, ISSN 1572-9672. Available from DOI: 10.1007/s11214-021-00825-8 (cit. on pp. 8, 28, 143, 155).

LONGHI, 2005. Phase Equilibria in the System CO2-H2O I: New Equilibrium Relations at Low Temperatures. *Geochimica et Cosmochimica Acta*. Vol. 69, no. 3, pp. 529–539. ISSN 00167037. Available from DOI: 10.1016/j.gca.2004.07.007 (cit. on p. 52).

LUBOW; SEIBERT; ARTYMOWICZ, 1999. Disk Accretion onto High-Mass Planets. *The Astrophysical Journal*. Vol. 526, pp. 1001–1012. ISSN 0004-637X. Available from DOI: 10.1086/308045 (cit. on p. 98).

LUGER et al., 2017. A Seven-Planet Resonant Chain in TRAPPIST-1. *Nature Astronomy*. Vol. 1, p. 0129. ISSN 2397-3366. Available from DOI: 10.1038/s41550-017-0129 (cit. on p. 141).

LUNINE; STEVENSON, 1985. Thermodynamics of Clathrate Hydrate at Low and High Pressures with Application to the Outer Solar System. *The Astrophysical Journal Supplement Series*. Vol. 58, p. 493. ISSN 0067-0049, ISSN 1538-4365. Available from DOI: 10.1086/191050 (cit. on pp. 12, 42, 52).

LUNINE; STEVENSON, 1982. Formation of the Galilean Satellites in a Gaseous Nebula. *Icarus*. Vol. 52, no. 1, pp. 14–39. ISSN 00191035. Available from DOI: 10.1016/0019-1035(82)90166-X (cit. on pp. 10, 42, 97, 98, 126).

LYNDEN-BELL; PRINGLE, 1974. The Evolution of Viscous Discs and the Origin of the Nebular Variables. *Monthly Notices of the Royal Astronomical Society*. Vol. 168, no. 3, pp. 603–637. ISSN 0035-8711, ISSN 1365-2966. Available from DOI: 10.1093/mnras/168.3.603 (cit. on pp. 53–55, 115, 155).

MADEIRA; IZIDORO; WINTER, 2021. Building the Galilean Moons System via Pebble Accretion and Migration: A Primordial Resonant Chain. *Monthly Notices of the Royal Astronomical Society*. Vol. 504, no. 2, pp. 1854–1872. ISSN 0035-8711, ISSN 1365-2966. Available from DOI: 10.1093/mnras/stab986 (cit. on pp. 140, 141).

MAHAFFY et al., 2000. Noble Gas Abundance and Isotope Ratios in the Atmosphere of Jupiter from the Galileo Probe Mass Spectrometer. *Journal of Geophysical Research*. Vol. 105, pp. 15061–15072. ISSN 0148-0227. Available from DOI: 10.1029/1999JE001224 (cit. on pp. 8, 32).

MAKALKIN; DOROFEEVA, 1995. Structure of the Protoplanetary Accretion Disk around the Sun at the T Tauri Phase: I. Initial Data, Equations, and Methods of Modeling. Vol. 29, no. 2, p. 20 (cit. on pp. 12, 102, 103, 115, 155).

MAKALKIN; DOROFEEVA, 2014. Accretion Disks around Jupiter and Saturn at the Stage of Regular Satellite Formation. *Solar System Research*. Vol. 48, no. 1, pp. 62–78. ISSN 0038-0946, ISSN 1608-3423. Available from DOI: 10.1134/S0038094614010067 (cit. on pp. 12, 100, 103).

MANDT et al., 2020. Tracing the Origins of the Ice Giants Through Noble Gas Isotopic Composition. *Space Science Reviews*. Vol. 216, no. 5, p. 99. ISSN 0038-6308, ISSN 1572-9672. Available from DOI: 10.1007/s11214-020-00723-5 (cit. on p. 42).

MARLEAU; KUIPER; BÉTHUNE; MORDASINI, 2023. *The Planetary Accretion Shock. III. Smoothing-free 2.5D Simulations and Calculation of H Alpha Emission*. 2023-05-02. Available from arXiv: 2305.01679 [astro-ph] (cit. on p. 97).

MASSET; PAPALOIZOU, 2003. Runaway Migration and the Formation of Hot Jupiters. *The Astrophysical Journal*. Vol. 588, no. 1, pp. 494–508. ISSN 0004-637X, ISSN 1538-4357. Available from DOI: 10.1086/373892 (cit. on p. 176).

MAYER; PLETZER, 1986. Astrophysical Implications of Amorphous Ice-a Microporous Solid. *Nature*. Vol. 319, pp. 298–301. ISSN 0028-0836. Available from DOI: 10.1038/319298a0 (cit. on pp. 28, 45).

MCBRIDE; GORDON; RENO, 1993. *Thermodynamic Data for Fifty Reference Elements*. 1993-01-01. Available also from: https://ui.adsabs.harvard.edu/abs/1993tdff.rept.....M (cit. on p. 154).

MELWANI DASWANI; VANCE; MAYNE; GLEIN, 2021. A Metamorphic Origin for Europa's Ocean. *Geophysical Research Letters*. Vol. 48, no. 18, e2021GL094143. ISSN 1944-8007. Available from DOI: 10.1029/2021GL094143 (cit. on pp. 135, 140).

METZLER; BISCHOFF; STÖFFLER, 1992. Accretionary Dust Mantles in CM Chondrites: Evidence for Solar Nebula Processes. *Geochimica et Cosmochimica Acta*. Vol. 56, no. 7, pp. 2873–2897. ISSN 0016-7037. Available from DOI: 10.1016/0016-7037(92)90365-P (cit. on p. 46).

MIURA et al., 2017. Comprehensive Study of Thermal Desorption of Grain-surface Species by Accretion Shocks around Protostars. *The Astrophysical Journal*. Vol. 839, no. 1, p. 47. ISSN 1538-4357. Available from DOI: 10.3847/1538-4357/aa67df (cit. on pp. 28, 46).

MONGA; DESCH, 2014. External Photoevaporation of the Solar Nebula: Jupiter's Noble Gas Enrichments. *The Astrophysical Journal*. Vol. 798, no. 1, p. 9. ISSN 1538-4357. Available from DOI: 10.1088/0004-637X/798/1/9 (cit. on p. 42).

MORAES; KLEY; VIEIRA NETO, 2018. Growth and Evolution of Satellites in a Jovian Massive Disc. *Monthly Notices of the Royal Astronomical Society*. Vol. 475, no. 1, pp. 1347–1362. ISSN 0035-8711, ISSN 1365-2966. Available from DOI: 10.1093/mnras/stx3268 (cit. on p. 81).

MORBIDELLI et al., 2014. Meridional Circulation of Gas into Gaps Opened by Giant Planets in Three-Dimensional Low-Viscosity Disks. *Icarus*. Vol. 232, pp. 266–270. ISSN 00191035. Available from DOI: 10.1016/j.icarus.2014.01.010 (cit. on p. 99).

MORBIDELLI; NESVORNY, 2020. Kuiper Belt: Formation and Evolution. In: pp. 25–59. Available from DOI: 10.1016/B978-0-12-816490-7.00002-3 (cit. on p. 83).

MORDASINI, 2013. Luminosity of Young Jupiters Revisited: Massive Cores Make Hot Planets. *Astronomy & Astrophysics*. Vol. 558, A113. ISSN 0004-6361, ISSN 1432-0746. Available from DOI: 10.1051/0004-6361/201321617 (cit. on pp. 13, 105, 115, 132, 155).

MORDASINI; ALIBERT; KLAHR; HENNING, 2012. Characterization of Exoplanets from Their Formation: I. Models of Combined Planet Formation and Evolution. *Astronomy & Astrophysics*. Vol. 547, A111. ISSN 0004-6361, ISSN 1432-0746. Available from DOI: 10.1051/0004-6361/201118457 (cit. on p. 105).

MOSQUEIRA; ESTRADA, 2003. Formation of the Regular Satellites of Giant Planets in an Extended Gaseous Nebula I: Subnebula Model and Accretion of Satellites. *Icarus*. Vol. 163, pp. 198–231. ISSN 0019-1035. Available from DOI: 10.1016/S0019-1035(03)00076-9 (cit. on pp. 12, 97).

MOUSIS, 2002. An Evolutionary Turbulent Model of Saturn's Subnebula: Implications for the Origin of the Atmosphere of Titan. *Icarus*. Vol. 156, no. 1, pp. 162–175. ISSN 00191035. Available from DOI: 10.1006/icar.2001.6782 (cit. on p. 126).

MOUSIS; AGUICHINE; HELLED; IRWIN; LUNINE, 2020. The Role of Ice Lines in the Formation of Uranus and Neptune. *Philosophical Transactions of the Royal Society A: Mathematical, Physical and Engineering Sciences*. Vol. 378, no. 2187, p. 20200107. ISSN 1364-503X, ISSN 1471-2962. Available from DOI: 10.1098/rsta.2020.0107 (cit. on p. 42).

MOUSIS et al., 2016a. Origin of Molecular Oxygen in Comet 67P/Churyumov–Gerasimenko. *The Astrophysical Journal*. Vol. 823, no. 2, p. L41. ISSN 2041-8213. Available from DOI: 10.3847/2041-8205/823/2/L41 (cit. on p. 176).

MOUSIS et al., 2016b. The Hera Saturn Entry Probe Mission. *Planetary and Space Science*. Vol. 130, pp. 80–103. ISSN 0032-0633. Available from DOI: 10.1016/j.pss.2015.06.020 (cit. on p. 176).

MOUSIS et al., 2018. Scientific Rationale for Uranus and Neptune in Situ Explorations. *Planetary and Space Science*. Vol. 155, pp. 12–40. ISSN 00320633. Available from DOI: 10.1016/j.pss.2017.10.005 (cit. on p. 81).

MOUSIS; GAUTIER, 2004. Constraints on the Presence of Volatiles in Ganymede and Callisto from an Evolutionary Turbulent Model of the Jovian Subnebula. *Planetary and Space Science*. Vol. 52, no. 5-6, pp. 361–370. ISSN 00320633. Available from DOI: 10.1016/j.pss.2003.06.004 (cit. on pp. 97, 126).

MOUSIS; LUNINE; AGUICHINE, 2021a. The Nature and Composition of Jupiter's Building Blocks Derived from the Water Abundance Measurements by the Juno Spacecraft. *The Astrophysical Journal Letters*. Vol. 918, no. 2, p. L23. ISSN 2041-8205, ISSN 2041-8213. Available from DOI: 10.3847/2041-8213/ac1d50 (cit. on pp. 42, 54, 81).

MOUSIS; LUNINE; MADHUSUDHAN; JOHNSON, 2012. NEBULAR WATER DEPLETION AS THE CAUSE OF JUPITER'S LOW OXYGEN ABUNDANCE. *The Astrophysical Journal*. Vol. 751, no. 1, p. L7. ISSN 2041-8205, ISSN 2041-8213. Available from DOI: 10.1088/2041-8205/751/1/L7 (cit. on p. 54).

MOUSIS; RONNET; LUNINE, 2019. Jupiter's Formation in the Vicinity of the Amorphous Ice Snowline. *The Astrophysical Journal*. Vol. 875, no. 1, p. 9. ISSN 1538-4357. Available from DOI: 10.3847/1538-4357/ab0a72 (cit. on pp. 32, 42, 45).

MOUSIS et al., 2009. Clathration of Volatiles in the Solar Nebula and Implications for the Origin of Titan's Atmosphere. *The Astrophysical Journal*. Vol. 691, no. 2, pp. 1780–1786. ISSN 0004-637X, ISSN 1538-4357. Available from DOI: 10.1088/0004-637X/691/2/1780 (cit. on pp. 54, 63, 176).

MOUSIS et al., 2014. New Insights On Saturn's Formation From Its Nitrogen Isotopic Composition. *The Astrophysical Journal*. Vol. 796, no. 2, p. L28. ISSN 2041-8213. Available from DOI: 10.1088/2041-8205/796/2/L28 (cit. on p. 63).

MOUSIS et al., 2021b. Cold Traps of Hypervolatiles in the Protosolar Nebula at the Origin of the Peculiar Composition of Comet C/2016 R2 (PanSTARRS). *The Planetary Science Journal*. Vol. 2, no. 2, p. 72. ISSN 2632-3338. Available from DOI: 10.3847/PSJ/abeaa7 (cit. on p. 42).

MOUSIS et al., 2023. Early Stages of Galilean Moon Formation in a Water-depleted Environment. *The Astrophysical Journal Letters*. Vol. 944, no. 2, p. L37. ISSN 2041-8205, ISSN 2041-8213. Available from DOI: 10.3847/2041-8213/acb5a4 (cit. on pp. 10, 47, 49, 126, 135, 137, 139, 149).

MOUSIS et al., 2024. Insights on the Formation Conditions of Uranus and Neptune from Their Deep Elemental Compositions. *The Planetary Science Journal*. Vol. 5, p. 173. ISSN 2632-3338. Available from DOI: 10.3847/PSJ/ad58d8 (cit. on pp. 89, 90, 94, 95).

MÜLLER; HELLED, 2024. Can Jupiter's Atmospheric Metallicity Be Different from the Deep Interior? *The Astrophysical Journal*. Vol. 967, no. 1, p. 7. ISSN 0004-637X. Available from DOI: 10.3847/1538-4357/ad3738 (cit. on p. 33).

NAKAMOTO; NAKAGAWA, 1994. Formation, Early Evolution, and Gravitational Stability of Protoplanetary Disks. *The Astrophysical Journal*. Vol. 421, p. 640. ISSN 0004-637X, ISSN 1538-4357. Available from DOI: 10.1086/173678 (cit. on p. 55).

NASH; FANALE; NELSON, 1980. SO2 Frost: UV-visible Feflectivity and Io Surface Coverage. *Geophysical Research Letters*. Vol. 7, pp. 665–668. ISSN 0094-8276. Available from DOI: 10.1029/GL007i009p00665 (cit. on p. 36).

NÉRI; GUYOT; REYNARD; SOTIN, 2020. A Carbonaceous Chondrite and Cometary Origin for Icy Moons of Jupiter and Saturn. *Earth and Planetary Science Letters*. Vol. 530, p. 115920. Available from DOI: 10.1016/j.epsl.2019.115920 (cit. on pp. 37, 38).

NESS et al., 1986. Magnetic Fields at Uranus. *Science*. Vol. 233, pp. 85–89. ISSN 0036-8075. Available from DOI: 10.1126/science.233.4759.85 (cit. on p. 96).

NESVORNÝ, 2011. Young Solar System's Fifth Giant Planet ? *The Astrophysical Journal*. Vol. 742, no. 2, p. L22. ISSN 2041-8205, ISSN 2041-8213. Available from DOI: 10.1088/2041-8205/742/2/L22 (cit. on p. 83).

NESVORNÝ; MORBIDELLI, 2012. Statistical Study of the Early Solar System's Instability with Four, Five, and Six Giant Planets. *The Astronomical Journal*. Vol. 144, p. 117. ISSN 0004-6256. Available from DOI: 10.1088/0004-6256/144/4/117 (cit. on p. 83).

OBERG; KAMP; CAZAUX; RAB, 2020. Photoevaporation of the Jovian Circumplanetary Disk: I. Explaining the Orbit of Callisto and the Lack of Outer Regular Satellites. *Astronomy & Astrophysics*. Vol. 638, A135. ISSN 0004-6361, ISSN 1432-0746. Available from DOI: 10.1051/0004-6361/202037883 (cit. on p. 140).

OBERG; KAMP; CAZAUX; RAB; CZOSKE, 2022a. *Observing Circumplanetary Disks with METIS*. 2022-12-06. Available from arXiv: 2212.03007 [astro-ph] (cit. on pp. 15, 38).

OBERG; KAMP; CAZAUX; WOITKE; THI, 2022b. *Circumplanetary Disk Ices. I. Ice Formation vs. Viscous Evolution and Grain Drift*. 2022-08-23. Available from arXiv: 2208.11053 [astro-ph] (cit. on pp. 37, 38).

OBERG et al., 2023. *Circumplanetary Disk Ices II. Composition*. 2023-02-28. Available from arXiv: 2302.14425 [astro-ph] (cit. on p. 160).

ÖBERG et al., 2021. *The TW Hya Rosetta Stone Project. I. Radial and Vertical Distributions of DCN and DCO+*. Vol. 161. No. 38. Available from DOI: 10.3847/1538-3881/abc74d (cit. on p. 159).

OGIHARA; KOKUBO; NAKANO; SUZUKI, 2022. Rapid-Then-Slow Migration Reproduces Mass Distribution of TRAPPIST-1 System. *Astronomy & Astrophysics*. Vol. 658, A184. ISSN 0004-6361, ISSN 1432-0746. Available from DOI: 10.1051/0004-6361/202142354 (cit. on p. 152).

OHNO; UEDA, 2021. Jupiter's "Cold" Formation in the Protosolar Disk Shadow: An Explanation for the Planet's Uniformly Enriched Atmosphere. *Astronomy & Astrophysics*. Vol. 651, p. L2. ISSN 0004-6361, ISSN 1432-0746. Available from DOI: 10.1051/0004-6361/202141169 (cit. on p. 54).

ORMEL; LIU; SCHOONENBERG, 2017. Formation of TRAPPIST-1 and Other Compact Systems. *Astronomy & Astrophysics*. Vol. 604, A1. ISSN 0004-6361, ISSN 1432-0746. Available from DOI: 10.1051/0004-6361/201730826 (cit. on pp. 141, 152).

OWEN et al., 1999. A Low-Temperature Origin for the Planetesimals That Formed Jupiter. *Nature*. Vol. 402, no. 6759, pp. 269–270. ISSN 0028-0836, ISSN 1476-4687. Available from DOI: 10.1038/46232 (cit. on pp. 42, 81).

PARK et al., 2015. Improved Detection of Tides at Europa with Radiometric and Optical Tracking during Flybys. *Planetary and Space Science*. Vol. 112, pp. 10–14. ISSN 0032-0633. Available from DOI: 10.1016/j.pss.2015.04.005 (cit. on p. 37).

PARKE LOYD et al., 2018. HAZMAT. IV. Flares and Superflares on Young M Stars in the Far Ultraviolet. *The Astrophysical Journal*. Vol. 867, no. 1, p. 70. ISSN 1538-4357. Available from DOI: 10.3847/1538-4357/aae2ae (cit. on pp. 14, 142).

PASEK et al., 2005. Sulfur Chemistry with Time-Varying Oxygen Abundance during Solar System Formation. *Icarus*. Vol. 175, no. 1, pp. 1–14. ISSN 00191035. Available from DOI: 10.1016/j.icarus.2004.10.012 (cit. on p. 63).

PEKMEZCI; JOHNSON; LUNINE; MOUSIS, 2019. A Statistical Approach to Planetesimal Condensate Composition beyond the Snowline Based on the Carbon-to-oxygen Ratio. *The Astrophysical Journal*. Vol. 887, p. 3. ISSN 0004-637X. Available from DOI: 10.3847/1538-4357/ab4c4a (cit. on p. 143).

PIANI; MARROCCHI; VACHER; YURIMOTO; BIZZARRO, 2021. Origin of Hydrogen Isotopic Variations in Chondritic Water and Organics. *Earth and Planetary Science Letters*. Vol. 567, p. 117008. ISSN 0012-821X. Available from DOI: 10.1016/j.epsl.2021.117008 (cit. on p. 46).

RADHAKRISHNAN, 1993. Description and Use of LSODE, the Livermore Solver for Ordinary Differential Equations. *NASA Reference Publication*. Vol. 1327. Available also from: https://computing.llnl.gov/sites/default/files/ODEPACK_pub2_u113855.pdf (cit. on p. 167).

AL-REFAIE; CHANGEAT; VENOT; WALDMANN; TINETTI, 2022. A Comparison of Chemical Models of Exoplanet Atmospheres Enabled by TauREx 3.1. *Astrophysical Journal*. Vol. 932, no. 2, p. 123. Available from DOI: 10.3847/1538-4357/ac6dcd (cit. on pp. 15, 154).

AL-REFAIE; CHANGEAT; WALDMANN; TINETTI, 2021. TauREx 3: A Fast, Dynamic, and Extendable Framework for Retrievals. *Astrophysical Journal*. Vol. 917, no. 1, p. 37. Available from DOI: 10.3847/1538-4357/ac0252 (cit. on pp. 15, 154).

REYNARD; SOTIN, 2023. Carbon-Rich Icy Moons and Dwarf Planets. *Earth and Planetary Science Letters*. Vol. 612, p. 118172. ISSN 0012-821X. Available from DOI: 10.1016/j.epsl.2023.118172 (cit. on p. 38).

RONNET; MOUSIS; VERNAZZA, 2017. Pebble Accretion at the Origin of Water in Europa. *The Astrophysical Journal*. Vol. 845, p. 92. ISSN 0004-637X. Available from DOI: 10.3847/1538-4357/aa80e6 (cit. on p. 140).

SAAD; SCHULTZ, 1986. GMRES: A Generalized Minimal Residual Algorithm for Solving Nonsymmetric Linear Systems. *SIAM Journal on Scientific and Statistical Computing*. Vol. 7, no. 3, pp. 856–869. ISSN 0196-5204, ISSN 2168-3417. Available from DOI: 10.1137/0907058 (cit. on p. 113).

SASAKI; STEWART; IDA, 2010. Origin of the Different Architectures of the Jovian and Saturnian Satellite Systems. *The Astrophysical Journal*. Vol. 714, pp. 1052–1064. ISSN 0004-637X. Available from DOI: 10.1088/0004-637X/714/2/1052 (cit. on pp. 14, 98, 126, 127, 131, 132, 135, 140).

SCHENK, 2002. Thickness Constraints on the Icy Shells of the Galilean Satellites from a Comparison of Crater Shapes. *Nature*. Vol. 417, pp. 419–421. ISSN 0028-0836. Available from DOI: 10.1038/417419a (cit. on p. 37).

SCHNEEBERGER; MOUSIS; AGUICHINE; LUNINE, 2023. Evolution of the Reservoirs of Volatiles in the Protosolar Nebula. *Astronomy & Astrophysics*. ISSN 0004-6361, ISSN 1432-0746. Available from DOI: 10.1051/0004-6361/202244670 (cit. on pp. 43–45, 53, 64, 66, 67, 69, 213).

SCHNEEBERGER; MOUSIS; DELEUIL; LUNINE, 2024. Formation of the Trappist-1 System in a Dry Protoplanetary Disk. *Astronomy & Astrophysics*. Vol. 682, p. L10. ISSN 0004-6361, ISSN 1432-0746. Available from DOI: 10.1051/0004-6361/202348309 (cit. on pp. 48, 231).

SCHNEIDER; BITSCH, 2021. How Drifting and Evaporating Pebbles Shape Giant Planets: II. Volatiles and Refractories in Atmospheres. *Astronomy & Astrophysics*. Vol. 654, A72. ISSN 0004-6361, ISSN 1432-0746. Available from DOI: 10.1051/0004-6361/202141096 (cit. on pp. 42, 176).

SCHUBERT; SOHL; HUSSMANN, 2009. *Interior of Europa*. Available also from: https://ui.adsabs.harvard.edu/abs/2009euro.book..353S (cit. on p. 135).

SCHUBERT; ZHANG; KIVELSON; ANDERSON, 1996. The Magnetic Field and Internal Structure of Ganymede. *Nature*. Vol. 384, pp. 544–545. ISSN 0028-0836. Available from DOI: 10.1038/384544a0 (cit. on p. 37).

SHAKURA; SUNYAEV, 1973. Black Holes in Binary Systems. Observational Appearance. *Astronomy and Astrophysics*. Vol. 24, pp. 337–355. ISSN 0004-6361. Available also from: https://ui.adsabs.harvard.edu/abs/1973A&A....24..337S (cit. on pp. 10, 53, 54, 57, 63, 100).

SHIBAIKE; ORMEL; IDA; OKUZUMI; SASAKI, 2019. The Galilean Satellites Formed Slowly from Pebbles. *The Astrophysical Journal*. Vol. 885, no. 1, p. 79. ISSN 1538-4357. Available from DOI: 10.3847/1538-4357/ab46a7 (cit. on p. 37).

SHKOLNIK; BARMAN, 2014. HAZMAT. I. THE EVOLUTION OF FAR-UV AND NEAR-UV EMISSION FROM EARLY M STARS. *The Astronomical Journal*. Vol. 148, no. 4, p. 64. ISSN 1538-3881. Available from DOI: 10.1088/0004-6256/148/4/64 (cit. on pp. 14, 142).

SIMONS; NIMMO; ANDERSON, 2021. *Journey to an Ice Giant System : Uranus Orbiter and Probe*. 2021-06-07. NASA (cit. on pp. 9, 33, 176).

SISSA et al., 2018. New Disk Discovered with VLT/SPHERE around the M Star GSC 07396-00759. *Astronomy & Astrophysics*. Vol. 613, p. L6. ISSN 0004-6361, ISSN 1432-0746. Available from DOI: 10.1051/0004-6361/201832740 (cit. on p. 29).

SROMOVSKY; FRY; KIM, 2011. Methane on Uranus: The Case for a Compact CH 4 Cloud Layer at Low Latitudes and a Severe CH 4 Depletion at High-Latitudes Based on Re-Analysis of Voyager Occultation Measurements and STIS Spectroscopy. *Icarus*. Vol. 215, pp. 292–312. ISSN 0019-1035. Available from DOI: 10.1016/j.icarus.2011.06.024 (cit. on pp. 33, 91).

SROMOVSKY et al., 2014. Methane Depletion in Both Polar Regions of Uranus Inferred from HST/STIS and Keck/NIRC2 Observations. *Icarus*. Vol. 238, pp. 137–155. ISSN 00191035. Available from DOI: 10.1016/j.icarus.2014.05.016 (cit. on pp. 33, 91).

STOLKER et al., 2021. Characterizing the Protolunar Disk of the Accreting Companion GQ Lupi B*. *The Astronomical Journal*. Vol. 162, no. 6, p. 286. ISSN 1538-3881. Available from DOI: 10.3847/1538-3881/ac2c7f (cit. on p. 34).

STULL, 1947. Vapor Pressure of Pure Substances. Organic and Inorganic Compounds. *Industrial & Engineering Chemistry*. Vol. 39, no. 4, pp. 517–540. ISSN 0019-7866, ISSN 1541-5724. Available from DOI: 10.1021/ie50448a022 (cit. on p. 50).

SUTTLE; KING; SCHOFIELD; BATES; RUSSELL, 2021. The Aqueous Alteration of CM Chondrites, a Review. *Geochimica et Cosmochimica Acta*. Vol. 299, pp. 219–256. ISSN 0016-7037. Available from DOI: 10.1016/j.gca.2021.01.014 (cit. on p. 46).

SZULÁGYI, 2017. Effects of the Planetary Temperature on the Circumplanetary Disk and on the Gap. *The Astrophysical Journal*. Vol. 842, no. 2, p. 103. ISSN 1538-4357. Available from DOI: 10.3847/1538-4357/aa7515 (cit. on pp. 97, 98, 101).

SZULÁGYI; BINKERT; SURVILLE, 2022. Meridional Circulation of Dust and Gas in the Circumstellar Disk: Delivery of Solids onto the Circumplanetary Region. *The Astrophysical Journal*. Vol. 924, p. 1. ISSN 0004-637X. Available from DOI: 10.3847/1538-4357/ac32d1 (cit. on pp. 99, 117).

SZULÁGYI; MORBIDELLI; CRIDA; MASSET, 2014. Accretion Of Jupiter-Mass Planets In The Limit Of Vanishing Viscosity. *The Astrophysical Journal*. Vol. 782, no. 2, p. 65. ISSN 0004-637X, ISSN 1538-4357. Available from DOI: 10.1088/0004-637X/782/2/65 (cit. on pp. 97, 99).

SZULÁGYI et al., 2016. Circumplanetary Disc or Circumplanetary Envelope? *Monthly Notices of the Royal Astronomical Society*. Vol. 460, no. 3, pp. 2853–2861. ISSN 0035-8711, ISSN 1365-2966. Available from DOI: 10.1093/mnras/stw1160 (cit. on pp. 12, 97, 98, 101).

THI et al., 2020. Warm Dust Surface Chemistry in Protoplanetary Disks: Formation of Phyllosilicates. *Astronomy & Astrophysics*. Vol. 635, A16. ISSN 0004-6361, ISSN 1432-0746. Available from DOI: 10.1051/0004-6361/201731747 (cit. on p. 46).

TRUMBO; BROWN, 2023. The Distribution of $CO_2$ on Europa Indicates an Internal Source of Carbon. *Science*. Vol. 381, no. 6664, pp. 1308–1311. ISSN 0036-8075, ISSN 1095-9203. Available from DOI: 10.1126/science.adg4155 (cit. on pp. 38, 128).

VAN DER WAALS, 1956. The Statistical Mechanics of Clathrate Compounds. *Trans. Faraday Soc.* Vol. 52, no. 0, pp. 184–193. ISSN 0014-7672. Available from DOI: 10.1039/TF9565200184 (cit. on p. 42).

VAN HOOLST et al., 2024. Geophysical Characterization of the Interiors of Ganymede, Callisto and Europa by ESA's JUpiter ICy Moons Explorer. *Space Science Reviews*. Vol. 220, no. 5, p. 54. ISSN 0038-6308, ISSN 1572-9672. Available from DOI: 10.1007/s11214-024-01085-y (cit. on p. 37).

VENOT et al., 2012. A Chemical Model for the Atmosphere of Hot Jupiters. *Astronomy & Astrophysics*. Vol. 546, A43. ISSN 0004-6361, ISSN 1432-0746. Available from DOI: 10.1051/0004-6361/201219310 (cit. on pp. 15, 154, 162, 166, 167, 173, 178).

VENOT, 2012. *Photochimie Des Exoplanètes Chaudes : Modélisations et Expériences*. Available also from: https://theses.fr/2012BOR14610. These de doctorat. Bordeaux 1 (cit. on pp. 15, 163).

VENTURINI; HELLED, 2020. Jupiter's Heavy-Element Enrichment Expected from Formation Models. *Astronomy & Astrophysics*. Vol. 634, A31. ISSN 0004-6361, ISSN 1432-0746. Available from DOI: 10.1051/0004-6361/201936591 (cit. on p. 176).

VILLENAVE et al., 2022. A Highly Settled Disk around Oph163131. *The Astrophysical Journal*. Vol. 930, p. 11. ISSN 0004-637X. Available from DOI: 10.3847/1538-4357/ac5fae (cit. on p. 54).

VISSER; JØRGENSEN; KRISTENSEN; van DISHOECK; BERGIN, 2013. HOT WATER IN THE INNER 100 AU OF THE CLASS 0 PROTOSTAR NGC 1333 IRAS2A. *The Astrophysical Journal*. Vol. 769, no. 1, p. 19. ISSN 0004-637X, ISSN 1538-4357. Available from DOI: 10.1088/0004-637X/769/1/19 (cit. on pp. 28, 46).

VOROBYOV; DESOUZA; BASU, 2013. The Burst Mode of Accretion in Primordial Protostars. *The Astrophysical Journal*. Vol. 768, no. 2, p. 131. ISSN 0004-637X, ISSN 1538-4357. Available from DOI: 10.1088/0004-637X/768/2/131 (cit. on p. 28).

WAGNER; RIETHMANN; FEISTEL; HARVEY, 2011. New Equations for the Sublimation Pressure and Melting Pressure of H $_2$ O Ice Ih. *Journal of Physical and Chemical Reference Data*. Vol. 40, no. 4, p. 043103. ISSN 0047-2689, ISSN 1529-7845. Available from DOI: 10.1063/1.3657937 (cit. on p. 50).

WAITE et al., 2009. Liquid Water on Enceladus from Observations of Ammonia and 40Ar in the Plume. *Nature*. Vol. 460, pp. 487–490. ISSN 0028-0836. Available from DOI: 10.1038/nature08153 (cit. on p. 140).

WARD, 1997. Survival of Planetary Systems. *The Astrophysical Journal*. Vol. 482, pp. L211–L214. ISSN 0004-637X. Available from DOI: 10.1086/310701 (cit. on p. 98).

WEIDENSCHILLING, 1997. The Origin of Comets in the Solar Nebula: A Unified Model. *Icarus*. Vol. 127, no. 2, pp. 290–306. ISSN 00191035. Available from DOI: 10.1006/icar.1997.5712 (cit. on p. 58).

WEIDENSCHILLING, 2011. Initial Sizes of Planetesimals and Accretion of the Asteroids. *Icarus*. Vol. 214, no. 2, pp. 671–684. ISSN 00191035. Available from DOI: 10.1016/j.icarus.2011.05.024 (cit. on p. 59).

WOITKE, 2023. *Physico-Chemical Processes in Planet-forming Discs*. 2023-12-06. Available from arXiv: 2312.03424 [astro-ph] (cit. on p. 162).

WOITKE; ARABHAVI; KAMP; THI, 2022. Mixing and Diffusion in Protoplanetary Disc Chemistry. *Astronomy & Astrophysics*. Vol. 668, A164. ISSN 0004-6361, ISSN 1432-0746. Available from DOI: 10.1051/0004-6361/202244554 (cit. on p. 162).

WOITKE et al., 2016. Consistent Dust and Gas Models for Protoplanetary Disks: I. Disk Shape, Dust Settling, Opacities, and PAHs. *Astronomy & Astrophysics*. Vol. 586, A103. ISSN 0004-6361, ISSN 1432-0746. Available from DOI: 10.1051/0004-6361/201526538 (cit. on pp. 15, 179).

WOITKE et al., 2023. *2D Disc Modelling of the JWST Line Spectrum of EX Lupi*. 2023-11-30. Available from arXiv: 2311.18321 [astro-ph] (cit. on p. 162).

WONG; MAHAFFY; ATREYA; NIEMANN; OWEN, 2004. Updated Galileo Probe Mass Spectrometer Measurements of Carbon, Oxygen, Nitrogen, and Sulfur on Jupiter. *Icarus*. Vol. 171, no. 1, pp. 153–170. ISSN 00191035. Available from DOI: 10.1016/j.icarus.2004.04.010 (cit. on pp. 8, 32, 81).

YANG; JOHANSEN; CARRERA, 2017. Concentrating Small Particles in Protoplanetary Disks through the Streaming Instability. *Astronomy & Astrophysics*. Vol. 606, A80. ISSN 0004-6361, ISSN 1432-0746. Available from DOI: 10.1051/0004-6361/201630106 (cit. on p. 81).

YOKOYAMA et al., 2022. Samples Returned from the Asteroid Ryugu Are Similar to Ivuna-type Carbonaceous Meteorites. *Science*. Vol. 379, no. 6634, eabn7850. Available from DOI: 10.1126/science.abn7850 (cit. on p. 46).

YOSHIDA et al., 2024. Outflow Driven by a Protoplanet Embedded in the TW Hya Disk. *The Astrophysical Journal Letters*. Vol. 971, no. 1, p. L15. ISSN 2041-8205. Available from DOI: 10.3847/2041-8213/ad654c (cit. on p. 38).

YOUNGBLOOD; PINEDA; FRANCE, 2021. FUMES. II. Ly$\alpha$ Reconstructions of Young, Active M Dwarfs. *The Astrophysical Journal*. Vol. 911, no. 2, p. 112. ISSN 0004-637X, ISSN 1538-4357. Available from DOI: 10.3847/1538-4357/abe8d8 (cit. on p. 142).

ZHANG, 2024. Chemistry in Protoplanetary Disks (cit. on p. 38).

ZHOU; ZHONG; LI; LI, 2022. Preconditioned Jacobian-free Newton–Krylov Fully Implicit High Order WENO Schemes and Flux Limiter Methods for Two-Phase Flow Models. *Nuclear Engineering and Technology*. Vol. 54, no. 1, pp. 49–60. ISSN 1738-5733. Available from DOI: 10.1016/j.net.2021.07.022 (cit. on p. 104).

ZHU; HARTMANN; NELSON; GAMMIE, 2012. Challenges In Forming Planets By Gravitational Instability: Disk Irradiation And Clump Migration, Accretion, And Tidal Destruction. *The Astrophysical Journal*. Vol. 746, no. 1, p. 110. ISSN 0004-637X, ISSN 1538-4357. Available from DOI: 10.1088/0004-637X/746/1/110 (cit. on pp. 98, 99, 115, 117).

ZIEBA et al., 2023. No Thick Carbon Dioxide Atmosphere on the Rocky Exoplanet TRAPPIST-1 c. *Nature*. Vol. 620, no. 7975, pp. 746–749. ISSN 0028-0836, ISSN 1476-4687. Available from DOI: 10.1038/s41586-023-06232-z (cit. on p. 141).

ZIMMER et al., 2016. SUPCRTBL: A Revised and Extended Thermodynamic Dataset and Software Package of SUPCRT92. *Computers and Geosciences*. Vol. 90, pp. 97–111. ISSN 0098-3004. Available from DOI: 10.1016/j.cageo.2016.02.013 (cit. on p. 47).

# ANNEXES

# A. Volatile radial distribution in the PPD : parameter variation

The parameter variation presented in section **??** discussion is is based on the examples of $CH_4$ and Xe radial profiles variation example. In this section we present the radial distribution profiles of all the volatile species in each cases. We recall the nominal parameters are presented in table **??**. The parameter variation is performed in the scenario with species' vapor, pure condensates and clathrate hydrates, refered in **??** as scenario 1. The goal of this variation of parameter is to assess the behavior of the different phases when varying the model's parameters.

## A.1. PPD initial mass

The PPD initial mass is varied between from $10^{-1}$ $M_\odot$ to $10^{-2}$ and $1.5 \times 10^{-3}$ $M_\odot$. Figure A.1 and A.2 show the species' enrichment with initial PPD mass of $10^{-2}$ and $1.5 \times 10^{-3}$ $M_\odot$ respectively. Both figures show that decreasing the PPD mass will shift the positions of the different lines inward.

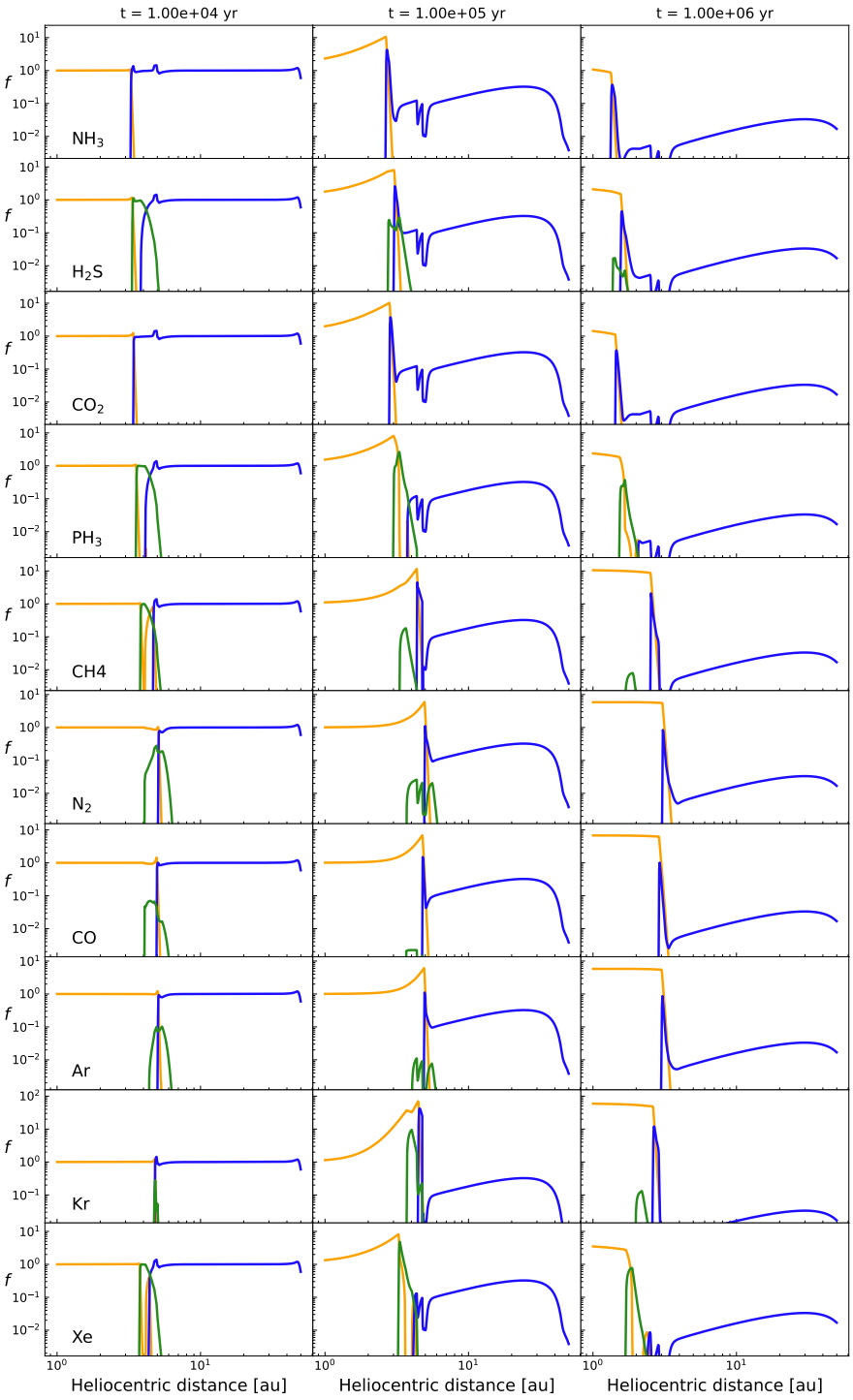


Figure A.1.: Time and Radial distribution of volatile species mass abundances normalized to their initial values in a PPD with an initial mass of $10^{-2}$ $M_{\odot}$. Species' enrichment are represented in gaseous phase (orange line), pure condensate (blue line) and clathrate (green line), at $10^4$, $10^5$ and $10^6$ yr.

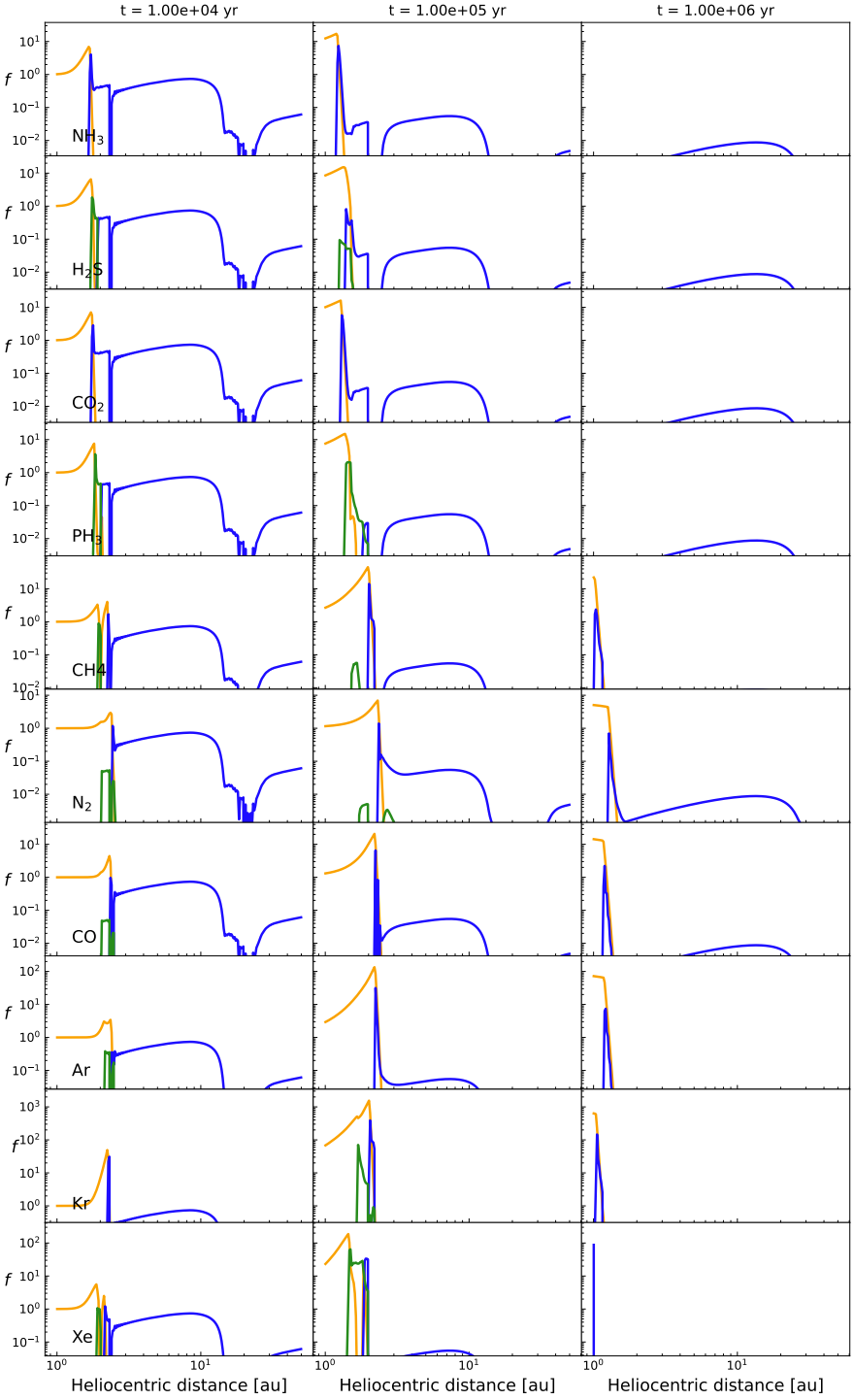


Figure A.2.: Time and Radial distribution of volatile species mass abundances normalized to their initial values in a PPD with an inial mass of $1.5 \times 10^{-3}$ $M_{\odot}$. Species' enrichment are represented in gaseous phase (orange line), pure condensate (blue line) and clathrate (green line), at $10^4$, $10^5$ and $10^6$ yr.

## A.2. Alpha viscosity

Figure A.3 show the species' distribution with an $\alpha$ of $10^{-2}$. When compared with the nominal model with and $\alpha$ of $10^{-3}$ it shows that an increased $\alpha$ smooth out the enrichment peaks. Due to the increased diffusivity of vapor and pebbles.

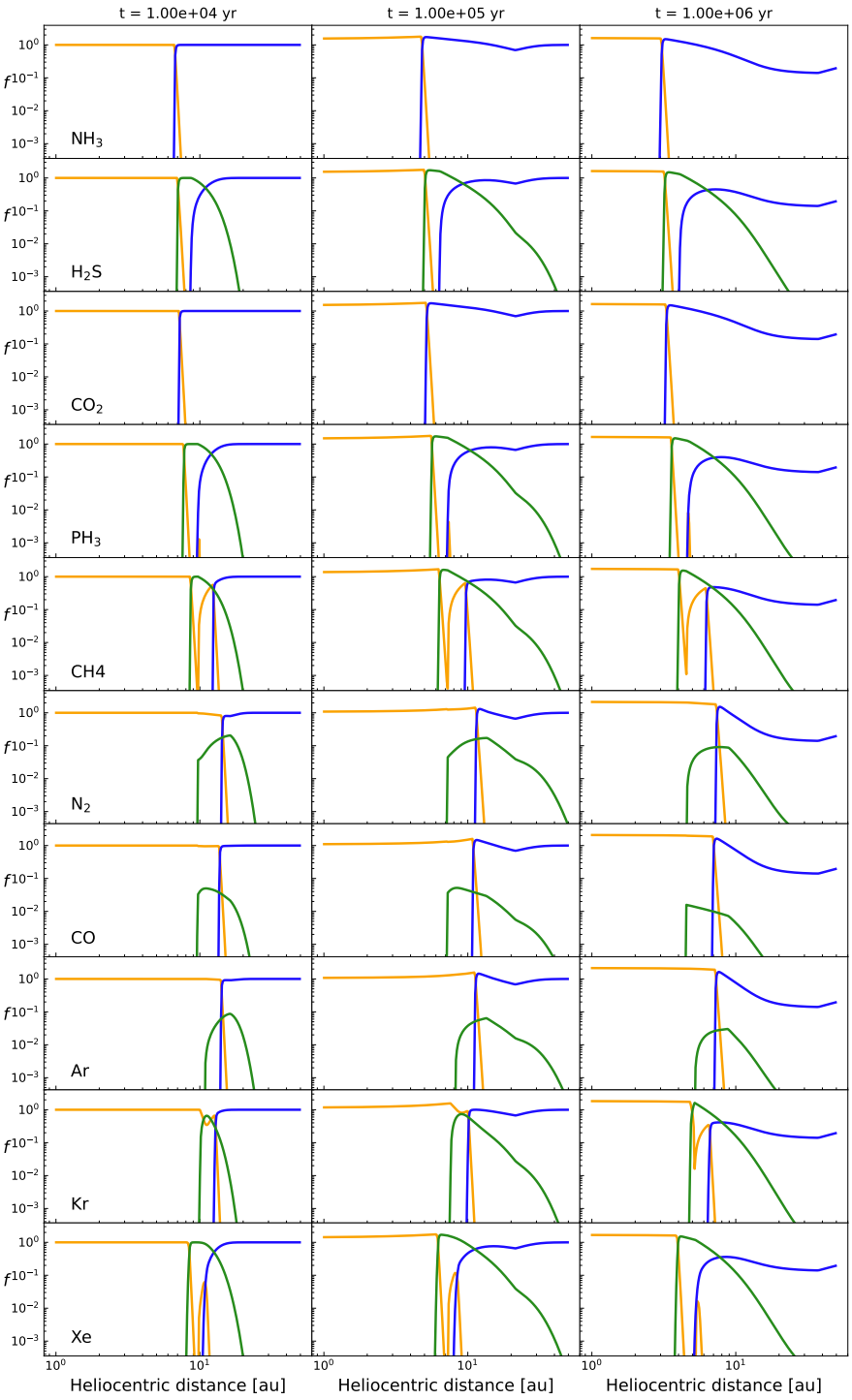


Figure A.3.: Time and Radial distribution of volatile species mass abundances normalized to their initial values with a $\alpha$ viscosity of $10^{-2}$. Species' enrichment are represented in gaseous phase (orange line), pure condensate (blue line) and clathrate (green line), at $10^4$, $10^5$ and $10^6$ yr.

## A.3. Initial accretion rates

The initial accretion rate is varied from the nominal

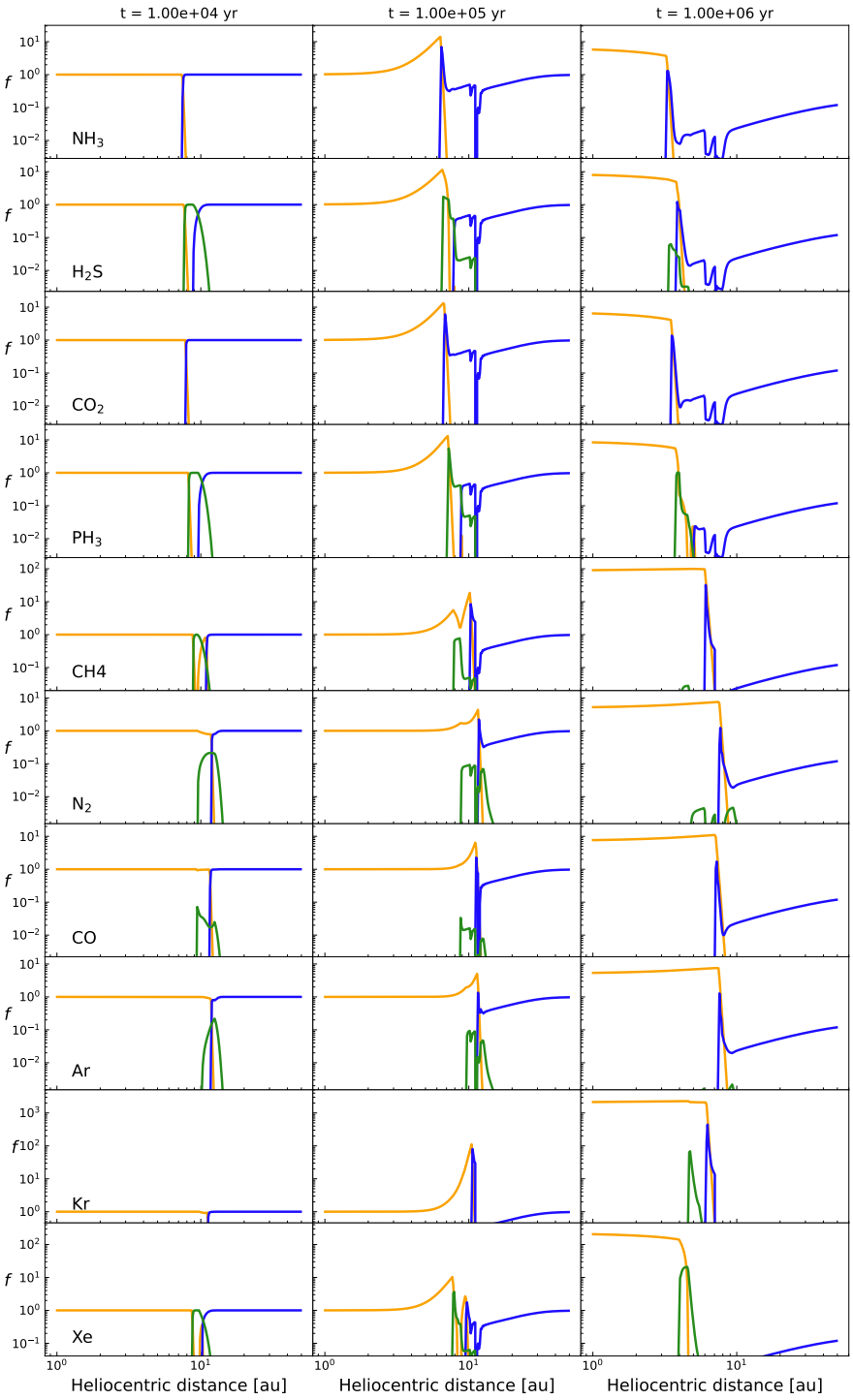


Figure A.4.: Time and Radial distribution of volatile species mass abundances normalized to their initial values in gaseous phase (orange line), pure condensate (blue line) and clathrate (green line), with an initial accretion of $10^{-6}$ $M_\odot$ $yr^{-1}$ at $10^4$, $10^5$ and $10^6$ yr.

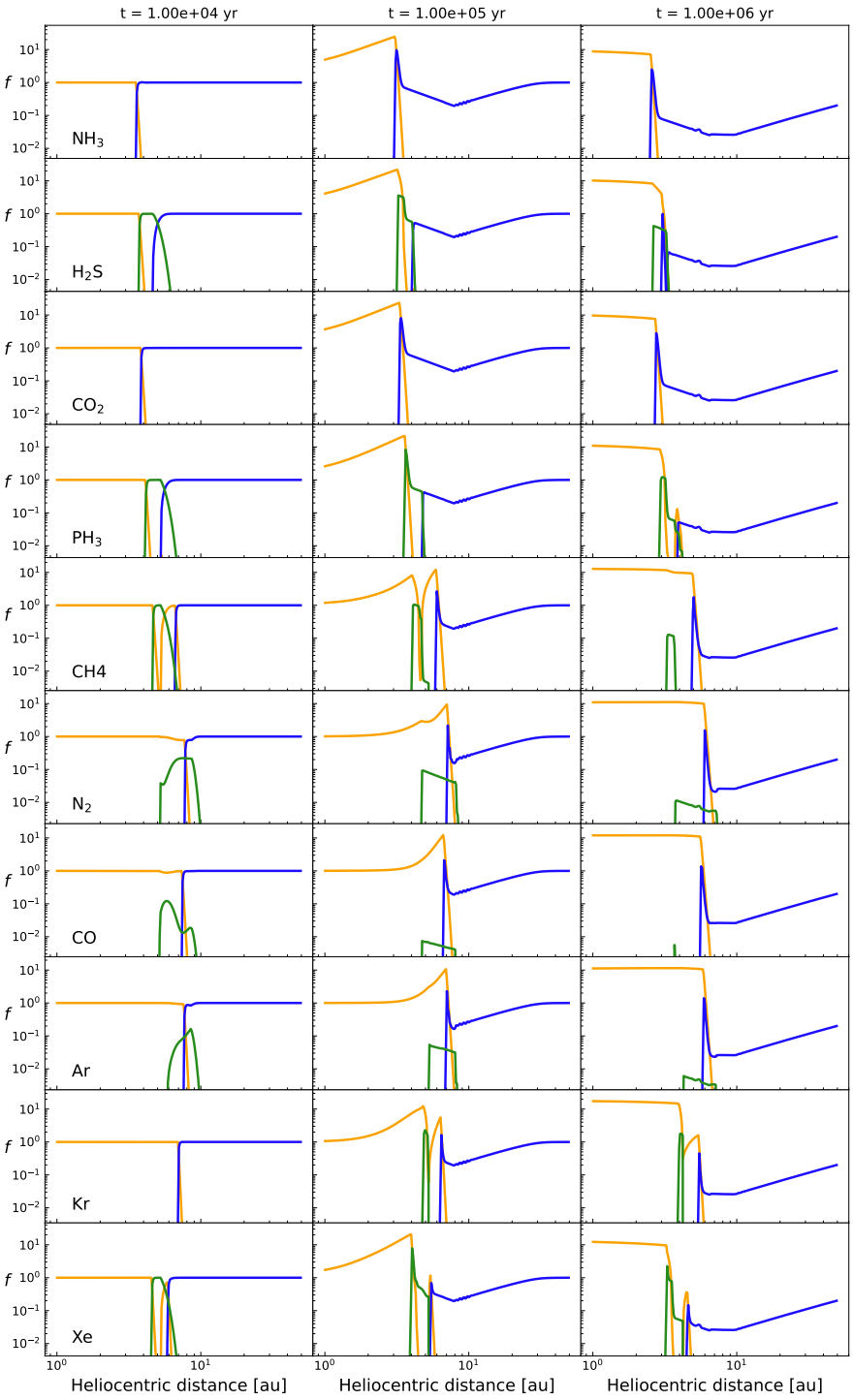


Figure A.5.: Time and Radial distribution of volatile species mass abundances normalized to their initial values in gaseous phase (orange line), pure condensate (blue line) and clathrate (green line), with an initial accretion of $10^{-8}$ $M_\odot$ $yr^{-1}$ at $10^4$, $10^5$ and $10^6$ yr.

## A.4. Pebble's density

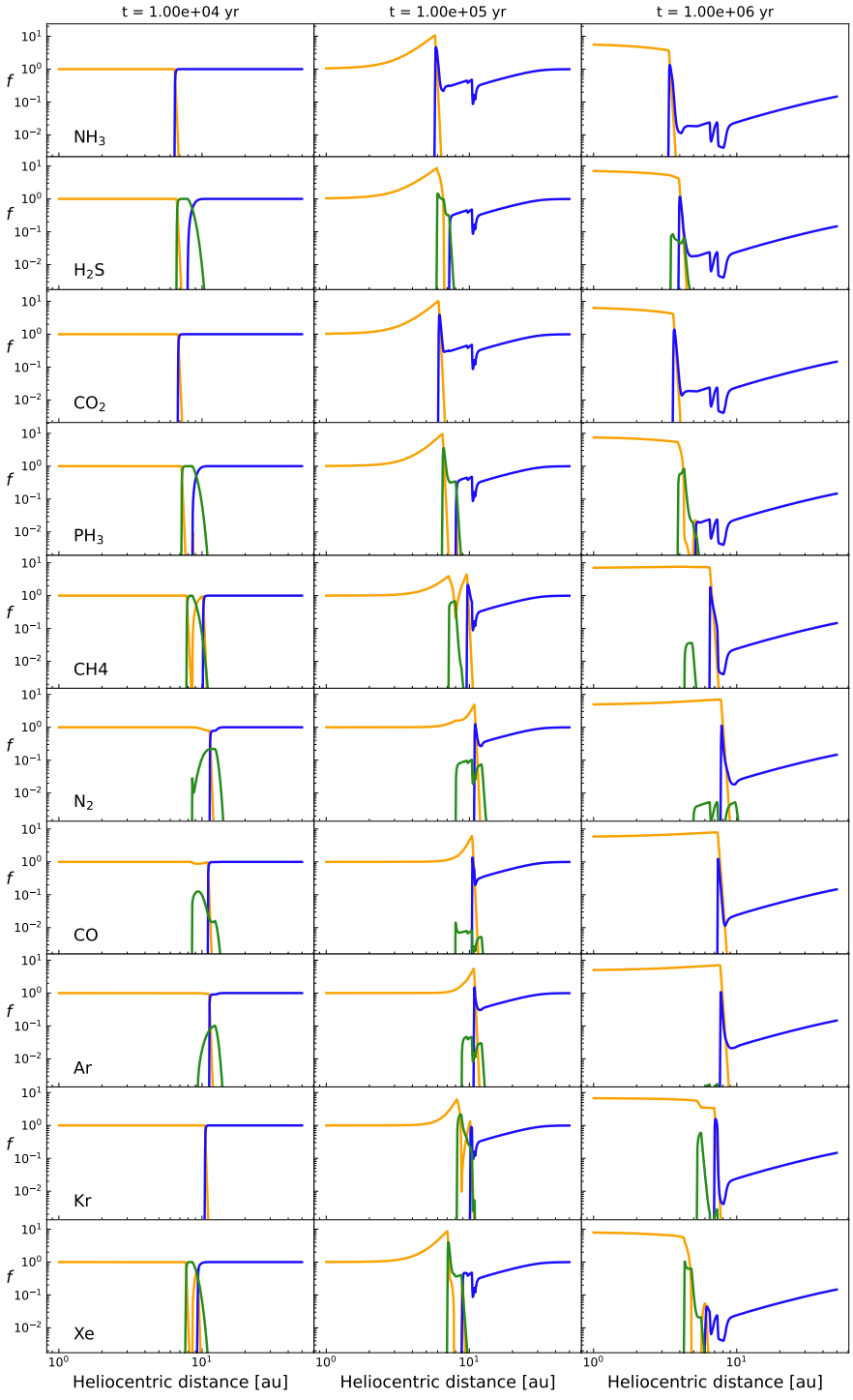


Figure A.6.: Time and Radial distribution of volatile species mass abundances normalized to their initial values in gaseous phase (orange line), pure condensate (blue line) and clathrate (green line), with a pebble density of $5 \times 10^{-1}$ , at $10^4$, $10^5$ and $10^6$ yr.

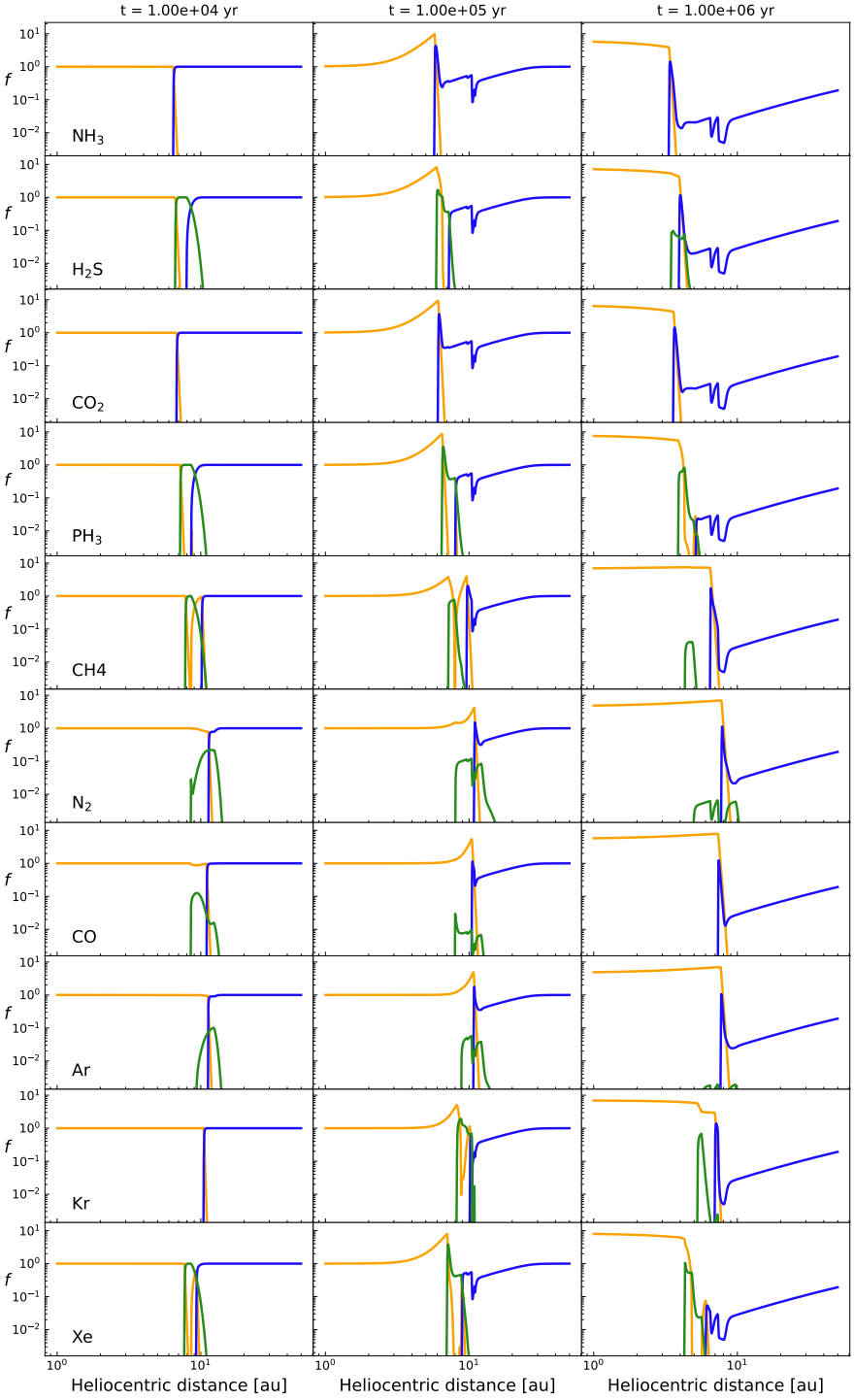


Figure A.7.: Time and Radial distribution of volatile species mass abundances normalized to their initial values in gaseous phase (orange line), pure condensate (blue line) and clathrate (green line), with a pebble density of $5 \times 10^{-2}$ , at $10^4$, $10^5$ and $10^6$ yr.

# B. List of publication

## B.1. Schneeberger et al. 2023

A&A 670, A28 (2023)
https://doi.org/10.1051/0004-6361/202244670
© The Authors 2023

Astronomy & Astrophysics

# Evolution of the reservoirs of volatiles in the protosolar nebula

Antoine Schneeberger[1], Olivier Mousis[1,2], Artyom Aguichine[1], and Jonathan I. Lunine[3]

[1] Aix-Marseille Université, CNRS, CNES, Institut Origines, LAM, 13388 Marseille, France
e-mail: antoine.schneeberger@lam.fr
[2] Institut Universitaire de France (IUF), 75231 Paris Cedex 05, France
[3] Department of Astronomy, Cornell University, Ithaca NY 14853, USA

Received 2 August 2022 / Accepted 30 November 2022

**ABSTRACT**

The supersolar abundances of volatiles observed in giant planets suggest that a compositional gradient was present at the time of their formation in the protosolar nebula. To explain this gradient, several studies have investigated the radial transport of trace species and the effect of icelines on the abundance profiles of solids and vapors formed in the disk. However, these models only consider the presence of solids in the forms of pure condensates or amorphous ice during the evolution of the protosolar nebula. They usually neglect the possible crystallization and destabilization of clathrates, along with the resulting interplay between the abundance of water and those of these crystalline forms. This study is aimed at pushing this kind of investigation further by considering all possible solid phases together in the protosolar nebula: pure condensates, amorphous ice, and clathrates. To this end, we used a one-dimensional (1D) protoplanetary disk model coupled with modules describing the evolution of trace species in the vapor phase, as well as the dynamics of dust and pebbles. Eleven key species are considered here, including $H_2O$, CO, $CO_2$, $CH_4$, $H_2S$, $N_2$, $NH_3$, Ar, Kr, Xe, and $PH_3$. Two sets of initial conditions are explored for the protosolar nebula. In a first scenario, the disk is initially filled with icy grains in the forms of pure condensates. In this case, we show that clathrates can crystallize and form enrichment peaks up to about ten times the initial abundances at their crystallization lines. In a second scenario, the volatiles were delivered to the protosolar nebula in the forms of amorphous grains. In this case, the presence of clathrates is not possible because there is no available crystalline water ice in their formation region. Enrichment peaks of pure condensates also form beyond the snowline up to about seven times the initial abundances. Our model can then be used to compare the compositions of its different volatile reservoirs with those of comet C/2016 R2 PanSTARRS, Jupiter, Uranus, and Neptune. We find that the two investigated scenarios provide compositions of solids and vapors consistent with those observed in the bodies considered.

**Key words.** protoplanetary disks – planets and satellites: formation – planets and satellites: composition – comets: individual: C/2016 R2 PanSTARR – solid state: volatile – astrobiology

## 1. Introduction

It is commonly assumed that Solar System bodies have bulk compositions that are representative of the material present in the protosolar nebula (PSN) from which they formed. If the PSN was homogeneous in composition, gas and ice giants would be expected to reflect this homogeneity. However, observations show that giant planets present a range of supersolar metallicities. In Jupiter's atmosphere, the abundances of volatile elements were found to be ∼1.5–6.1 times higher than their protosolar values (Atreya et al. 2003; Mousis et al. 2018; Li et al. 2020), with a few exceptions attributed to interior processes. In Uranus and Neptune, volatile abundances can reach up to about 100 times their protosolar values (Lindal et al. 1987, 1990; Baines et al. 1995; Karkoschka & Tomasko 2009; Sromovsky et al. 2014).

Numerical models show that the dynamics of icy pebbles and their vapors around icelines is an efficient mechanism to produce local changes in the composition of the PSN (Booth et al. 2017; Desch et al. 2017). This process efficiently concentrates species around their respective icelines, creating the compositional gradient that may be responsible for the volatile enrichment in giant planets of our Solar System. The radial transport of trace species and the effect of icelines have been investigated using accretion disk models to assess the composition of the PSN. The resulting compositional profiles would then be used to constrain the formation conditions of gas giants (Mousis et al. 2019; Schneider & Bitsch 2021; Aguichine et al. 2022) or ice giants (Owen et al. 1999; Monga & Desch 2015; Mousis et al. 2020). This approach has also been used to explain the diversity among the cometary compositions and to determine their source or the general origins of their building blocks (Mandt et al. 2020; Mousis et al. 2021a).

The form taken by volatiles that have fallen from the interstellar medium (ISM) onto the PSN is still an open question. Icy pebbles that are present at the earliest stages of the PSN may have formed in the very cold environment of the ISM, at temperatures of 10 K or below (Gibb et al. 2004). At such low temperatures, $H_2O$ condenses in an amorphous structure that can efficiently trap other volatile species (Mayer & Pletzer 1986; Jenniskens et al. 1995). At ∼135 K, the amorphous ice transitions to crystalline ice and releases trapped volatiles (Bar-Nun et al. 2007). This temperature is much higher than the usual sublimation temperature of pure condensates. In the PSN, the heliocentric distance at which this release occurs is called the Amorphous to Crystalline Transition Zone (ACTZ), and is located at approximately 5 au (Mousis et al. 2019). However, it is not clear whether this amorphous ice survives the fall onto the PSN. For instance, it has been proposed that amorphous dust was heated up to crystallization when entering the PSN (Visser et al. 2013), as a consequence of the presence of shockwaves in



Open Access article, published by EDP Sciences, under the terms of the Creative Commons Attribution License (https://creativecommons.org/licenses/by/4.0), which permits unrestricted use, distribution, and reproduction in any medium, provided the original work is properly cited.

the accreting PSN (Miura et al. 2017; Burkhardt et al. 2019). As a result, many circumstellar disk models treat volatile species as pure condensates, with sublimation temperatures computed from thermodynamic tables (Dodson-Robinson et al. 2009; Ciesla et al. 2015; Öberg & Wordsworth 2019). Alternatively, volatile species may also be trapped in clathrate form in the PSN, when sufficient amounts of $H_2O$ are available (Lunine & Stevenson 1985; Gautier & Hersant 2005; Mousis et al. 2021b). A species, $i$, is usually trapped in clathrate at a higher temperature than the one needed to sublimate its pure condensate form, except for the cases of $CO_2$ and $NH_3$. Because $CO_2$ clathrate and $NH_3$ monohydrate form at lower temperatures than their respective condensates at nebular pressures, they are not considered in our model. In the following, we refer to the heliocentric distance at which volatiles are entrapped in or released from clathrates as the clathration line. For this reason, volatile species can remain adsorbed on amorphous ice or trapped in clathrates, then they are released several au closer to the Sun – than they otherwise would be if they were in the form of pure condensates.

In this study, we aim to quantify the influence of the presence of various icelines in the PSN, including the ACTZ and multiple clathration lines, on the nature of the main volatile reservoirs that were at play during the formation of the first icy grains in the disk. To do so, we use an existing PSN model that already describes the condensation and sublimation of pure ices, as well as the transport of species in solid and vapor forms (Aguichine et al. 2020, 2022), along with prescriptions of amorphous ice destabilization, as well as clathrate crystallization and dissociation added. Eleven key species are considered in our approach, namely: $H_2O$, CO, $CO_2$, $CH_4$, $H_2S$, $N_2$, $NH_3$, Ar, Kr, Xe, and $PH_3$. Each of these species can exist in the forms of vapor, crystalline ice, clathrate (monohydrate in the case of $NH_3$), or amorphous ice in the PSN. Two scenarios are investigated, each of them corresponding to a different initial state of the system. In scenario 1: the PSN is filled with volatile species in pure condensates or vapor form, depending on their location in the PSN. In scenario 2: the PSN is filled with volatile species adsorbed on amorphous ice beyond the ACTZ, and in vapor form in regions closer to the Sun. Because the ACTZ is located beyond the snowline, $H_2O$ is found in crystalline form between the snowline and the ACTZ. Figure 1 represents the different forms of volatiles in the PSN in these two cases. In scenario 1, volatile species are in the vapor phase between the snowline and their respective icelines. If enough $H_2O$ is available, these vapors can form clathrates. In scenario 2, icy grains of amorphous ice that drifted inward of the ACTZ release the adsorbed volatile species as vapors. The outward diffusion of these vapors can lead to the formation of clathrates or pure condensates (or both).

Section 2 describes the PSN model, as well as the transport modules used in our calculations. It also depicts the different formalisms that have been added to the disk model to mimic the formation and destabilization of clathrates, as well as the desorption of volatiles from the amorphous ice particles crossing the ACTZ. In Sect. 3, the radial profiles of the abundances of the different species are represented in various forms as a function of time in the PSN and in the individual cases described by the two scenarios. Section 4 is devoted to a discussion of the sensitivity of our results in light of the variation of the disk parameters. Our model is then used to compare the compositions of its resulting volatile reservoirs with those of the $H_2O$–poor comet C/2016 R2 PanSTARRS (R2), Jupiter, Uranus, and Neptune. This allows us to discuss the formation conditions of those bodies in the context of the two scenarios. Section 5 presents our conclusions.

## 2. Volatile transport and evolution model

In this section, we describe the protosolar nebula model employed in our simulations, along with the modules calculating the transport of dust particles and vapors within the disk. Source and sink terms related to sublimation and condensation of pure ices as well as to clathrate destabilization and formation within the disk are also depicted.

### 2.1. Protoplanetary disk model

The disk model used here is the one described in Aguichine et al. (2020) and Mousis et al. (2020). The evolution of the PSN is governed by the following differential equation (Lynden-Bell & Pringle 1974):

$$\frac{\partial \Sigma_g}{\partial t} = \frac{3}{r}\frac{\partial}{\partial r}\left[r^{1/2}\frac{\partial}{\partial r}\left(r^{1/2}\Sigma_g \nu\right)\right], \tag{1}$$

which describes the time evolution of a viscous accretion disk of surface density, $\Sigma_g$, and viscosity, $\nu$, assuming invariance in the orbital direction and hydrostatic equilibrium in the azimuthal direction. This equation can be rewritten as a set of two first-order differential equations coupling the gas surface density, $\Sigma_g$, field and mass accretion rate, $\dot{M}$:

$$\begin{cases} \dfrac{\partial \Sigma_g}{\partial t} = \dfrac{1}{2\pi r}\dfrac{\partial \dot{M}}{\partial r} \\ \dot{M} = 3\pi\Sigma_g \nu\left(1 + 2\dfrac{\partial \ln \nu\Sigma_g}{\partial \ln r}\right). \end{cases} \tag{2}$$

The first equation is a mass conservation law and the second one is a diffusion equation. The mass accretion rate is expressed as a function of the gas velocity field, $v_g$, and the radius, $r$, as $\dot{M} = -2\pi\Sigma_g v_g \mathbf{r}$.

The dynamical viscosity $\nu$ is calculated using the prescription of Shakura & Sunyaev (1973):

$$\nu = \alpha\frac{c_s^2}{\Omega_K}, \tag{3}$$

where $\alpha$ is the viscosity coefficient, $c_s$ is the sound speed in the PSN, and $\Omega_K$ is the Keplerian frequency; also, $\alpha$ is estimated to be in the $10^{-4}$–$10^{-2}$ range, based on models calibrated on disk observations (Hartmann et al. 1998; Hersant et al. 2004; Gautier & Hersant 2005; Birnstiel et al. 2012; Drążkowska & Alibert 2017; Armitage 2019). The sound speed, $c_s$, is expressed as follows:

$$c_s = \sqrt{\frac{RT}{\mu_g}}, \tag{4}$$

where $\mu_g$ is the mean molecular mass of the gas in the PSN, assumed here to be equal to 2.31 g mol$^{-1}$, $T$ is the midplane temperature, and $R$ is the ideal gas constant.

Two energy sources are considered in our model, namely viscous heating, and the constant irradiation by the local environment of ambient temperature, $T_{amb}$ = 10 K. Irradiation from the young Sun is neglected because the presence of shadowing is assumed in the outer part of the disk (Ohno & Ueda 2021). This allows the disk temperature to decrease to the condensation temperature of Ar (~20 K), allowing this species to be trapped in Jupiter's building blocks in a way consistent with the super-solar abundance observed in its envelope (Mousis et al. 2009b,

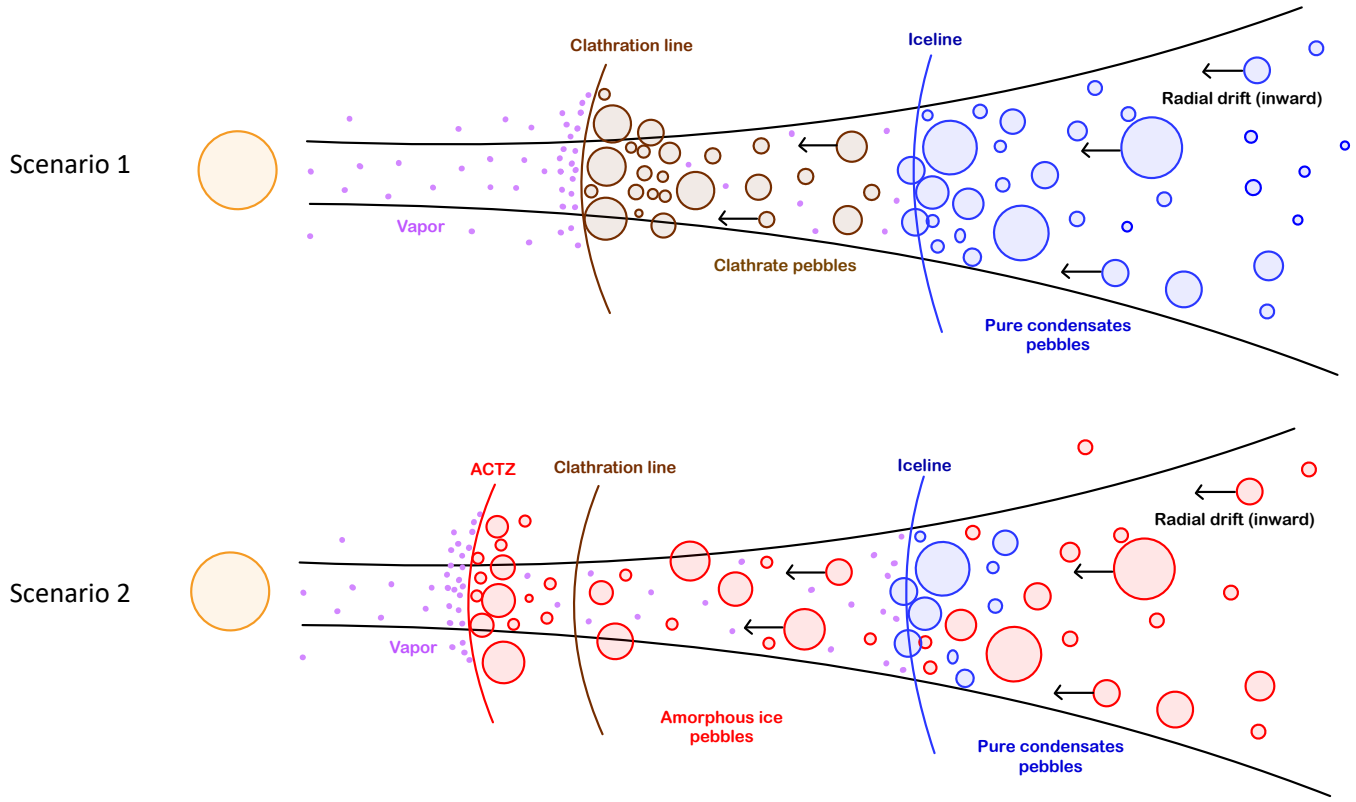


**Fig. 1.** Two outcome scenarios for volatile species explored in this paper. *Top panel*: the case where volatiles are initially delivered in pure condensate form to the PSN (scenario 1). *Bottom panel*: the case where volatiles are released in vapor form in the PSN when amorphous grains cross the ACTZ region (scenario 2). Pure condensates, clathrate, and amorphous ice pebbles are represented as blue, brown and red circles, respectively. Vapor is represented as purple dots. The iceline, clathration line, and ACTZ are represented as blue, brown, and red solid lines, respectively. Once delivered to the disk, the phase (solid or gaseous) of each species is determined by the positions of the corresponding condensation, hydration, or clathration lines. Except for the case of $CO_2$, which vaporises at a higher temperature than its clathrate form, hydration, or clathration lines of the volatiles considered are closer to the Sun than their respective icelines. Gaseous volatiles condense or become entrapped (depending on the availability of water ice) when diffusing outward of the locations of their condensation, hydration, or clathration lines. Conversely, volatiles condensed or entrapped in grains or pebbles are released in vapor form when drifting inward of their lines. Peaks of abundances form close to each phase-transition line (see text). Those enrichments are represented by higher solid and vapor concentrations in the panels.

2012, 2021b). The temperature profile is computed by summing the energy production rates of both energy sources (Hueso & Guillot 2005):

$$T^4 = \frac{1}{2\sigma_{\rm SB}}\left(\frac{3}{8}\tau_{\rm R} + \frac{1}{2\tau_{\rm P}}\right)\Sigma_{\rm g}\nu\Omega_{\rm K}^2 + T_{\rm amb}^4, \tag{5}$$

where $\sigma_{\rm sb}$ is the Stefan-Boltzmann constant, while $\tau_{\rm R}$ and $\tau_{\rm P}$ are the Rosseland and Planck optical depth, respectively. Here, we assume $\tau_{\rm P} = 2.4\tau_{\rm R}$, a case corresponding to the opacity generated by dust grains smaller than 10 µm (Nakamoto & Nakagawa 1994); $\tau_{\rm R}$ is derived from the Rosseland mean opacity, $\kappa_{\rm R}$, via the following expression (Hueso & Guillot 2005):

$$\tau_{\rm R} = \frac{\Sigma_g \kappa_{\rm R}}{2}. \tag{6}$$

Here, $\kappa_{\rm R}$ is computed as a sequence of power laws of the form $\kappa_{\rm R} = \kappa_0 \rho^a T^b$, where $\rho$ denotes the gas density at the midplane, and $\kappa_0$, $a$, and $b$ are constants that are obtained by fits on observational data in different opacity regimes (Bell & Lin 1994).

The initial state of the model is computed from the self-similar solution derived by Lynden-Bell & Pringle (1974):

$$\Sigma_{\rm g}\nu \propto \exp\left[-\left(\frac{r}{r_{\rm c}}\right)^{2-p}\right]. \tag{7}$$

By combining Eqs. (7) and (2), and assuming $p = \frac{3}{2}$, which corresponds to the case for an early disk (Lynden-Bell & Pringle 1974), the initial profiles of the dust surface density and mass accretion rate are given by:

$$\begin{cases} \Sigma_{\rm g,0} = \dfrac{\dot{M}_{\rm acc,0}}{3\pi\nu}\exp\left[-\left(\dfrac{r}{r_{\rm c}}\right)^{0.5}\right] \\ \dot{M}_0 = \dot{M}_{\rm acc,0}\left(1-\left(\dfrac{r}{r_{\rm c}}\right)^{0.5}\right)\exp\left[-\left(\dfrac{r}{r_{\rm c}}\right)^{0.5}\right], \end{cases} \tag{8}$$

where $r_{\rm c}$ is the centrifugal radius and $\dot{M}_{\rm acc,0}$ is the initial mass accretion rate onto the central star, set to $10^{-7.6}\,M_\odot\,{\rm yr}^{-1}$ (Hartmann et al. 1998). The disk mass is related to the surface density profile via the following expression:

$$M_{\rm disk} = 2\pi\int_{R_{\rm min}}^{R_{\rm max}}\Sigma r {\rm d}r, \tag{9}$$

where $R_{\rm min}$ and $R_{\rm max}$ are the inner and outer bounds of our model. The total disk mass is set to $0.1\,M_\odot$ and most of it (99%) is encapsulated within ~200 au. The centrifugal radius, $r_{\rm c}$, is determined by solving Eqs. (8) with (9) for the chosen values of mass accretion rate and disk mass. Figure 2 represents the thermodynamic profiles of our PSN model assuming $\alpha = 10^{-3}$, and at $t = 10^4$, $10^5$, and $10^6$ yr of the disk evolution.

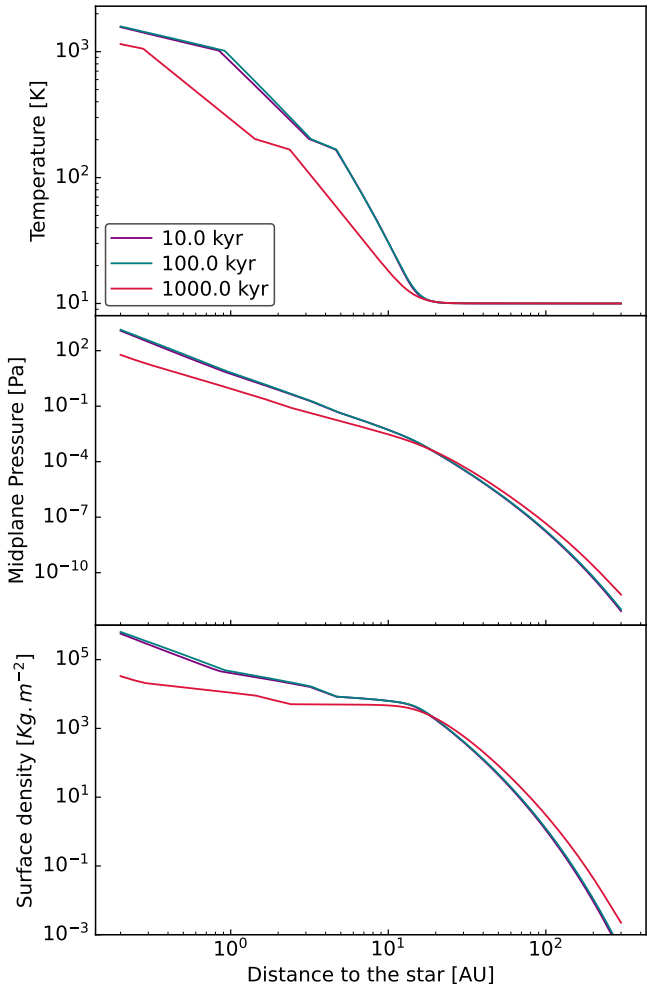


**Fig. 2.** Profiles of the disk midplane temperature, pressure and surface density calculated at $t = 10^4$, $10^5$, and $10^6$ yr as a function of heliocentric distance, assuming $\alpha = 10^{-3}$, shown from *top to bottom*.

### 2.2. Dust dynamics

To determine the size of the dust pebbles, we rely heavily on the two-population algorithm developed by Birnstiel et al. (2012). This algorithm relies on the key idea that the dynamics of dust pebbles of many different sizes can be well approximated by the dynamics of only two populations of particles, in which all particles have the same representative sizes. The first group corresponds to the small population, where grains are of constant size: $a_0 = 0.1$ µm. The second group represents a large population, where pebbles have a representative size $a_1$, which depends on the characteristics of the flow.

In the disk, pebbles grow by sticking collisions via the following law:

$$a_1(t) = a_0 \exp\left(\frac{t}{\tau_{\rm growth}}\right), \tag{10}$$

where $\tau_{\rm growth}$ is the growth timescale,

$$\tau_{\rm grow} = \frac{4\Sigma_{\rm g}}{\sqrt{3}\epsilon_{\rm g}\Sigma_{\rm b}\Omega_{\rm K}}, \tag{11}$$

where $\Sigma_{\rm b}$ is the total surface density of solids, and $\epsilon_{\rm g}$ is the dust growth efficiency through mutual sticking set to 0.5 (Lambrechts & Johansen 2014). Then, we compute the Stokes number of pebbles as a function of their sizes (Johansen et al. 2014):

$$\mathrm{St} = \begin{cases} \sqrt{2\pi}\dfrac{a_1\rho_{\rm b}}{\Sigma_{\rm g}} \text{ If } a_1 \leq \dfrac{9}{4}\lambda \\ \dfrac{8}{9}\dfrac{a_1^2\rho_b c_{\rm s}}{\Sigma_{\rm g}\nu} \text{ If } a_1 \geq \dfrac{9}{4}\lambda \end{cases}. \tag{12}$$

The top and bottom lines of Eq. (12) correspond to the Epstein and Stokes regimes, respectively. The limit between both regimes is fixed by the gas mean free path $\lambda = \sqrt{\pi/2}\cdot\nu/c_{\rm s}$, computed by equating the two terms in Eq. (12). The term $\rho_{\rm b}$ is the pebbles mean bulk density:

$$\rho_{\rm b} = \frac{\sum_i \Sigma_{{\rm b},i}\rho_{{\rm b},i}}{\sum_i \Sigma_{{\rm b},i}}, \tag{13}$$

computed as the average of each species' bulk density, $\rho_{{\rm b},i}$, weighted by their solid surface density, $\Sigma_{{\rm b},i}$.

Observations indicate that disks are rich in small dust and suggest that fragmentation is a dominant process (Williams & Cieza 2011). Based on this observation, our approach considers fragmentation and radial drift as the growth-limiting mechanisms. These mechanisms set an upper limit on the highest Stokes number that particles can achieve. The first limitation results from the fragmentation occurring when the relative speed between two pebbles due to turbulent motion exceeds the fragmentation velocity, $u_{\rm f}$. This upper limit is given by (Birnstiel et al. 2012):

$$\mathrm{St}_{\rm frag} = f_{\rm f}\frac{1}{3\alpha}\frac{u_{\rm f}^2}{c_{\rm s}^2}, \tag{14}$$

where $u_{\rm f}$ is set to $10\,\mathrm{m\,s^{-1}}$ and the factor $f_{\rm f} = 0.37$ accounts for the fact that the representative size of the large population is smaller than the biggest size particles can achieve before they fragment.

A second limitation for dust growth is determined by the drift velocities of the different pebbles. When pebbles drift faster than they grow, this sets another upper limit for the Stokes number (Birnstiel et al. 2012):

$$\mathrm{St}_{\rm drift} = f_{\rm d}\frac{\Sigma_{\rm b}v_{\rm K}^2}{\Sigma_{\rm g}c_{\rm s}^2}\left|\frac{{\rm d}\ln P}{{\rm d}\ln r}\right|^{-1}, \tag{15}$$

where $P$ is the disk midplane pressure, $v_{\rm K}$ the keplerian velocity, and $f_{\rm d} = 0.55$ has the same origin as $f_{\rm f}$.

When dust grains drift at a high velocity and collide with other particles on their path, they can fragment. This induces a third upper limit for the Stokes number (Birnstiel et al. 2012), given by:

$$\mathrm{St}_{\rm df} = \frac{1}{1-N}\frac{u_{\rm f}v_{\rm K}}{c_{\rm s}}\left(\frac{{\rm d}P}{{\rm d}r}\right)^{-1}, \tag{16}$$

where the factor $N = 0.5$ accounts for the fact that only larger grains fragment when colliding.

In the algorithm, all limiting Stokes numbers are computed and compared with the Stokes number derived from Eq. (12). At each time step, the smallest Stokes number found in this comparison becomes the reference Stokes number which, in turn, sets the value for the representative size, $a_1$, of the large population. The representative size of the small population is always $a_0$, and

their Stokes number is always computed in the Epstein regime (top line of Eq. (12)).

Finally, the two-population algorithm of Birnstiel et al. (2012) introduces $f_m$ the fraction of the mass contained in the large population. Among the three size-limiting mechanisms, if particle drift is the most limiting one ($St_{drift} = \min\left(St_{frag}, St_{drift}, St_{df}\right)$), then the fraction of the mass contained in the large population is $f_m = 0.97$. Otherwise, $f_m$ is set to 0.75 (Birnstiel et al. 2012). The mean grain size $\bar{a}$ is then given by:

$$\bar{a} = f_m a_1 + (1 - f_m)\, a_0. \tag{17}$$

### 2.3. Trace species evolution model

Trace species are considered in four distinct forms: vapors, pure condensates, entrapped in clathrates, or forming a monohydrate (case for $NH_3$ only), and adsorbed in amorphous ice. In our model, a distinct surface density is attributed to each of these forms, with $\Sigma_{v,i}$, $\Sigma_{p,i}$, $\Sigma_{c,i}$, and $\Sigma_{a,i}$ corresponding to species $i$ in vapor, pure condensate, clathrate or hydrate, or amorphous ice phases, respectively. Their time and radial evolution is governed by the advection-diffusion equation (Birnstiel et al. 2012; Desch et al. 2017):

$$\frac{\partial \Sigma_i}{\partial t} + \frac{1}{r}\frac{\partial}{\partial r}\left[r\left(\Sigma_i v_i - D_i \Sigma_g \frac{\partial}{\partial r}\left(\frac{\Sigma_i}{\Sigma_g}\right)\right)\right] - \dot{Q}_i = 0, \tag{18}$$

where $D_i$ is the diffusion coefficient and is $v_i$ is the radial speed. $\dot{Q}_i$ is a source or sink term that accounts for phase changes, counted positive/negative when some matter is created or lost.

For surface densities of vapors, we assume $D_i = D_g$ and $v_i = v_g$ because vapors are well coupled to the PSN gas and evolve similarly. The gas diffusivity, $D_g$, is assumed to be equal to the viscosity, $\nu$, and the gas velocity is (Shakura & Sunyaev 1973):

$$v_g = -\frac{\dot{M}_{acc}}{2\pi r \Sigma_g}. \tag{19}$$

At each time and location, we assume that dust particles are formed from a mixture of all available solids. As a consequence, surface densities of solid phases, namely clathrates (and $NH_3$ monohydrate), amorphous ices, and pure condensates, are evolved with the same diffusion coefficient, $D_s$, and radial velocity, $v_s$. For particles of a given size, $a$, and Stokes number, St, the diffusion coefficient is given by (Birnstiel et al. 2012):

$$D_s = \frac{D_g}{1 + St^2}. \tag{20}$$

The dust radial velocity is expressed as the sum of gas drag and drift velocities (Birnstiel et al. 2012):

$$v_s = \frac{1}{1 + St^2} v_g + \frac{2St}{1 + St^2} v_{drift}, \tag{21}$$

where the drift velocity is (Weidenschilling 1997):

$$v_{drift} = \frac{c_s^2}{v_K}\frac{d \ln P}{d \ln r}. \tag{22}$$

The diffusion coefficient and radial velocity of solids are computed for the small and the large populations, that is, for particles of sizes $a_0$ and $a_1$. The diffusion coefficient, $D_s$, and radial velocity $v_s$ used to evolve surface densities of solids are then given by mass-averaged diffusivities and velocities of the small and large population (Birnstiel et al. 2012):

$$\begin{cases} v_s = f_m v_{d,a_1} + (1 - f_m) v_{d,a_0}. \\ D_s = f_m D_{d,a_1} + (1 - f_m) D_{d,a_0}. \end{cases} \tag{23}$$

### 2.4. Sources and sinks of trace species

We follow the approach of Aguichine et al. (2020) to depict the sources and sinks for both the solid and vapor phases of the different species. A pure condensate of species $i$ undergoes sublimation if its partial pressure is lower than the corresponding equilibrium pressure. Sublimation results in a sink term for pure condensates during the time step, $\Delta t$ (Drążkowska & Alibert 2017):

$$\dot{Q}_{p,i} = -\min\left(\sqrt{\frac{8\pi\mu_i}{RT}}\frac{3}{\pi \bar{a}\bar{\rho}} P_{eq,i}\Sigma_{p,i};\ \frac{\Sigma_{p,i}}{\Delta t}\right), \tag{24}$$

where $\mu_i$ is the molar mass of species $i$, $\bar{\rho}$ is the mean bulk density of grains, $P_{eq,i}$ is the equilibrium pressure, and $\bar{a}$ is the mean size of grains. The second part of the minimum function ensures that no more than the available quantity of pure condensate sublimates. Equilibrium curves of pure condensates are given in Appendix A.

Conversely, a gas of species $i$ forms a pure condensate if its partial pressure is larger than the corresponding equilibrium pressure. The condensation rates results in a source term for pure condensates (Drążkowska & Alibert 2017):

$$\dot{Q}_{p,i} = \min\left(\left(P_i - P_{eq,i}\right)\frac{2H\mu_i}{RT\Delta t};\ \frac{\Sigma_{v,i}}{\Delta t}\right). \tag{25}$$

We also added the possibility of $NH_3$ monohydrate and clathrate crystallization in the PSN. Assuming that enough crystalline water is available, these solids form first during the cooling of the disk because their crystallization temperatures are higher than those of the corresponding pure condensates (see Fig. 3). The only exceptions to that rule are $CO_2$ and $NH_3$, namely the only species that condense at a higher temperature than their hydrates at nebular conditions (see Fig. 3). To compute the source and sink terms of trace species in clathrates, we used the same prescription as that used for pure condensates (Eqs. (24) and (25)). The equilibrium pressures of pure condensates are replaced by those of clathrates and $NH_3$ monohydrate (see Appendix B). The formation of clathrates and $NH_3$ monohydrate also requires the presence of a minimum amount of crystalline water, resulting in a limit for their source term $\dot{Q}_{c,i}$:

$$\dot{Q}_{c,i}\,\Delta t \leq \frac{\mu_i}{S_i\,\mu_{H_2O}}\left[\Sigma_{p,H_2O} - \sum_k \Sigma_{c,k}\frac{S_k\,\mu_{H_2O}}{\mu_k}\right]. \tag{26}$$

This expression takes the amount of available crystalline water $\Sigma_{p,H_2O}$ and subtracts the amount of water that is already used to trap currently existing clathrates. In this expression, $S_k$ is the stoichiometric ratio between the species $k$ and water. This ratio is set to 5.75, 5.66, and 1 in the cases of type I clathrate, type II clathrate, and $NH_3$ monohydrate, respectively. This condition sets an upper limit on the clathrate source term, that can be equal to 0 if all the crystalline water is already holding clathrates. If all conditions are met for a trace species to be able to form pure condensates, clathrates, and monohydrates, we prioritize the solid phase that has the greatest $P_i - P_{eq,i}$ value. Prioritizing the largest $P_i - P_{eq,i}$ value is equivalent to prioritizing the highest solidification rate. Such considerations are not taken into account when performing a prioritization test among clathrate formation and condensation of pure condensates, since clathrates only form when pure condensates are not stable.

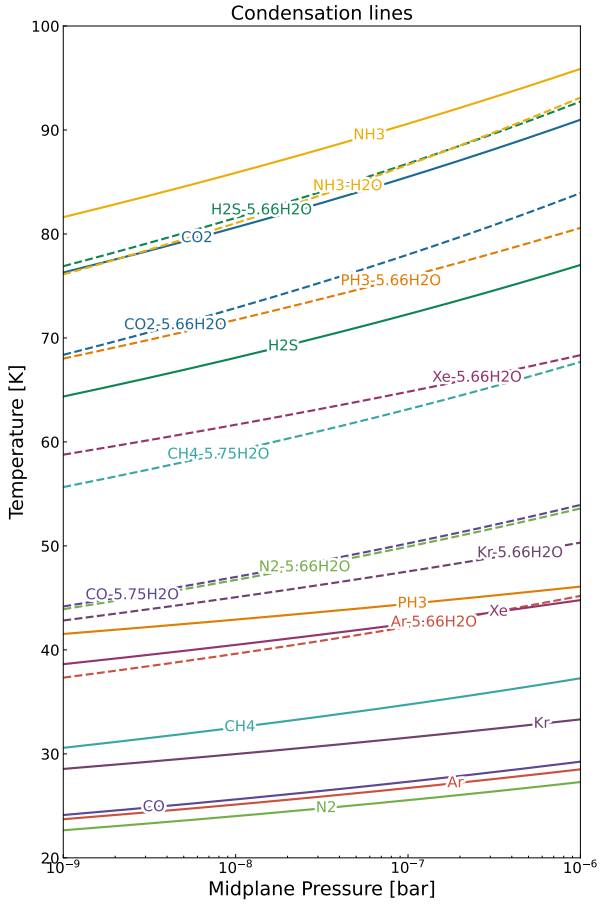


**Fig. 3.** Equilibrium curves of pure condensates (solid lines), clathrates, and $NH_3$ monohydrate (dashed lines) in a pressure-temperature domain relevant to PSN conditions (see the appendix for the relevant data). Two clathrate structures are considered in our model, namely, type I and type II with stoichiometric factors of 5.75 and 5.66, respectively. Partial pressures are calculated by considering the species abundances given in Table 1.

When grains containing amorphous ice cross the ACTZ, water crystallizes and releases all the adsorbed volatiles irreversibly. The corresponding sink term is then:

$$\dot{Q}_{\rm a} = -\frac{\Sigma_{\rm a}}{\Delta t}, \tag{27}$$

with the only condition that must be satisfied is: $T > T_{\rm ACTZ}$.

From the various rates of condensation, crystallization and sublimation, we can finally derive the overall sink and source term for the vapor:

$$\dot{Q}_{{\rm v},i} = -\dot{Q}_{{\rm p},i} - \dot{Q}_{{\rm c},i} - \dot{Q}_{{\rm a},i}. \tag{28}$$

## 3. Results

Simulations have been performed in the case of two distinct scenarios. In scenario 1, particles initially released in the PSN are only made from pure condensates. During their inward drift, they can sublimate, condense again and/or form various clathrates and a $NH_3$ monohydrate, depending on the local temperature and pressure conditions of the disk. In scenario 2, particles initially released in the PSN are only made from amorphous ice. During their inward drift, water contained in these particles transitions to a crystalline structure when crossing the ACTZ and leads to the release of adsorbed volatiles in the gas phase. The released vapors can in turn condense into pure ices and/or form various clathrates and $NH_3$ monohydrate, following the prescription described in the previous section. Both scenarios are explored with the assumption of 0.1 $M_\odot$ for the mass of the PSN and a viscosity parameter of $\alpha = 10^{-3}$.

**Table 1.** Initial molar abundances of the considered trace species.

| Trace species | $(X/H_2)_\odot$ | Trace species | $(X/H_2)_\odot$ |
|---|---|---|---|
| $H_2O$ | $5.479 \times 10^{-4}$ | $NH_3$ | $5.456 \times 10^{-5}$ |
| CO | $3.698 \times 10^{-4}$ | $PH_3$ | $6.368 \times 10^{-7}$ |
| $CO_2$ | $1.479 \times 10^{-4}$ | Ar | $7.150 \times 10^{-6}$ |
| $CH_4$ | $3.698 \times 10^{-5}$ | Kr | $4.310 \times 10^{-9}$ |
| $H_2S$ | $1.633 \times 10^{-5}$ | Xe | $4.210 \times 10^{-10}$ |
| $N_2$ | $5.456 \times 10^{-5}$ | | |

The initial surface density of a species, $i$, is:

$$\Sigma_{0,i} = x_{0,i}\Sigma_{\rm g}, \tag{29}$$

where $x_{0,i}$ is the initial mass fraction of the species, $i$. At $t = 0$, the partial pressures of the different species are computed at each point of the grid. In scenario 1, if the partial pressure of a given species is below its equilibrium pressure, then the corresponding location is filled with vapor. Otherwise, this location filled with pure ice. In scenario 2, species are in the vapor phase where $T \geq T_{\rm ACTZ}$ and in an amorphous ice phrase otherwise. In both scenarios, thermodynamic equilibrium is established after a few time steps (~1 yr).

The initial PSN composition is derived from the protosolar elemental abundances tabulated by Lodders et al. (2009). We assume that all C is distributed between CO, $CO_2$, or $CH_4$, with the remaining O forming $H_2O$. We have set $CO:CO_2:CH_4$ = 10:4:1 in the PSN gas phase. The $CO:CO_2$ ratio is derived from ROSINA measurements of comet 67P/C-G between 2014 August and 2016 September (Mousis et al. 2014). The $CO:CH_4$ ratio is consistent with the production rates measured in the southern hemisphere of the 67P/C-G in October 2014 by the ROSINA instrument (Le Roy et al. 2015). Sulfur is assumed to be half in $H_2S$ form and half in refractory sulfide components (Pasek et al. 2005). We also assumed $N_2:NH_3$ = 1:1, a value predicted by thermochemical models that take into account catalytic effects of Fe grains on the kinetics of $N_2$ to $NH_3$ conversion of the PSN (Fegley 2000; Mousis et al. 2009a). The molar abundances of the different species are derived from the gas phase abundances given in Table 1.

Figure 4 represents the radial evolution of the water mass abundance in the PSN at different epochs of its evolution in scenario 1 and scenario 2 (top row and bottom row, respectively). Both cases produce very similar water abundances and show a water enrichment peak that is about 10 times its initial abundance at the location of the snowline (~2.8 au). However, the availability of crystalline ice is much more limited in scenario 2 due to $H_2O$ being mostly in an amorphous state. Indeed, in this case, crystalline ice is present only in the ~2.8–4 au region.

### 3.1. Scenario 1: initial delivery of pure condensates

Figure 5 represents the time and radial evolution of the abundance ratios (with respect to initial abundances) of the different

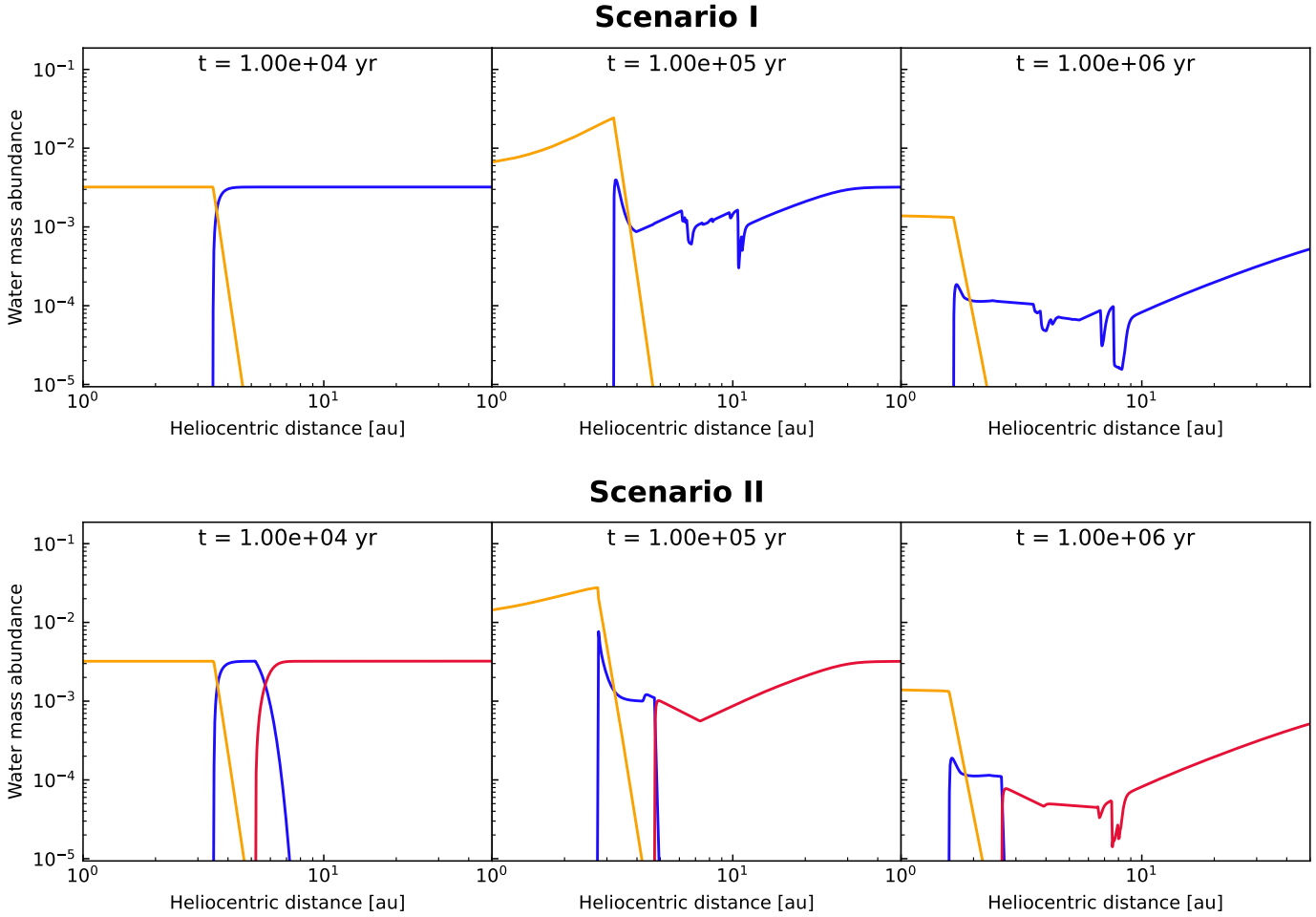


**Fig. 4.** Time evolution of the mass abundance of water, defined as the radial profile of $\Sigma_{H_2O}/\Sigma_g$, for both scenarios at $t = 10^4$, $10^5$, and $10^6$ yr. Solid lines represent $H_2O$ in the gaseous phase (orange line), crystalline phase (blue line), and in amorphous phase (red line).

species existing in various phases in the case of scenario 1, respectively. After 10 kyr of PSN evolution, the species considered are present under all their possible forms – except for $CO_2$ and $NH_3$, which are never enclathrated. By successive order with progressing heliocentric distance (and decreasing temperature and pressure conditions), we first find the different vapors, then narrow regions corresponding to the presence of clathrates, and, finally, an outer region that is only populated with pure condensates. Regions where clathrates exist expand from 7 to 12 au, depending on the species considered. At this early stage of the PSN evolution, there is no significant enrichment that can be observed for any species.

After 0.1 Myr of disk evolution, Fig. 5 also shows that beyond 6 au, clathrates coexist with pure condensates and their abundances decrease steeply – except for $CO_2$ and $NH_3$, which that exist only as pure ices. A few au beyond that, pure condensates become the only solid structures existing in the outer PSN. Depending on the PSN ther modynamic conditions and the availability of crystalline water, when the different species become fully enclathrated, their abundances form unique enrichment peaks located at their clathration lines, reaching up to ∼15 times their initial values. On the other hand, if the budget of crystalline water is not high enough, then the species are only partly enclathrated. They then form two narrow enrichment peaks at their condensation and clathration lines, reaching ∼5 and ∼15 times their initial abundances, respectively. Table 2 displays the heliocentric distance and the value of the enrichment peak (relative to the initial abundance) for each species under consideration at $t = 0.1$ Myr of the PSN evolution. Depending on the species considered, the enrichment peaks range between 2 and 18 times the protosolar values and are located in the 2–11 au region. The closest and furthest peaks from the Sun are those of the water snow line at 2.8 au and $N_2$ iceline at 10.8 au, respectively. Two enrichment peaks, located at the clathration and icelines, are found in the cases of $CH_4$ and Kr.

In Fig. 5, all species, except CO, $N_2$, and Ar, exhibit a dip in the surface densities of the pebbles of pure condensates around 10.5 au. In this region, the total surface density of icy pebbles is increased due to the combined actions of CO, $N_2$, and Ar icelines located at 10.4, 10.9, and 10.7 au, respectively. The condensations rates of CO, $N_2$, and Ar locally increase the surface density of solids, which are in excess compared with their loss rates via inward drift. On the other hand, because the icelines of the other species are located closer to the Sun, their surface densities progressively decrease in this region, as a result of the inward drift of particles.

After 1 Myr of PSN evolution, all peaks are smoothed out in the gas phase. Because of the inward drift of pebbles, most of the species are in vapor form when the solids start to deplete. The total mass of solids has decreased by a factor of four compared to the beginning of the simulation. This effect is more significant in the case of clathrates forming at very low temperatures (less than 50 K), since the fraction of crystalline water used to form higher temperature clathrates increases with time.

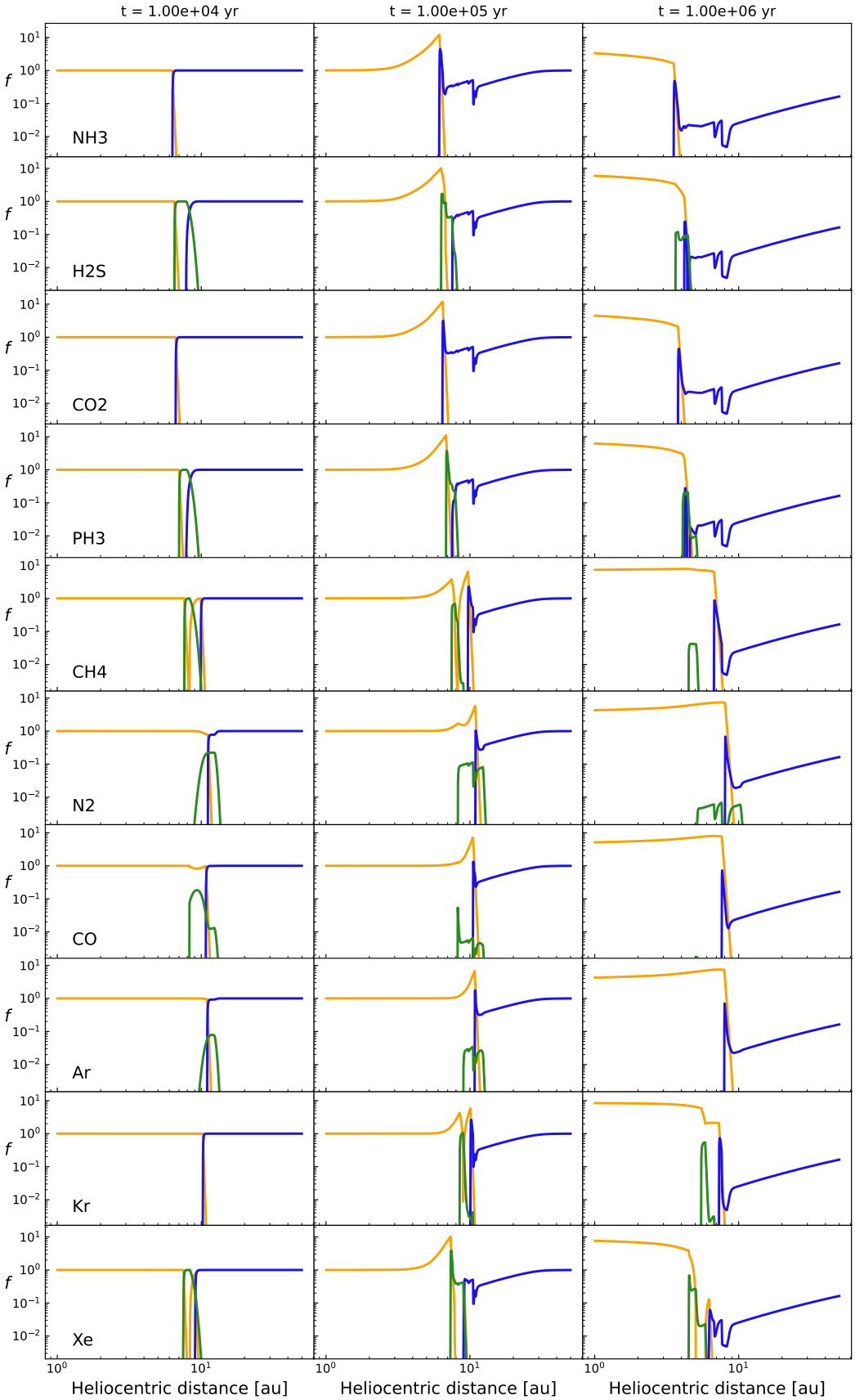


**Fig. 5.** Time and radial evolution of species' mass abundances normalized to their initial values in gaseous phase (orange line), pure condensate form (blue line), and clathrate (green line), at t = $10^4$, $10^5$, and $10^6$ yr in scenario 1.

**Table 2.** Heliocentric distance and value of the enrichment peak (relative to the initial abundance) for each species under consideration at $t$ = 0.1 Myr in the case of scenario 1 (middle column of Fig. 5).

| Element | Peak location (au) | Peak value |
|---|---|---|
| $H_2O$ | 2.7 | 11.0 |
| CO | 10.4 | 8.1 |
| $CO_2$ | 6.0 | 16.0 |
| $CH_4$ | 7.1 | 4.7 |
| | 9.5 | 9.4 |
| $H_2S$ | 5.9 | 14.0 |
| $N_2$ | 10.9 | 5.6 |
| $NH_3$ | 5.6 | 17.2 |
| Ar | 10.7 | 7.3 |
| Kr | 8.2 | 9.12 |
| | 9.8 | 23.5 |
| Xe | 7.0 | 14.3 |
| $PH_3$ | 6.4 | 15.4 |

**Notes.** Both vapor and solid forms are considered.

**Table 3.** Heliocentric distance and value of the enrichment peak (relative to the initial abundance) for each species under consideration at $t$ = 0.1 Myr in the case of scenario 2 (middle column of Fig. 6).

| Element | Peak location (au) | Peak value |
|---|---|---|
| $H_2O$ | 2.7 | 8.5 |
| CO | 4.8 | 7.0 |
| $CO_2$ | 4.7 | 7.5 |
| $CH_4$ | 4.7 | 7.0 |
| $H_2S$ | 4.7 | 7.1 |
| $N_2$ | 4.7 | 7.0 |
| $NH_3$ | 5.6 | 10.1 |
| Ar | 4.7 | 7.0 |
| Kr | 4.7 | 7.0 |
| Xe | 4.7 | 7.0 |
| $PH_3$ | 4.7 | 7.1 |

**Notes.** Both vapor and solid forms are considered.

### 3.2. Scenario 2: initial delivery of amorphous ices

Figure 6 represents the time and radial evolutions of the abundance ratios (with respect to the initial abundances) of the different species existing in various phases in the case of scenario 2. After 10 kyr of PSN evolution, with progressing heliocentric distance, first the different vapors are found, then an outer region that is only populated with amorphous ice. The budget of solid phase is dominated by species trapped in amorphous ice. Pure condensates only form when the vapors desorb from amorphous ice at the ACTZ (shown at ~5 au), diffuse outward and cross an iceline. Such a process is efficient only if the condensation line is close to the ACTZ, leading to very narrow regions with the presence of pure condensates only in the case of $NH_3$.

After 0.1 Myr of disk evolution, it is notable that only pure condensates of $NH_3$, $H_2S$, $CO_2$, and $PH_3$ form. Table 3 displays the heliocentric distance and the value of the enrichment peak (relative to the initial abundance) for each species under consideration at this epoch of the PSN evolution. All peaks are located in a much narrower region, centered at the location of the ACTZ, compared with the scenario 1, with values ranging from 7 to 10 times the initial abundances. The peak locations are influenced by the presence of narrow (less than 1 au) regions filled with pure condensates. In those regions, corresponding to the icelines, the abundance of pure condensates exceed that of amorphous ice, thus influencing the location of the enrichment peaks.

After 1 Myr of PSN evolution, as a result of pebble drift, all peaks have been smoothed and the volatiles trapped in amorphous water ice phase are strongly depleted by factors reaching more than 100, compared with their gaseous abundances in the inner disk. The amount of pure condensates exceeds that of amorphous ice in some narrow regions, except in the cases of $H_2S$ and $PH_3$. For reasons identical to those invoked at the same epoch of PSN evolution in scenario 1, the surface density of solids is strongly decreased in the region centered at ~7 au.

## 4. Discussion

In this section, we discuss the implications of our model for various bodies of the solar system. We first investigate the sensitivity of our model to the variation of its input parameters and then provide fits of the volatile composition of comet R2 and those of Uranus and Neptune.

### 4.1. Sensitivity to parameters

The stability of our results has been tested against the variations of the pebble density, disk's mass, and the viscosity parameter in the 0.1–1 g cm$^{-2}$, $10^{-2}$–$10^{-1}$ $M_\odot$, and $10^{-4}$–$10^{-2}$ ranges, respectively. Variation in pebble density leads to results similar to those presented in Sects. 3.1 and 3.2. Lower density pebbles drift over shorter timescales at given size, but are also smaller because of a lower fragmentation limit (see Sect. 2.2). On the other hand, smaller pebbles drift over longer timescales, implying that both effects are (roughly) mutually counterbalanced and produce only minor variations in the abundance profiles. Both the mass and $\alpha$ viscosity parameter of the disk affect its viscous evolution and, thus, the locations of the various icelines. Less massive disks are cooler because of their reduced viscous dissipation (see Eq. (5)) and display their icelines closer to the host star. For example, we find that the condensation and clathration lines of the species investigated in our study are ~2 au closer to the Sun in a $10^{-2}$ $M_\odot$ disk, compared with a $10^{-1}$ $M_\odot$ disk. As another example, the enrichment peak associated with the CO iceline ranges between 7 and 11 au from the Sun when the $\alpha$–value is varied between $10^{-4}$ and $10^{-2}$. The magnitude of the abundance peaks is also affected by the variation of $\alpha$. The abundance of the CO peak ranges between about 10 and 5 times, respectively, its initial PSN abundance when the $\alpha$ value is varied between $10^{-4}$ and $10^{-2}$. In our disk model, the contribution from the irradiation by the Sun to the disk's midplane temperature is not considered because it is assumed that the outer PSN is shadowed by its inner region (Ohno & Ueda 2021). This allows the disk to reach temperatures low enough to enable the condensation of ultravolatiles (CO, $N_2$, Ar, etc.) at the current locations of the giant planets, assuming the absence of migration during formation. When this contribution is included by considering the formalism depicted in Adams et al. (1988) and Ruden & Pollack (1991), the temperature profile becomes slightly warmer, implying that the icelines and clathration lines are moved outward by 1–2 au. Despite these changes, the general trend of our results is not impacted.

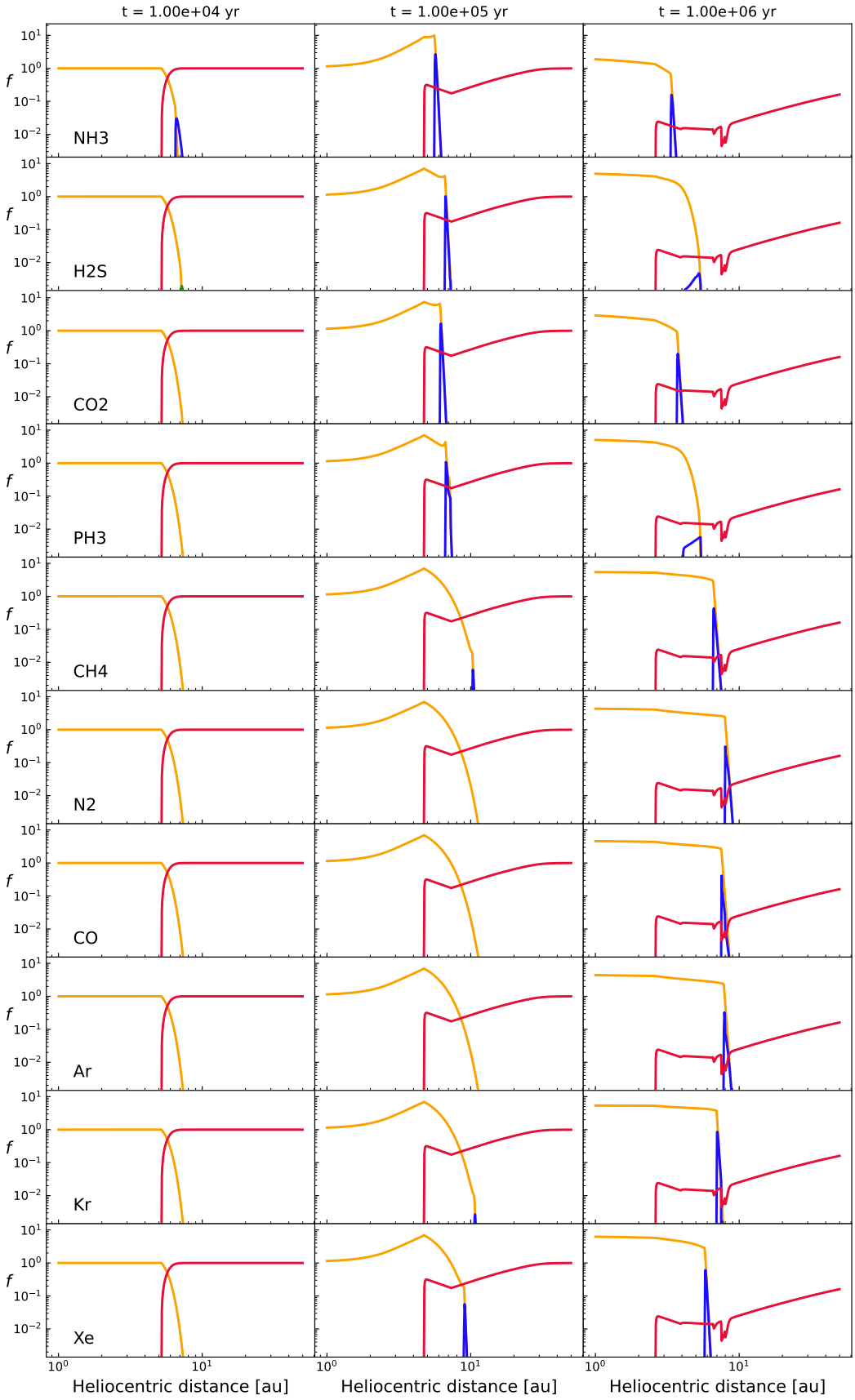


**Fig. 6.** Time and radial evolution of species' mass abundances normalized to their initial values in gaseous phase (orange line), pure condensate form (blue line), and amorphous form (red line), compared with their initial mass abundances, at $t = 10^4$, $10^5$, and $10^6$ yr in scenario 2.

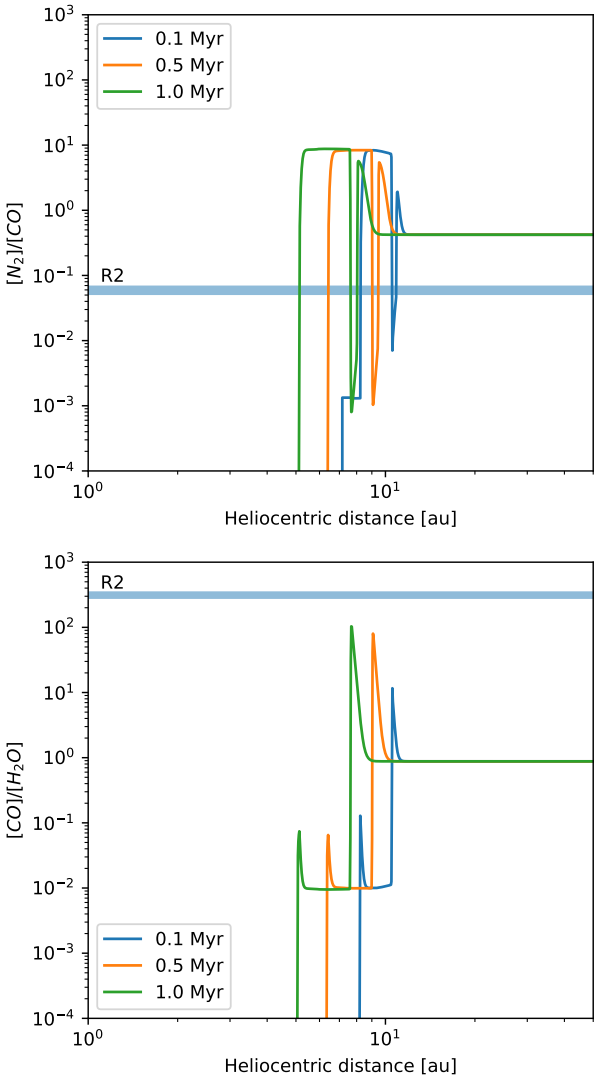


**Fig. 7.** $N_2$/CO (*top panel*) and CO/$H_2O$ (*bottom panel*) abundance ratios in pebbles represented as a function of heliocentric distance in the case of scenario 1, and compared with those measured in R2's coma (blue bar) at 0.1, 0.5, and 1 Myr of the PSN evolution. Both ratios measured in R2 are simultaneously matched by our model at a distance of 7 au and 1 Myr.

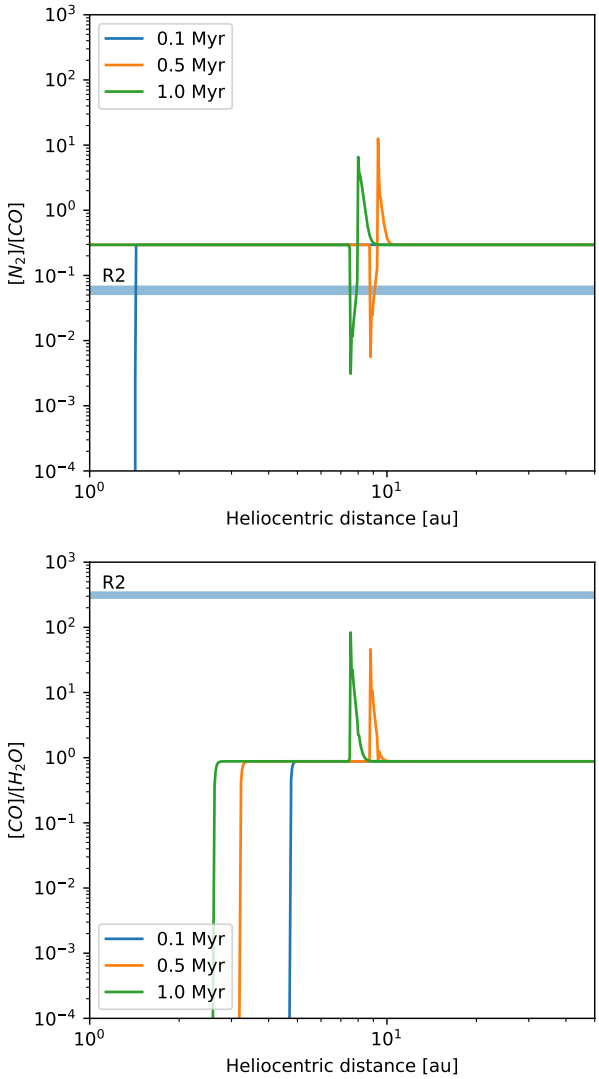


**Fig. 8.** $N_2$/CO (*top panel*) and CO/$H_2O$ (*bottom panel*) abundance ratios in pebbles represented as a function of heliocentric distance in the case of scenario 2, and compared with those measured in R2's coma (blue bar) at 0.1, 0.5 and 1 Myr of the PSN evolution. Only the $N_2$/CO ratio is reproduced in R2 at 8 au and 1 Myr. The CO/$H_2O$ ratio is however approached by our model at the same location and epoch of the PSN evolution.

### *4.2. Implications for comet R2*

R2 is a long-period comet displaying an unusually high $N_2$/CO ratio of 0.006–0.008 (Biver et al. 2018; Opitom et al. 2019). Another peculiar characteristic of this comet is its heavy depletion in terms of $H_2O$, with a CO/$H_2O$ ratio of about 312 (McKay et al. 2019).

Figures 7 and 8 represent the radial profiles of the CO/$H_2O$ and $N_2$/CO ratios calculated in the PSN pebbles with our nominal model as a function of time in the cases of scenario 1 and scenario 2, respectively. Both ratios are compared with those measured in R2's coma (blue horizontal bar). Assuming that R2 formed from a unique set of building blocks, we require both ratios to be reproduced by our model at the same heliocentric distance and epoch. Simulations performed in the case of scenario 1 reproduce both ratios at a heliocentric distance of 7 au, after 1 Myr of PSN evolution. Our result is then consistent with those derived from the study of Mousis et al. (2021b), based on a simple approach that does not consider the interplay between the clathrate and water ice reservoirs.

Simulations performed in the case of scenario 2 reproduce the $N_2$/CO ratio at 8 au after 1 Myr of PSN evolution. However, the CO/$H_2O$ ratio is not matched by our model, even if a peak is seen at 8 au and 1 Myr. We should note that the positions and magnitudes of those peaks can change when the $\alpha$–parameter and mass of our disk model are varied. This implies that, even if scenario 1 provides a better match of R2's composition with our nominal model, scenario 2 cannot be excluded. Interestingly, our calculated peaks are within a zone of dynamic instability in the early Solar System, which is more likely to result in ejection of planetesimals than capture by the Oort Cloud. This is a possible explanation for the lack of R2-like comets observed today (Anderson et al. 2022).

### *4.3. Implications for the composition of Jupiter*

One-$\sigma$ error bar measurements made at Jupiter by the Galileo probe and the Juno spacecraft indicate C, N, O, S, P, Ar, Kr,

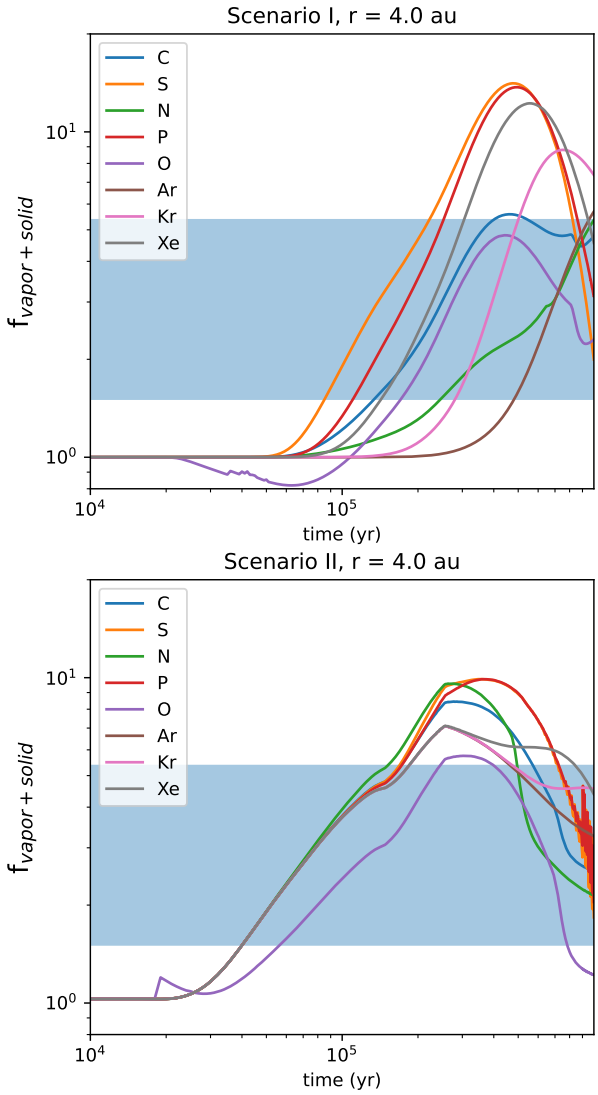


**Fig. 9.** Time evolution of the elemental abundances (relatives to the protosolar values) at a heliocentric distance of 4 au in the cases of scenario 1 (*top panel*) and scenario 2 (*bottom panel*). The blue area corresponds to the range covered by the elemental abundances derived from spacecraft measurements (see text).

and Xe abundances that are ∼1.5 to 6 times higher than the protosolar values (Atreya et al. 2003; Wong et al. 2004; Mousis et al. 2018; Li et al. 2020). To explain those features, it has been proposed that Jupiter's atmosphere could reflect the composition of icy planetesimals either made of amorphous ice (Owen et al. 1999) or from pure condensates and/or clathrates (Gautier et al. 2001; Gautier & Hersant 2005; Mousis et al. 2018, 2021b). Alternatively, it has been proposed that this supersolar metallicity could result from the accretion of already pre-enriched PSN gas (Mousis et al. 2019; Aguichine et al. 2022).

Figure 9 represents the time evolution of the sum of the elemental enrichments calculated in vapor and solid phases at the heliocetric distance of 4 au, compared with their protosolar values, and in the cases of our two scenarios. Following the approach of Aguichine et al. (2022), we focused on the composition of the PSN at 4 au, chosen as the location of Jupiter's formation. This distance is, in the model, beyond the water iceline but inward of the icelines of all other trace species. The dust-to-gas ratio can easily become greater than 2 to 3 times the protosolar composition in this region and could ease the formation of a proto-Jupiter core via the streaming instability (Yang et al. 2017).

Figure 9 shows that the measured elemental enrichments are all matched by our model after 0.8–1 Myr and 50–100 kyr of the PSN evolution in scenario 1 and scenario 2, respectively. Our models suggest that the consideration of clathrate formation in addition to the crystallization of pure condensates in the PSN (scenario 1) still allow for the formation of a Jupiter-like planet from supersolar gases originating from the disk, compared with models considering the crystallization of pure condensates only, such as that developed by Aguichine et al. (2022). Our model also suggests that the presence of multiple condensation and clathration lines does not alter the formation of supersolar vapors subsequent to their release from amorphous ice (scenario 2). Previous works exploring this possibility did not consider the formation of icelines in their models (Monga & Desch 2015; Mousis et al. 2019). In particular, Saturn's tropospheric abundances of C, N, S, and P have been measured to be between 3 and 13 times their protosolar abundances (Atreya et al. 2018), suggesting that its metallicity is higher than that of Jupiter. Assuming that Saturn formed in the vicinity of the $CO_2$ iceline to account for its high carbon enrichment, which corresponds to a heliocentric distance of ∼6 au at early epochs in our PSN model, our calculations show that this range of enrichments is reproduced within 0.2–0.3 Myr in scenario 1 and 0.2 Myr in scenario 2. This implies that Saturn could have formed earlier than Jupiter in scenario 1, whereas in scenario 2, it could have formed later. An earlier formation of Saturn could have reduced the inward flux of pebble and vapors, lowering the value of elemental enrichment peaks at Jupiter's location. However, the height of enrichment peaks is highly sensitive to the disk parameters (e.g., the $\alpha$-value; see Aguichine et al. 2022). Therefore, if the accretion of pebbles by Saturn reduces the height of the enrichment peaks at Jupiter's location, it is still possible to achieve a metallicity similar to what is measured in its atmosphere.

### *4.4. Implications for the composition of Ice Giants*

The composition of the deep atmospheres of Uranus and Neptune is shrouded in mystery since most of the heavy constituents condense at pressures deeper than may readily be probed remotely (Mousis et al. 2020). The only determinations that can be used so far in our model are the C/N and C/S ratios, which have been found equal to or higher than ∼175 and ∼35, respectively (Asplund et al. 2009; Karkoschka & Tomasko 2009, 2011; Irwin et al. 2018, 2019a,b). Figures 10 and 11 represent the radial profiles of the C/N and C/S elemental ratios in pebbles as a function of time in the PSN, compared with the minimum values measured in the tropospheres of the two ice giants. In both cases, these ratios can be reproduced in the ∼7–8 au region after 1 Myr of PSN evolution. The formation distance of solids in the PSN is model-dependent, but our simulations suggest that the giant planets did form in a more compact configuration than the current one – which is also in agreement with several dynamical models (Tsiganis et al. 2005; Lykawka et al. 2010; Guilera et al. 2011). Given their high metallicities, the formation of Uranus and Neptune requires a higher surface density of solids than the values derived here for the outer PSN. This assumption is at odds with the fact that the planetesimal density and collision probability are both low in the outer disk. One way to overcome this difficulty would be to assume the formation of the two giants via the accretion of pebbles directly onto the planetary

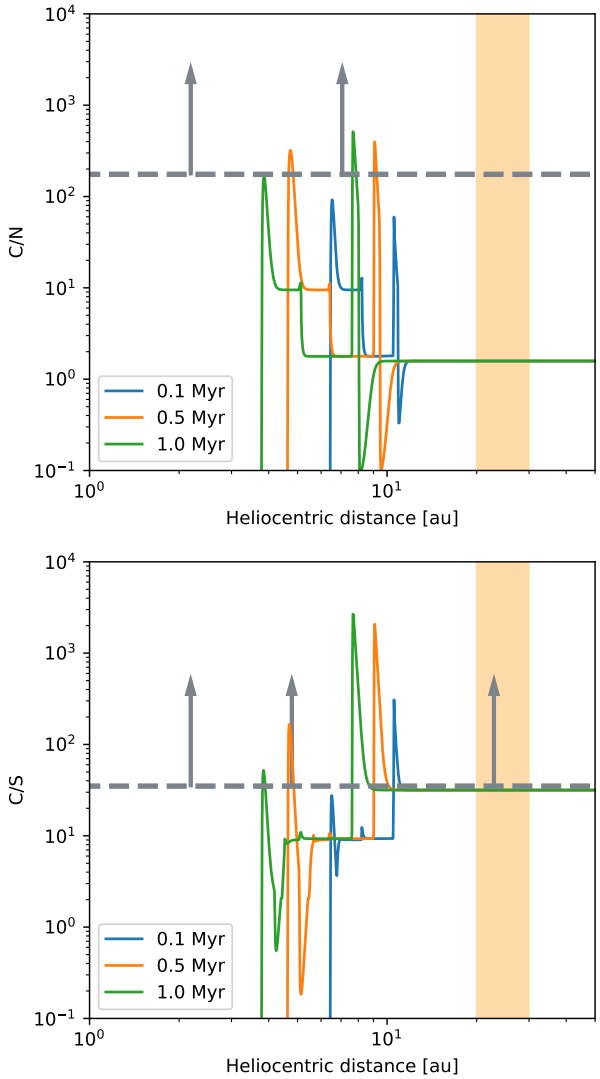


**Fig. 10.** Radial profiles of the C/N (*top panel*) and C/S (*bottom panel*) ratios calculated in pebbles at different epochs of the PSN evolution in the case of scenario 1. The horizontal dashed line represents the minimum ratio measured in the tropospheres of Uranus and Neptune. The orange area encompasses the current locations of the ice giants in the solar system.

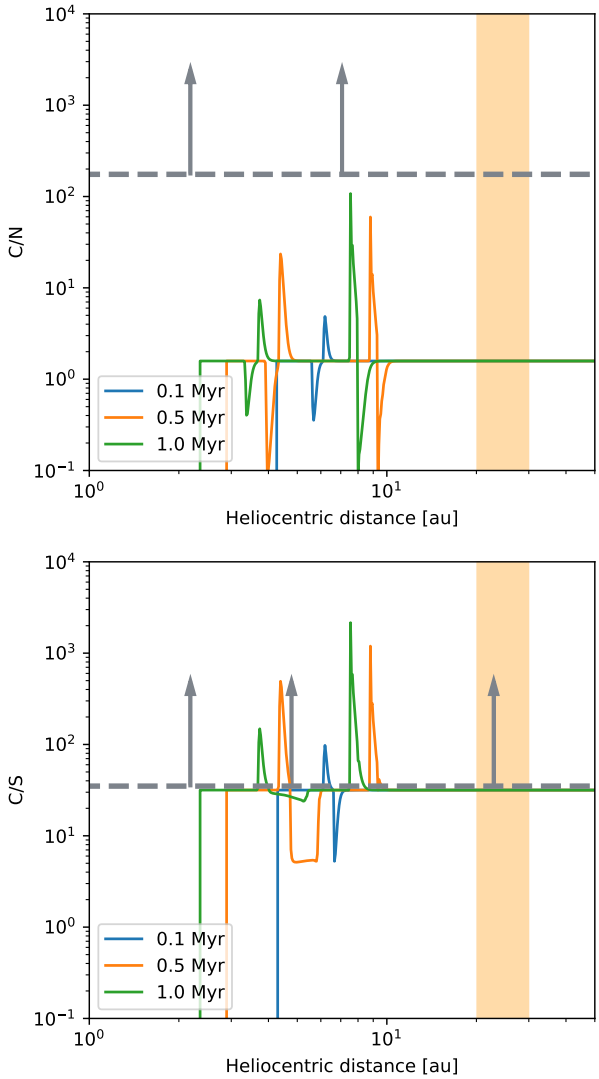


**Fig. 11.** Radial profiles of the C/N (*top panel*) and C/S (*bottom panel*) ratios calculated in pebbles at different epochs of the PSN evolution in the case of scenario 2. The horizontal dashed line represents the minimum ratio measured in the tropospheres of Uranus and Neptune. The orange area encompasses the current locations of the ice giants in the Solar System.

embryo, which can still work efficiently far from the host star (Helled et al. 2014; Bitsch et al. 2015, 2018; Armitage 2019).

### 4.5. Limitations of the model

Over the recent years, substructures have been largely observed in protoplanetary disks. The ALMA/DSHARP survey showed that protoplanetary disks are not smooth and that substructures are ubiquitous (Andrews et al. 2020; Jennings et al. 2022). Substructures can be produces by planet-disk interactions, in the form of spiral density waves (Muto et al. 2012; Zhang et al. 2021) and gaps (Bae et al. 2017). Radiative hydrodynamic models show that these substructures can be also formed by instabilities in the disk (Lovelace et al. 1999; Lovelace & Romanova 2014; Blanco et al. 2021). Such features translate into local density and pressure variations that act as dust traps which locally enhance the dust surface density. Although our model does not take into account such disk substructures, we show that the icelines, clathration lines, and the ACTZ correspond to vapor and pebble enrichment peaks, which can lead to instabilities.

In this work, giant planets are assumed to be formed in situ. In scenario 1, Jupiter is formed within 0.8–1 Myr. This timescale is compatible with a formation via pebble accretion (Bitsch et al. 2015, 2018; Alibert et al. 2018; Armitage 2019; Venturini & Helled 2020) and gravitational instability (Boss 1997; Zhu et al. 2012; Kratter & Lodato 2016). On the other hand, in scenario 2, Jupiter forms in less than 0.1 Myr. This timescale is consistent with a gravitational instability which can be triggered as early as 0.1 Myr (Zhu et al. 2012). An early formation of Jupiter allows us to account for the observed carbonaceous chondrites dichotomy (Kleine et al. 2020). Although, the disk instability model is consistent with formation timescales found in both scenario 1 and scenario 2, it is important to note that observations and models suggest that, at minimum, amorphous ice should be heated up to its crystallization temperature when falling from the presolar cloud onto the PSN (Visser et al. 2013). Those findings

suggest that scenario 1 is the most likely scenario, implying that our results remain consistent with the core accretion model.

One limitation of our model is the fact that planet migration is not considered. During or after formation, planets migrate inward or outward (Masset & Papaloizou 2003; Bitsch et al. 2015; Schneider & Bitsch 2021). During migration, planets accrete material from different parts of the disk with various compositions. Although planetary migration contradicts an in situ formation hypothesis, 3D hydrodynamical simulations indicate that the rates of type I and type II migrations could be several times slower than the prescription usually employed in the literature of planet formation (Chrenko & Nesvorný 2020; Lega et al. 2021; Chametla & Chrenko 2022). Assuming an in situ formation of Jupiter in our model to reproduce its observed metallicity is expected to remain valid in light of these revised migration rates because our derived timescales are still quite short, compared to the PSN evolution.

## 5. Conclusion

In this work, we investigate the impact of clathrate formation on the radial distribution of volatiles in the PSN, considering two scenarios, each of them corresponding to a distinct initial condition. To do so, we used a 1D protoplanetary disk model coupled with modules describing the evolution of trace species in the vapor phase, as well as the dynamics of dust and pebbles. This model also considers the different sources and sinks for the volatile phases considered (vapors, pure condensates, or clathrates).

In scenario 1, we assume that the volatiles were delivered to the PSN in the form of pure condensate grains. In this case, we show that clathrates can crystallize and form enrichment peaks at about 10 times the value of the initial abundances at their clathration lines, which are closer to the Sun than their corresponding icelines. The amount of clathrates formed in the PSN depends on the local abundance of crystalline water, which in many cases, acts as a limiting factor in our model. In scenario 2, we assumed that the volatiles were delivered to the PSN in the form of amorphous grains. Under those conditions, volatiles are only released from amorphous ice when the icy grains are heated up to ∼135 K, namely, at the ACTZ location. An enrichment peak up to about seven times the initial abundances then forms at the ACTZ location. In this case, clathrate formation is not possible because there is no crystalline water ice available beyond the ACTZ in the PSN. All the enrichment peaks of pure condensates are also located close to the ACTZ. Our investigation shows that both scenario 1 and scenario 2 can reproduce the known compositions of comet R2, Jupiter, Uranus, and Neptune. This implies that our model does not allow us to formally rule out the presence of amorphous ice during the early phases of the PSN, assuming that those planetary bodies accreted from pebbles or pebble-made planetesimals. More planetary composition data, such as the in situ measurements of Saturn's atmosphere, are needed to understand the initial formation conditions of the PSN.

*Acknowledgements.* The project leading to this publication has received funding from the Excellence Initiative of Aix-Marseille Université – A*Midex, a French "Investissements d'Avenir programme" AMX-21-IET-018. This research holds as part of the project FACOM (ANR-22-CE49-0005-01_ACT) and has benefited from a funding provided by l'Agence Nationale de la Recherche (ANR) under the Generic Call for Proposals 2022. O.M. acknowledges support from CNES. J.I.L. was supported by the Juno project. We acknowledge Sarah E. Anderson for helpful discussions about her dynamical simulations regarding the origin of comet R2. We thank the anonymous referee for their useful comments that improved the quality of this paper.

## References

Adams, F. C., Lada, C. J., & Shu, F. H. 1988, ApJ, 326, 865
Aguichine, A., Mousis, O., Devouard, B., et al. 2020, ApJ, 901, 97
Aguichine, A., Mousis, O., & Lunine, J. I. 2022, Planet. Sci. J. , 3, 141
Alibert, Y., Venturini, J., Helled, R., et al. 2018, Nat. Astron., 2, 873
Anderson, S. E., Petit, J.-M., Noyelles, B., et al. 2022, LPI Contrib., 2678, 2395
Andrews, S. M., Huang, J., Perez, L. M., et al. 2020, VizieR Online Data Catalog: J/ApJ/869/L41
Armitage, P. J. 2019, Saas-Fee Adv. Course, 45, 1
Asplund, M., Grevesse, N., Sauval, A. J., et al. 2009, ARA&A, 47, 481
Atreya, S. K., Mahaffy, P. R., Niemann, H. B., et al. 2003, Planet. Space Sci., 51, 105
Atreya, S. K., Crida, A., Guillot, T., et al. 2018, Saturn in the 21st Century (Cambridge: Cambridge University Press), 5
Bae, J., Zhu, Z., & Hartmann, L. 2017, ApJ, 850, 201
Baines, K. H., Mickelson, M. E., Larson, L. E., et al. 1995, Icarus, 114, 328
Bar-Nun, A., Notesco, G., & Owen, T. 2007, Icarus, 190, 655
Bell, K. R., & Lin, D. N. C. 1994, ApJ, 427, 987
Birnstiel, T., Klahr, H., & Ercolano, B. 2012, A&A, 539, A148
Bitsch, B., Lambrechts, M., & Johansen, A. 2015, A&A, 582, A112
Bitsch, B., Lambrechts, M., & Johansen, A. 2018, A&A, 609, C2
Biver, N., Bockelée-Morvan, D., Paubert, G., et al. 2018, A&A, 619, A127
Blanco, D., Ricci, L., Flock, M., et al. 2021, ApJ, 920, 70
Boss, A. P. 1997, Science, 276, 1836
Booth, R. A., Clarke, C. J., Madhusudhan, N., et al. 2017, MNRAS, 469, 3994
Burkhardt, A. M., Shingledecker, C. N., Le Gal, R., et al. 2019, ApJ, 881, 32
Chametla, R. O., & Chrenko, O. 2022, MNRAS, 512, 2189
Chrenko, O., & Nesvorný, D. 2020, A&A, 642, A219
Ciesla, F. J., Mulders, G. D., Pascucci, I., et al. 2015, ApJ, 804, 9
Desch, S. J., Estrada, P. R., Kalyaan, A., et al. 2017, ApJ, 840, 86
Dodson-Robinson, S. E., Willacy, K., Bodenheimer, P., et al. 2009, Icarus, 200, 672
Drążkowska, J., & Alibert, Y. 2017, A&A, 608, A92
Fegley, B. J. 2000, Space Sci. Rev., 92, 177
Fray, N., & Schmitt, B. 2009, Planet. Space Sci., 57, 2053
Gautier, D., & Hersant, F. 2005, Space Sci. Rev., 116, 25
Gautier, D., Hersant, F., Mousis, O., et al. 2001, ApJ, 550, L227
Gibb, E. L., Whittet, D. C. B., Boogert, A. C. A., et al. 2004, ApJS, 151, 35
Guilera, O. M., Fortier, A., Brunini, A., et al. 2011, A&A, 532, A142
Hartmann, L., Calvet, N., Gullbring, E., et al. 1998, ApJ, 495, 385
Helled, R., Bodenheimer, P., Podolak, M., et al. 2014, Protostars and Planets VI (Tucson: University of Arizona Press), 643
Hersant, F., Gautier, D., & Lunine, J. I. 2004, Planet. Space Sci., 52, 623
Hueso, R., & Guillot, T. 2005, A&A, 442, 703
Irwin, P. G. J., Toledo, D., Garland, R., et al. 2018, Nat. Astron., 2, 420
Irwin, P. G. J., Toledo, D., Garland, R., et al. 2019a, Icarus, 321, 550
Irwin, P. G. J., Toledo, D., Braude, A. S., et al. 2019b, Icarus, 331, 69
Jennings, J., Booth, R. A., Tazzari, M., et al. 2022, MNRAS, 509, 2780
Jenniskens, P., Blake, D. F., Wilson, M. A., et al. 1995, ApJ, 455, 389
Johansen, A., Blum, J., Tanaka, H., et al. 2014, Protostars and Planets VI (Tucson: University of Arizona Press), 547
Karkoschka, E., & Tomasko, M. 2009, Icarus, 202, 287
Karkoschka, E., & Tomasko, M. G. 2011, Icarus, 211, 780
Kratter, K., & Lodato, G. 2016, ARA&A, 54, 271
Kleine, T., Budde, G., Burkhardt, C., et al. 2020, Space Sci. Rev., 216, 55
Lambrechts, M., & Johansen, A. 2014, A&A, 572, A107
Lega, E., Nelson, R. P., Morbidelli, A., et al. 2021, A&A, 646, A166
Le Roy, L., Altwegg, K., Balsiger, H., et al. 2015, A&A, 583, A1
Li, C., Ingersoll, A., Bolton, S., et al. 2020, Nat. Astron., 4, 609
Lindal, G. F., Lyons, J. R., Sweetnam, D. N., et al. 1987, J. Geophys. Res., 92, 14987
Lindal, G. F., Lyons, J. R., Sweetnam, D. N., et al. 1990, Geophys. Res. Lett., 17, 1733
Lodders, K., Palme, H., & Gail, H.-P. 2009, Landolt Börnstein, 4B, 712
Longhi, J. 2005, Geochim. Cosmochim. Acta, 69, 529
Lovelace, R. V. E., Li, H., Colgate, S. A., et al. 1999, ApJ, 513, 805
Lovelace, R. V. E., & Romanova, M. M. 2014, Fluid Dyn. Res., 46, 041401
Lunine, J. I., & Stevenson, D. J. 1985, ApJS, 58, 493
Lykawka, P. S., Horner, J., Jones, B. W., et al. 2010, MNRAS, 404, 1272
Lynden-Bell, D., & Pringle, J. E. 1974, MNRAS, 168, 603
Mandt, K. E., Mousis, O., Lunine, J., et al. 2020, Space Sci. Rev., 216, 99
Masset, F. S., & Papaloizou, J. C. B. 2003, ApJ, 588, 494

Mayer, E., & Pletzer, R. 1986, Nature, 319, 298
McKay, A. J., DiSanti, M. A., Kelley, M. S. P., et al. 2019, AJ, 158, 128
Miura, H., Yamamoto, T., Nomura, H., et al. 2017, ApJ, 839, 47
Monga, N., & Desch, S. 2015, ApJ, 798, 9
Mousis, O., Lunine, J. I., Thomas, C., et al. 2009a, ApJ, 691, 1780
Mousis, O., Marboeuf, U., Lunine, J. I., et al. 2009b, ApJ, 696, 1348
Mousis, O., Lunine, J. I., Madhusudhan, N., et al. 2012, ApJ, 751, L7
Mousis, O., Lunine, J. I., Fletcher, L. N., et al. 2014, ApJ, 796, L28
Mousis, O., Atkinson, D. H., Cavalié, T., et al. 2018, Planet. Space Sci., 155, 12
Mousis, O., Ronnet, T., & Lunine, J. I. 2019, ApJ, 875, 9
Mousis, O., Aguichine, A., Helled, R., et al. 2020, Philos. Trans. R. Soc. A, 378, 20200107
Mousis, O., Aguichine, A., Bouquet, A., et al. 2021a, Planet. Sci. J. Planet. Sci. J. , 2, 72
Mousis, O., Lunine, J.I., & Aguichine, A. 2021b, ApJ, 918, L23
Muto, T., Grady, C. A., Hashimoto, J., et al. 2012, ApJ, 748, L22
Nakamoto, T., & Nakagawa, Y. 1994, ApJ, 421, 640
Öberg, K. I., & Wordsworth, R. 2019, AJ, 158, 194
Ohno, K., & Ueda, T. 2021, A&A, 651, L2
Opitom, C., Hutsemékers, D., Jehin, E., et al. 2019, A&A, 624, A64
Owen, T., Mahaffy, P., Niemann, H. B., et al. 1999, Nature, 402, 269
Pasek, M. A., Milsom, J. A., Ciesla, F. J., et al. 2005, Icarus, 175, 1
Ruden, S. P., & Pollack, J. B. 1991, ApJ, 375, 740
Schneider, A. D., & Bitsch, B. 2021, A&A, 654, A72
Shakura, N. I., & Sunyaev, R. A. 1973, X- and Gamma-Ray Astronomy, 55, 155
Sromovsky, L. A., Karkoschka, E., Fry, P. M., et al. 2014, Icarus, 238, 137
Stull, D. R. 1947, Ind. Eng. Chem., 39, 517
Tsiganis, K., Gomes, R., Morbidelli, A., et al. 2005, Nature, 435, 459
Venturini, J., & Helled, R. 2020, A&A, 634, A31
Visser, R., Jørgensen, J. K., Kristensen, L. E., et al. 2013, ApJ, 769, 19
Wagner, W., Riethmann, T., Feistel, R., et al. 2011, J. Phys. Chem. Ref. Data, 40, 043103
Weidenschilling, S. J. 1997, Icarus, 127, 290
Williams, J. P., & Cieza, L. A. 2011, ARA&A, 49, 67
Wong, M. H., Mahaffy, P. R., Atreya, S. K., et al. 2004, Icarus, 171, 153
Yang, C.-C., Johansen, A., & Carrera, D. 2017, A&A, 606, A80
Zhang, S., Hu, X., Zhu, Z., et al. 2021, ApJ, 923, 70
Zhu, Z., Hartmann, L., Nelson, R. P., et al. 2012, ApJ, 746, 110

## Appendix A: Vapor pressures of pure condensates

The vapor pressures of the pure condensates considered in this work, except $H_2O$ and $NH_3$, follow the law:

$$\ln P_{\rm eq} = \sum_k a_k \left(\frac{1}{T}\right)^k , \tag{A.1}$$

where the $a_k$ factors have been determined experimentally (Fray & Schmitt 2009) and are summarized in Table A.1.

The vapor pressures of $H_2O$ is given by (Wagner et al. 2011):

$$\begin{aligned} P_{\rm eq} =& P_{\rm tp} \exp\left(\frac{T_{\rm tp}}{T}\right)\left(-21.2144006\left(\frac{T_{\rm tp}}{T}\right)^{1/300}\right. \\ &+ 27.3203819\left(\frac{T_{\rm tp}}{T}\right)^{2.10666667} \\ &\left.-6.10598130\left(\frac{T_{\rm tp}}{T}\right)^{1.70333333}\right), \end{aligned} \tag{A.2}$$

where $P_{\rm tp}$ and $T_{\rm tp}$ are the pressure and the temperature of the triple point of water, respectively.

The phosphine equilibrium pressure is given by Stull (1947):

$$\log_{10} P_{\rm eq} = 4.02591 - \frac{702.651}{T - 11.065}. \tag{A.3}$$

**Table A.1.** Polynomial factors for the vapor pressure equations of pure condensates

| Element | Temperature range (K) | $a_0$ | $a_1$ | $a_2$ | $a_3$ | $a_4$ | $a_5$ | $a_6$ |
|---|---|---|---|---|---|---|---|---|
| CO | T ≤ 61.55 | 10.43 | -721.3 | -10740 | $2.341 \times 10^5$ | $-2.392 \times 10^6$ | $9.478 \times 10^6$ | ∅ |
| | T > 61.55 | 10.25 | -748.2 | -5843 | $3.939 \times 10^4$ | ∅ | ∅ | ∅ |
| $CO_2$ | T ≤ 40 | $10^{-40}$ | ∅ | ∅ | ∅ | ∅ | ∅ | ∅ |
| | 40.0 < T ≤ 194.7 | 14.76 | -2571 | $-7.781 \times 10^4$ | $4.325 \times 10^6$ | $-1.207 \times 10^8$ | $1.350 \times 10^9$ | ∅ |
| | T > 194.7 | 18.61 | -4154 | $1.041 \times 10^5$ | ∅ | ∅ | ∅ | ∅ |
| $CH_4$ | all | 10.51 | -1110 | -4341 | $1.035 \times 10^5$ | $-7.910 \times 10^5$ | ∅ | ∅ |
| $H_2S$ | T ≤ 127.0 | 12.98 | -2707 | ∅ | ∅ | ∅ | ∅ | ∅ |
| | T > 127.0 | 8.933 | -726.0 | $-3.504 \times 10^5$ | $2.724 \times 10^7$ | $-8.582 \times 10^8$ | ∅ | ∅ |
| $N_2$ | T ≤ 35.61 | 12.40 | -80.74 | -3926 | $6.297 \times 10^4$ | $-4.633 \times 10^5$ | $1.325 \times 10^5$ | ∅ |
| | T > 35.61 | 8.514 | -456.4 | $-1.987 \times 10^4$ | $4.800 \times 10^5$ | $-4.524 \times 10^6$ | ∅ | ∅ |
| $NH_3$ | all | 15.96 | -3537 | $-3.310 \times 10^4$ | $1.742 \times 10^6$ | $-2.995 \times 10^7$ | ∅ | ∅ |
| Ar | all | 10.69 | -893.2 | -3567 | $6.574 \times 10^4$ | $-4.280 \times 10^5$ | ∅ | ∅ |
| Kr | all | 10.77 | -1223 | -8903 | $2.635 \times 10^5$ | $-4.260 \times 10^6$ | $3.575 \times 10^7$ | $-1.210 \times 10^8$ |
| Xe | all | 10.698 | -1737 | $-1.332 \times 10^4$ | $4.349 \times 10^5$ | $-7.027 \times 10^6$ | $4.447 \times 10^7$ | ∅ |

## Appendix B: Dissociation pressures of $NH_3$ monohydrate and clathrates

The dissociation pressures of $NH_3$ monohydrate and clathrates follow the Antoine law:

$$\ln P_{\rm eq} = \frac{A}{T} + B, \tag{B.1}$$

with $A$ and $B$ parameters determined from experiments and summarized in Table B.1.

**Table B.1.** Parameters for the dissociation pressure equations of $NH_3$ monohydrate and clathrates

| Element | A | B | Reference |
|---|---|---|---|
| CO | -1685.54 | 10.9946 | Hersant et al. (2004) |
| $CO_2$ | -2544.395 | 11.411518 | Longhi (2005) |
| $CH_4$ | -2161.81 | 11.1249 | Hersant et al. (2004) |
| $H_2S$ | -3111.02 | 11.3801 | Hersant et al. (2004) |
| $N_2$ | -1677.62 | 11.1919 | Hersant et al. (2004) |
| $NH_3$ | -2878.28 | 8.00205 | Hersant et al. (2004) |
| Ar | -1481.78 | 9.95523 | Hersant et al. (2004) |
| Kr | -1987.5 | 9.99046 | Hersant et al. (2004) |
| Xe | -2899.19 | 11.0354 | Hersant et al. (2004) |
| $PH_3$ | -3011.28 | 11.95 | Lunine & Stevenson (1985) |

## B.2. Schneeberger et al. 2024

A&A, 682, L10 (2024)
https://doi.org/10.1051/0004-6361/202348309
© The Authors 2024

Astronomy & Astrophysics

LETTER TO THE EDITOR

# Formation of the Trappist-1 system in a dry protoplanetary disk

Antoine Schneeberger[1], Olivier Mousis[1,2], Magali Deleuil[1,2], and Jonathan I. Lunine[3]

[1] Aix-Marseille Université, CNRS, CNES, Institut Origines, LAM, Marseille, France
e-mail: antoine.schneeberger@lam.fr
[2] Institut Universitaire de France (IUF), Paris, France
[3] Department of Astronomy, Cornell University, Ithaca, NY, USA

Received 18 October 2023 / Accepted 18 January 2024

**ABSTRACT**

A key feature of the Trappist-1 system is its monotonic decrease in bulk density with growing distance from the central star, which indicates an ice mass fraction that is zero in the innermost planets, b and c, and about 10% in planets d through h. Previous studies suggest that the density gradient of this system could be due to the growth of planets from icy planetesimals that progressively lost their volatile content during their inward drift through the protoplanetary disk. Here we investigate the alternative possibility that the planets formed in a dry protoplanetary disk populated with pebbles made of phyllosilicates, a class of hydrated minerals with a water fraction possibly exceeding 10 wt%. We show that the dehydration of these minerals in the inner regions of the disk and the outward diffusion of the released vapor up to the ice-line location allow the condensation of ice onto grains. Pebbles with water mass fractions consistent with those of planets d–h would have formed at the snow-line location. In contrast, planets b and c would have been accreted from drier material in regions closer to the star than the phyllosilicate dehydration line.

**Key words.** methods: numerical – planets and satellites: composition – planets and satellites: formation – protoplanetary disks

## 1. Introduction

Because of its compactness and density gradient, the Trappist-1 exoplanetary system is the closest analog to the well-characterized Galilean moon system. It is also an outstanding laboratory for exploring planet formation around ultracool M dwarfs. The Trappist-1 system contains seven exoplanets in a resonance chain, three of which are within the habitable zone (Gillon et al. 2016, 2017), with semimajor axes ranging between 0.015 and 0.062 AU (Luger et al. 2017; Agol et al. 2021). This resonance chain could be a sign of a past inward drift of the whole system before orbital capture (Ormel et al. 2017; Bitsch et al. 2019; Coleman et al. 2019; Izidoro et al. 2021; Madeira et al. 2021).

The measured densities of the Trappist-1 planets are among the most accurate ones available for an exoplanetary system (Luger et al. 2017). These densities have been used by Acuña et al. (2021) to assess their interiors and compositions. The authors show evidence for an increasing water mass fraction (WMF) of the planets with increasing distance from the host star. The planets can be separated into two groups, with planets b–c containing little to zero water, and planets d–h presenting significant amounts of water (see Table 1). The significant amount of water estimated in the five outermost planets has been interpreted as a sign that they formed beyond the position of the snow line (SL), within the water-rich protoplanetary disk (PPD), prior to their inward migration (Ormel et al. 2017; Johansen et al. 2023). Such a mechanism requires a rapid growth of the planets, which could be eased by the formation of planetesimals via streaming instability triggered by a solid-to-gas ratio above unity at the SL due to ice enrichment (Ormel et al. 2017).

However, red dwarfs produce far-ultraviolet (FUV) and extreme-ultraviolet (XUV) irradiation during their early evolution (Shkolnik & Barman 2014). This can cause the photolytic destruction of the water present in the PPD or in the material originating from the interstellar medium and accreted by the PPD (Shkolnik & Barman 2014; Loyd et al. 2018; Youngblood et al. 2021). Furthermore, repeated episodes of accretional outbursts by Trappist-1 could have produced rapid temperature rises in the PPD that would dehydrate pebbles (Houge & Krijt 2023). Finally, sequestration of oxygen in rock- and metal-forming species must be considered when the carbon-to-oxygen (C/O) ratio exceeds the solar value (0.55; Lodders 2021) in the PPD. When the C/O ratio reaches or exceeds 0.8, the depletion of oxygen is severe; it is bound up in rock, metal oxides, CO, and $CO_2$, hindering the production of water (Pekmezci et al. 2019).

In systems where one or both of the water loss processes occur, an interesting alternative is to consider the case where water would be embedded in phyllosilicate particles. Phyllosilicates form a large group of hydrous minerals, which are structured in layers bounded by cation–anion couples that contain OH groups in their crystalline structure. They can contain $H_2O$ molecules between layers, and dehydration experiments show that serpentinite minerals (one of the most common forms) can hold up to ∼13 wt% of water (Bezacier et al. 2010; Chauviré et al. 2021; Pettke & Bretscher 2022).

Detection of phyllosilicate grains was claimed in the interstellar medium and PPDs (Zaikowski et al. 1975; Whittet et al. 1997; Reach et al. 2009). However, this evidence has since been reinterpreted as a mixture of amorphous silicates and water ice (Gibb et al. 2004; Potapov et al. 2021). On the other hand,



Open Access article, published by EDP Sciences, under the terms of the Creative Commons Attribution License (https://creativecommons.org/licenses/by/4.0), which permits unrestricted use, distribution, and reproduction in any medium, provided the original work is properly cited.
This article is published in open access under the Subscribe to Open model. Subscribe to A&A to support open access publication.

phyllosilicates are found in CI and CM chondrites, which have WMFs as high as 10% (Beck et al. 2010, 2014; Alexander 2019). The current consensus is that phyllosilicates found in CM chondrites are formed by aqueous alteration of silicates in water-rich planetesimals (Bischoff 1998; Suttle et al. 2021). Such ice-rich solids can form in the vicinity of the water SL and become precursors of phyllosilicate-rich pebbles (Bischoff 1998) via collisional evolution.

However, hydrous mineral inclusions within chondritic meteorites exhibit a distinct D/H ratio and hydration heterogeneity, favoring a primitive origin (Metzler et al. 1992; Ciesla et al. 2003; Piani et al. 2021). This supports models that show that micrometric phyllosilicate grains can result from the alteration of silicate grains by water vapor over a time period of ~100 kyr in the PPD (D'Angelo et al. 2019; Thi et al. 2020). This is also consistent with the idea that phyllosilicate nanocrystals could form in the wake of shock waves crossing the PPD (Ciesla et al. 2003). These shock waves would produce a temperature rise of up to 2000 K (Ciesla et al. 2003; Burkhardt et al. 2019), which would evaporate water ice and melt silicates. As the molten silicate recrystallized, it would react with the surrounding water vapor to form phyllosilicate nanocrystals within a few days of the shock wave. Both processes require the presence of water vapor, which implies that they occurred early in the history of the PPD.

The possible dearth of water as ice in red dwarf PPDs suggests an alternative scenario where (i) the Trappist system formed in a dry PPD devoid of volatiles, and (ii) water was only delivered to the inner disk in the form of phyllosilicate minerals. Figure 1 qualitatively describes this scenario in which three distinct regions coexist in the disk: an inner region occupied by dehydrated phyllosilicates that is located inside the phyllosilicate dehydration line (PDL), a second region containing hydrated phyllosilicates and bracketed by the PDL and the SL, and an outer region populated by phyllosilicates coated with ice and extending from the SL. In this scenario, phyllosilicates dehydrate in the inner part of the disk due to increasing temperature and release water vapor at the PDL, which viscously diffuses inward and outward, eventually crossing the SL, where it condenses onto grains. This formation mechanism has been successfully applied to the Galilean moons to account for their observed density gradient (Mousis et al. 2023).

We have investigated the evolution of the WMF of phyllosilicate-rich pebbles during their transport and growth in a dry PPD. We used the one-dimensional volatile evolution model in a PPD from Aguichine et al. (2020, 2022) and Schneeberger et al. (2023), to which we added the dehydration of phyllosilicates at the PDL location. We tracked the WMF evolution of pebbles at the SL location, assuming a starting WMF in the phyllosilicate grains in the 1–10% range. We then studied the impact of the proposed scenario on the formation history of the Trappist-1 system.

## 2. Disk model

Our PPD model is based on the PPD model presented in Aguichine et al. (2020, 2022), Mousis et al. (2020), and Schneeberger et al. (2023). To size the model to the Trappist-1 system, the central star mass was scaled down to 0.0802 $M_\odot$ (Gillon et al. 2016). We also opted to linearly scale the disk mass and accretion rate from 0.1 $M_\odot$ and $10^{-7.6}$ $M_\odot\,\mathrm{yr}^{-1}$ for the PPD (Hartmann et al. 1998) to 0.1 $M_\star$ and $10^{-7.6}$ $M_\star\,\mathrm{yr}^{-1}$ for the Trappist-1 system, with $M_\star$ being the mass of Trappist-1.

**Table 1.** Estimated masses and WMFs for Trappist-1 planets (Acuña et al. 2021).

| Planet | Mass ($M_\oplus$) | WMF |
|---|---|---|
| b | $1.375 \pm 0.041$ | $(3.1^{+0.5}_{-3.1}) \times 10^{-5}$ |
| c | $1.300 \pm 0.036$ | $(0.0^{+4.4}_{-0.0}) \times 10^{-6}$ |
| d | $0.388 \pm 0.007$ | $0.084 \pm 0.071$ |
| e | $0.699 \pm 0.013$ | $0.094 \pm 0.067$ |
| f | $1.043 \pm 0.019$ | $0.105 \pm 0.073$ |
| g | $1.327 \pm 0.024$ | $0.119 \pm 0.080$ |
| h | $0.327 \pm 0.012$ | $0.081^{+0.059}_{-0.081}$ |

Our PPD model follows the differential equation (Lynden-Bell & Pringle 1974)

$$\frac{\partial \Sigma_\mathrm{g}}{\partial t} = \frac{3}{r}\frac{\partial}{\partial r}\left[r^{1/2}\frac{\partial}{\partial r}\left(r^{1/2}\Sigma_\mathrm{g}\nu\right)\right], \tag{1}$$

where $\Sigma_\mathrm{g}$ is the gas surface density and $\nu$ is the gas viscosity. Our model assumes invariance in the orbital direction and hydrostatic equilibrium in the azimuthal direction. The viscosity is given by (Shakura & Sunyaev 1973)

$$\nu = \alpha\frac{C_\mathrm{s}^2}{\Omega_k}, \tag{2}$$

where $\alpha$ is the viscosity parameter set to the canonical value of $10^{-3}$ (Shakura & Sunyaev 1973; Lynden-Bell & Pringle 1974), $C_\mathrm{s}$ the sound of speed, and $\Omega_k$ the Keplerian pulsation.

The initial disk profile was computed from the self-similar solution derived by Lynden-Bell & Pringle (1974):

$$\Sigma_{\mathrm{g},0} = \frac{\dot{M}_{\mathrm{acc},0}}{3\pi\nu}\exp\left[-\left(\frac{r}{r_\mathrm{c}}\right)^{0.5}\right], \tag{3}$$

with $\dot{M}_{\mathrm{acc},0}$ the initial accretion rate onto the PPD and $r_\mathrm{c}$ the centrifugal radius of the disk. The centrifugal radius was self-consistently computed at its initialization as described in Aguichine et al. (2020).

Figure 2 shows the surface density, midplane pressure, and temperature profiles derived from our Trappist-1 PPD model and from the PPD model used by Schneeberger et al. (2023) after 0.01, 0.1, and 1 Myr of disk evolution. The comparison shows that the Trappist-1 PPD is cooler and less dense by a factor of ~5–10 in the 0.5–10 AU region of the disk. The midplane pressure of the Trappist-1 PPD is also ~30–70 times lower than in the PPD model of Schneeberger et al. (2023).

The evolution of the different water phases follows the advection-diffusion equation (Birnstiel et al. 2012; Desch et al. 2017):

$$\frac{\partial \Sigma_i}{\partial t} + \frac{1}{r}\frac{\partial}{\partial r}\left[r\left(\Sigma_i v_i - D_i\Sigma_\mathrm{g}\frac{\partial}{\partial r}\left(\frac{\Sigma_i}{\Sigma_\mathrm{g}}\right)\right)\right] - \dot{Q}_i = 0, \tag{4}$$

where $\Sigma_i$ is the water surface density of phase $i$, either in vapor or ice form, $v_i$ and $D_i$ are the drift velocity and diffusivity, respectively, and $Q_i$ is the source or sink term of phase $i$, which takes the condensation and vaporization of water into account. The evolution of grains is governed by the two-population algorithm, which provides their mean drift speed and diffusivity (Birnstiel et al. 2012).

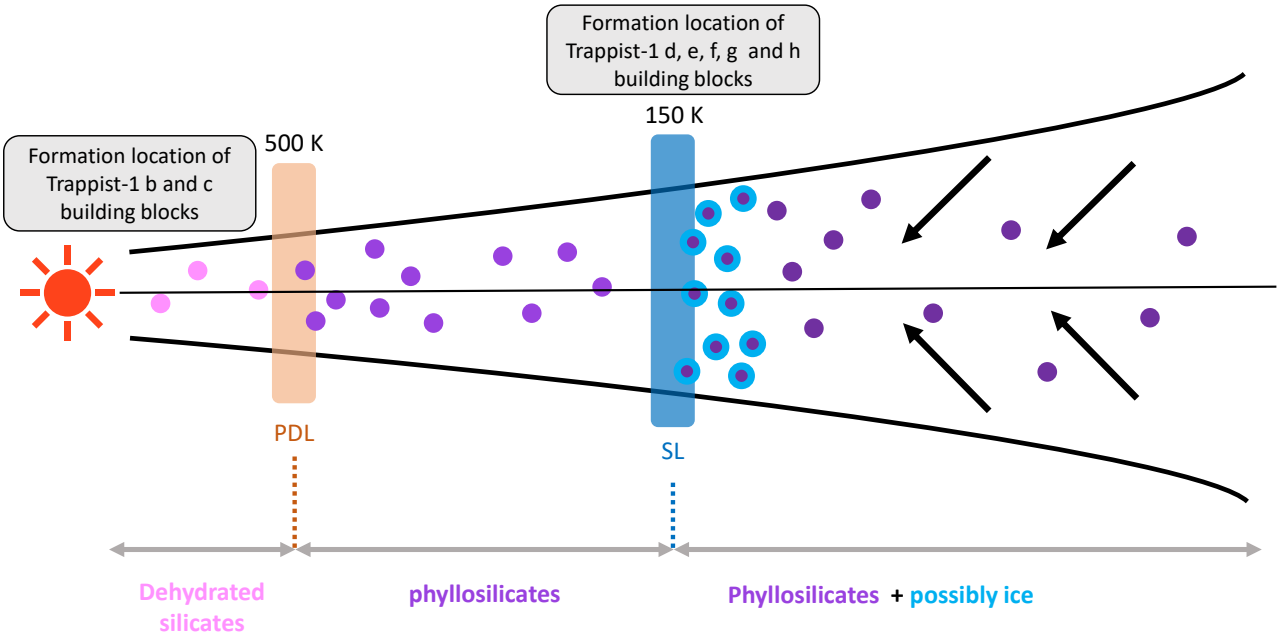


**Fig. 1.** Structure of Trappist-1's PPD. Phyllosilicate grains (purple dots) drift inward in the disk. When these grains cross the PDL (orange bar), they dehydrate and release water as vapor. Only silicate grains remain inside the PDL (pink dots). The vapor viscously diffuses inward and outward and eventually crosses the SL (blue bar), where it condenses and coats phyllosilicate grains with ice (blue shell).

The water source and sink terms are governed by its equilibrium pressure (Wagner et al. 2011):

$$P_{\rm eq} = P_{\rm tp} \exp\left(\frac{T_{\rm tp}}{T}\right)\left(-21.2144006\left(\frac{T_{\rm tp}}{T}\right)^{1/300} + 27.3203819\left(\frac{T_{\rm tp}}{T}\right)^{2.10666667} - 6.10598130\left(\frac{T_{\rm tp}}{T}\right)^{1.70333333}\right), \quad (5)$$

where $P_{\rm tp}$ and $T_{\rm tp}$ are the water triple point pressure (611.65 Pa) and temperature (273.16 K), respectively. The equilibrium pressure is compared with the partial pressure of water:

$$P_{\rm v} = \frac{\Sigma_{\rm v} R T}{\sqrt{2\pi}\mu_{H_2O} H}, \quad (6)$$

where $\Sigma_{\rm v}$ is the water vapor surface density, $R$ is the perfect gas constant, $T$ is the disk temperature, $\mu_{\rm H_2O}$ is the water molar mass, and $H$ is the disk scale height. If the vapor partial pressure is higher than the equilibrium one, then it condenses onto the pebbles and forms an icy shell. Condensation then results in a source term for water ice of

$$\dot{Q}_{\rm ice} = \min\left(\left(P_{\rm v} - P_{\rm eq}\right)\frac{2H\mu_{\rm H_2O}}{RT\Delta t}; \frac{\Sigma_{{\rm v},i}}{\Delta t}\right). \quad (7)$$

Conversely, if the vapor partial pressure is lower than the equilibrium pressure, ice vaporizes, resulting in a sink term for water ice of

$$\dot{Q}_{\rm ice} = -\min\left(\sqrt{\frac{8\pi\mu_i}{RT}}\frac{3}{\pi\bar{a}\bar{\rho}}P_{\rm eq}\Sigma_{\rm ice}; \frac{\Sigma_{\rm ice}}{\Delta t}\right), \quad (8)$$

where $\bar{a}$ and $\bar{\rho}$ are the grains' mean size and mean density as given by the two-population algorithm, respectively.

We added a module that takes the dehydration of phyllosilicates into account. We considered that phyllosilicates dehydrate when they reach a temperature of 500 K in the disk (Mousis et al. 2023). Phyllosilicate-rich particles release water vapor at the PDL location in the PPD, which corresponds to the following source term for water vapor:

$$\dot{Q} = {\rm WMF}_{\rm phyllo}\frac{\Sigma_{\rm p}}{{\rm d}t}, \quad (9)$$

where $\rm WMF_{phyllo}$ is the WMF in the phyllosilicates, which is varied in the 1–10% range, and $\Sigma_{\rm p}$ is the surface density of phyllosilicates. We assumed that the phyllosilicate dehydration timescale is much shorter than the drift timescale (Ciesla & Lauretta 2005; Mousis et al. 2023). All the water stored in the phyllosilicate dust or pebbles is released when they cross the PDL location. The PPD model was initialized with phyllosilicate grains of 0.1 µm in size. The initial phyllosilicate abundance, $x_{\rm p}^0 = \Sigma_{\rm p}^0/\Sigma_{\rm g}^0$, was set to $3.212 \times 10^{-3}$ (Lodders et al. 2009).

## 3. Results

Figure 3 displays water ice and vapor enrichment profiles in the PPD, with respect to the initial water abundance, after 0.01, 0.1, and 1 Myr of disk evolution. The initial water abundance is defined as

$$x_{\rm H_2O}^0 = {\rm WMF}_{\rm phyllo}\, x_{\rm p}^0. \quad (10)$$

Since the disk only contains phyllosilicate at $t = 0$, the starting water abundance only depends on the water contained in phyllosilicate particles. $\rm WMF_{phyllo}$ of 1%, 5%, and 10% were used in the simulations. The distance between the SL and the central star increases from 0.67 to 0.85 AU, 0.53 to 0.66 AU, and 0.35 to 0.43 AU when the $\rm WMF_{phyllo}$ value is ranged between 1% and 10% at 0.01, 0.1, and 1 Myr of PPD evolution, respectively.

The increase in this distance range is the direct consequence of the decrease in the amount of water vapor released from the

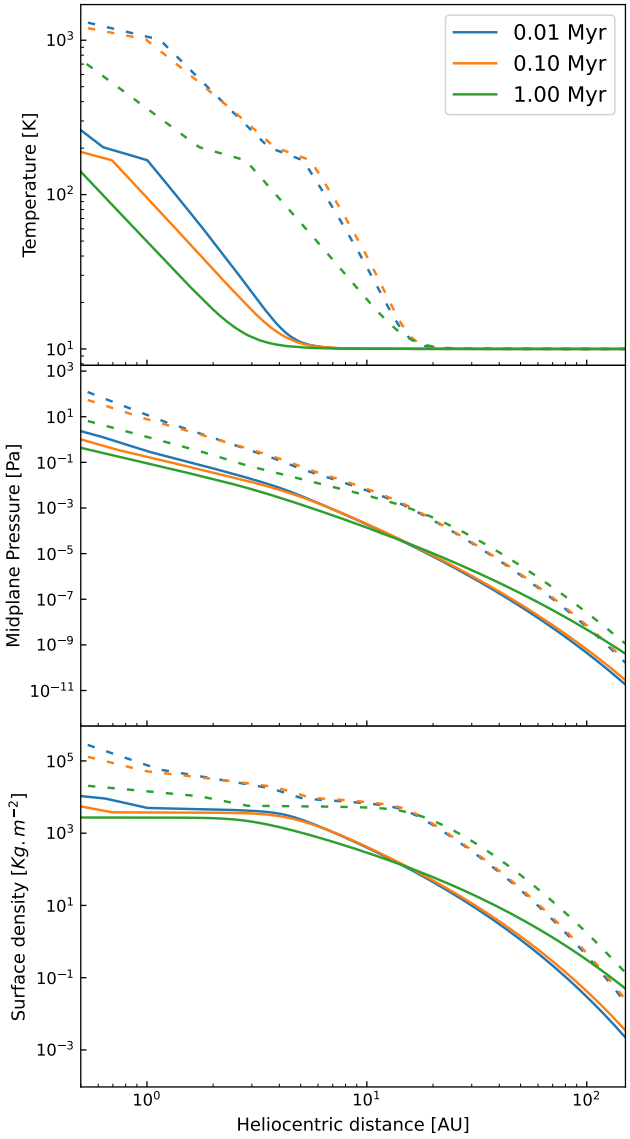


**Fig. 2.** From top to bottom: Temperature, pressure, and surface density profiles of the Trappist-1 PPD (solid lines) superimposed onto those of the PPD taken from Schneeberger et al. (2023; dashed lines) after 0.01, 0.1, and 1 Myr of evolution.

pebbles into the PPD. Vapor accumulates at the PDL because its diffusion rate in the PPD is much lower than its production rate. A fraction of this vapor diffuses outward and crosses the SL.

Figure 3 shows that the water ice enrichment reaches a maximum at ∼0.4, 1.3, and 2 times the initial water abundance before 0.01 Myr of PPD evolution, assuming a $WMF_{phylo}$ of 1, 5, and 10%, respectively. Between 0.01 and 0.1 Myr of PPD evolution, the water enrichment decreases by a factor of ∼20–30 down to 0.02, 0.04, and 0.07 times the initial water abundance. After 0.1 Myr, the ice enrichment remains almost constant up to 1 Myr, which corresponds to the end of our simulations.

Figure 4 represents the time evolution of the pebbles' WMF at the SL location when $WMF_{phyllo}$ varies between 1 and 10%. The dark orange area corresponds to the range of nominal WMFs (8.1–11.9% ) computed by Acuña et al. (2021) for Trappist-1 d, e, f, g, and h. The light orange area brackets the $1\sigma$ error bars (0–19.9%) associated with those measurements. The WMF of pebbles takes both the fraction of water in ice form and water trapped in phyllosilicates into account:

$$WMF = \frac{WMF_{phyllo}\Sigma_p + \Sigma_{ice}}{\Sigma_p + \Sigma_{ice}}, \quad (11)$$

with $\Sigma_{ice}$ the surface density of ice in the PPD. Figure 4 shows that even in the absence of ice in the PPD at initialization, the pebbles' WMF is 2–3 times larger than $WMF_{phyllo}$ after only 0.01 Myr of evolution. The pebbles' WMF ranges between 2 and 28% when $WMF_{phyllo}$ is varied between 1 and 10%. As the PPD depletes, the amount of water vapor released from the phyllosilicates decreases, reducing the amount of ice condensed at the SL. Consequently, the pebbles' WMF converges toward $WMF_{phyllo}$ after 0.07 Myr of PPD evolution. This implies that only cases with $WMF_{phyllo}$ in the 8–10% range match the WMF of planets d–h after 0.07 Myr of PPD evolution. Interestingly, cases with pebbles that assume a $WMF_{phyllo}$ in the 4–7% range also match the WMF of planets d–h before 0.07 Myr of PPD evolution. However, after this epoch, water ice is too depleted in the PPD.

## 4. Discussion

The scenario we have explored for the Trappist-1 system divides the PPD into three distinct regions: (i) an inner region interior to the PDL in which solids consist of pebbles made of dehydrated silicates, (ii) an intermediary region located between the PDL and the SL populated with pebbles assembled from hydrated phyllosilicates, and (iii) a region located beyond the SL populated with pebbles consisting of hydrated phyllosilicate pebbles coated with water ice.

In this scenario, the building blocks of planets b and c would have formed in regions interior to the PDL, while those of planets d–h would have formed at the SL. Planets b and c would have grown close to the star, possibly at their present-day location. On the other hand, planets d–h would have grown farther from the star than their current location (Ormel et al. 2017; Coleman et al. 2019; Huang & Ormel 2022; Ogihara et al. 2022). They could have migrated inward to their present-day location after formation. The inward migration of all planets could have led to the observed mean motion resonance chain formed by the seven planets (Ormel et al. 2017; Bitsch et al. 2019; Coleman et al. 2019; Izidoro et al. 2021).

The dehydration temperature of phyllosilicates at pressure conditions relevant to those of PPDs is not well established. In our study we chose a dehydration temperature of 500 K to explore its effect on the pebbles' WMF (Mousis et al. 2023). Varying the dehydration temperature between 400 K and 600 K has a significant impact on the timescales and extents of ice enrichment in the PPD. A higher dehydration temperature results in a PDL located closer to the star than in cases with lower temperatures. Therefore, colder dehydration temperatures reduce the distance between the PDL and SL, enhance the amount of vapor diffusing throughout the SL, and lead to higher abundances of solid water. A dehydration temperature of 400 K induces an ice enrichment up to ∼20 times the initial water abundance after 0.01 Myr of PPD evolution, assuming $WMF_{phyllo}$ = 10% in phyllosilicates. In contrast, only an ice enrichment of ∼0.5 is generated in the PPD, assuming a dehydration temperature of 600 K. These results show that our simulations are highly sensitive to the dehydration temperature. This variability impacts the evolution of the pebbles' WMF at the SL. Consequently, a lower dehydration temperature enables the formation of pebbles with WMFs consistent with those of planets d–h, assuming they

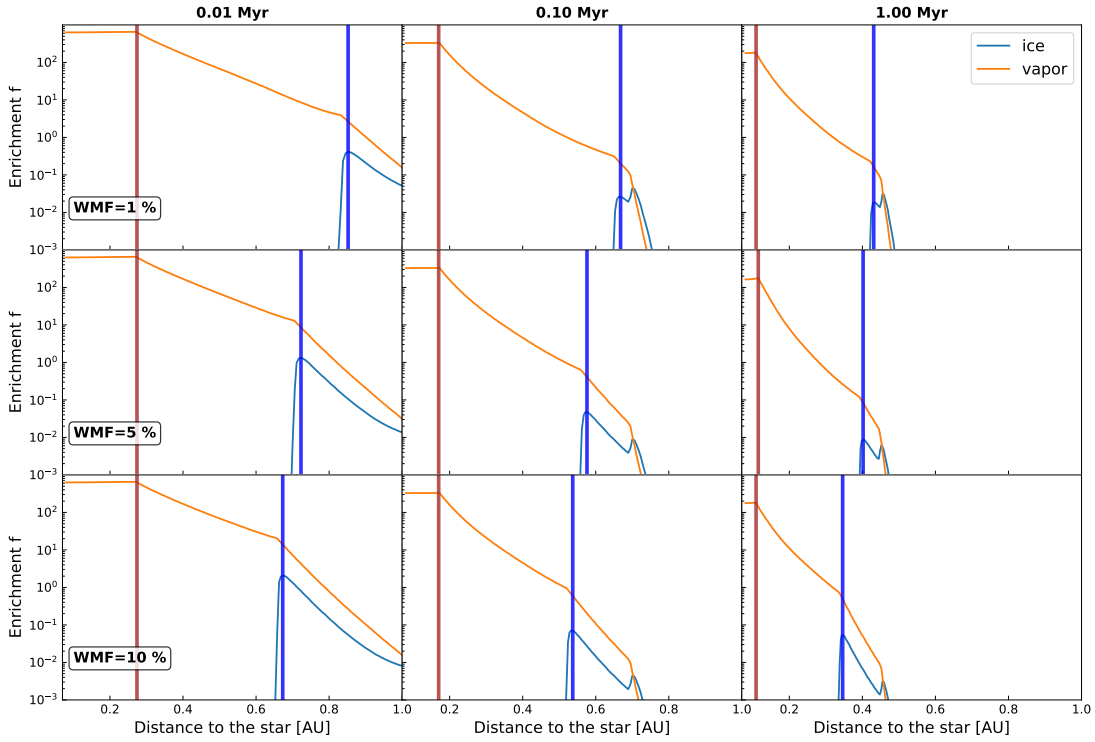


**Fig. 3.** From left to right: Enrichment profiles of water vapor (orange lines) and ice (blue lines) normalized with the initial abundance of water in phyllosilicates at $t$ = 0.01, 0.1, and 1 Myr. The initial WMFs in phyllosilicates here are 1%, 5%, and 10%. The PDL and SL are represented as brown and blue bars, respectively.

start with $WMF_{phyllo}$ lower than the nominal value (8%) after 1 Myr of PPD evolution. Conversely, a higher dehydration temperature requires higher $WMF_{phyllo}$ values to reproduce the WMFs of planets d–h after 1 Myr of PPD evolution.

To compare the sensitivity of our results against the PPD parameters, we reduced the PPD's initial mass from $10^{-1}$ to $10^{-2}$ $M_\star$. A less massive PPD has a lower density, resulting in reduced temperature and diffusion factor profiles. As a consequence, despite a reduced distance between the SL and the PDL of ∼0.3 AU, there is a decrease in the amount of vapor crossing the SL and condensing into ice. The water enrichment at the SL is reduced by a factor of ∼200 after 0.1 Myr of PPD evolution compared with the nominal enrichment, assuming a 10% $WMF_{phyllo}$. After 1 Myr of PPD evolution, the disk dissipates almost completely and very few phyllosilicate grains remain, resulting in an even lower water vapor production. This indicates that the PPD has a somewhat significant mass (allowing it to generate pebbles) that is consistent with the WMFs of planets d–h.

The proposed scenario relies on water loss by photolysis driven by FUV/XUV radiation from Trappist-1, whose intensity and time evolution remain unknown. If the FUV/XUV radiation levels were very low, it is likely that primordial water ice would remain abundant in the PPD. On the other hand, an extreme FUV/XUV radiation episode of sufficient duration would destroy the vapor released by phyllosilicate grains and pebbles, thereby preventing any ice formation at the SL. Consequently, a dry disk model represents an alternative scenario to the formation of the Trappist planets from volatile-rich material (Ormel et al. 2017; Bitsch et al. 2019). An observational test to investigate a dry disk scenario would be the discovery of a planet more distant than Trappist-1 h but with a density close to those of Trappist-1 b–c. This would imply that this planet formed from

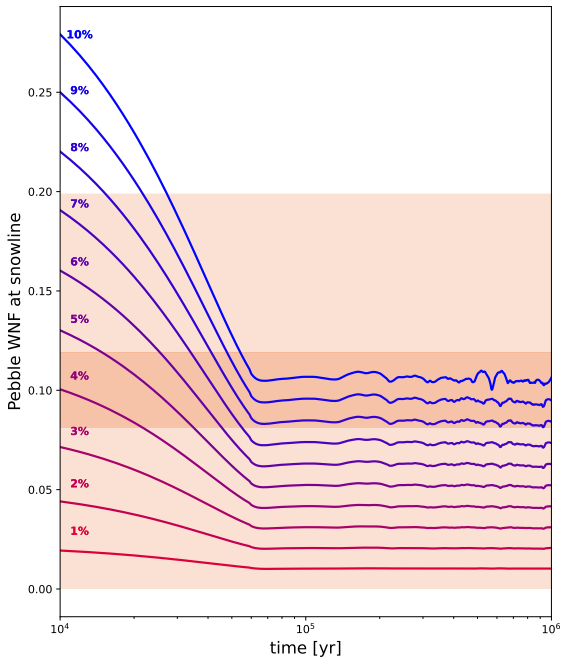


**Fig. 4.** Time evolution of the pebbles' WMFs at the SL location. The phyllosilicate WMF is varied between 1 and 10%. The range of the WMF central values of the different Trappist-1 planets is bracketed by the dark orange box (Acuña et al. 2021), and the 1$\sigma$ errors are shown in light orange.

phyllosilicate-rich building blocks beyond the SL. In contrast, the same planet formed in a wet disk would have a density similar to those of planets d–h. Both scenarios could have been at

play during the Trappist system formation. In this case, the inner planets would have formed from pebbles made of dehydrated phyllosilicates. The outer planets would have accreted from ice-rich pebbles sourced from (i) water vapor condensation after outward diffusion from the inner regions and (ii) pristine ice delivered from the outer regions.

*Acknowledgements.* The project leading to this publication has received funding from the Excellence Initiative of Aix-Marseille Université–A*Midex, a French "Investissements d'Avenir program" AMX-21-IET-018. This research holds as part of the project FACOM (ANR-22-CE49-0005-01_ACT) and has benefited from a funding provided by l'Agence Nationale de la Recherche (ANR) under the Generic Call for Proposals 2022. We acknowledge Maxime Pineau for helpful discussions about phyllosilicate properties and experiments.

## References

Acuña, L., Deleuil, M., Mousis, O., et al. 2021, A&A, 647, A53
Agol, E., Dorn, C., Grimm, S. L., et al. 2021, Planet. Sci. J, 2, 1
Aguichine, A., Mousis, O., Devouard, B., et al. 2020, ApJ, 901, 97
Aguichine, A., Mousis, O., & Lunine, J. I. 2022, Planet. Sci. J, 3, 141
Alexander, C. M. O. 2019, Geochim. Cosmochim. Acta, 254, 246
Beck, P., Quirico, E., Montes-Hernandez, G., et al. 2010, Geochim. Cosmochim. Acta, 74, 4881
Beck, P., Garenne, A., Quirico, E., et al. 2014, Icarus, 229, 263
Bezacier, L., Reynard, B., Bass, J. D., et al. 2010, Earth Planet Sci. Lett., 289, 198
Birnstiel, T., Klahr, H., & Ercolano, B. 2012, A&A, 539, A148
Bischoff, A. 1998, Meteor. Planet. Sci., 33, 1113
Bitsch, B., Raymond, S. N., & Izidoro, A. 2019, A&A, 624, A109
Burkhardt, A. M., Shingledecker, C. N., Le Gal, R., et al. 2019, ApJ, 881, 32
Chauviré, B., Pineau, M., Quirico, E., et al. 2021, Earth Planet. Sci. Lett., 576, 117239
Ciesla, F., & Lauretta, D. 2005, Earth Planet. Sci. Lett., 231, 1
Ciesla, F. J., Lauretta, D. S., Cohen, B. A., et al. 2003, Science, 299, 549
Coleman, G. A. L., Leleu, A., Alibert, Y., et al. 2019, A&A, 631, A7
D'Angelo, M., Cazaux, S., Kamp, I., et al. 2019, A&A, 622, A208
Desch, S. J., Estrada, P. R., Kalyaan, A., et al. 2017, ApJ, 840, 86
Gibb, E. L., Whittet, D. C. B., Boogert, A. C. A., et al. 2004, ApJS, 151, 35
Gillon, M., Jehin, E., Lederer, S. M., et al. 2016, Nature, 533, 221
Gillon, M., Triaud, A. H. M. J., Demory, B.-O., et al. 2017, Nature, 542, 456
Hartmann, L., Calvet, N., Gullbring, E., et al. 1998, ApJ, 495, 385
Houge, A., & Krijt, S. 2023, MNRAS, 521, 5826
Huang, S., & Ormel, C. W. 2022, MNRAS, 511, 3814
Izidoro, A., Bitsch, B., Raymond, S. N., et al. 2021, A&A, 650, A152
Johansen, A., Ronnet, T., Schiller, M., et al. 2023, A&A, 671, A74
Lodders, K. 2021, Space Sci. Rev., 217, 44
Lodders, K., Palme, H., & Gail, H.-P. 2009, Landolt-Börnstein, 4B, 712
Loyd, R. O. P., Shkolnik, E. L., Schneider, A. C., et al. 2018, ApJ, 867, 70
Luger, R., Sestovic, M., Kruse, E., et al. 2017, Nat. Astron., 1, 0129
Lynden-Bell, D., & Pringle, J. E. 1974, MNRAS, 168, 603
Madeira, G., Izidoro, A., & Giuliatti Winter, S. M. 2021, MNRAS, 504, 1854
Metzler, K., Bischoff, A., & Stoeffler, D. 1992, Geochim. Cosmochim. Acta, 56, 2873
Mousis, O., Aguichine, A., Helled, R., et al. 2020. Philos. Trans. R. Soc. London Ser. A, 378, 20200107
Mousis, O., Schneeberger, A., Lunine, J. I., et al. 2023, ApJ, 944, L37
Ogihara, M., Kokubo, E., Nakano, R., et al. 2022, A&A, 658, A184
Ormel, C. W., Liu, B., & Schoonenberg, D. 2017, A&A, 604, A1
Pettke, T., & Bretscher, A. 2022, Earth Sci. Rev., 225, 103896
Piani, L., Marrocchi, Y., Vacher, L. G., et al. 2021, Earth Planet. Sci. Lett., 567, 117008
Pekmezci, G. S., Johnson, T. V., Lunine, J. I., et al. 2019, ApJ, 887, 3
Potapov, A., Bouwman, J., Jäger, C., et al. 2021, Nat. Astron., 5, 78
Reach, W. T., Faied, D., Rho, J., et al. 2009, ApJ, 690, 683
Schneeberger, A., Mousis, O., Aguichine, A., et al. 2023, A&A, 670, A28
Shakura, N. I., & Sunyaev, R. A. 1973, A&A, 24, 337
Shkolnik, E. L., & Barman, T. S. 2014, AJ, 148, 64
Suttle, M. D., King, A. J., Schofield, P. F., et al. 2021, Geochim. Cosmochim. Acta, 299, 219
Thi, W. F., Hocuk, S., Kamp, I., et al. 2020, A&A, 635, A16
Wagner, W., Riethmann, T., Feistel, R., et al. 2011, J. Phys. Chem. Ref. Data, 40, 043103
Whittet, D. C. B., Boogert, A. C. A., Gerakines, P. A., et al. 1997, ApJ, 490, 729
Youngblood, A., Pineda, J. S., & France, K. 2021, ApJ, 911, 112
Zaikowski, A., Knacke, R. F., & Porco, C. C. 1975, Ap&SS, 35, 97